UNIVERSIDAD COMPLUTENSE DE MADRID

FACULTAD DE CIENCIAS FÍSICAS
Departamento de Física de la Tierra, Astronomía y Astrofísica II

TESIS DOCTORAL

Analysis of flares in the chromosphere and corona of main-and pre-main sequence M-type stars

Análisis de fulguraciones en la cromosfera y corona de estrellas tipo M de la secuencia principal y jóvenes

MEMORIA PARA OPTAR AL GRADO DE DOCTOR

PRESENTADA POR

Inés Crespo Chacón

Directores

Mª José Fernández-Figueroa
David Montes Gutiérrez

Madrid, 2016

Universidad Complutense de Madrid
Facultad de CC. Físicas
Departamento de Física de la Tierra, Astronomía y Astrofísica II
(Astrofísica y CC. de la Atmósfera)

Analysis of flares in the chromosphere and corona of main- and pre-main-sequence M-type stars

Análisis de fulguraciones en la cromosfera y corona
de estrellas tipo M de la secuencia principal y jóvenes

Dissertation submitted by
Inés Crespo Chacón
for the degree of
PHILOSOPHIAE DOCTOR in Physics
Madrid, October 2015

Supervised by
Dr. M^{a} José Fernández-Figueroa & Dr. David Montes Gutiérrez
(Emeritus and Permanent Professors - Universidad Complutense de Madrid)

Some of the chapters included in this document have already been published in “Astronomy & Astrophysics” or in “The Astrophysical Journal”.

Agradecimientos

La presente tesis doctoral ha supuesto más de lo que se describe en este libro. Esta tesis se ha llevado sin duda parte de mí. Es fruto de años de dedicación, esfuerzo y sacrificio. Sin embargo, he tenido la fortuna de no realizar sola el largo viaje que me ha traído hasta aquí, a pesar de que en determinados momentos de la travesía me haya sentido sola ante el "peligro". Algunas personas me han acompañado desde el principio hasta el fin del camino. Otras se unieron durante trayectos más o menos largos del mismo. A todas ellas dedico las siguientes líneas, que desearía sirviesen para expresarles mi más profundo y sincero agradecimiento.

En primer lugar debo agradecer al Ministerio de Educación, Cultura y Deporte la financiación proporcionada a través de la beca AP2001-0475 del Programa Nacional de Formación de Profesorado Universitario (F.P.U.), que me fue concedida para llevar a cabo el Doctorado. De igual forma agradezco los fondos procedentes de la subvención europea MERGCT-2007-046535 incluida dentro de las "Marie Curie Actions"; así como los fondos recibidos de los proyectos AYA2004-03749, AYA2005-02750, AYA2008-00695 y AYA2008-06423-C03-03 del Programa Nacional de Astronomía y Astrofísica. Todos ellos han contribuido en mayor o menor medida a la realización de esta obra y/o a mi formación como investigadora.

Agradezco a los directores de esta tesis, los Doctores Mª José Fernández Figueroa y David Montes Gutiérrez, que me abrieran las puertas de su equipo de investigación, que confiaran en mí para sacar adelante este trabajo y que me permitieran desde el primer momento participar activamente en sus proyectos científicos.

Mención especial merecen los Doctores Giuseppina Micela y Fabio Reale, grandes profesionales y aún mejores personas, que durante mi estancia en el Observatorio Astronómico de Palermo y posteriormente en la distancia pusieron a mi disposición sus conocimientos, prestándome su valiosa ayuda de forma totalmente desinteresada. Ha sido un privilegio conocerlos y trabajar a su lado. Sin ellos esta tesis no sería la que ahora es.

Hago extensivo mi agradecimiento al resto de co-autores de las publicaciones que dan forman a la presente tesis, en especial a los Doctores Javier López Santiago, David García Álvarez, Marilena Caramazza e Ignazio Pillitteri, por contribuir al desarrollo de esta investigación con su tiempo, experiencia y sabiduría.

No puedo dejar de agradecer a Giovanni Peres y Laura Affer que hayan dedicado su tiempo a leer y valorar esta memoria, así como sus valiosos comentarios, que han ayudado a mejorarla.

Asimismo, me gustaría expresar mi gratitud hacia todos los que han formado parte, desde 2001 hasta la fecha, del grupo de *estrellas frías y actividad estelar* de la Universidad

Complutense de Madrid (UCM). En especial doy las gracias a los Profesores Elisa de Castro Rubio y Manuel Cornide Castro-Piñeiro, por brindarme su ayuda siempre que la he necesitado; y a mis compañeras Mª Magdalena Hernán Obispo, Raquel Mercedes Martínez Arnáiz y Mª Cruz Gálvez Ortiz, por haber compartido conmigo el día a día, por la ciencia intercambiada, por escucharme y proporcionarme su apoyo, por los buenos momentos que hemos pasado juntas y en definitiva, por su amistad.

Vaya también mi agradecimiento para el lugar donde se encontraba adscrita mi beca F.P.U.: el Departamento de Física de la Tierra, Astronomía y Astrofísica II de la UCM. De entre los miembros del mismo que aún no han sido nombrados, especial reconocimiento merecen: Manuel Rego Fernández, por el gran interés demostrado durante la evolución de este trabajo y sus palabras de ánimo; Sergio Pascual Ramírez y Pablo Guillermo Pérez González, por regalarme su tiempo para ayudarme y enseñarme a resolver los problemas informáticos surgidos cuando "mi linux" y yo dejábamos de entendernos; y Antonio Verdet Paredes y Mª del Carmen Eliche Moral por su compañía, respaldo y todo lo que he reído (y a veces llorado) a su lado.

Agradezco al Observatorio Astronómico de Palermo que me acogiese durante la estancia que llevé a cabo para enriquecer los contenidos de mi tesis doctoral. Agradezco igualmente al que era su director por aquel entonces, Salvatore Sciortino, su disposición a la hora de agilizar los trámites necesarios para solicitar dicha estancia. Del mismo modo no puedo dejar de agradecer a Jorge Sanz Forcada que me facilitara el camino para establecer un primer contacto con este centro. Gracias a todos los trabajadores del mismo y al resto de personas que en Palermo conocí, por hacerme sentir como en casa desde el primer día... "Grazie a Tutti!', especialmente a los ya mencionados Giusi, Fabio, Ignazio, Marilena, Giovanni y Laura, así como a Sara, Marco, Facundo, Daniela, Costanza, Luigi, Ettore y Germano. Sois alucinantes y os llevo en el corazón.

Doy las gracias a Santiago Pérez Hoyos por estar y tenerme presente a pesar de la distancia, por las risas y la alegría compartidas, por saber ver el potencial que hay en mí. Gracias por escucharme pacientemente, por hacerme pensar, por reconfortarme y mostrarme la luz en los momentos de oscuridad. Gracias, pequeño saltamontes, por abrirme tu mundo y hacer del mío un lugar mejor.

Quiero agradecer a mis compañeros del Centro de Estudios y Experimentación de Obras Públicas su apoyo. Gracias a todos por animarme a poner el punto final a esta etapa.

Agradezco a Mayte, Patricia, Gracia, Sofía, María, Ricardo y Silvia que estén ahí para arroparme cuando lo necesito. Gracias por vuestra amistad. Los buenos ratos que he pasado a vuestro lado son inolvidables.

Me gustaría expresar mi gratitud hacia Mª Carmen, Emilio, Clara y Jesús por el cariño y respaldo que me han proporcionado. A estos dos últimos les agradezco además los dos soles que han traído al mundo: mis sobrinos Fernando y Pablo. Gracias, pequeños, por todo lo que aportáis a mi vida.

Gracias a mi hermano, Daniel, y a mi tía Carmen por todo lo que me dan, por valorarme y apoyarme cada día, por escucharme y ayudarme a levantarme cuando caía, y por animarme siempre a seguir adelante.

Doy las gracias a mis abuelos Angustias y Zacarías por quererme como lo hicieron, por implicarse activamente en mi educación, por sus ganas de vivir y por llenar mi vida

de momento felices. Vuestro recuerdo me alegra el alma. Os quiero.

Comentaba al principio que la realización de esta tesis ha supuesto años de esfuerzo. He de decir aquí que el sacrificio no ha sido sólo mío sino también de mis padres, Dionisio y Riánsares. Si he podido estudiar y dedicar tiempo a lo que ha sido mi pasión desde que era niña, ha sido gracias a vosotros, que siempre me habéis respaldado en todos los sentidos. GRACIAS por vuestro apoyo, por los valores que con vuestro ejemplo me habéis inculcado, por saber ver que el mejor legado que me podíais dejar era una buena educación y por motivarme desde pequeña para desarrollar mis capacidades y esforzarme al máximo. Por vuestra entrega y vuestro amor incondicional, os estoy y estaré eternamente agradecida. Os adoro.

Dicen que los últimos serán los primeros... Quizás por ello he dejado para el final mi agradecimiento a Javier. Sin duda, este trabajo es en parte tuyo, que has puesto todo lo que estaba en tu mano para que yo pudiera culminarlo. Gracias por haber participado en él como si hubieses sido un director más. Y sobre todo, gracias por compartir tu vida conmigo y enriquecer mi existencia cada día. Tu apoyo ha sido fundamental durante estos últimos años. Gracias, Javi, por tu infinita paciencia, por infundirme serenidad en los momentos de caos, por tu cariño y por estar a mi lado en lo bueno y lo malo.

During these years some people have asked me what a Ph.D. is...

An illustrated guide to a Ph.D.

(by Matt Might, Professor of Computer Science at the University of Utah).

1) Imagine a circle that contains all of human knowledge:

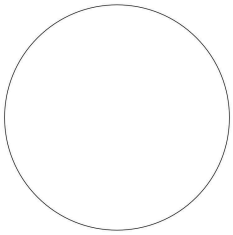

2) By the time you finish elementary school, you know a little:

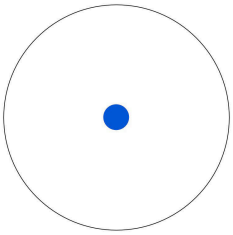

3) By the time you finish high school, you know a bit more:

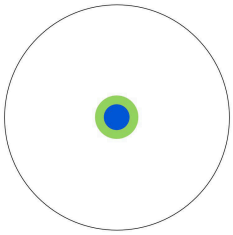

4) With a bachelor's degree, you gain a specialty:

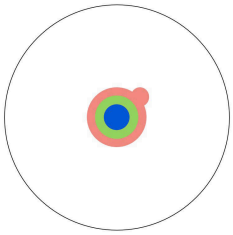

5) A master's degree deepens that specialty:

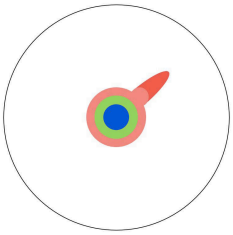

6) Reading research papers takes you to the edge of human knowledge:

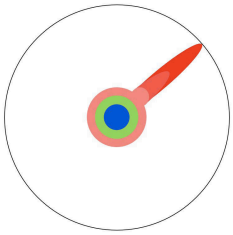

7) Once you're at the boundary, you focus:

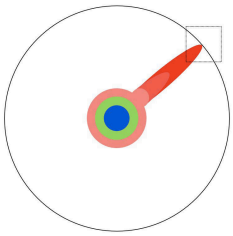

8) You push at the boundary for a few years:

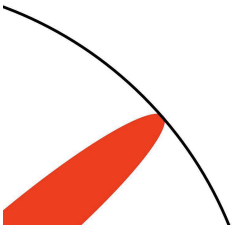

9) Until one day, the boundary gives way:

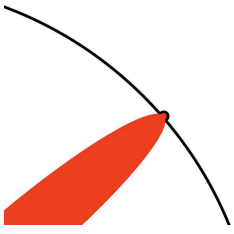

10) And, that dent you've made is called a Ph.D.:

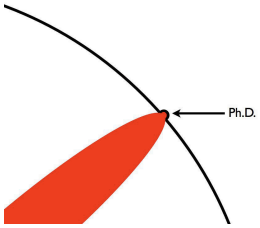

11) Of course, the world looks different to you now:

12) So, don't forget the bigger picture:

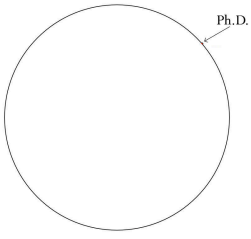

Keep pushing.

A mis padres y abuelos.

Resumen (versión en castellano)

Las fulguraciones son la más extrema evidencia de la presencia de actividad magnética en las atmósferas estelares. Se cree que la gran cantidad de energía liberada en este tipo de evento se produce a través de reconexiones de líneas de campo magnético en la parte baja de la corona. Como consecuencia de la liberación de dicha energía se desencadenan diversos mecanismos en la atmósfera de la estrella que inducen cambios en prácticamente todo el rango del espectro electromagnético.

Esta Tesis Doctoral gira en torno a fulguraciones en estrellas tipo M de la secuencia principal y jóvenes. Para el estudio, se han empleado observaciones en diferentes rangos de longitud de onda con el objetivo de analizar el efecto ocasionado por las fulguraciones en diferentes capas de las atmósferas estelares. En particular, se han utilizado observaciones en el óptico y rayos X, permitiéndonos estudiar cómo afectan las fulguraciones a la cromosfera y corona de las estrellas, respectivamente.

En el rango óptico hemos llevado a cabo un seguimiento espectroscópico de estrellas tipo UV Ceti con alta resolución temporal, con el objetivo de detectar fulguraciones sin emisión en luz blanca (el tipo más común de fulguraciones solares) en estrellas distintas del Sol. Con los datos recogidos se ha confirmado que las fulguraciones sin emisión en luz blanca son un fenómeno frecuente en estrellas tipo UV Ceti, al igual que sucede en el Sol. Durante las fulguraciones detectadas en AD Leo, se ha estudiado e interpretado el comportamiento de diferentes líneas de emisión cromosféricas. Por otro lado, el modelo de capas de Jevremović et al. (1998) nos ha permitido determinar los parámetros físicos (tempe-ratura y densidad electrónicas) del plasma cromosférico afectado por las fulguraciones, la fracción de la superficie estelar cubierta por dicho plasma y la temperatura de la capa subyacente. Asimismo se han buscado posibles correlaciones entre los parámetros físicos del plasma afectado por la fulguración con otros factores tales como la duración de la misma, el área, el flujo máximo alcanzado y la energía total liberada. Gracias a este trabajo se ha ampliado considerablemente la muestra de fulguraciones estelares analizadas a partir de espectros de alta calidad en el óptico.

En rayos X se ha sacado partido de la gran sensibilidad, amplio rango espectral, alta resolución y continua cobertura temporal de los detectores EPIC – situados a bordo del satélite XMM-Newton – con el propósito de realizar análisis espectral con resolución temporal de fulguraciones coronales. En particular, en la estrella tipo UV Ceti CC Eri se han estudiado en profundidad dos fulguraciones más débiles que las que típicamente se suelen examinar (permitiéndonos de este modo investigar la importancia que las fulguraciones puedan tener como agente de calentamiento en las atmósferas estelares); mientras que en la estrella pre-secuencia principal de tipo M TWA 11B (sin signos de poseer disco de acrecimiento) hemos llevado a cabo un detallado análisis de una fase impulsiva de

duración extrema y de una fulguración débil y corta (permitiéndonos comparar los resultados con lo observado en otras estrellas jóvenes que, por el contrario, sí poseen disco). Para describir el plasma coronal implicado en las fulguraciones se han supuesto modelos multi-temperatura. Hemos calculado la abundancia metálica, las temperaturas electrónicas representativas y las correspondientes medidas de emisión ajustando los espectros observados con el código APEC incluido en el software XSPEC, el cual calcula modelos espectrales para plasmas de alta temperatura y ópticamente delgados. Por otra parte, se ha estimado la longitud de los bucles coronales mediante el uso de modelos teóricos. El tamaño de dichas estructuras nos indica la extensión de la corona de dichas estrellas. Para aquellas fulguraciones en las que el calentamiento no gobierna por completo su evolución, se han usado los modelos desarrollados por Reale (2007) y Reale et al. (1997), según se esté analizando la fase impulsiva o la de decaimiento, respectivamente, incluyendo el efecto de calentamiento sostenido durante el decaimiento. Sin embargo, para las fulguraciones en las que el calentamiento residual domina por completo la evolución, por encima del propio enfriamiento del plasma, ha sido necesario emplear la versión estelar (Poletto et al. 1988) del modelo de fulguraciones solares tipo "two-ribbon" (fulguraciones con forma de de dos cintas, Kopp & Poletto 1984). Posteriormente, aplicamos las denominadas leyes de escala RTV (Rosner et al. 1978) y otras ecuaciones fundamentales de la física para determinar otras características del plasma coronal afectado por las fulguraciones (densidad electrónica y presión), así como el volumen que ocupa dicho plasma, la tasa de calentamiento por unidad de volumen y el campo magnético necesario para que el plasma se mantenga confinado. Haciendo algunas suposiciones somos también capaces de estimar el número de bucles implicados en las fulguraciones detectadas y la clase de estructuras magnéticas que caracteriza la atmósfera de estos tipos de estrellas.

Finalmente, se discuten e interpretan los hallazgos en el contexto de los resultados obtenidos por otros autores tanto para fulguraciones estelares como solares.

Abstract (English version)

Flares are the most extreme evidence of magnetic activity in stellar atmospheres. They are supposed to be the result of the energy release from magnetic field reconnection in the lower corona. The large amount of released energy triggers subsequent mechanisms in the stellar atmospheres that involve changes at almost all frequencies in the electromagnetic spectrum.

This Ph.D. Thesis revolves around flares on main- and pre-main-sequence M-type stars. We use observations in different wavelength ranges with the aim of analysing the effects of flares at different layers of stellar atmospheres. In particular, optical and X-ray observations are used so that we can study how flares affect, respectively, the chromosphere and the corona of stars.

In the optical range we carry out a high temporal resolution spectroscopic monitoring of UV Ceti-type stars aimed at detecting non-white-light flares (the most typical kind of solar flares) in stars other than the Sun. With these data we confirm that non-white-light flares are a frequent phenomenon in UV Ceti-type stars, as observed in the Sun. We study and interpret the behaviour of different chromospheric lines during the flares detected on AD Leo. By using a simplified slab model of flares (Jevremović et al. 1998), we are able to determine the physical parameters of the chromospheric flaring plasma (electron density and electron temperature), the temperature of the underlying source, and the surface area covered by the flaring plasma. We also search for possible relationships between the physical parameters of the flaring plasma and other properties such as the flare duration, area, maximum flux and released energy. This work considerably extends the existing sample of stellar flares analysed with good quality spectroscopy in the optical range.

In X-rays we take advantage of the great sensitivity, wide energy range, high energy resolution, and continuous time coverage of the EPIC detectors – on-board the XMM-Newton satellite – in order to perform time-resolved spectral analysis of coronal flares. In particular, in the UV Ceti-type star CC Eri we study two flares that are weaker than those typically reported in the literature (allowing us to speculate about the role of flares as heating agents of stellar atmospheres); while in the pre-main-sequence M-type star TWA 11B (with no signatures of having an accretion disk) we carry out a detailed analysis of an extremely long rise phase and of a shorter, weaker flare (allowing us to compare the results with those reported for young stars but surrounded by disks). Assuming multi-temperature models to describe the coronal flaring plasma, we have calculated the metal abundance, the electron temperatures and the respective emission measures by fitting the spectra with the Astrophysical Plasma Emission Code included in the XSPEC software, which calculates spectral models for hot, optically thin plasmas. Moreover, we are able to estimate the size of the flaring loops by using theoretical models. These sizes give us

an idea about the extent of the corona. For those flares in which heating does not entirely drive the flare evolution we use the models reported by Reale (2007) and Reale et al. (1997) for the rise and decay phases, respectively, including the effect of sustained heating during the decay. Instead, the stellar version of the Kopp & Poletto (1984)'s solar two-ribbon flare model (Poletto et al. 1988) is used when the residual heating completely drives the flare over the plasma cooling. Later, we apply the so-called RTV scaling laws (Rosner et al. 1978) and other fundamental laws of physics to determine additional characteristics of the plasma contained in the flaring loops (electron density and pressure), as well as the volume of the flaring region, the heating rate per unit volume, and the strength of the magnetic field required to confine this plasma. Making some assumptions we are also able to estimate the number of loops involved in the observed flares and the kind of magnetic structures present in the atmosphere of these types of stars.

Finally, we discuss and interpret the results in the context of solar and stellar flares reported so far.

Contents

List of Figures

List of Tables

Chapter 1

Introduction to solar and stellar flares

The basic working hypothesis used to study observations of stellar flares is that they are the stellar counterparts of solar flares, evolving as a consequence of the same elementary physical mechanisms. Many stellar observations have supported this picture (see review by Pallavicini 1990). Since this hypothesis has constituted the most important guide to understand the physical processes involved in stellar flares, this introduction starts reviewing the main aspects of solar flares.

1.1 Solar flares: main flare diagnostics and physical mechanisms at work

Without warning, the relatively calm solar atmosphere can be torn asunder by brief (usually lasting no more than 10 min) and catastrophic outbursts of incredible energy. They are called solar flares and are the biggest explosions in the solar system.

A substantial fraction of this energy goes into accelerating electrons and ions to nearly the velocity of light, hurling them out into the solar system and down into the Sun. The high-energy particles going down into the Sun are responsible for subsequent physical processes that produce changes in almost all the wavelengths of solar electromagnetic radiation. In fact, an essential aspect of any flare is that much of its energy output is in electromagnetic radiation. This characteristic sets it apart from phenomena called solar ejecta, even though in many cases flares and ejecta overlap in space and time.

The first solar flare ever recorded occurred on 1 September 1859. It was detected in white-light[1] by Carrington (1859), when he observed a large sunspot group looking at the photosphere, and independently confirmed by observations from Hodgson (1859). The development of the spectroheliograph, which made it possible to observe continuously the whole solar surface in monochromatic light, boosted observational flare research, mainly in the light of the Hα line. Thus, since the early 1930s solar flares have been observed regularly at many observatories throughout the world and listed in monthly reports. The 1940s saw the first observations of flare-associated radio and particle emissions and dur-

[1] "White-light" refers to the light resulting from combining all the colors of starlight that are visible by the naked eye (i.e., integrated optical light, which is primarily formed in the stellar photosphere).

ing the Space Age[2] the full gamut of flare extreme-ultraviolet, X-ray and gamma-ray data became available along with observations of accompanying transient coronal activity.

Since radiation in each wavelength range provides information about different physical processes, in this section we review solar flares as seen in the different spectral ranges across the full electromagnetic spectrum. It is not our aim to do a complete review about solar flare observations and models, but to make the reader (which is assumed to be familiarized at least with basic concepts about solar magnetic activity) know and understand the main physical processes involved in solar flares.

1.1.1 X-ray flare emission

Much of the energy radiated during solar flares is emitted as X-rays. In these events the high-energy, hard X-ray radiation (energies between 10 and 100 keV) is produced by non-thermal electrons accelerated to nearly the velocity of light. They tell us about the acceleration, propagation, and confinement of very energetic electrons. The soft X-rays (energies between 0.1 and 10 keV) describe the thermal radiation of hot electrons of lower energy. Thermal X-rays are emitted by plasma at coronal temperatures that range from 1 to 2 MK in regions where the Sun is "quiet" (i.e., weak magnetic fields), from 4 to 5 MK in active regions (where magnetic fields are stronger) and are of order of 10 MK in X-ray flaring loops. The energy of the X-ray radiation is a measure of the energy of the electrons that produce it. Electrons with a given amount of energy produce X-rays (or gamma rays[3]) with about the same energy.

The radiation at different X-ray wavelengths, the hard and soft varieties, describes different parts of the flare time profile and is attributed to different physical mechanisms. They are known as the impulsive hard-X-ray phase and gradual soft X-ray decay phase of a solar flare. At the impulsive stage electrons are accelerated rapidly, in a second or less, to energies that can exceed 1 MeV. The high-energy electrons emit hard X-rays and gamma rays that mark the flare onset. The soft X-rays emitted during solar flares gradually build up in strength and peak a few minutes after the impulsive emission. Thus, the soft X-rays are a delayed effect of the main flare outburst.

The soft X-rays emitted during solar flares are thermal radiation, released by virtue of their intense heat and dependent upon the random thermal motions of very hot electrons. At such high temperatures, the electrons are set free from atoms and move off at high speed, leaving the ions (primary protons) and emitting electromagnetic radiation known as *bremsstrahlung*[4].

There are two kinds of bremsstrahlung emitted at X-rays during solar flares: thermal

[2]The Space Age is generally considered to have begun on October 4, 1957, when the Soviet Union successfully launched Sputnik I

[3]Gamma rays are even more energetic than X-rays, exceeding 100 keV in energy.

[4]When an electron moves rapidly and freely outside an atom, it inevitably moves near a proton in the ambient gas. There is an electrical attraction between the electron and the proton, which pulls the electron toward the proton (because of their greater mass, the protons move more slowly than the electron with the same temperature or kinetic energy). This pulls the electron toward the proton, bending the electron's trajectory and altering its speed. The electron emits electromagnetic radiation in the process. This radiation is known as bremsstrahlung. Bremsstrahlung can be emitted at all wavelengths, from long radio waves to short X-rays, but during solar flares it becomes very intense at X-ray wavelengths.

bremsstrahlung and non-thermal bremsstrahlung. They distinguish both the method of electron acceleration and the energy of the emitted X-rays (or the energy of the electrons that produce it).

The thermal, soft X-ray bremsstrahlung predominates during the decay phase of a solar flare. This radiation is produced when electrons are heated to high temperatures of about 10^7 K, moving at speeds of about 0.05 times the velocity of light. Instead, the electrons accelerated to high velocities during the impulsive phase of a flare radiate hard X-rays by non-thermal bremsstrahlung, which is the same process as the thermal one excepting the fact that the electrons are moving at non-thermal speeds near the velocity of light (faster than possible in a hot gas), which implies radiation with photon energy much greater.

The intensity of thermal bremsstrahlung falls off rapidly with increasing photon energy, while that of the non-thermal hard X-ray flare radiation follows a less steep, power-law drop at increasing energy. Therefore, the number of non-thermal electrons with energy ϵ varies as $\epsilon^{-\delta}$, where the power-law index δ is a small positive number. So the observation of non-thermal bremsstrahlung provides a way to study the accelerated electrons and specify this index.

The physical processes that give rise to the soft X-ray and hard X-ray flare emission were first suggested by observations from the *Solar Maximum Mission* (*SMM*), and amplified, confirmed and extended with instruments aboard *Yohkoh*, with improved angular and temporal resolution and a wider energy range. Images from *Yohkoh*'s Hard X-ray Telescope, or HXT, clarified, for example, the double-source structure of impulsive hard X-ray flares with unprecedented clarity. It established a double-source structure for the hard X-ray emission of roughly half the flares observed in the purely non-thermal energy range above 30 keV. The other half of the flares detected with *Yohkoh* were either single sources (which could be double ones that are too small to be resolved) or multiple sources (which could be an ensemble of double sources).

When the two hard X-ray sources (above 30 keV) are seen from *Yohkoh*, they are located on opposite sides of the line that separates regions of different magnetic polarity (the magnetic neutral line), strongly suggesting that the hard X-rays are emitted from the footpoints of a flaring magnetic loop. The fact that the hard X-ray sources occur and vary nearly simultaneously in time, within 0.1 s or less, excludes transport mechanisms other than high-energy electrons in coronal loops.

The Neupert effect

It was first shown by Neupert (1968) that the slow, smooth rise of the soft X-ray flares resembles the time integration of the rapid, impulsive radio bursts at centimeter wavelengths (or microwave bursts). This temporal correlation is now known as the Neupert effect. After *SMM* was launched, the Neupert effect was extended and confirmed for the soft X-rays from solar flares vs. the time integration of the impulsive hard X-rays. This suggests that the energetic electron beams that gives rise to the hard X-ray flare is the main source of heating and mass supply of the coronal plasma that emits the soft X-ray flare.

In solar flares the hard X-ray and radio light curves tend to be similar (see e.g., Lu &

Petrosian 1990, and references therein). Therefore, the radio emission is believed to be produced by synchrotron radiation from the same non-thermal distribution of accelerated particles which later produces the hard X-rays, when moving down the loop[5].

The theory of chromospheric evaporation

Doppler shifts of X-ray spectral lines to shorter wavelengths (blueshifts) during solar flares, that disappears after the rise phase, indicate that some gas is moving upwards at typical speeds of 300 km s^{-1} (Doschek 1990). This rise in material is described by the theory of chromospheric evaporation, first suggested by Hirayama (1974). Initially, chromospheric material at 10000 K is heated by thermalization of the down flowing, energetic electrons, expanding upwards into the low-density corona along magnetic loops that shine brightly in soft X-rays after filling. Data from *Yohkoh* (see Doschek et al. 1996; Doschek & Warren 2005, and references therein) indicate that when replenished in full, the post-impulsive flare loops contain gas heated to a maximum electron temperature of $10 - 20 \times 10^6$ K.

A model of flaring X-ray emission

Fig. 1.1 shows schematically a well-developed model that describes the hard X-ray and soft X-ray radiation of solar flares. According to this picture, a solar flare is triggered by an instability or rearrangement in the magnetic configuration (magnetic reconnection) in the low corona (Kopp & Pneuman 1976; Tsuneta et al. 1992). This results in the rapid release of stored, non-potential magnetic energy and the acceleration of non-thermal particles (electrons and ions, primarily protons) to high speed by processes that are still not well understood.

Using *Yohkoh* observations of solar flares, Masuda (1994); Masuda et al. (1994, 1995) detected, in addition to double-footpoint sources, a hard X-ray source well above the corresponding soft X-ray flaring loop structure around the peak time of the impulsive phase. This hard X-ray source showed an intensity variation similar to double-footpoint sources and a spectrum that is relatively hard compared with that of loop-top gradual source which appeared later in the flare. They suggested that either this "loop-top" hard X-ray source represents the reconnection site itself or the site where the downward plasma stream, ejected from the reconnection point far above the hard X-ray source, collides with the underlying closed magnetic loop.

The accelerated (non-thermal) particles are beamed into the lower, denser layers of the solar chromosphere, along the newly linked coronal loop, or hurled out into space along open magnetic field lines[6]. As the non-thermal electrons move either out or down along magnetic channels, they generate intense radio emission. Those non-thermal electrons that were channeled down the loop strike the chromosphere at nearly the speed of light, emitting hard X-rays by electron-ion bremsstrahlung at the loop footpoints. The

[5]Note that for magnetic field strength in the range 300 – 700 G, the bulk of the radio emission at centimeter wavelengths is produced by electrons with energy $E_{e^-} \gtrsim 200$ keV, while most of the hard X-rays are produced by lower energy electrons $E_{e^-} \lesssim 100$ keV.

[6]Solar energetic particles (SEPs) consist of electrons and ions that range in energy from 10 keV to about 100 MeV and from 1 MeV to 20 GeV, respectively (see e.g., Chupp 1987).

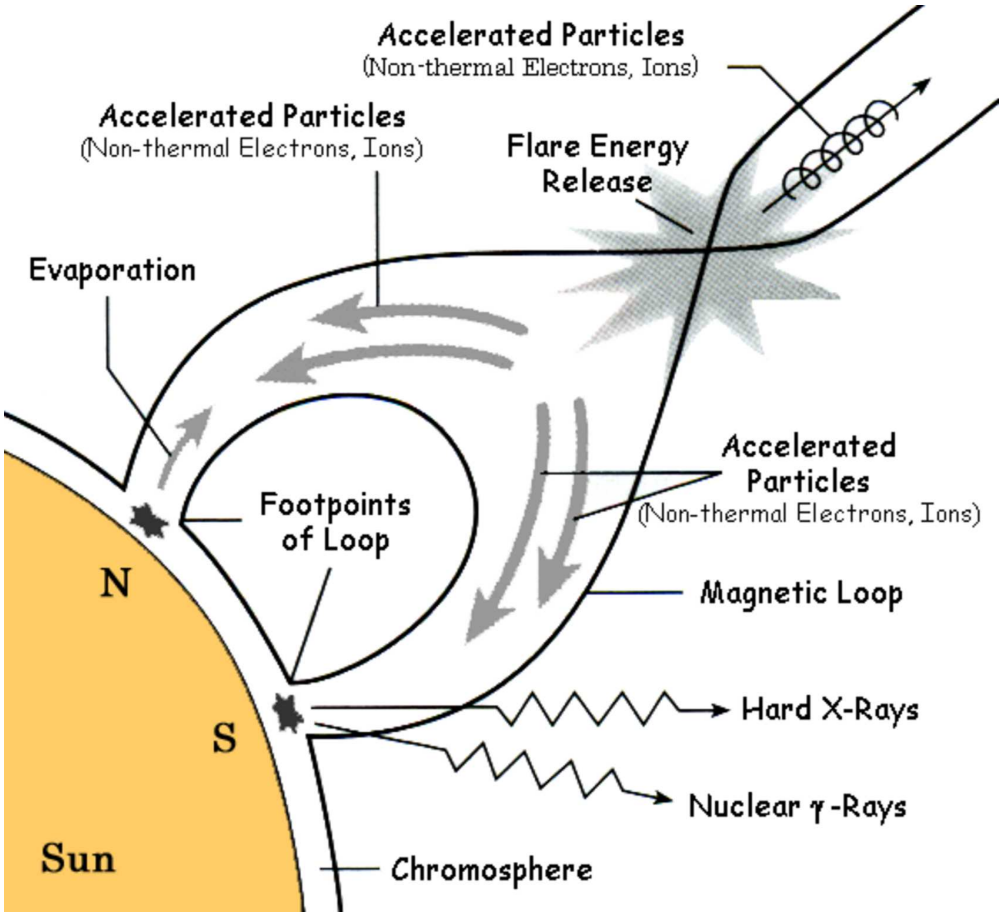

Figure 1.1: Solar X-ray flare model. (Adapted from Lang 2009).

Table 1.1: Solar flare X-ray classification.

Class	Peak soft X-ray flux[a] ($W\ m^{-2}$)
A	$< 10^{-7}$
B	$[10^{-7}, 10^{-6})$
C	$[10^{-6}, 10^{-5})$
M	$[10^{-5}, 10^{-4})$
X	$\geq 10^{-4}$

[a]Measured from the *GOES* spacecraft near Earth at soft X-ray wavelengths between 1.6 and 12 keV

chromospheric material at the loop footpoints is then heated (to temperatures which can be as large as tens of millions of degrees) very quickly (in seconds) by the accelerated particles that slam into it. The high-temperature material in the chromosphere is driven upward by the large pressure gradients and rises into the loop along the guiding magnetic field, accompanied by a slow, gradual increase in soft X-ray radiation by thermal bremsstrahlung that lasts tens of minutes. This upwelling of heated material is called chromospheric evaporation. Thus, the thermal decay phase, detected by the gradual build up of soft X-rays, is viewed as an atmospheric response to the energetic charged particles during the impulsive hard X-ray phase.

Solar flare X-ray classification

To classify the power of a solar flare, scientists use the soft X-ray flux at its maximum, in $W\ m^{-2}$, measured near the Earth with a *GOES* spacecraft in the wavelength range 1.6 – 12 keV (e.g., Lang 2009). The *GOES* scheme (see Table 1.1) classifies solar flares as A, B, C, M, or X, from the weakest to the strongest, according to their peak detected flux. Each class has a peak soft X-ray flux 10 times greater than the preceding one, being the peak soft X-ray flux in A class flares lower than 10^{-7} W m^{-2}. A given class of X-ray flares has nine linear subdivisions, numbered from 1 to 9 in increasing flux, excepting the X class flares, with so many subdivisions as needed. For example, the largest X-ray flare on record to date occurred on 4 November 2003. It saturated the *GOES* X-ray detectors at X17.4 and had an estimated classification of X28, or 0.0028 W m^{-2}.

1.1.2 White-light flare emission

As mentioned before, the first detection of a solar flare came from white-light observations performed in 1859. But from that moment on, no more than about 100 solar white-light flares (WLFs) have been reported from ground-based observatories[7].

Although the WLFs detected on the Sun so far are usually among its most energetic flare events, white-light emission occurs also in weaker flares ("big flare syndrome").

[7]The bulk of solar white-light flare observations was summarized by Neidig (1989).

Hudson et al. (2006) showed its presence in solar flares as weak as *GOES* class C1.6, supporting the conclusion of Neidig (1989) that all solar flares may cause an enhancement in white-light, attaining a detectable level of brightness only in relatively few cases.

The model for white-light emission is unclear, but it is generally believed that the continuum emission in WLFs originates from either the lower chromosphere through recombination (after heating and ionization[8]) of hydrogen atoms (producing enhanced Balmer and Paschen contributions), or the upper photosphere through emission from negative hydrogen ions, or both. Correspondingly, semi-empirical models of WLFs require either a heated and condensed layer in the chromosphere or a temperature increase in the photosphere in order to reproduce the observed continuum increase (e.g., Avrett et al. 1986; Mauas et al. 1990; Ding et al. 1994). So, the height at which the continuum enhancement occurs is still debated, and ranges from the photosphere itself through the temperature minimum region and the upper chromosphere (see, e.g., Hudson 1972; Aboudarham & Hénoux 1986b; Ding et al. 2003; Fletcher et al. 2007).

Therefore, the question is how the lower atmosphere gets heated during WLFs? Many heating mechanisms have been proposed, including heating by a non-thermal electron beam (Hudson 1972; Aboudarham & Hénoux 1986a) or a proton beam (Machado et al. 1978), soft X-ray irradiation (e.g., Hénoux & Nakagawa 1977), EUV irradiation (e.g., Poland et al. 1988), dissipation of Alfvén waves (e.g., Emslie & Sturrock 1982), return current instability (Matthews et al. 1998), and chromospheric radiative back-warming (Machado et al. 1989; Metcalf et al. 1990b; Gan & Mauas 1994).

In recent decades, it has been shown that the white-light emission correlates well with the hard X-ray emission from solar flares in both time and space. That is, the white-light flare usually occurs during the impulsive phase of a solar flare and is found at the footpoints of coronal loops, suggesting that this visible radiation may be related to non-thermal quasi-relativistic electrons accelerated in the low corona and beamed down into the chromosphere and upper photosphere (Rust & Hegwer 1975; Hudson et al. 1992; Neidig & Kane 1993).

Neidig (1989) concluded that: (i) heat conduction, irradiation by soft X-rays and heating by high-energy protons are not sufficient to power the white-light flare emission at the time of its peak luminosity; and (ii) heating by an electron beam, which might be important in the chromospheric component of white-light flares, is totally inadequate for the upper photospheric component of the white-light flare emission. In fact, direct excitation of the lower levels would indeed require high-energy electrons, as electron energies ≥ 900 keV are necessary for penetration to these depths. Aboudarham & Hénoux (1986b) calculated that an electron energy of the order of 100 keV is necessary to reach the lower chromosphere, which places strong demands on the overall flare energetics. Metcalf et al. (2003) found that there is sufficient energy in the electron beam to power the white-light flare emission, provided that the energy can come from the lower energy portion of the electron spectrum. Since the low-energy electrons cannot penetrate deep into the atmosphere, they concluded that the electron energy is deposited in the upper chromosphere and transported to the deeper layers of the atmosphere via back-warming, primarily in the Balmer and Paschen continua.

[8] In the meantime, the Balmer lines can be Stark broadened owing to an overpopulated electron density.

WLFs fall into two general categories, type I and type II (Machado et al. 1986). So far, this section has been focused on the more common WLFs, i.e. type I events. To summarize, type I WLFs show strong and broadened hydrogen Balmer lines and a Balmer and Paschen jump and demonstrate a good correlation between the continuum emission and the hard X-rays (Fang & Ding 1995), indicating that the type I WLF is closely connected with flare energy deposition by non-thermal particles in the chromosphere. The continuum emission is produced predominately by hydrogen recombination, and energy transport to lower levels in the atmosphere is by radiative back-warming (Hudson 1972; Metcalf et al. 1990a,b; Ding & Fang 1996). The type II events do not show this strong chromospheric effect. Comparatively, type II WLFs appear less frequently, and their heating mechanisms are less well-known. Semiempirical models for this type of WLF imply a significant temperature rise in the upper photosphere or around the temperature minimum region relative to the undisturbed area (e.g., Mauas et al. 1990; Ding et al. 1994). Any heating mechanism involving non-thermal quasi-relativistic electrons from the corona will inevitably produce chromospheric line emission and is therefore unable to account fully for the spectral features of type II WLFs. On the one hand, the high color temperature, together with the lack of a noticeable Balmer jump in a stellar flare, led Hawley & Fisher (1992a) to suggest (also for the WLFs on the Sun showing these features, which would be type II events according to the latter condition) that the optical continuum is due to blackbody emission in the photosphere[9] through reprocessing of UV/EUV metal line radiation emitted from the upper chromosphere[10] (back-warming), which is, in turn, probably formed by intense heating from energetic electrons. On the other hand, Ding et al. (1999) suggested that type II WLFs are the result of energy release through reconnections in the photosphere or temperature minimum region, although this has yet to be verified observationally.

1.1.3 Gamma-ray flare emission

Gamma-rays exceed 100 keV in energy. The intensity of gamma-rays from the Sun is usually too low to be detected with the available instruments, even from the outer space. But during solar flares, gamma-rays can be detected.

Gamma-ray lines from solar flares were first observed in 1972 by Chupp et al. (1973). But it was not until 1980 that routine observations of gamma-ray lines and continuum became possible (see some results from different missions in Chupp 1984, 1987; Yoshimori 1990; Ramaty & Mandzhavidze 2000; Smith et al. 2003; Hurford et al. 2006, and references therein). The main processes giving rise to gamma-rays during solar flares are summarized below.

On the one hand, some of the electrons accelerated during a solar flare and chan-

[9]The only viable location for a blackbody in the solar atmosphere is the photosphere; there is simply not enough opacity within the chromosphere for a blackbody spectrum to form, even within the exceedingly dense "chromospheric condensations" which can be created during the impulsive phase.

[10]None of the particle heating mechanisms (energetic electrons or protons) can reach the photosphere directly with any efficiency (see, e.g., Machado et al. 1978; Metcalf et al. 2003). Furthermore, other photospheric flare heating mechanisms (e.g., electric currents or heating by Alfvén waves) were shown to be either ineffective or inconsistent with observations in solar flares (Metcalf et al. 1990b).

neled down the loop are energetic enough to radiate gamma-rays by bremsstrahlung (see § 1.1.1). On the other hand, the ions (primarily protons) accelerated during a solar flare and also channeled down the loop (see § 1.1.1) slam into the dense, lower atmosphere, emitting gamma-rays in spectral lines as well as energetic neutrons. Some of the flare-accelerated protons shatter abundant heavy nuclei in the lower atmosphere, in a process called spallation. The lighter nuclear fragments are left in an excited state, but promptly calm down, emitting gamma-rays. Other abundant nuclei in the lower solar atmosphere are directly excited by collision with the flare-accelerated protons, radiating the extra energy in gamma-rays when they relax to their former unexcited state. During bombardment by flare-accelerated ions, energetic neutrons can be torn out of the nuclei of atoms. Some of these neutrons escape from the Sun, while the remainder are eventually captured by ambient (or non-flaring) hydrogen nuclei in the photosphere, making deuterons and emitting one of the Sun's strongest gamma-ray lines, at 2.223 MeV. Another strong gamma-ray line emitted during solar flares is the 0.511 MeV positron[11] annihilation line.

1.1.4 Radio flare emission

Radio bursts[12] are produced by energetic electrons interacting with the magnetic field or with the ambient plasma (see Bastian et al. 1998; Murdin 2001; Kallenrode 2004; Benz 2008; Lang 2009, for some reviews about radio emission from solar flares). On the one hand, energetic electrons interacting with the magnetic field produce incoherent gyrosynchrotron emission that usually dominates the radiation at millimeter and centimeter wavelengths (frequencies in the range 3 – 300 GHz). On the other hand, coherent plasma radiation plays a dominant role at decimeter wavelengths (frequencies in the range 0.3 – 3 GHz) and meter wavelengths (frequencies $\lesssim 0.3$ GHz).

Synchrotron and Gyrosynchrotron radio emission

Electrons moving in a magnetic field experience the Lorentz force and therefore gyrate at the electron gyrofrequency $\nu_{g,e} \approx 2.8 B_\perp/\gamma$ MHz, being $B_\perp$ the magnetic field component perpendicular to the electron's path, in Gauss, and γ the Lorentz factor. Thermal or non-thermal (relativistic) electron distributions emit a broadband continuum of radiation by this mechanism. If the electrons are non-relativistic, it is called gyrosynchrotron radiation, while if the electrons are relativistic it is called synchrotron radiation (for theory about this kind of radiation coming from single particles and from an ensemble of particles, see Verschuur & Kellermann 1988).

Impulsive continuum radiation at centimeter wavelengths lasting just a few minutes is observed at the onset of flares of all sizes. It is interpreted as gyrosynchrotron radiation of high speed electrons accelerated to energies of 100 – 1000 keV that are moving down, along magnetic channels, from the site of acceleration (located above the tops of coronal loops) to lower solar atmospheric layers. If these electrons are accelerated up to a few

[11] Positrons, the anti-matter counterpart of electrons, are released during the decay of radioactive nuclei produced when flare-accelerated protons and heavier nuclei interact with the lower solar atmosphere.

[12] The radio emission of a solar flare is often called radio burst to emphasize its brief, energetic, and eruptive characteristics.

MeV[13], its gyrosynchrotron radio emission reach millimeter wavelengths when moving downwards along the magnetic field lines.

Gyrosynchrotron emission offers a powerful and sensitive diagnostic of physical conditions in flaring sources (Bastian et al. 1998). Similar to X-ray radiation, it may be used to infer the electron distribution function and its evolution in time. Unlike X-ray radiation, gyrosynchrotron emission is also a sensitive function of magnetic field strength and orientation and can therefore be used to constrain the coronal magnetic field in the flaring source.

Plasma radio emission

As first shown by Payne-Scott et al. (1947), the radio bursts during solar flares do not occur simultaneously at the different radio frequencies, but instead drift to later arrival times at lower frequencies. This is explained by a flare-associated disturbance that travels out through the progressively more rarefied layers of the solar corona, making the local electrons vibrate at their natural frequency of oscillation (plasma frequency[14], $\nu_{\rm p,e} \approx 9000\,\sqrt{n_{\rm e}}$, where the electron density, denoted by $n_{\rm e}$ is in units of electrons per cubic centimeter). Thus, plasma radiation at radio wavelengths results from the nonlinear conversion of electron energy to plasma waves and from thence to electromagnetic waves at a frequency near the local plasma frequency $\nu_{\rm p,e}$, or its harmonic $2\nu_{\rm p,e}$ (e.g., Bastian et al. 1998). The plasma frequency depends on the local electron density, with a higher plasma frequency at greater coronal densities. Thus, as beams of high-speed electrons, thrown out from solar flares, or flare-associated shock waves moves out through the progressively more rarefied layers of the corona, it excites radiation at lower and lower radio frequencies. Plasma radiation at decimeter wavelengths is generated low in the corona, while that at meter wavelengths is generated at heights $\sim 1R_\odot$ and that at kilometer wavelengths originates in the interplanetary medium (Murdin 2001).

The most common type of solar radio bursts[15] related to flares is the type III radio burst. It last for a short period of time and occurs at the very onset (impulsive phase) of solar flares. Type III bursts extend over a wide range of frequencies (from 0.1 to 1000 MHz) and show a fast drift from high to lower radio frequencies (at a rate of up to 100 MHz/s). Since the radial speed of the radio source responsible for the type III bursts is estimated to be $c/3$, they are interpreted as plasma waves generated by a stream of electrons thrown from the Sun (with kinetic energies from 10 to 100 keV and velocities of

[13]Note that these electrons would also be responsible for electron bremsstrahlung γ-ray emission (see § 1.1.3).

[14]At the high temperatures in the solar corona ($\sim 10^6$ K), electrons are stripped from the gaseous atoms by innumerable collisions. The resulting plasma is therefore made up of electrons and positive ions, that are free to move about. When a flare-associated disturbance, such as an electron beam or a shock wave moves through the coronal plasma, the local electrons are displaced with respect to the positive ions, which are more massive than the electrons. The electrical attraction between the electrons and positive ions pulls the electrons back in the opposite direction, but they overshoot the equilibrium position. The light, free electrons therefore oscillate back and forth when a moving disturbance passes through the corona. The natural frequency of oscillation is called the plasma frequency. This explanation is extracted and adapted from Lang (2009).

[15]Relevant information about types of solar radio bursts has been taken from Kraus (1966), Murdin (2001), Kallenrode (2004) and Lang (2009).

up to half the velocity of light) and propagating along open field lines into interplanetary space. Occasionally, the drift of the type III burst is suddenly reversed (U-type bursts), indicating electrons captured in a closed magnetic field loop: as the electrons propagate upward, the burst shows the normal frequency drift which is reversed as the electrons propagate downward on the other leg of the loop. Type III bursts are often accompanied by a radio broadband continuum emission confined at meter wavelengths, named Type V burst. Type V bursts are believed to result from synchrotron emission from the energetic electrons moving along open field lines into space.

In short flares, only the above sequence of bursts (type III and V) may be observed. In large duration flares, however, a longer-duration sequence of radio bursts (type II and IV) follows the type III and V radio bursts. In the type II bursts the frequency drift, from high frequencies (100 MHz) to lower ones ($\sim$ 0.1 MHz), is much slower than in type III bursts. Its value (of about 1 MHz/s) suggest a radial outward motion at about 1000 km/s for the radio source, which is very much less than the velocities of the electron jet in type III radio bursts. Type II bursts are interpreted as evidence of shock excited by a coronal mass ejection (CME) set up at the start time of a solar flare and moving out into space. Due to the low propagation speed of the radio source of type II bursts, they last much more than type III bursts, being present even during the gradual decay or extended phase of solar flares.

Sometimes the type II bursts are followed by a very broad-band, stable, continuum radio emission that may last for hours or even days. This radiation is designated as type IV burst. Type IV emission has been attributed to gyrosynchrotron emission from energetic electrons trapped within magnetic clouds that travel out into space, resulting from magnetic reconnection in the wake of a CME. Type IV bursts are therefore interpreted as the associated continua of type II bursts.

1.1.5 Flare ribbons

Frequent and routine observations of solar flares have been carried out from ground-based telescopes since the 1930s, by monitoring the Sun's chromosphere in the red light of the Balmer alpha transition of Hydrogen, designated Hα (at a laboratory wavelength of 6563 Å). In the Sun, Hα emission is mainly formed by chromospheric plasma at temperatures in the range $5 - 10 \times 10^3$ K. In this chromospheric line, a solar flare appears as a sudden flash followed by a slower decay. The Hα increase during solar flares usually occurs in strong, complex magnetic regions. In particular, they are located near the line or place of magnetic neutrality (polarity-inversion line), between regions of opposite magnetic polarity. They often appear on each side of the magnetic neutral line as two extended, parallel ribbons (two-ribbon flares). In addition, the polarity-inversion line is usually overlain by a filament before the flare onset. This filament may disappear early during the flare event.

Evolution of two-ribbon flares is morphologically characterized by the separation of the two ribbons in the chromosphere, traditionally observed in Hα (see the development of a two-ribbon flare in Fig. 1.2). The increase in the distance between the two ribbons is believed to be the lower atmospheric signature of magnetic reconnection progressively occurring at higher levels in the corona, in the sense that the separation velocity of flare-

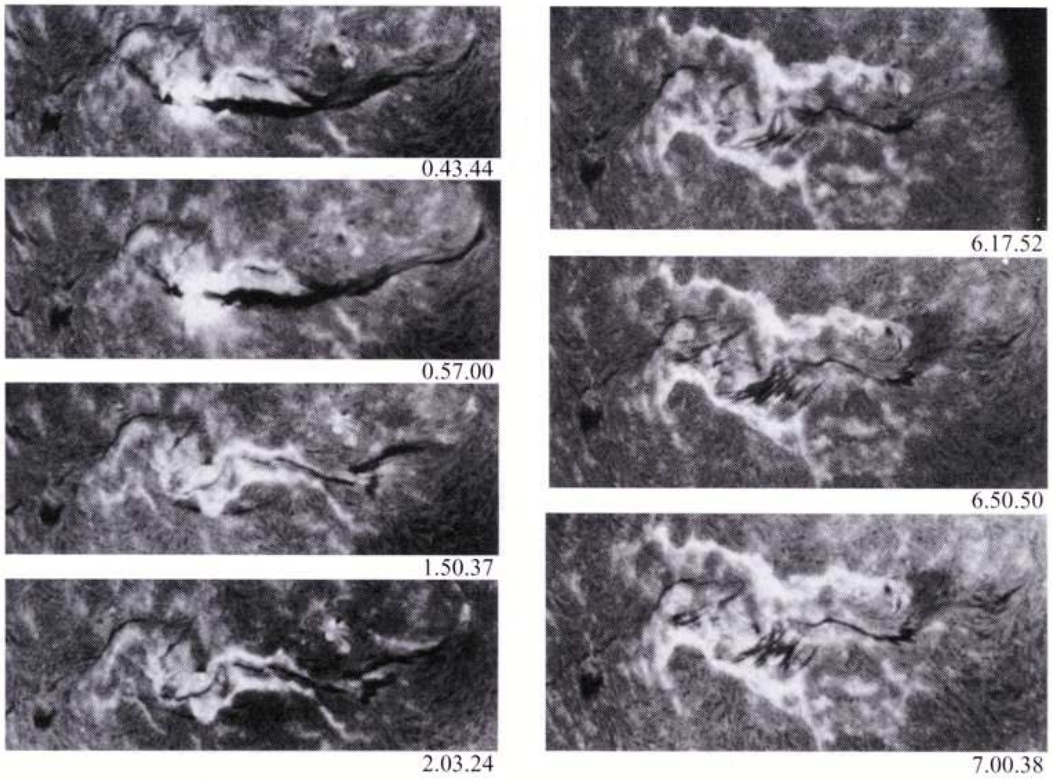

Figure 1.2: Development of an eruptive flare on 3 – 4 September 1982, photographed in the Hα line. Time is given in UT. Initially, two bright ribbons are formed. The distance between them increases with time. Note that, in the process, a dark filament disappears. Extracted from Švestka (2003); original image from Morishita (1987).

ribbons depends on the reconnection rate of magnetic-field lines. Note that much of the energy released as consequence of magnetic reconnection in the low corona goes into accelerating large numbers of electrons and ions to a good fraction of the speed of light (see § 1.1.1). These charged particles move away from the flare-initiation site in the low corona, down along magnetic field lines into the lower, denser layers of the upper chromosphere. As seen in § 1.1.1, the chromospheric material in the footpoints of the newly linked coronal loop is heated and evaporated into the coronal portion of the loop. This loop is initially very hot and visible in X-rays and extreme ultraviolet (EUV) wavelengths. Only its footpoints can be observed in chromospheric lines such as Hα. When magnetic reconnection is occurring in an arcade of loops, the two sets of footpoints at each side of the loop arcade appear as two elongated ribbons.

As the hot material in the flaring loops cools down, the temperature and density may reach the chromospheric values for which Hα emission is typically observed. Therefore, the whole or part of these loops may be temporarily visible in Hα. These are called Hα (post-) flare loops. Flare ribbons and (post-) flare loops are also observed in the rest of the Balmer lines, whose emission mainly comes from the same plasma responsible for Hα emission. The flaring emission process for other chromospheric lines is similar to the one just described. That is, the plasma in the chromospheric footpoints of the newly

Table 1.2: Some activity/flare chromospheric radiative diagnostics, together with the region in which they are mainly formed in the quiet solar chromosphere.

Chromospheric lines	Main formation region in the quiet Sun
He I D_3	High chromosphere
He I λ4026Å	High chromosphere
Balmer series	Intermediate chromosphere
Ca II H & K	Intermediate chromosphere
Na I D_1 & D_2	Low chromosphere
Ca II IRT	Low chromosphere

reconnected coronal loops and the heated and evaporated material in the (post-) flare loops can reach physical conditions at which the different chromospheric lines are formed. So radiation in these lines is emitted as the (post-) flare loops cool down after been heated. Table 1.2 lists several chromospheric lines with emission usually increased by flares. The region in which they are formed within the quiet solar chromosphere is also shown.

Such flare ribbons are also detected at extreme-ultraviolet wavelengths (using, for example, instruments aboard *SOHO* and *TRACE*). Recent and detailed measurements of the motion of ribbons in the Hα line, extreme ultraviolet, and hard X-rays by Fletcher & Hudson (2001, 2002); Wang et al. (2003) and Fletcher et al. (2004) support the hypothesis that the flare Hα and ultraviolet ribbons map out the chromospheric footpoints of reconnected, newly formed coronal loops.

1.1.6 Phases of solar flares

Solar flare light curves at different wavelengths do not peak at the same time. Their evolution responds to the physical processes involved in each one of the flare phases. The general pattern of the time emission in different wavelength ranges is shown in Figure 1.3 and described in the following lines (Murdin 2001):

- **Pre-flare phase** – Solar flares often start with a brightening in soft X-rays and extreme ultraviolet wavelengths. In this phase magnetic flux continues to emerge and the field configuration is thought to become more sheared and twisted. One of the outstanding questions, still unanswered, is the conditions under which a flare is triggered.

- **Impulsive phase** – The start of this phase is characterized by the onset of hard X-ray and centimetric gyrosynchrotron radiation of the energetic electrons as well as gamma-ray line emission caused by energetic ions. Throughout the impulsive phase, the soft X-ray emission increases in both size and total flux. Growing emission in Balmer lines indicates that also the lower chromosphere is increasingly affected. The bulk of the flare energy is released in the impulsive phase.

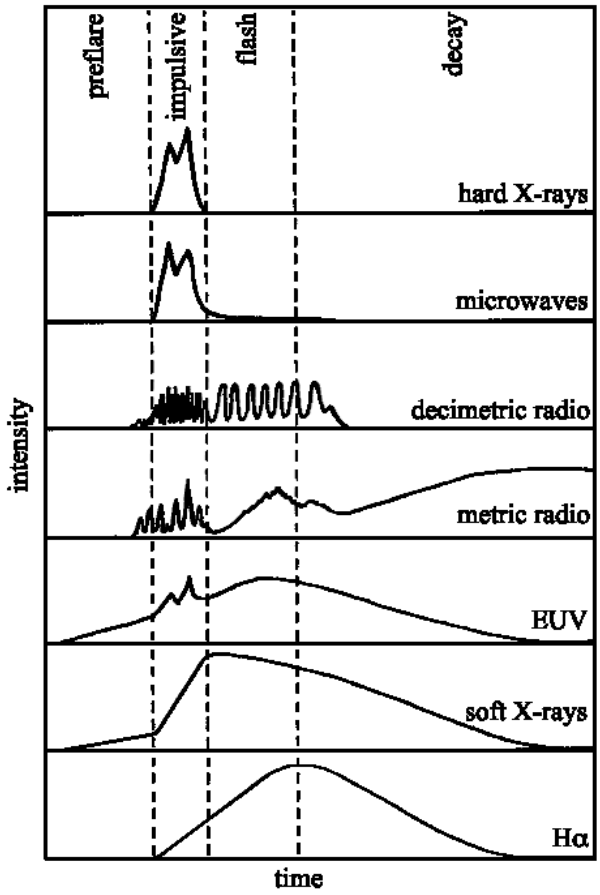

Figure 1.3: A schematic time evolution of flare intensities at different wavelengths. The phases indicated at the top vary greatly in duration. In large solar flares, the preflare phase lasts ~ 10 min, the impulsive phase ~ 1 min, the flash phase ~ 5 min and the decay phase ~ 1 h. (Adapted from Murdin 2001).

- **Flash phase** – In the flash phase the non-thermal particles and their emissions have mostly disappeared but the impact of the energy released in the previous phases is still visible. During this phase, the temperature of the hot plasma decreases. Sometimes, however, gigantic soft X-ray emitting loops cool slowly, indicating that energy is still being released in this phase.

- **Decay phase** – The flare develops gradually into the decay phase, during which the thermal flare emissions disappear. In the dense flare plasma evaporated into the coronal post-flare loops, hydrogen recombines making these structures visible in Balmer lines. The post-flare loops often show down-moving material. It is the signature of a cooling loop. Thus the plasma evaporated by the flare is "raining" back to the chromosphere.

1.1.7 Magnetic reconnection during solar flares

It has just been shown that solar flares are intriguing, intensely-studied phenomena. Much progress has been made in the understanding of the processes that occur on the Sun during a flare. However, as pointed out by Miklenic et al. (2009), flare events remain a partly-unsolved mystery because our observations are still insensitive to the primary energy-release process, since the energy release site cannot be resolved with the current technical equipment. As stressed by Gold & Hoyle (1960), the Sun's magnetic field provides the only plausible source of energy for solar flares, and now it is believed to be most likely released during magnetic reconnection. Erupting prominences and CMEs are believed to be also triggered by magnetic reconnection. In fact, solar flares are sometimes accompanied by these other two kinds of solar outbursts. However, in a recent review, Lang (2009) notes that:

> The notion that there is a cause-effect relation between the three phenomena is not now in vogue. There instead seems to be a growing consensus that flares, erupting prominences and CMEs are a different manifestation of the same magnetic energy-release process in the corona, possibly via magnetic reconnection[16].

In most of the cosmos, magnetic fields are attached or "frozen" to the plasma and move around with it. This is equivalent to say that magnetic field topology is conserved[17]. This is what follows from the Maxwell induction equation and the generalized Ohm's law for perfectly conducting plasmas (that is, the magnetic field flux in plasmas with infinite conductivity is conserved through any surface which moves along with the plasma – see e.g., Syrovatskii 1978). The exception is in singular regions where the "diffusion term"[18] in the Maxwell induction equation prevails over the "convection term"[19]. When the gradient of the magnetic field is very large, the diffusion term cannot be neglected even in plasmas with low resistivity. It is in these singularities that the diffusion term becomes important and the magnetic field can diffuse through the plasma and reconnect, releasing magnetic energy. In astrophysical plasmas, these singular regions tend to form as sheets, often although not only at null points, where the magnetic field vanishes. Locally opposite magnetic fields have indeed been proposed in many large-scale configurations. But theory shows that it is not necessary that fields are oppositely directed for reconnection in 3D. It is sufficient for reconnection that there is some shear.

Magnetic reconnection is therefore a fundamental process by which magnetic field lines are carried into the singularity, broken and rejoined in a lower energy state. The energy difference between the initial and final configurations is released and converted into other forms such as thermal energy (by direct heating) as well as kinetic energy of

[16] Ongoing studies about pre-eruptive magnetic configurations on the Sun will shed light on how the magnetic fields and plasmas in the low corona, chromosphere, and photosphere shear, twist, writhe, interact, and otherwise change prior to and during the different kinds of solar outbursts, on both a local and global scale.

[17] In other words, two points in the plasma which are initially connected by a magnetic field line will continue to be connected independently of where they move.

[18] The "diffusion term" represents ohmic losses due to resistivity.

[19] The "convection term" expresses the advection of magnetic field with the fluid flow

plasma flows and fast (accelerated) particles in the surroundings of the reconnection point. The distribution of released magnetic energy into the various channels (flows, particles, and thermal energy) varies from flare to flare (see e.g., Mullan 2010).

Sweet (1958) studied magnetic reconnection in oppositely directed magnetic fields that are brought into contact at a neutral point boundary. Parker (1963) derived the detailed mathematics of various forms of Sweet's mechanism and concluded that none of them is sufficiently rapid to account for the solar flare from the annihilation of magnetic fields. Petschek (1964) described how a faster rate of magnetic field annihilation might be achieved, showing that this fast reconnection could permit the rapid conversion of magnetic energy within the observed minute-length duration of solar flares. Carmichael (1964) proposed that the outermost loops are extended up into the corona by the solar wind. The final shape is termed helmet streamer (see left picture in Fig. 1.4). He also discussed how the surrounding corona or loop twisting might lead the new magnetic configuration to accelerate high-energy particles. Similar ideas about solar flares were expressed by Sturrock (1966, 1968), who described how footpoint motions of sheared coronal loops could trigger the release of magnetic energy in ways that might account for particle acceleration in a downward direction and shock waves and plasma ejection in the outward direction. Hirayama (1974) added an erupting prominence to the solar flare model, proposing that the prominence is rising above the locus where magnetic reconnection occurs (see right picture in Fig. 1.4). He also suggested that some of the non-thermal particles accelerated at the reconnection site move down into the chromosphere, forming flare ribbons and causing chromospheric evaporation (see § 1.1.1) that fill the newly linked magnetic loops with X-ray emitting material (see Fig. 1.5). So, when the prominence rises further, the magnetic reconnection point goes higher and the distance between its corresponding flare ribbons increases. Refinements to this model were made by Kopp & Pneuman (1976). The final theoretical model for both solar flares and erupting prominences developed by all these authors became known as the CSHKP[20] model. *Yohkoh* and *RHESSI* have provided scientists with observational features in agreement with the classical CSHKP model.

Some examples of large-scale geometries giving rise to reconnection are shown in Fig. 1.6. In the most popular solar flare scenario, the top of a loop expands and rises (Fig. 1.6a). This motion constricts the magnetic flux lines below the driving plasmoid. Then opposite field lines approach each other and reconnect. Hot (thermal X-ray) plasma forms a cusp below the reconnection site. On the other hand, colliding loops (Fig. 1.6b) are expected when new magnetic flux emerges through the photosphere. Fig. 1.6c shows interchange reconnection of a field line that is open to interplanetary space and a closed loop. It occurs when emerging flux pushes against open field lines or an open field line is dragged over a closed loop. Another example is given in Fig. 1.6d, that represents how magnetic reconnection may occur when the footpoints of different loops in an arcade move at different speeds and the arcade is sheared. This may lead to a large two-ribbon flare (see § 1.1.5). Finally, Fig. 1.6e shows reconnection in magnetic field lines braiding themselves by footpoint rotation.

[20]The name CSHKP comes from the firsts letters of the last names of the five people who developed this model, in a chronological listing by publication date.

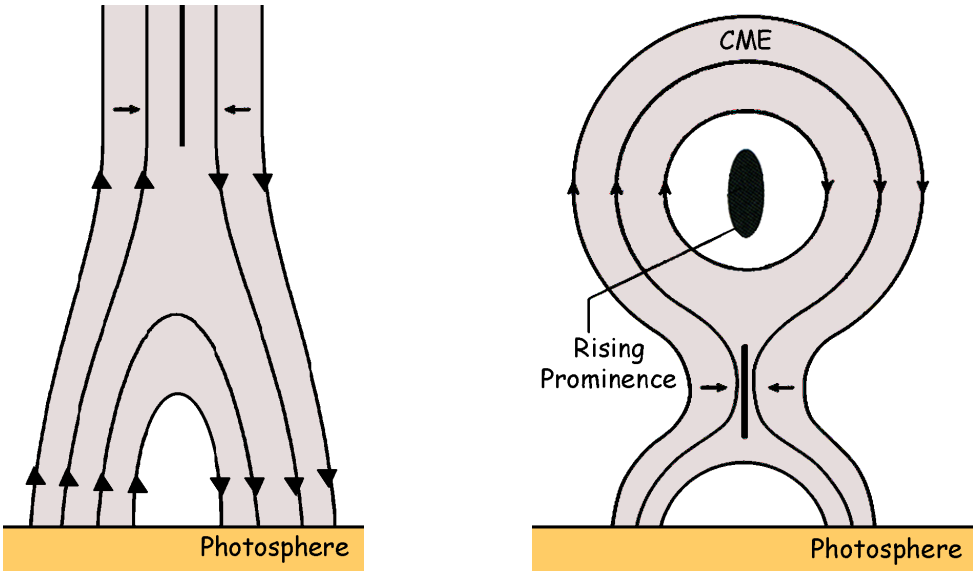

Figure 1.4: *Left)* Model of solar helmet-type structure. *Right)* Model of solar eruption. (Adapted from Martens & Kuin 1989). In both figures, a thick black straight line marks the region where magnetic fields may be reconnected. The two short arrows in each plot show how magnetic field lines should be pushed to lead to magnetic reconnection.

1.1.8 Energy budget

Magnetohydrodynamic theory of reconnection predicts equal shares of energy for local ohmic heating and motion of the plasma ejected from the reconnection region (textbook by Priest & Forbes 2000). Flares are sometimes accompanied by CMEs, but we have not included the energy that leaves the corona with them in the energy budget. Ohmic heating may amount to accelerating particles to non-thermal energy distribution. Lin & Hudson (1971, 1976) inferred that the $10 - 10^2$ keV electrons accelerated during the initial phase constitute the bulk of the total flare energy output. These electrons are thought to produce much of the observed flare emission in different wavelengths through their various interactions with the solar atmosphere (see above).

Non-thermal electron energy

The non-thermal electrons accelerated to relativistic velocities in the reconnection site transport to the chromosphere their (total) kinetic energy ($E_{\rm kin}$). The value of $E_{\rm kin}$ can be obtained by using Eq. 1.1, where ϵ is the electron energy and $F(\epsilon)$ is the electron flux distribution per energy unit impinging on the target. If the accelerated electrons have a power-law distribution with spectral index $-\delta$, the emitted bremsstrahlung by a thick target[21] provides necessary information to calculate the value of this index.

[21] The thick target model assumes that all the X-ray and γ-ray emissions are produced by particles which stop in the solar atmosphere, and none by particles escaping to the interplanetary medium.

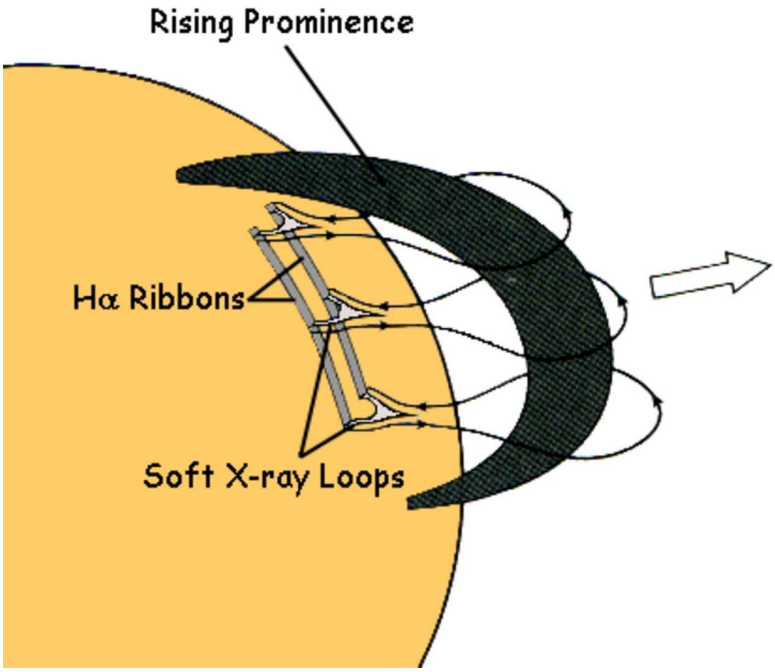

Figure 1.5: 3D model of solar eruption: the prominence rises through the lower corona, followed by sequential magnetic reconnection, flare ribbons at the footpoints of the loop arcade and soft X-ray loops. (Adapted from Lang 2009).

$$E_{\rm kin} = \int_{\epsilon_{\rm min}}^{\epsilon_{\rm max}} F(\epsilon)\epsilon \, d\epsilon \tag{1.1}$$

As $\delta > 2$ in all observations, the integral in Eq. 1.1 depends strongly on the low-energy cut-off $\epsilon_{\rm min}$. Since the emission of the non-thermal electrons and that of the thermal plasma (see below) are usually cospatial and overlap in photon energies in the range from about 10 to 25 keV, it is difficult to determine the value of $\epsilon_{\rm min}$. Thus the low-energy turnover of the electron distribution measured and reported to be at 20 keV (Saint-Hilaire & Benz 2005) is unconfirmed and may be an upper limit.

Thermal energy

Part of the non-thermal energy is converted into thermal energy of the plasma heated through chromospheric evaporation (see § 1.1.1). Even though the evaporated chromospheric material contains plasma at different temperatures and the best way of describing it is by giving its distribution of emission measure with temperature, $EM(T)$, it is often (well-) modeled with a single temperature for simplicity, and sometimes with an additional much hotter, but smaller second component. It is indeed consistent with results obtained by Reale et al. (2001) for a sample of flares with different intensity and morphol-

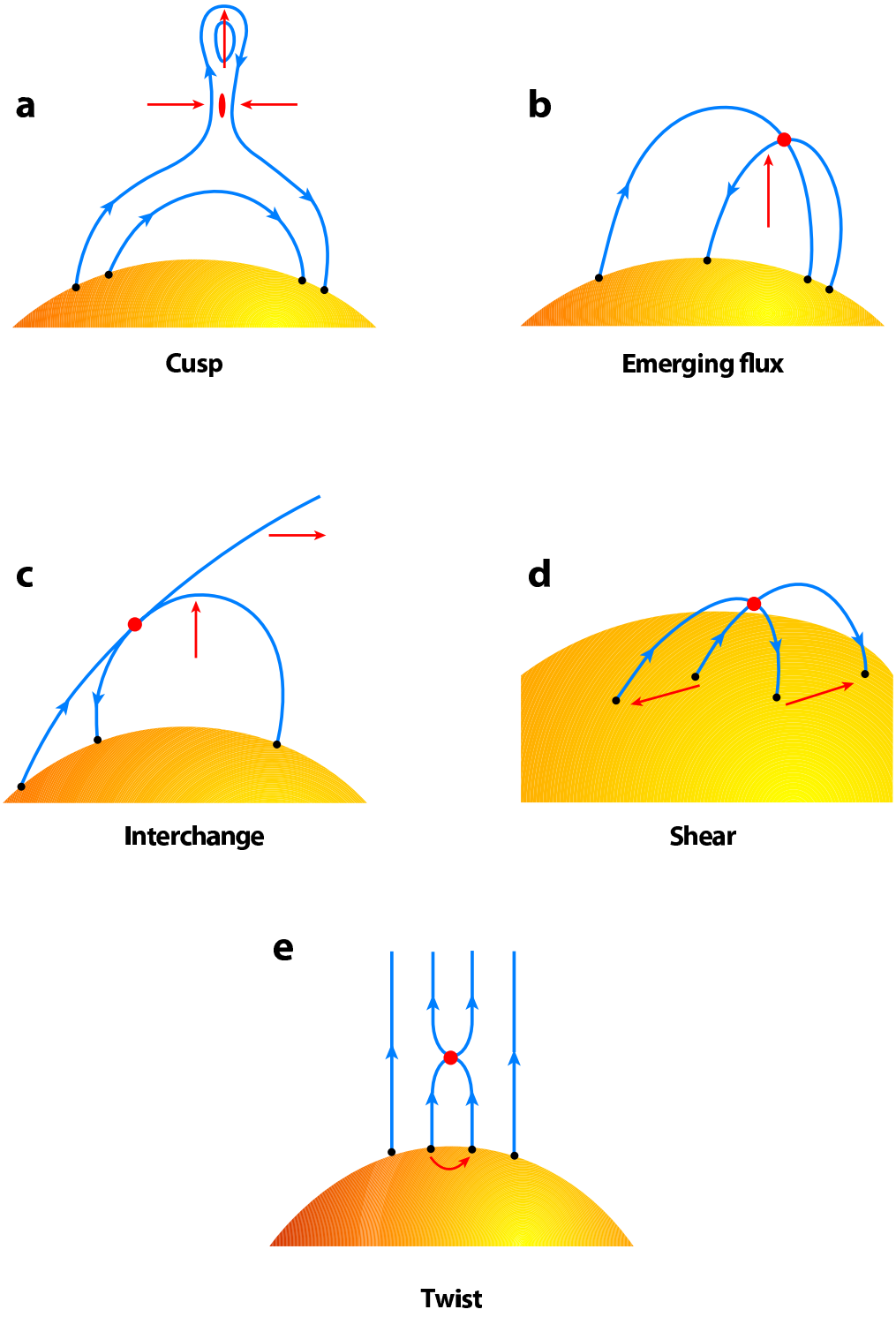

Figure 1.6: Example of large-scale geometries leading to reconnections (a – e). Magnetic field lines are shown with blue lines. The direction of the magnetic field is given by blue arrows. Red arrows symbolize the driving forces and the reconnection site in each scenario is marked with a red dot. (Extracted from Benz & Güdel 2010).

ogy. They showed that at any flare phase[22] the $EM(T)$ is typically quite narrow (and much narrower than the $EM(T)$ of the whole Sun in any phase of its activity cycle), practically independent of the flare intensity and flaring region morphology, and covers a temperature decade around $\sim 10^7$ K. Exceptions are the $EM(T)$ profiles obtained for the most intense flare in the sample, which shows significant amounts of hotter plasma, at temperatures up to 10^8 K. The flaring (X-ray) plasma is therefore assumed to be evaporated chromospheric material, and its thermal energy $E_{\rm th}$ amounts to:

$$E_{\rm th} = 3k_B T \sqrt{EM_{\rm F} V}, \tag{1.2}$$

where T and $EM_{\rm F}$ are the final temperature and total emission measure (respectively) of the newly heated, evaporated plasma. The observations suggest that $E_{\rm kin}$ is larger by a factor of 1 – 10 than $E_{\rm th}$ for plasma at $T > 10$ MK (Emslie et al. 2004; Saint-Hilaire & Benz 2005). This factor agrees with the expectation that heating to coronal temperature is not a loss-free process. The result is also consistent with the observations in white light suggesting that a major part of the non-thermal energy is lost to low-temperature plasma.

Typical energies in solar flares

As the resolving power of solar instruments improved, smaller and smaller flares and flare-like phenomena have been detected on the Sun. The non-thermal energy in giant solar flares is of order 10^{33} – 10^{34} erg (e.g., Kane et al. 1995, 2005). Flares of this size occur on the Sun only in the maximum phase of magnetic activity. The non-thermal emission in the smallest flares observed in active regions lasts for only ≈ tens of seconds and amounts to $\sim 10^{26}$ erg (Hannah et al. 2008). In addition, these authors estimated the thermal energy of these flares to be as low as $\sim 10^{26}$ erg. Using EUV data from *TRACE*, (Sakamoto et al. 2008) detected flare-like events on the Sun with thermal energies of only a few times 10^{23} erg. As far as we are concerned, these are the weakest flare-like events ever detected on the Sun.

1.2 Stellar Flares

The first detection of a non-solar flare was performed by Joy & Humason (1949). In particular, they observed an enhancement of both the optical line and optical continuum emission (similar to what is observed during intense, white-light solar flares) from the star UV Ceti, that is classified in the CNS3R catalogue as a star with spectral type M6 and luminosity class V. This prompted the search for stellar flares, at first by optical photometry of stars similar to UV Ceti in the solar neighbourhood, i.e. late K- and M-type dwarfs with emission lines in their spectrum (dK7e and dMe stars). For this reason, they are known as ***UV Ceti-type stars*** or ***classical flare stars***. These red stars are main-sequence

[22] As stated by Reale et al. (2001), the $EM(T)$ of all flares in their sample clearly follows a common evolution path: "it starts low but already at a relatively high temperature, centered at $\sim 10^7$ K; it grows toward higher EM values, maintaining a more or less constant shape and sometimes shifting slightly rightward to higher temperatures; then it decays by gradually cooling (lower T) and decreasing (lower EM values)".

stars, or still-contracting stars that have nearly reached the zero-age main sequence. Note that many UV Ceti-type stars are also classified as *BY Dra variables*[23].

Detector improvements and access to new spectral regions allowed detecting (sometimes unexpected) flare-type activity in many other kinds of stars across the HR diagram (non-classical flare stars, see Pettersen 1989). In his review, Pettersen (1989) concluded that flares are confirmed to take place in stars with outer convection zones, on or above the main sequence in the HR diagram, which also show a high level of background magnetic activity. This includes both young stars still contracting towards the main sequence (***pre-main-sequence stars*** or ***PMS stars***, see main stages of their evolution together with some properties in Fig. 1.7) and late-type (as cool as, or cooler than F–type) main sequence stars, singles or members of multiple stellar systems; as well as various types of evolved stars (*RS CVn systems*[24] and *Algols*[25], see also Bastian 1994). Very few flare-like events have been reported outside this domain of cool stars, but they are thought to be caused by an unnoticed cool companion or an unnoticed cool star within the source area.

Stellar flares are most easily detected in X-rays, ultraviolet emission lines and radio. In these wavelengths the contrast between the flare emission and the quiescent emission from the star is large. The low photospheric temperatures of M dwarfs allows flares to be detected easily also in the optical, especially in the U band and the Balmer lines.

The wide variety of flare morphologies found in stellar light curves complicates the understanding of the mechanism(s) involved in flares. Tovmassian et al. (2003) presented a phenomenological model to explain a wide variety of white-light curves of stellar flares. This model is based primarily on geometrical considerations in which the position of the flare with respect to the stellar observable disk (i.e., a projection effect) gives rise to different flare morphologies. They decomposed white-light curves of flares into two different components. The first component (prime flare) consists of a fast and strong increase of brightness followed by a relatively slow decline that may be approximated as "proportional to" $e^{-\beta t}$. A second, fainter component appears at some point during the evolution of the prime flare. The rise and decay of the second component are much slower than those in the prime.

Flare energy ranges from 10^{22} erg in solar nanoflares to 10^{38} – 10^{40} erg in huge flares observed on RS CVn and pre-main-sequence stars. Flares typically follow a common pattern, showing impulsive and gradual stages and a remarkably similar distribution of energy among the different radiating channels (analogous to that shown for solar flares in Figure 1.3). Although flares on the Sun and different classes of stars vary greatly in

[23]The BY Dra-type stars are chromospherically active K- or M-type main sequence stars showing broad-band light variations that are attributed to starspots. Some of them are close binaries, but others are not. The rotational periods of these stars are in the range 1 to 5 days. This high rotation rate suggests that they are young stars or tidally locked stars in a short-period binary system.

[24]The RS CVn systems are close but detached, tidally locked binaries with orbital period between 0.5 and 20 days in which the components are very active stars of spectral type late F, G or early K, and luminosity class V, IV or III with at least one component being a evolved (subgiant) star. Note that RS CVn stars have negligible mass exchange.

[25]The Algol-type binaries are semidetached binary systems made up with a cool (G-, K- or M-type) subgiant or giant and an early-type (late B-, A- or early F-type) main sequence star. Mass transfer in these systems takes place from the Roche-lobe filling secondary to the primary star, which results in the more evolved star being the least massive.

PROPERTIES	*Infalling Protostar*	*Evolved Protostar*	*Classical T Tauri Star*	*Weak-lined T Tauri Star*	*Main Sequence Star*
SKETCH	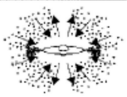	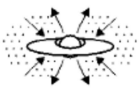			
AGE (YEARS)	10^4	10^5	10^6 - 10^7	10^6 - 10^7	$> 10^7$
mm/INFRARED CLASS	Class 0	Class I	Class II	Class III	(Class III)
DISK	Yes	Thick	Thick	Thin or Non-existent	Possible Planetary System
X-RAY	?	Yes	Strong	Strong	Weak
THERMAL RADIO	Yes	Yes	Yes	No	No
NON-THERMAL RADIO	No	Yes	No ?	Yes	Yes

Figure 1.7: The stages of low-mass young stellar evolution. (From Feigelson & Montmerle 1999).

energy, times scales and volumes (see Table 1.3), their similar phenomenology points to a common physical origin for all of them. Therefore the analysis of stellar flares relies heavily upon the assumption that they are basically similar to solar flares except for the fact that they are more energetic.

As this Ph.D. Thesis is about flares on UV Ceti-type and PMS stars, the next sections are focused on their main properties.

1.2.1 Flares on UV Ceti-type stars

UV Ceti-type stars exhibit flares over a wide variety of energies. Nevertheless, the properties of all these flares show a remarkable consistency. Pettersen (1989) pointed out that UV Ceti-type stars show no change in the kind of flare activity corresponding to the transition from stars with deep convective envelopes to fully convective stars (for main sequence stars, this transition is believed to occur at spectral type M4, see Stassun et al. 2011, and references therein). Provided that stellar flare activity is supposed to result from magnetic field interactions, he suggested that if different types of dynamos originated magnetic fields on these two types of stars (e.g., Durney et al. 1993), their corresponding dynamo efficiency would not be very different. This suggestion is also in agreement with the fact that analyses of different activity diagnostics show no obvious transition in magnetic activity for main sequence stars at spectral types ~ M4 (see, e.g., § 1.2 in Browning 2008).

Table 1.3: Comparison of main characteristics of flares on the Sun and other stars. Extracted from Linsky (2000).

Property	Star type	Values
Energy	Sun:	10^{22} – 10^{32} erg
	dMe:	10^{31} – 10^{34} erg
	RS CVn:	10^{34} – 10^{38} erg
	PMS:	10^{36} – 10^{40} erg
Time scale	Sun:	ms – 1 hour
	dMe:	s – hours
	RS CVn:	hours – days
	PMS:	hours

Linsky (2000) listed some of the characteristic properties of flares on UV Ceti-type stars as follows:

- Optical flares typically show very fast rise times (from seconds to a few minutes in the U band) during the impulsive phase followed by the decay or gradual phase (exponential type) lasting from some tens of minutes to several hours (see e.g. Moffett & Bopp 1976).

- The impulsive phase is dominated by the optical and continuum emission while the gradual phase is dominated by the Balmer and UV emission lines and the soft X-ray emission.

- The energy radiated during the impulsive phase is about two or three times the energy radiated during the gradual phase.

- Multiwavelength observations show that the flare energy emitted through different channels (Balmer lines, optical and UV continuum, and X-rays) are roughly proportional over a wide range of flare energies. In particular, the total soft X-ray emission is approximately equal to the energy radiated in the U band continuum. Each one of these energies corresponds to about 1/6 of the total optical and UV continuum emission.

- The main difference between giant flares and much lower energy flares is probably due to the longer duration of the heating and larger area coverage of the large flares rather than to enhanced heating per unit area and time. Linsky (2000) concluded that the heating rate and magnetic recombination rate per unit area on the star appear to be roughly the same, indicating that the physics of magnetic field reconnection limits to within a narrow range the rate at which magnetic energy can be converted to other forms of energy.

- The radiative output of flares observed on dMe stars tend to follow a pattern consistent with that of solar flares. For this reason, many authors (e.g., Haisch et al.

1983; van den Oord et al. 1996) have argued that flares on dMe stars are scaled up versions of solar compact or two-ribbon flares. Nevertheless, this conclusion must be viewed as tentative because the radiative response of the atmosphere to the impulsive input of energy could be the same (and would be that of a plasma following the rules of hydrodynamics, atomic physics and radiative transfer) for a variety of different energy input mechanisms.

- Intense radio emission is commonly detected during flares. This is usually interpreted as gyrosynchrotron emission from relativistic electrons, although some radio flares are naturally explained by coherent maser or plasma emission processes.

- Beams of nonthermal electrons cannot be directly observed. However, their presence can be inferred from the Neupert effect (see § 1.1.1). The verification of the Neupert effect during the 1993 March 1–3 flare of AD Leo (Hawley et al. 1995) provides support for electron beam heating of flares on dMe stars. Since hard X-rays are difficult to observe during stellar flares, Hawley et al. (1995) used the white light continuum emission (most easily seen in the U-band) as a proxy for the hard X-ray emission. This was assumed because during the impulsive phase of solar flares, the white light emission and the hard X-ray emission are coincident in space and time (Hudson et al. 1992), indicating their common origin from the electron beams accelerated by magnetic field reconnection.

- X-ray flares on dMe stars typically show X-ray fluxes increasing by a factor of 10 – 100 over quiescent values, flare plasma peak temperatures of the order of 3×10^7 K, and a delay of about 5 min between the peak temperature and the maximum coronal emission measure (the temperature peaks before).

1.2.2 Flares on pre-main-sequence stars

Flare activity starts at an early phase in the evolution of the stars, being a common phenomenon in young stars. In fact, flares have been confirmed to be detected even in the very young Class I protostars (Feigelson & Montmerle 1999; Favata & Micela 2003), that are very young, low-mass stellar objects that include, according to current models, a central star (still in the process of formation) surrounded by an accretion disk and an extended, infalling envelope of gas and dust (see Fig. 1.7).

Pre-main-sequence stars are observed to flare more frequently than the Sun (Favata & Micela 2003). Besides, long-duration flares are more common in pre-main-sequence stars than in the UV Ceti-type ones. For example, during the 13 days observing run of the ORION Nebula Complex (ONC) by *Chandra*, at least 19 flares with duration above half a day were detected (Favata et al. 2005). Long-duration flares were also observed in the Taurus star-forming complex (Franciosini et al. 2007; Stelzer et al. 2007).

A well studied flare among those observed in Class I protostars is the powerful X-ray flare exhibited by YLW 15, in the ρ Ophiuchi cloud core (Grosso et al. 1997). The total X-ray energy of this flare was estimated to be 10^{38} – 10^{40} erg. This value is $\sim 10^5$ times the X-ray energy emitted by the strongest flares observed on the Sun (see § 1.1.8).

Favata et al. (2005) determined general properties of flaring loops, in terms of temperature and semi-length, for young stellar objects in the ONC. From their analysis, the authors inferred loop semi-lengths comparable to the stellar radius in some cases. A similar work was done for the Taurus star-forming region (Franciosini et al. 2007), where the authors remarked that some coronal loops extended up to a distance comparable with the stellar radius (see also Giardino et al. 2004).

The long duration and the extreme energy released by flares on different pre-main sequence stars surrounded by disks, together with the very large sizes (relative to their host star) obtained for their corresponding flaring structures, in comparison to those of flares on the Sun and UV Ceti-type stars, are strong arguments that these flares are not scaled up solar two-ribbon flares. Grosso et al. (1997) and Favata et al. (2005) speculate that the magnetic structures that confine the flaring plasma in these young objects are actually the same type of structures that channel the plasma in the magnetospheric accretion paradigm. These flares are therefore more likely due to magnetic reconnection events that occur when the magnetic fields connecting the star's photosphere with the accretion disk shear and interconnect as forced by their different rotation rates.

However, in more evolved (Class III, non-accreting) Young Stellar Objects (YSOs), the X-ray emission mechanism is likely to be very similar to the one operating in main-sequence active stars. This scenario would involve that coronae of class III YSOs are a scaled-up version of the solar corona. Thus, the emitting X-ray plasma would be entirely confined in magnetic loop structures and heated by similar mechanisms as those operating in the Sun (e.g., Favata et al. 2005). Thus, flares in these objects are expected to be scaled-up versions of solar flares.

1.3 Flares as a mechanism of chromospheric and coronal heating

The question of what heats the solar chromosphere and corona has baffled scientists for decades and they are still trying to explain where all the heat is coming from[26].

The existence of chromospheres on late F, G, K and early M main-sequence stars has been known for decades: the chromospheres reveal their existence in the form of emission lines of hydrogen and other elements in the spectrum. In addition, X-ray telescopes aboard modern spacecrafts have observed steady, "quiescent"[27] X-ray radiation from these stars. Late F, G, K and early M main-sequence stars have roughly the same mass, size and luminosity as the Sun. Like the Sun, their X-ray emission is attributed to

[26]The visible solar disk (the photosphere) is closer to the Sun's center than the corona, but the photosphere is several hundred times cooler ($T_{\mathrm{eff},\odot} \approx 5780$ K) than the corona, in which the plasma reach a temperature of about 2×10^6 K. We know that visible sunlight emitted by the photosphere cannot heat the corona to such high temperatures. In fact, there is so little material in the corona that it is transparent to almost all of the photospheric radiation. Visible sunlight therefore passes right through the corona without depositing substantial quantities of energy in it, traveling out from the Sun. Thus, under normal thermodynamic considerations, the atmosphere above the photosphere should decrease in temperature as one travels away from the Sun, instead of increasing dramatically.

[27]In solar and stellar atmospheres, the term "quiescent" refers to spatial or temporal regions in which no sign of activity is detected.

the thermal radiation of electrons in stellar coronas with temperatures of 1 to 10 million degrees. Since the visible light from these stars is emitted from photospheres with effective temperatures[28] between 7200 K (for spectral type F0) and 3370 K (for type M4), the chromospheric and coronal heating problem also applies to these stars.

As pointed out in the review by Klimchuk (2006), finding a definitive solution for the coronal (also chromospheric) heating problem involves a number of challenging steps: identification of the energy source; realistic modeling of both the energy release process and the response of plasma to the heating; and, finally, prediction of observable quantities that can be compared directly with actual observations.

Skylab observations made it clear for the first time that the X-ray emitting hot and bright coronal regions on the Sun and the underlying surface magnetic field concentrations are strongly correlated, suggesting that coronal heating and magnetism are intimately linked with each other.

In these days, it is widely accepted that mechanical motions and magnetic fields in and below the photosphere, which supply the kinetic energy of moving material and the magnetic energy stored in the solar and stellar atmospheres, are the ultimate source of energy responsible for their heating. Everything is in motion within the photosphere and the turbulent convection zone beneath it, and magnetic fields thread their way through the entire solar atmosphere. These motions displace the footpoints of magnetic field lines, stressing the field, and generate a large flux of upwardly propagating magnetic waves. Dissipation of magnetic stresses is referred to as direct current (DC) heating, while dissipation of magnetic waves is referred to as alternating current (AC) heating. DC and AC heating operate when the plasma is embedded in magnetic fields, as it is in most parts of the solar atmosphere, for which the framework of magnetohydrodynamics may be the more appropriate approach. For magnetic-free regions (e.g., in the chromosphere of quiet Sun), instead, one may suggest heating mechanisms that can be described within the framework of hydrodynamics (hydrodynamic heating). Examples of hydrodynamic heating are, among others, acoustic waves and pulsations.

There are no doubt many different heating mechanisms are operating in the solar and stellar atmospheres (see reviews by, e.g., Walsh & Ireland 2003; Klimchuk 2006; Erdélyi & Ballai 2007, and references therein), and the real goal is to determine which one is dominant, both in general and specific situations. This time, we are particularly interested on a DC heating mechanism: the magnetic reconnection.

Magnetic reconnection may not merely be responsible for the largest energy releases in the Sun and solar-like stars: such events are unambiguously identifiable as distinct bona fide flares (see previous sections). The proposal that the quiescent corona in the Sun might also be (quasi-)continuously heated by a multitude of sporadic magnetic reconnection events in "nanoflares" (flare-like events releasing energies of order $10^{-9}E_{\rm F}$, where $E_{\rm F}$ is the energy released in the largest solar flares) was analysed by Parker (1983, 1988). Note that recent instruments have allowed the detection of flare-like events with energies down to 10^{23} erg (see e.g. Sakamoto et al. 2008) and the nanoflare concept (a flare so small that it is unresolved) has been extrapolated even to lower energies, where hypothetical flare-like events are named "picoflares" (releasing energies of order $10^{-12}E_{\rm F}$).

[28] Note that the Sun is a main-sequence G2 star, so the effective temperature of its photosphere is 5780 K.

In the nanoflare scenario, coronal loops are collections of unresolved strands that braid, twist and writhe, becoming entangled by the random motion of their footpoints caused by turbulent convection. Thus, energized from below, the tangled magnetic strands eventually generate currents and reconnect into new configurations, releasing stored magnetic energy and powering nanoflares. So plasma is impulsively heated by nanoflares to high temperatures of several MK and then cool down to the 1 MK range. In this picture a nanoflare is the basic unit of impulsive energy release, and the steady emission from a coronal loop would result from the sum of the radiation simultaneously emitted by all the strands in the loop, which are assumed to be heated by random, intermittent and impulsive nanoflares. In addition, impulsively heated sub-resolution strands can also be invoked to explain the emission from areas not containing resolved coronal loops, i.e., diffuse background areas.

The nanoflare-heating concept is still a subject of controversy and has been subjected to extensive observational and numerical testing (see, e.g., Cargill 1994; Cargill & Klimchuk 1997; Dahlburg et al. 2005; Patsourakos & Klimchuk 2009; Susino et al. 2010, and references therein). In view of these studies, it appears that even the so-called quiescent corona may be heated by reconnection phenomena occurring as scaled-down versions of "regular" (or, as above-mentioned, bona fide) flares. In this way, beams of electrons may be accelerated to relativistic velocities in multiple sites throughout the magnetic corona. These non-thermal electrons would act as emitters of synchrotron radiation at centimetric radio wavelengths, as explained in § 1.1.4, and later would lose most of their energy by collisions, increasing the coronal emission in soft X-rays, as seen in § 1.1.1 ("causal relation" between non-thermal and thermal energy). Therefore, this could explain why the quiescent centimetric radio luminosity ($L_{\rm rad}$) is observed to be positively correlated with the quiescent luminosity in soft X-rays ($L_{\rm X}$) over almost five orders of magnitude in $L_{\rm X}$ ($27.6 \lesssim \log L_{\rm X}(\mathrm{erg\ s^{-1}}) \lesssim 32.2$) across spectral types from F to mid-M ($L_{\rm rad} \sim 10^{-15.5} L_{\rm X}$), as reported by Güdel & Benz (1993). Note that the thermal radio emission from the Sun's corona would be undetectable with even the world's largest radio telescope if the Sun was placed at the distance of the next-nearest star. Therefore, the radio emission from stars other than the Sun has to be non-thermal radiation.

During the last two decades, the debate over the nanoflare heating scenario has been focused on extrapolations from observations of "regular" flares, to determine if undetected weaker ones might provide sufficient energy to heat and power the quiet[29] corona. Indeed, the distribution law that gives the number of flares dN per unit area and per unit time within an energy-interval $[E, E + dE]$ allows us to estimate the energy budget of the corona. In particular, solar flares are distributed following a power law (Datlowe et al. 1974; Lin et al. 1984; Dennis 1985), that is,

$$\frac{dN}{dE} = N_0 \left(\frac{E}{E_0} \right)^{-\alpha} , \tag{1.3}$$

where N_0 and E_0 are constants which together form a normalization factor[30], and α is the power-law index ($\alpha > 0$). Let the total power P be the total energy released by flare-like

[29] For spatial regions, the adjective "quiet" can be used as a synonym of "quiescent".

[30] Note that the normalization factor varies with the degree of activity.

events per unit area and per unit time in the the energy range from the weakest flare-like event ($E_{\rm min}$) to the the strongest one ($E_{\rm max}$) (see Eq. 1.4). For $\alpha \neq 2$, P is given by Eq. 1.5.

$$P = \int_{E_{\rm min}}^{E_{\rm max}} \frac{dN}{dE} E\, dE \tag{1.4}$$

$$P = \frac{N_0 E_0^2}{2-\alpha} \left(\left(\frac{E_{\rm max}}{E_0} \right)^{2-\alpha} - \left(\frac{E_{\rm min}}{E_0} \right)^{2-\alpha} \right) \tag{1.5}$$

Note that $E_{\rm max} >> E_{\rm min}$. With this in mind, as pointed out by Hudson (1991), if $\alpha > 2$ Eq. 1.5 can be approximated by Eq. 1.6, implying that large flares would provide the dominant contribution to the heating. On the contrary, if $\alpha < 2$, Eq. 1.5 can be approximated by Eq. 1.7, implying that small-scale flare-like events would dominate the heating.

$$P \approx \frac{N_0 E_0^2}{2-\alpha} \left(\frac{E_{\rm max}}{E_0} \right)^{2-\alpha} \tag{1.6}$$

$$P \approx \frac{N_0 E_0^2}{\alpha-2} \left(\frac{E_{\rm min}}{E_0} \right)^{2-\alpha} \tag{1.7}$$

Inspired by the summary Fig. 14 in Aschwanden & Parnell (2002) for the flare distribution law observed on the Sun by different authors, Berghmans (2002) estimates a value for both N_0 and E_0. From the same figure, Aschwanden & Parnell (2002) also inferred the value of $E_{\rm max}$ for active and quiet regions in the Sun, obtaining that the largest flares in solar active regions are two orders of magnitude more energetic than the largest flares in the quiet Sun. Thus, the coronal heating rate by flares, P, is a function of only 2 free parameters ($E_{\rm min}$ and α) left to be determine observationally. It is often said that for flaring activity to heat the corona, α needs to be larger than 2. This statement however oversimplifies the situation. For example, Berghmans (2002) concluded that in the quiet Sun $\alpha > 2$ is a necessary condition but not a sufficient condition, because its coronal heating requirements also put severe constraints on the parameter $E_{\rm min}$ (see Eq. 1.6). On the other hand, for active coronal regions in the Sun, the heating requirements could be fulfilled even if $\alpha < 2$, given that their flares can release larger energies than those from the quiet Sun (see Eq. 1.7).

Observations of solar flares releasing large or moderate energy (flares and microflares) indicate a power law for their energy distribution with a slope $\alpha \approx 1.8$ (see, e.g., Hudson 1991). Thus, Hudson (1991) pointed out that for the corona to be heated by nanoflares, α would need to be larger than 2, i.e., the nanoflares must satisfy a different distribution function and, therefore, they may be generated by a different physical mechanism. Studies of small-scale brightenings in the quiet Sun and active regions have shown a power law both steeper and shallower than that with $\alpha = 2$ (Krucker & Benz 1998; Parnell & Jupp 2000; Aschwanden et al. 2000).

Observational studies of magnetically active stars other than the Sun are also affected by a sensitivity limit that impedes the detection of very small flares. If $\alpha > 2$, very small flares can in principle contribute an unlimited amount of energy (so any energy release power could be attained), because Eq.1.5 diverges for $E_{\rm min} \rightarrow 0$. Clearly, in such cases

there must either be a lower cut-off to the flare energies, or the power law must turn over to $\alpha < 2$ at low unresolved energies. For stellar flares, Collura et al. (1988), Osten & Brown (1999) and Wolk et al. (2005) found $\alpha \approx 1.5 - 1.7$, while other authors have reported $\alpha > 2$ (Audard et al. 1999, 2000; Kashyap et al. 2002; Güdel et al. 2003; Caramazza et al. 2007; Stelzer et al. 2007).

Therefore, at this time studies of power law distributions give us no definitive conclusion about if nanoflares are or not the main heating mechanism in the upper levels of the solar and stellar atmospheres. Moreover, all theoretical models of nanoflare heating predict loops with an unresolved multi-temperature structure even for the finest observable loop strands in the solar corona, but according to Aschwanden (2008), this is in discrepancy with the quasi-isothermal cross sections observed in these solar structures with TRACE. For this reason, he proposes modifying the theoretical models by relocating the hypothetical nanoflare events from their coronal location down to the chromosphere/transition region, where high-resolution magnetograms reveal many low-lying magnetic loops. But how would be the energy released by these magnetic reconnections propelled up to heat the corona high above? According to Ryutova & Tarbell (2003), merging low-lying magnetic loops can form shock waves that are launched by the bent magnetic fields in slingshot fashion, flinging heated gas through the overlying transition region. So to sum up, there is abundant evidence that the quiet corona outside active regions is linked to reconnection of magnetic loops, either lying within the corona or residing beneath it.

1.4 On the interest of studying solar and stellar flares

Solar flares have been known to cause widespread power outages and communication disruptions. They pose radiation hazards to instruments and reduce low-orbit-spacecraft lifetimes.

Flares originate in out-of-equilibrium magnetic field-plasma interactions rather than in gravitational, thermonuclear, or radiative processes in near equilibrium. They allow us to study how magnetically confined plasma behaves under extreme conditions of temperature.

Flares are essential in removing strong magnetic fields that are created by the dynamos operating in most late-type stars. In the process of reconnecting these fields, the observed energetic flares and the far more numerous nanoflares are probably responsible for most of the energy that heats the corona of late-type stars.

Flares also offer diagnostics of solar and stellar magnetic activity that supplement those inferred from spectral features, such us line broadening and slowly varying outer-atmospheric emissions. For instance, the cooling times deduced from flares observed in soft X-rays allows estimates on the extent and density of the emitting coronal regions. Moreover, flare properties may reveal aspects of stellar dynamos that cannot be inferred from other disk-integrated diagnostics.

Flare activity is observed to be very common or always present in the early phases of stellar evolution. Due to its high energetics, the understanding of flare events may lead to a better understanding of stellar formation and early evolution. However, flares are almost

completely ignored in star formation theories.

In addition, flares produce strong ultraviolet radiation that in the past may have played a role in forming the organic molecules out of which life formed.

Chapter 2

Description, aims and scope of this Ph.D. Thesis

Broadly, the research works included in this thesis revolve around flares on main- and pre-main-sequence M-type stars and chromospheric activity indicators of this kind of stars. We study flares through observations in different wavelength ranges in order to analyse their effects at different layers of stellar atmospheres. In particular, optical and X-ray observations are used so that we can investigate how flares affect, respectively, the chromosphere and the corona of stars. By using theoretical models, we are able of estimating physical properties of flaring plasma as well as sizes of flaring loops. We discuss and interpret the results in the context of solar and stellar flares reported so far.

On the one hand, the main work in this thesis has given rise to three different papers that we have published in international peer-reviewed journals. These articles are included in this volume as Chapter 3, Chapter 4 and Chapter 5, respectively, and they are entitled:

- Chapter 3: *Analysis and modeling of high temporal resolution spectroscopic observations of flares on AD Leo*.[1]
- Chapter 4: *X-ray flares on the UV Ceti-type star CC Eridani: a "peculiar" time-evolution of spectral parameters*.[2]
- Chapter 5: *A detailed study of the rise phase of a long duration X-ray flare in the young star TWA 11B*.[3]

On the other hand, two different appendixes (A and B) have been included to extend and reinforce the content of the previous chapters. The content of Appendix A was published as a proceeding of an international workshop while the work shown in Appendix B

[1] *"Analysis and modeling of high temporal resolution spectroscopic observations of flares on AD Leonis"*, Crespo-Chacón, I., Montes, D., García-Alvarez, D., Fernández-Figueroa, M. J., López-Santiago, J., & Foing, B. H., 2006, A&A, 452, 987.

[2] *"X-ray flares on the UV Ceti-type star CC Eridani: a "peculiar" time-evolution of spectral parameters"*, Crespo-Chacón, I., Micela, G., Reale, F., Caramazza, M., López-Santiago, J., & Pillitteri, I., 2007, A&A, 471, 929.

[3] *"A Detailed Study of the Rise Phase of a Long Duration X-Ray Flare in the Young Star TWA 11B"*, López-Santiago, J., Crespo-Chacón, I., Micela, G., & Reale, F., 2010, ApJ, 712, 78.

is part of an additional article that we have published in an international peer-reviewed journal. These appendixes are entitled:

- Appendix A: *Spectroscopic monitoring of an additional sample of UV Ceti-type stars*.
- Appendix B: *Peculiarities in the chromospheric activity indicators of flare stars*.

2.1 Aims and scope of Chapter 3

In solar flares, no detectable signature in white-light is generally observed. Even though this kind of flare (non white-light flare) is the most typical in the Sun, very few such events had been previously detected in stars. Conversely to the Sun, previous to this work very little time was dedicated to stellar spectroscopy in the optical range, in comparison to photometry. Moreover, although spectral emission lines are the most appropriate diagnostics to constrain the physical properties and motion of the flaring plasma, previously to this work only a few sets of observations with adequate time and spectral resolution were available. Furthermore, there were also few attempts to derive the physical parameters of the flaring plasma. Good quality spectroscopic observations, as those analysed in this work, were required to search for non white-light flares on stars other than the Sun and also to constrain numerical simulations to estimate physical properties of the flaring plasma.

Specifically, in this chapter we present the results of a high temporal resolution spectroscopic monitoring in the optical range of AD Leo, a fast rotating M3Ve dwarf, carried out with an intermediate dispersion spectrograph. More than 600 spectra were taken in four nights. Fourteen weak, short flares were detected. These events result to be non white-light flares: within the studied wavelength range they only affect the emission in the chromospheric lines, but not the continuum. The behaviour of different chromospheric lines (Balmer series from Hα to H_{11}, Ca II H & K, Na I D_1 & D_2, He I 4026 Å and He I D_3) is studied in detail for these flares. The physical parameters of the chromospheric flaring plasma are estimated from the Balmer decrements by using the Jevremović et al. (1998) procedure, which assumes a simplified slab model of flares. The projected surface area covered by the flaring plasma is also derived. Finally, we study the relationships between the physical parameters and the area, duration, maximum flux and energy released during the detected flares. In brief, with this work we considerably extend the existing sample of stellar flares analysed with good quality spectroscopy in the optical range.

2.2 Aims and scope of Chapter 4

A recurrent idea in the literature is that flares are the main heating agent of the outer layers of stellar atmospheres, so that the "quiescent" radiation emitted by these layers would result from a superposition of multiple weak flares. However, due to instrumental limitations, until recent years only large flares have been studied in detail. At the present time, the great sensitivity, wide energy range, high energy resolution, and continuous

time coverage of the EPIC (European Photon Imaging Cameras) detectors – on-board the XMM-Newton satellite – also enable the detection and analysis of small flares. UV Ceti-type flare stars are specially indicated for this purpose because of its proximity. For this reason, we looked for observations of UV Ceti-type flare stars in the XMM-Newton public archive. After inspecting them, we decided to perform a deeper study of the X-ray data available for the very active star CC Eri (spectroscopic binary consisting of a K7.5Ve primary and a M3.5Ve secondary), for which the EPIC-PN CCD camera detected two flares weaker than those typically studied in addition to a great variability of its basal level.

We carry out time-resolved spectroscopy of the XMM-Newton data of CC Eri in order to obtain the evolution of coronal properties through its whole observation. A multi-temperature model is used to fit the spectra by a self-consistent "iterative" procedure. We are able to infer the size of the loops responsible for the observed flares from the density-temperature diagram and the Reale et al. (1997) flare loop model, which includes the effect of sustained heating during the decay. These sizes give us an idea about the extent of the corona. Later, we apply the so-called RTV scaling laws (Rosner et al. 1978) and other fundamental laws of physics to derive additional characteristics of the plasma contained in the flaring loops and the strength of the magnetic fields required to confine this plasma. Making some assumptions we are also able to estimate the number of loops involved in the observed flares. Shortly, in this work we take advantage of the goodness of the EPIC-PN detector to reveal for the first time details about the behaviour of coronal plasma during two flares weaker than those typically analysed in other active dM stars. From the obtained results we discuss about the possibility that the whole X-ray light curve of CC Eri could be originated, to a large fraction, by a superposition of multiple flares with different intensity.

2.3 Aims and scope of Chapter 5

As in Chapter 4, in the work described in this Chapter we also take advantage of the good quality of the EPIC detectors on-board the XMM Newton satellite in order to perform a time-resolved spectral analysis of a flare. But this time we are not analysing a flare on a UV Ceti-type star but on a younger star. In particular, we carry out a deep study of a long duration X-ray flare in the pre-main sequence star TWA 11B, a weak-line T Tauri M2.5 star with an age of $\sim$ 8 Myr. This large flaring episode lasted more than the entire observation. Only the rise phase of the flare was observed, with the X-ray emission suffering a continuous increase during approximately 35 ks. So long rise phases have been previously observed only in T Tauri stars, some of them with accretion disks, and several RS CVn systems (rise-phase times from 8 to 55 ks). Past studies of flares detected on very young stellar objects in the Orion Nebula Cluster (1 Myr old) and the Taurus star-forming region (3 Myr old) yield loop semi-lengths comparable to the stellar radius in some cases. The authors speculated that these large structures are connected with the protoplanetary disk and are, in fact, the same structures that channel the plasma producing accretion. However, more evolved stars (main-sequence stars as those studied in previous chapters of this Thesis) show flaring loops with semi-lengths of $\sim 0.2 - 0.5\ R_\star$, i.e., a relatively

compact flaring corona. While TWA 11B shows no signatures of being surrounded by an accretion disk, it is still contracting. The analysis of the X-ray flare rise observed on TWA 11B allows us to get an idea about the size of the corona of M-type stars older than 3 Myr but still not reaching the main-sequence branch.

The study of the time-resolved light curve, hardness-ratio curve, and spectra consistently indicates that the very first part of the rise (event A) was consequence of a flare originated mainly a single loop while the later rise (event B, probably triggered by event A) involved a loop arcade, i.e., a proper two-ribbon flare. Therefore, for the first time we combine tools for the analysis of single loops and arcades to determine physical properties of the flaring plasma as well as geometry and magnetic configuration of the flaring loops. On the one hand, event A is analysed by using a procedure which assumes the flare to be produced in a single loop where heating does not entirely drive the flare decay (Reale 2007). Note that this approach is the same as that used in Chapter 4 (Reale et al. 1997, 2004) but extended to allow its use also for the rise phase. On the other hand, for studying event B a different technique must be used because heating is supposed to drive totally this flare evolution, so we use the stellar version of the Kopp & Poletto (1984)'s solar two-ribbon flare model (Poletto et al. 1988), that is able to provide some limited information about the late flaring structures. The fluorescent iron emission line at 6.4 keV was detected during event B. As far as we are concerned, this is only the third clear detection of Fe photospheric fluorescence in stars other than the Sun.

2.4 Scope of the appendices

During the development of the work presented in this document, we have also performed a large amount of optical observations of UV Ceti-type stars using both medium and high resolution spectrographs. As a result, we carry out two additional statistical works on the properties of chromospheric emission originated in these stars. These studies are shown in Appendix A and Appendix B, which are included in this dissertation to extend and reinforce the content of the previous chapters.

Appendix A supplements the work described in Chapter 3, where we analyse high temporal resolution spectroscopic observations of the star AD Leo. With the aim of testing whether non white-light flares (as those observed on AD Leo) are or not common among UV Ceti-type stars, we present the results of a high temporal resolution spectroscopic monitoring of a sample of red dwarfs with spectral types from K7 to M4.

Appendix B puts the chromospheric emission of UV Ceti-type stars in the context of that from the rest of active stars by using high resolution optical *echelle* spectra.

Chapter 3

Analysis and modeling of high temporal resolution spectroscopic observations of flares on AD Leo

I. Crespo-Chacón[1], D. Montes[1], D. García-Alvarez[2,3], M. J. Fernández-Figueroa[1], J. López-Santiago[1,4], B. H. Foing[5]

[1] Departamento de Astrofísica y Ciencias de la Atmósfera, Facultad de Ciencias Físicas, Universidad Complutense de Madrid, E-28040 Madrid, Spain
[2] Harvard-Smithsonian Center for Astrophysics, 60 Garden Street, Cambridge, MA 02138, USA
[3] Armagh Observatory, College Hill, Armagh BT61 9DG, N. Ireland
[4] Osservatorio Astronomico di Palermo, Piazza del Parlamento 1, I-90134 Palermo, Italy
[5] Research Division, ESA Space Science Department, ESTEC/SCI-R, P.O. Box 299, 2200 AG Noordwijk, The Netherlands

Originally published in Astronomy and Astrophysics (A&A) **452**, 987-1000 (2006)

Received 10 June 2005 / Accepted 1 February 2006

Abstract

We report the results of a high temporal resolution spectroscopic monitoring of the flare star AD Leo. During 4 nights, more than 600 spectra were taken in the optical range using the Isaac Newton Telescope (INT) and the Intermediate Dispersion Spectrograph (IDS). We observed a large number of short and weak flares occurring very frequently (flare activity > 0.71 hours^{-1}). This is consistent with the very important role that flares can play in stellar coronal heating. The detected flares are non white-light flares and, although most solar flares are of this kind, very few such events have been observed previously in stars. The behaviour of different chromospheric lines (Balmer series from Hα to H_{11}, Ca II H & K, Na I D_1 & D_2, He I 4026 Å and He I D_3) was studied in detail for a total of 14 flares. We estimated the physical parameters of the flaring plasma by using a procedure that assumes a simplified slab model of flares. All the obtained physical parameters are consistent with previously derived values for stellar flares, and the areas – less than 2.3 %

of the stellar surface – are comparable with the size inferred for other solar and stellar flares. We studied the relationships between the physical parameters and the area, duration, maximum flux and energy released during the detected flares.

Key words. Stars: activity – Stars: chromospheres – Stars: flare – Stars: late-type – Stars: individual: AD Leo

3.1 Introduction

Stellar flares are events where a large amount of energy is released in a short interval of time, with changes taking place at almost all frequencies in the electromagnetic spectrum. Flares are believed to be the result of the release of part of the magnetic energy stored in the corona through magnetic reconnection (see reviews by Mirzoyan 1984; Haisch et al. 1991; García-Alvarez 2000). However, the exact mechanisms leading to the energy release and subsequent excitation of various emission features remain poorly understood. Many types of cool stars produce flares, sometimes at levels several orders of magnitude more energetic than their solar counterparts (Pettersen 1989; García-Alvarez et al. 2002). In dMe stars (UV Ceti-type stars) optical flares are a common phenomenon. On the contrary, in more luminous stars flares are usually only detected through UV or X-ray observations (Doyle et al. 1989), although some optical flares have been observed in young early K dwarfs like LQ Hya and PW And (Montes et al. 1999; López-Santiago et al. 2003).

We would like to be able to trace all the energetic processes in a flare to a common origin, although the released energy can be very different. The largest solar flares involve energies of 10^{32} erg (Gershberg 1989). Large flares on dMe stars can be two orders of magnitude larger (Doyle & Mathioudakis 1990; Byrne & McKay 1990), while very energetic flares are produced by RS CVn binary systems, where the total energy may exceed 10^{38} erg (Doyle et al. 1992; Foing et al. 1994; García-Alvarez et al. 2003). Such a change in the star's radiation field modifies drastically the atmospheric properties over large areas, from photospheric to coronal layers. Models by Houdebine (1992) indicate that heating may be propagated down to low photospheric levels, with densities higher than 10^{16} cm^{-3}. However, electrons with energies in the MeV range would be required to attain such depths.

Spectral emission lines are the most appropriate diagnostics to constrain the physical properties and motion of the flaring plasma (see Houdebine 2003, and references therein). Unfortunately, only a few sets of observations with adequate time and spectral resolution are available so far (Rodonò et al. 1989; Hawley & Pettersen 1991; Houdebine 1992; Gunn et al. 1994b; García-Alvarez et al. 2002; Hawley et al. 2003). Furthermore, there are also few attempts to derive the physical parameters of the flaring plasma (Donati-Falchi et al. 1985; Kunkel 1970; Gershberg 1974; Katsova 1990; Jevremović et al. 1998). García-Alvarez et al. (2002) obtained the first detailed trace of physical parameters during a large optical flare, on AT Mic, using the Jevremović et al. (1998) procedure. Good quality spectroscopic observations, such as those analysed in this work for AD Leo, and a correct description of the different flare components are required to constrain numerical

simulations.

AD Leo is well-known as a frequent source of flares. It has been the subject of numerous studies in the optical, EUV and X-ray because of its nature as one of the most active M dwarfs (Pettersen et al. 1984, 1990; Lang & Willson 1986; Güdel et al. 1989; Hawley & Pettersen 1991; Hawley et al. 1995, 2003; Abada-Simon et al. 1997; Cully et al. 1997; Favata et al. 2000a; Sanz-Forcada & Micela 2002; van den Besselaar et al. 2003; Maggio et al. 2004; Robrade & Schmitt 2005; Smith et al. 2005). AD Leo (GJ 388) is classified as dM3Ve (Henry et al. 1994). This star has an unseen companion – detected using speckle interferometry – with a period of about 27 years, which is expected to have a very low mass (Balega et al. 1984). AD Leo is located in the immediate solar neighbourhood, at a distance of ~ 4.9 pc (from the ground-based parallax (Gray & Johanson 1991) – it was not a Hipparcos target). Its high activity is probably due to its high rotation rate ($P_{\rm phot} \sim 2.7$ days, Spiesman & Hawley 1986). Its rotational velocity ($v\sin i = 6.2 \pm 0.8$ km s^{-1}) places AD Leo in the tail of rare fast rotating M dwarfs (Delfosse et al. 1998). The radius and mass of AD Leo are $R \sim 0.44\ R_{\odot}$ and $M \sim 0.40\ M_{\odot}$ (Pettersen 1976; Favata et al. 2000a). At this mass, stars are expected to have a substantial radiative core, so that the interior structure is still "solar-like" (Chabrier & Baraffe 1997). Saar & Linsky (1985) detected, through infrared line measurements, photospheric fields on AD Leo showing the presence of strong magnetic fields. They inferred that 73 % of AD Leo's surface is covered by active regions outside of dark spots containing a mean field strength of $B = 3800 \pm 260$ G.

Here we present the results of a long spectroscopic monitoring of AD Leo that was carried out using an intermediate dispersion spectrograph and high temporal resolution. This work has considerably extended the existing sample of stellar flares analysed with good quality spectroscopy in the optical range. Details about the technical information of the observations and data reduction are given in § 3.2. Section 3.3 describes the analysis of the observations and the detected flares, including equivalent widths, line fluxes, released energy, line profiles and asymmetries. In § 3.4 we present the main physical plasma parameters obtained for the observed flares using the code developed by Jevremović et al. (1998). The discussion of the results and conclusions are given in § 3.5, where the relationships between the physical and observational parameters are also analysed. The preliminary results for this star and V1054 Oph were presented by Montes et al. (2003) and Crespo-Chacón et al. (2004).

3.2 Observations and data reduction

The data were taken during the MUlti-SIte COntinuous Spectroscopy (MUSICOS) 2001 campaign. It involved observations at two sites: El Roque de los Muchachos Observatory from La Palma (Spain) and SAAO (South Africa). However, due to poor weather conditions, the only useful data were those taken at La Palma. This observing run was carried out with the 2.5 m Isaac Newton Telescope (INT) from 2 to 5 April 2001. The Intermediate Dispersion Spectrograph (IDS) was utilized together with the 2148x4200 EEV10a CCD detector. Two gratings were used: R1200B (every night) and R1200Y (second half of the last night). The wavelength covered by R1200B (blue spectrum) ranges from

Table 3.1: Observing log INT/IDS (2 – 5 April 2001).

Night	R1200B								R1200Y				
	N	UT start–end	t_{exp}(s) min–max	SNR min–max					N	UT start–end	t_{exp}(s) min–max	SNR min–max	
				Hβ	Hγ	Hδ	Ca II H Ca II K	H_8 H_9 H_{10}				Hα	Na I D_1 Na I D_2 He I D_3
1	18	00:02–01:47	180–300	76–85	53–58	45–49	33–37	28–31	0	–	–	–	–
2	91	20:19–01:58	60–120	46–73	32–48	26–40	20–29	17–25	0	–	–	–	–
3	246	20:10–02:37	15–120	33–89	21–58	18–51	13–38	12–31	0	–	–	–	–
4	104	20:28–22:44	15–120	27–72	18–48	15–41	11–30	10–25	189	23:38–03:13	5–120	32–172	23–114

3554 Å to 5176 Å (including the Balmer lines from Hβ to H_{11} as well as the Ca II H & K and He I 4026 Å lines). The reciprocal dispersion of these spectra is 0.48 Å/pixel. The wavelength covered by R1200Y (red spectrum) ranges from 5527 Å to 7137 Å (including the Hα, Na I D_1 & D_2 and He I D_3 lines) with a reciprocal dispersion of 0.47 Å/pixel. The spectral resolution, determined as the full width at half maximum (FWHM) of the arc comparison lines, is 1.22 Å for the blue region and 1.13 Å for the red one.

We took series of spectra with short exposure times: from 15 to 300 s for R1200B and from 5 to 120 s for R1200Y. The spectra in each series were separated only by the CCD readout time (less than 60 s) in order to obtain the highest temporal resolution possible. During 4 nights, a total of 459 spectra of AD Leo were obtained with R1200B and 189 with R1200Y. The observing log (Table 3.1) lists the number of spectra taken each night (N), the universal time (UT) at the beginning and end of the AD Leo observations, the minimum and maximum exposure time ($t_{\rm exp}$) of the spectra, and the signal-to-noise ratio (SNR) of the continuum near each line region. These quantities are given for both gratings (R1200B and R1200Y). Note that, despite the short exposure times, the SNR is large enough to perform a reliable analysis.

The reduction was done following the standard procedure: bias and dark subtraction, flat-field correction using exposures of a tungsten lamp, cosmic rays correction, and sky background subtraction from the region of the aperture chosen for doing an optimal extraction of each spectrum. The software packages of IRAF[1] were used. The wavelength calibration was done by using spectra of Cu–Ar lamps. All the spectra were normalized to their maximum flux value of the observed continuum.

3.3 Analysis of the observations

In Fig. 3.1 we have plotted the observed blue spectrum of AD Leo in its quiescent state (minimum observed emission level) and at the maximum of the strongest flare detected with the R1200B grating (flare 2, see § 3.3.1). Figure 3.2 is similar to Fig. 3.1 but for the red spectra, taken with the R1200Y grating, and the strongest flare detected with this spectral configuration (flare 12, see § 3.3.1). In addition, the spectra of Gl 687B and GJ 725B have been plotted as examples of inactive stars with a spectral type and luminosity class (M3.5V) very similar to those of AD Leo (M3V). Note that the origin of the Y-axis is different for each spectrum in order to avoid overlap between them.

AD Leo shows a high level of chromospheric activity. A strong emission in the Balmer series and the Ca II H & K lines is observed even in its quiescent state (see Figs. 3.1 and 3.2). The greatest emission in these lines is found at the maximum of the detected flares. The He I D_3 and He I 4026 Å lines also show emission above the continuum, which is more noticeable during the strongest flares. The Na I D_1 & D_2 absorption lines only present a slight filled-in profile in the quiescent state, although a low emission is observed in their core during flares. High resolution spectroscopic observations of the quiescent state of AD Leo confirm the presence of chromospheric emission lines that range from a

[1] IRAF is distributed by the National Optical Astronomy Observatories, which are operated by the Association of Universities for Research in Astronomy, Inc., under cooperative agreement with the National Science Foundation.

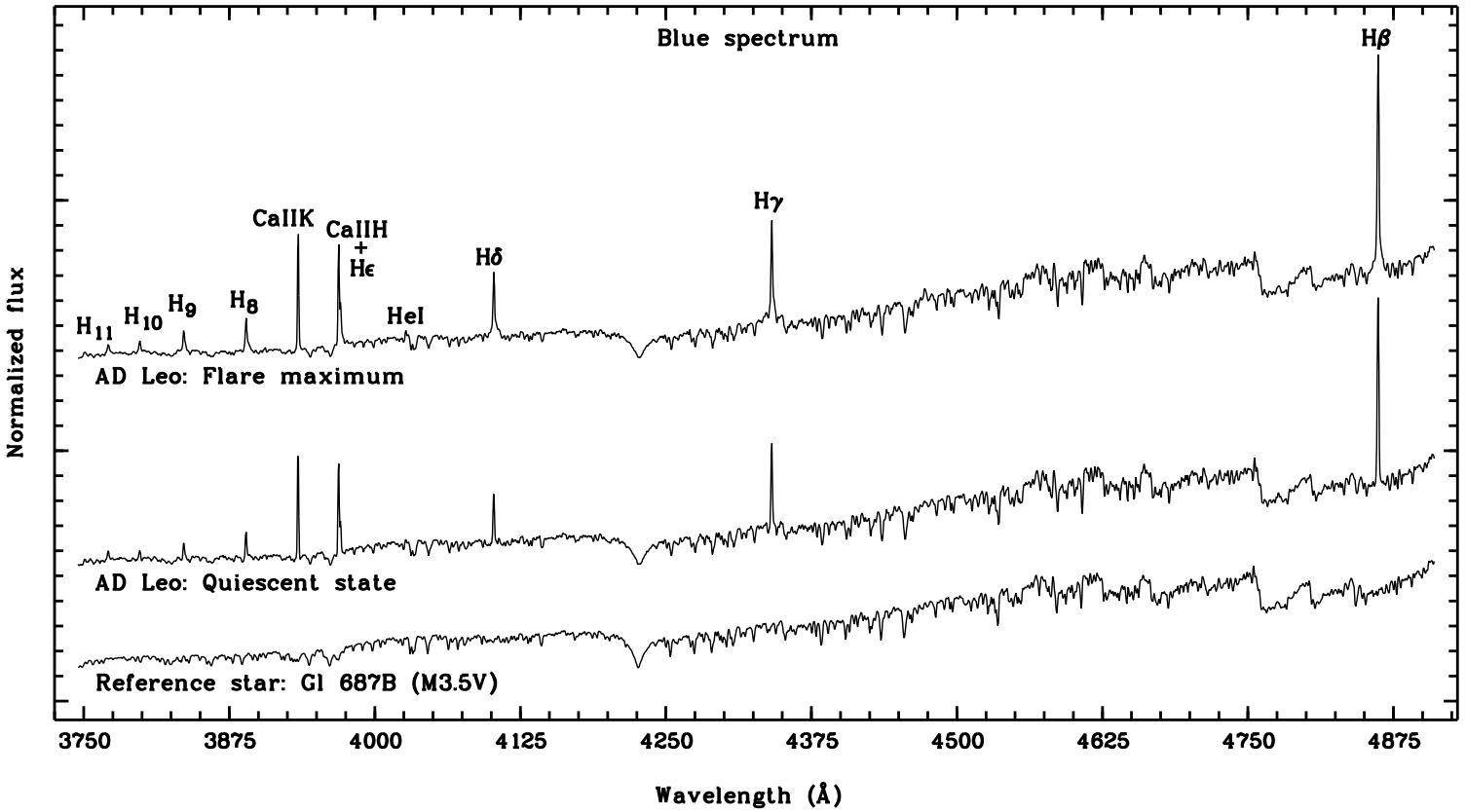

Figure 3.1: Observed spectrum of AD Leo at the maximum of the strongest flare detected with the R1200B grating (flare 2, see § 3.3.1) and in its quiescent state. The observed spectrum of the reference star Gl 687B is shown at the bottom. The chromospheric lines are identified.

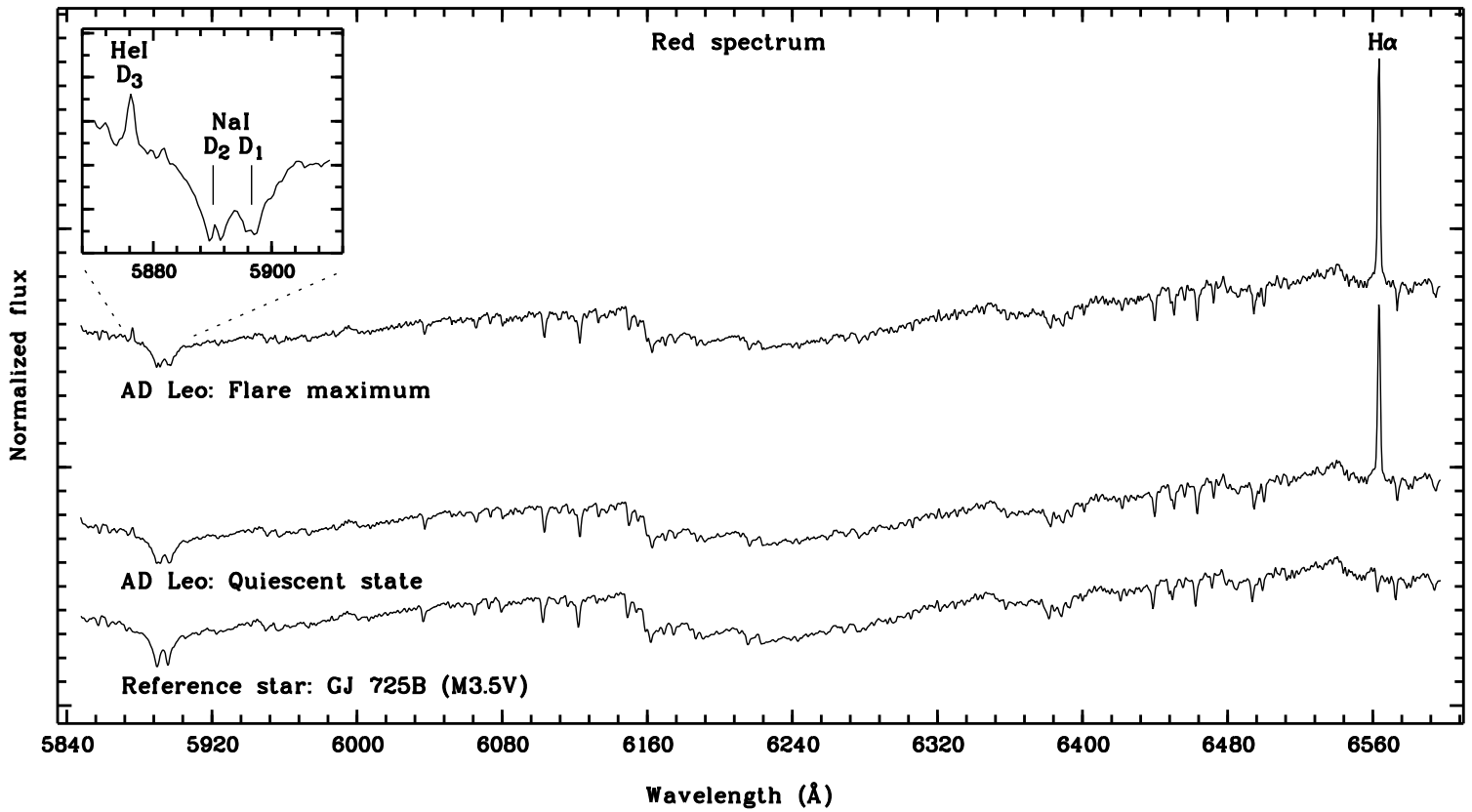

Figure 3.2: As Fig. 3.1 but for the spectra taken with the R1200Y grating, the strongest flare detected using this spectral configuration (flare 12, see § 3.3.1), and the reference star GJ 725B.

weak emission in the center of the Ca II IRT and the Na I D_1 & D_2 lines to a strong emission in the He I D_3, Mg II h & k, Ca II H & K and H I Balmer lines (Pettersen & Coleman 1981; Doyle 1987; Crespo-Chacón et al. 2006). In addition, Sundland et al. (1988) suggested that Balmer lines are the most important components of chromospheric radiation loss.

AD Leo is well-known for having strong flares (see, for example, Hawley & Pettersen 1991). However, after overlapping the normalized spectra and comparing the depth of the absorption lines and the shape of the continuum, we have not detected any noticeable continuum change (see also Figs. 3.1 and 3.2). Therefore the flares analysed in this work are non white-light flares and, within the studied wavelength range, they only affect the emission in the chromospheric lines. Even though this kind of flare is the most typical in the Sun, in which no detectable signature in white-light is generally observed, very few such events had been detected previously in stars (see Butler et al. 1986; Houdebine 2003). Conversely to the Sun, stellar non white-light flares seldom have been observed because very little time has been dedicated to spectroscopy in comparison to photometry. However, Houdebine (1992) suggested that the low frequency observed for stellar non white-light flares could be due to a strong contrast effect. In other words, many flares have been detected as white-light flares on dMe stars because of the relative weakness of their photospheric background, but they would have been classified as non white-light flares on the Sun because of its much higher photospheric background.

3.3.1 Equivalent widths

The equivalent width (EW) of the observed chromospheric lines has been measured very carefully in order to detect possible weak flares in our observations. Two methods have been used. The first one consists of obtaining the EW with the routine SPLOT included in IRAF, taking the same wavelength limits for each line in all the spectra. The second method uses the routine SBANDS of IRAF, which generally introduces less noise in the EW measurement because it takes into account a larger number of points to calculate the continuum value. For this reason, we only present the results obtained with SBANDS. Note that the line regions have been taken wide enough to include the enhancement of the line wings during flares.

SBANDS uses Eq. 3.1 to obtain the EW of a line: W_l is the width at the base of the line, d is the reciprocal dispersion (pixel size in Å), $F_{\mathrm{c,i}}$ is the flux per pixel in the continuum under the line, $F_{\mathrm{l,i}}$ is the observed flux in the pixel i of the line, and n is the number of pixels within the line region.

$$EW = W_\mathrm{l} - \frac{d}{F_{\mathrm{c,i}}} \sum_{\mathrm{i}=1}^{\mathrm{i}=n} F_{\mathrm{l,i}} \tag{3.1}$$

The EW uncertainty has been estimated using Eq. 3.2. We have considered $\triangle W_\mathrm{l} = 0$ Å and $\triangle d = 0.01$ Å/pixel. Equation 3.2 has been obtained by applying the standard quadratic error propagation theory to Eq. 3.1, taking into account that $n = W_\mathrm{l}/d$ and assuming $\triangle F_{\mathrm{l,i}} \approx \triangle F_{\mathrm{c,i}} = F_{\mathrm{c,i}}/\mathrm{SNR}$.

$$\triangle EW = \sqrt{(C_1)^2 + (C_2)^2 + (C_3)^2 + (C_4)^2} \tag{3.2}$$

Table 3.2: Minimum and maximum relative error in the EW of the different chromospheric lines.

Night	$\triangle EW_{\rm rel}$ (%) (min–max)													
	Hβ	Hγ	Hδ	He I λ4026Å	Ca II K	Ca II H+Hϵ	H_8	H_9	H_{10}	H_{11}	Hα	Na I D_1	Na I D_2	He I D_3
1	10–13	6–9	8–14	20–46	5–8	5–8	9–20	9–17	11–24	16–37	–	–	–	–
2	9–15	6–10	7–17	19–57	5–9	5–10	9–23	9–22	12–34	17–62	–	–	–	–
3	10–17	6–12	8–20	24–109	5–13	5–13	10–28	9–29	12–41	17–61	–	–	–	–
4	10–20	6–15	8–23	27–152	5–14	6–15	10–34	10–39	12–56	18–145	9–20	2–5	1–5	32–328

where

$$C_1 = \frac{\partial EW}{\partial W_\mathrm{l}} \triangle W_\mathrm{l} = \triangle W_\mathrm{l}$$

$$C_2 = \frac{\partial EW}{\partial d} \triangle d = \frac{EW - W_\mathrm{l}}{d} \triangle d$$

$$C_3 = \frac{\partial EW}{\partial F_\mathrm{c,i}} \triangle F_\mathrm{c,i} = \frac{W_\mathrm{l} - EW}{\mathrm{SNR}}$$

$$C_4 = \frac{\partial EW}{\partial F_\mathrm{l,i}} \triangle F_\mathrm{l,i} = \frac{\sqrt{W_\mathrm{l}\, d}}{\mathrm{SNR}}$$

Table 3.2 shows the minimum and maximum values of the relative error in EW ($\triangle EW_\mathrm{rel}$) for each chromospheric line and each night. The $\triangle EW_\mathrm{rel}$ of the Ca II H & K, Na I D_1 & D_2, Hβ, Hγ and Hδ lines is between 1 % and 20 %. For H_8 and H_9 the $\triangle EW_\mathrm{rel}$ is less than 40 %, while for H_{10} and H_{11} is higher than the uncertainty estimated for the other Balmer lines (up to 50 % in the case of H_{10} and even larger than 100 % in the case of H_{11}). The $\triangle EW_\mathrm{rel}$ of He I D_3 and He I 4026 Å is frequently greater than 100 %. For this reason, the results obtained for the He I lines are less reliable. In addition, because of the short exposure times and the relative faintness of AD Leo in the blue, the region blueward of H_{10} is usually too noisy for reliable measurements.

The observed flares have been detected using the Hβ and Hα lines (for the blue and red spectra, respectively). Hβ and Hα were chosen because they suffer from large variations during flares and are the chromospheric lines with the best SNR in each spectral configuration.

Figure 3.3 shows the temporal evolution found for the EW of the Hβ line. The observed flares are marked with numbers. Other smaller changes can also be seen. The temporal evolution found for the EW of the Hα line is given in Fig. 3.4. No strong variations have been observed during our spectroscopic monitoring. However, 14 short and weak flares have been detected: 11 among the blue spectra and 3 among the red ones. The Julian Date (JD) at the beginning of each flare (JD_start) is shown in Table 3.3. These flares also have been observed in the other chromospheric lines. Nevertheless, it is more difficult to distinguish between flares and noise for lower SNR and/or weaker lines. In addition, a modulation with a period of ~ 2 days is also observed in the quiescent emission of AD Leo, although the photometric period of this star was found to be 2.7 days (Spiesman & Hawley 1986).

The flare frequency is very high, and sometimes new flares take place when others are still active (see, for example, flares 8 and 11 and the points before flares 2 and 7 in Fig. 3.3). Note also that the flares on night 4 seem to erupt over the gradual decay phase of another stronger flare (Fig. 3.4). To calculate the flare frequency we have taken the total observed time as the sum of $\mathrm{UT_{end}} - \mathrm{UT_{start}}$ for all the nights (see Table 3.1). Note that, within a night, the series of observations are not continuous in time. Therefore the flare frequency should be greater than the obtained one. This implies that the flare activity of AD Leo, found from the variations of the chromospheric

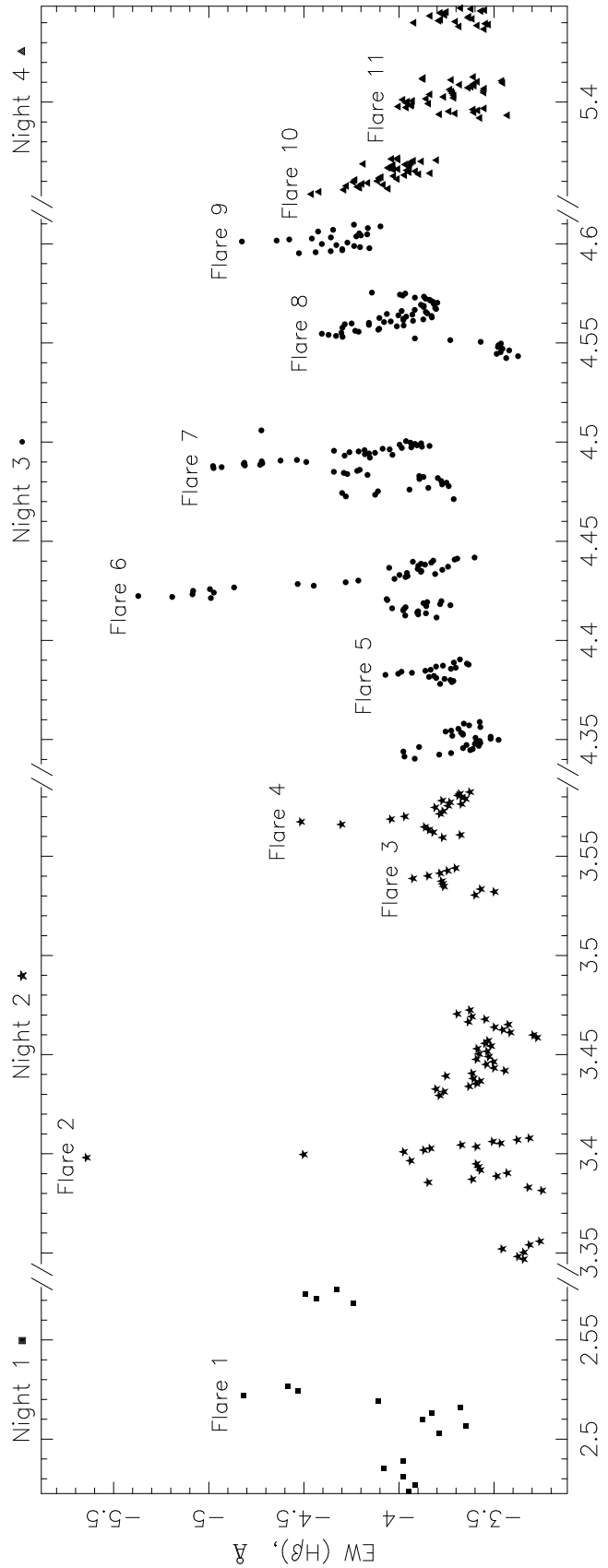

Figure 3.3: Temporal evolution of the EW of the Hβ line. The strongest observed flares are labeled.

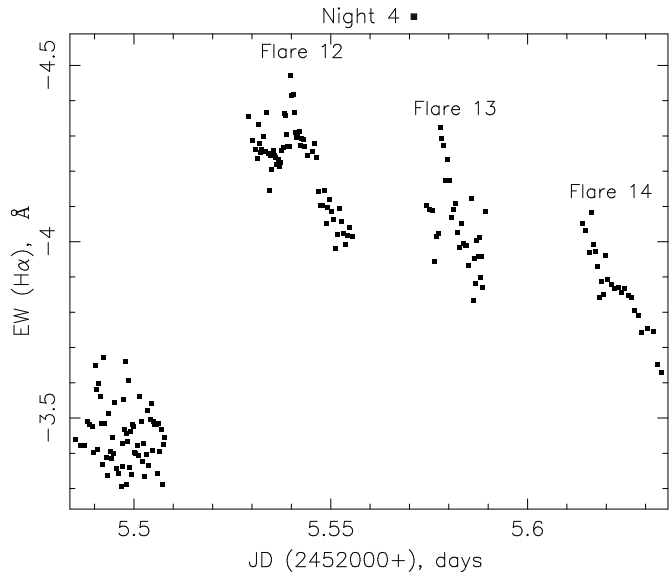

Figure 3.4: As Fig. 3.3 but for the Hα line. The observed flares have been numbered following the order in Fig. 3.3.

Table 3.3: *JD* of the flare onset ($JD_{\rm start}$), total duration of the detected flares and length of their phases (seen in the Hβ line in the case of flares 1 to 11 and seen in the Hα line in the case of flares 12 to 14). The time delay between the maximum of the chromospheric lines and the one of Hβ or Hα, depending on the spectral configuration, is also shown. Blanks are given when the beginning, maximum and/or end of the flare was not observed in the line under consideration.

Flare	$JD_{\rm start}$ (days) (2452000+)	Duration (min)			Delay of the maximum (min)	
		Total (Hβ)	Impulsive phase (Hβ)	Gradual decay (Hβ)	Ca II K	He I 4026 Å
1	2.513±0.003	–	13±7	–	–	0±6
2	3.3903±0.0016	25±4	11±5	14±4	0±5	0±5
3	3.5321±0.0016	–	10±4	–	0±4	0±4
4	3.5608±0.0013	31±3	10±4	22±3	0±4	0±4
5	4.3781±0.0010	18±4	6±2	11±3	0±1	–
6	4.4193±0.0005	22±1	4±2	17±2	5±3	0±3
7	4.4804±0.0010	25±2	9±3	16±2	3±2	1±2
8	4.5479±0.0009	–	10±2	–	1±1	1±1
9	4.5978±0.0005	17±2	5±1	12±2	2±1	–
10	–	–	–	–	–	–
11	5.3968±0.0005	14±1	1±1	12±1	3±1	–
Flare	$JD_{\rm start}$ (days) (2452000+)	Duration (min)			Delay of the maximum (min)	
		Total (Hα)	Impulsive phase (Hα)	Gradual decay (Hα)	Na I D_1, D_2	He I D_3
12	5.5341±0.0003	31±2	5.9±0.9	25±2	0.9±0.9	–
13	5.5763±0.0005	14±1	2±1	12±1	1±1	1±1
14	–	–	–	–	–	–

emission lines, is > 0.71 flares/hour. This value is slightly higher than those that other authors measured by using photometry: Moffett (1974) observed 0.42 flares/hour, Pettersen et al. (1984) detected 0.57 flares/hour, and Konstantinova-Antova & Antov (1995) found 0.33 - 0.70 flares/hour. Given that the detected flares are non white-light flares, we conclude that non white-light flares may be more frequent on stars than white-light flares as observed on the Sun. As the total time of the gaps between the series of observations is similar to the total real observed time, the flare activity of AD Leo could even double that obtained. As far as we know, this is the first time that such a high flare frequency is inferred from the variation of the chromospheric emission lines.

3.3.2 Equivalent widths relative to the quiescent state

In order to compare the behaviour of the different chromospheric lines, we have used the equivalent width relative to the quiescent state (*EWRQ*), defined as the ratio of the *EW* to the *EW* in the quiescent state. Figures 3.5 and 3.6 show the *EWRQ* of several lines for a representative sample of the detected flares (those in which all the phases have been observed). The chromospheric lines plotted in these two figures are those with less uncertainty in the *EW* measurement. We can observe two different kinds of flares: for some of them (see flares 6, 9, 11, 12 and 13) the gradual decay phase of the Balmer lines is much longer than the impulsive phase; in contrast, other flares (2, 4, 5 and 7) are less impulsive. This resembles the classification of solar flares made by Pallavicini et al. (1977): *eruptive flares* or *long-decay events* and *confined* or *compact flares*. However, all these flares always show the same behaviour in the Ca II H & K lines, that is, a slow evolution throughout all the event. The evolution of the Na I D_1 & D_2, He I D_3 and He I 4026 Å lines is quite similar to that of the Balmer series. However, it is less clear for the He I lines because sometimes they have a very high error.

In some flares (5, 6, 11, 12 and 13) we can see two maxima in the Na I and Balmer lines, but it is not so evident for the He I and Ca II lines. Sometimes variations on shorter time scales are also detected during the gradual decay phase, in which different peaks, decreasing in intensity, are observed in the *EWRQ* (see, for instance, flare 12). This could be interpreted as the succession of different reconnection processes, decreasing in efficiency, within the same flare – following the original suggestion of Kopp & Pneuman (1976) – or as a series of flares occurring as a result of wave disturbances along the stellar surface from the first flare region.

Table 3.3 contains the total duration of the detected flares, the length of their impulsive and gradual decay phases, and the time delay between the maximum of each chromospheric line and that of Hβ or Hα (depending on the spectral configuration). The detected flares last from 14 ± 1 to 31 ± 3 min. Regarding the first maximum of emission, we have found that the Balmer series reach it simultaneously while the rest of the lines are delayed. The delay is negligible for the He I and Na I lines ($\sim$ 1 min) but it is very evident for Ca II H & K (up to 5 ± 3 min). It seems that this delay is greater for the flares with a shorter impulsive phase of the Balmer lines. However, the total duration of the flare does not seem to be related. For the first five flares, we cannot assume that the delay of the maximum is completely zero because their uncertainties, particularly those of He I 4026 Å, are even greater than the delay found in the other cases. The moment at

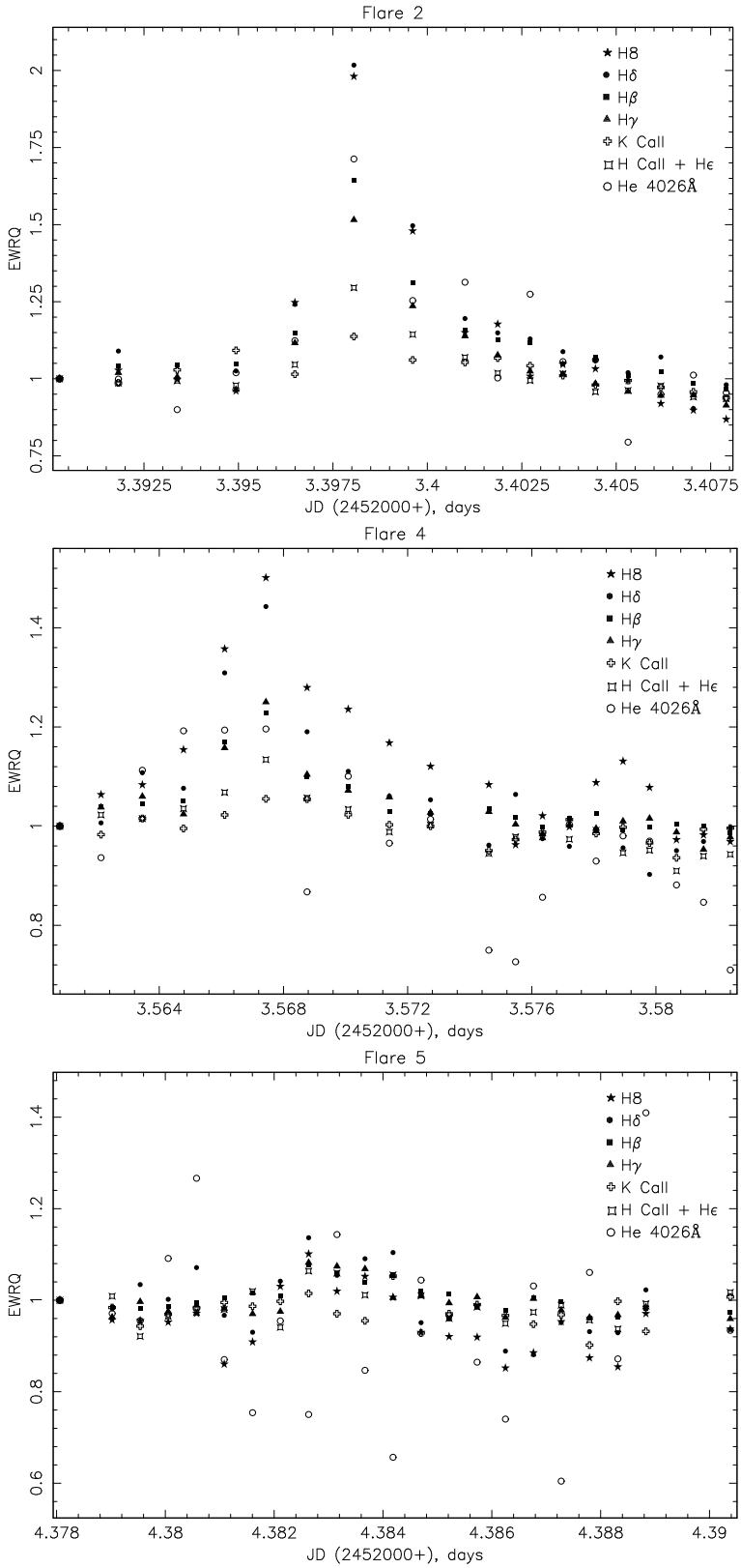

Figure 3.5: *EWRQ* of the flares (detected using the R1200B grating) in which all the phases have been observed (lines: Hβ, Hγ, Hδ, H_8, Ca II H + Hϵ, Ca II K, He I 4026 Å).

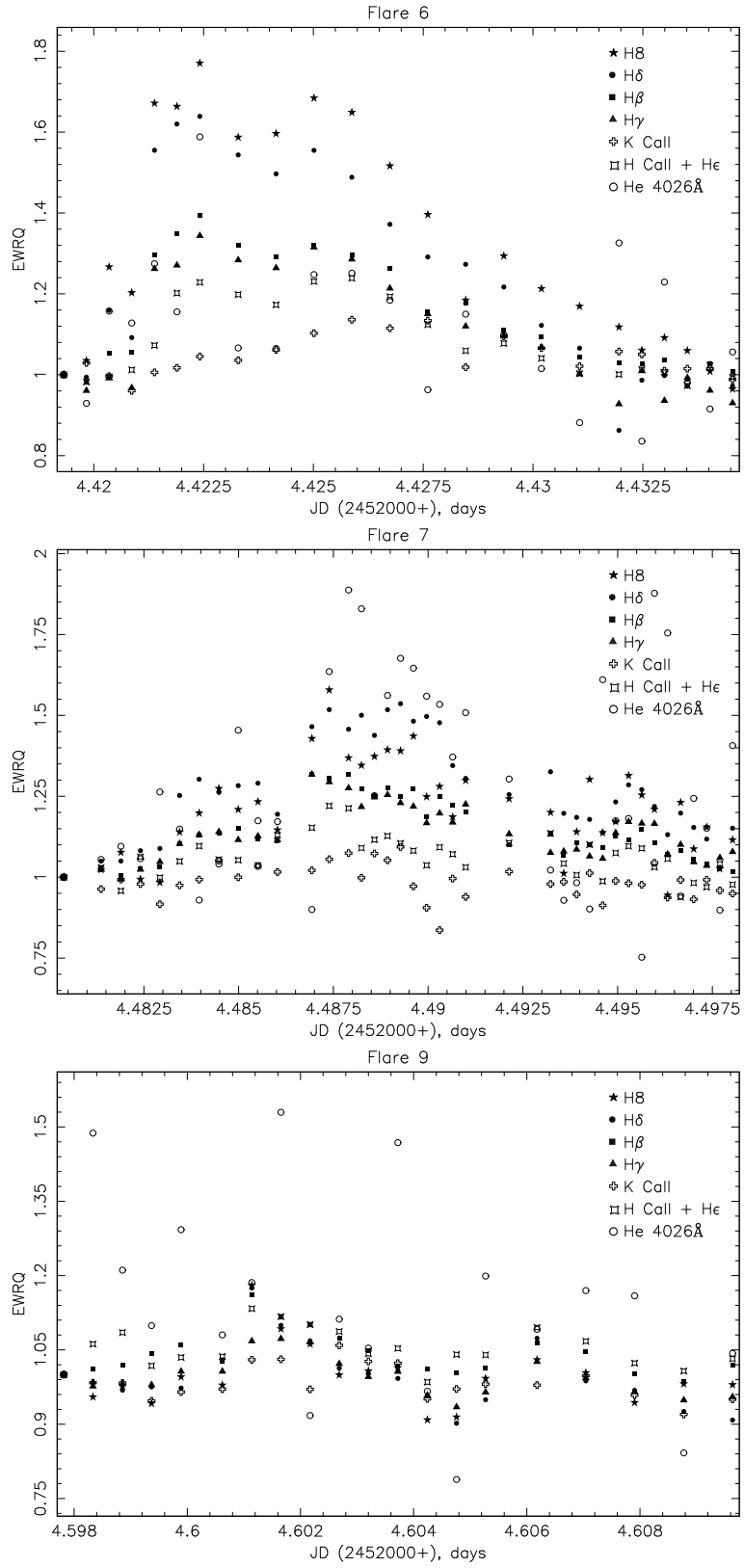

Figure 3.5: Continuation.

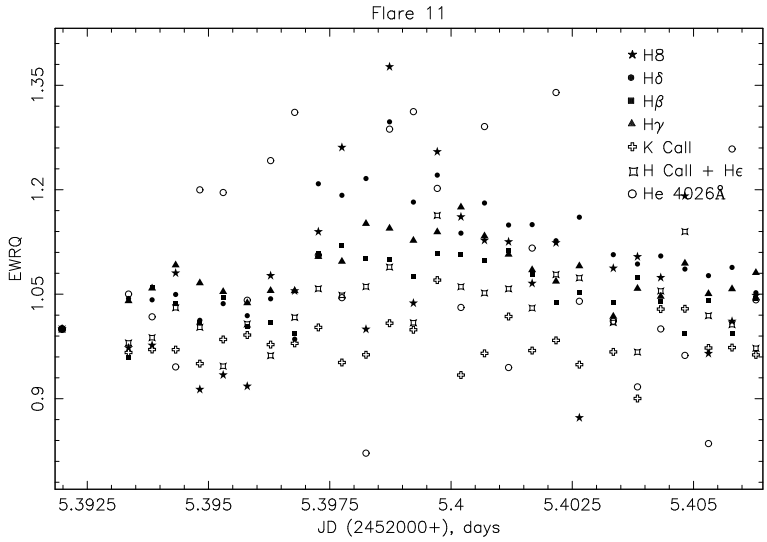

Figure 3.5: Continuation.

which a line reaches its maximum is related to the height where the line is formed above the stellar surface. This is also related to the temperature that characterizes the formation of the line. According to the line formation models in stellar atmospheres, the Ca II H & K lines are formed at deeper and cooler layers than the Balmer series. Therefore, the gas that is heated and evaporated into the newly formed loop after magnetic reconnection (Cargill & Priest 1983; Forbes & Malherbe 1986) cools and reaches the formation temperature of the Balmer series before the one of the Ca II H & K lines. Houdebine (2003) found that the rise and decay times in the Ca II K and Hγ lines obey good relationships, which implies that there is a well-defined underlying mechanism responsible for the flux time profiles in these lines.

Table 3.4 lists the $EWRQ$ of the chromospheric lines at their maximum in each flare ($EWRQ_{\max}$). The lower the wavelength, the greater $EWRQ_{\max}$ is found for the Balmer lines. However, Hβ and Hγ have a very similar variation. For He I 4026 Å and He I D_3 the $EWRQ_{\max}$ is analogous to that of the Balmer series, whereas for the Ca II H & K and Na I D_1 & D_2 lines is smaller. Our results show that the duration of flares tends to be larger when the $EWRQ_{\max}$ of the Balmer lines is greater. This effect is more noticeable for the less impulsive flares. Nevertheless, there are no clear relationships between the $EWRQ_{\max}$ of the other lines and the duration of the flare.

3.3.3 Line fluxes and released energy

In order to estimate the flare energy released in the observed chromospheric lines, we have converted the EW into absolute surface fluxes and luminosities.

The absolute line fluxes (F) have been computed from the EW measured for each line and its local continuum. The absolute flux of the continuum near each line has been determined making use of the method given by Pettersen & Hawley (1989). For AD Leo, they interpolate between the R and I filter photometric fluxes to estimate the observed flux in

Table 3.4: $EWRQ$ at flare maximum ($EWRQ_{\max}$) for the different chromospheric lines. Blanks are given when the flare maximum was not detected in the line under consideration. Flares with no maximum data in any line have been omitted.

Flare	$EWRQ_{\max}$									
	Hβ	Hγ	Hδ	H_8	H_9	H_{10}	H_{11}	Ca II H + Hϵ	Ca II K	He I 4026 Å
1	1.26±0.18	1.28±0.11	1.47±0.17	1.53±0.22	1.52±0.20	1.7±0.3	1.6±0.4	1.16±0.09	–	1.5±0.5
2	1.65±0.25	1.52±0.14	2.0±0.3	2.0±0.3	1.8±0.3	1.5±0.3	2.0±0.7	1.30±0.11	1.14±0.09	1.7±0.6
3	1.09±0.19	1.06±0.10	1.10±0.17	1.11±0.21	1.13±0.22	0.99±0.23	1.0±0.4	1.1±0.1	1.01±0.09	1.3±0.5
4	1.23±0.20	1.25±0.12	1.44±0.21	1.5±0.3	1.5±0.3	1.6±0.3	1.6±0.6	1.13±0.10	1.06±0.09	1.2±0.5
5	1.08±0.20	1.08±0.13	1.14±0.21	1.1±0.3	1.1±0.3	1.0±0.3	1.5±0.6	1.06± 0.13	1.01±0.12	–
6	1.4±0.3	1.34±0.17	1.6±0.3	1.8±0.5	1.4±0.4	1.5±0.5	1.3±0.5	1.23±0.16	1.14±0.13	1.6±0.9
7	1.32±0.24	1.32±0.17	1.5±0.3	1.4±0.4	1.7±0.4	1.5±0.5	1.9±0.8	1.15±0.15	1.09±0.14	1.9±1.1
8	1.27±0.23	1.25±0.14	1.49±0.25	1.5±0.3	1.5±0.3	1.4±0.4	1.5±0.6	1.16±0.13	1.06±0.11	1.6±0.8
9	1.16±0.21	1.07±0.13	1.18±0.21	1.2±0.3	1.3±0.3	1.1±0.3	1.0±0.4	1.13±0.14	1.06±0.14	–
11	1.12±0.22	1.10±0.15	1.19±0.24	1.3±0.3	1.1±0.3	1.2±0.4	1.0±0.5	1.05±0.13	1.07±0.13	–

Flare	$EWRQ_{\max}$			
	Hα	Na I D_1	Na I D_2	He I D_3
12	1.09±0.15	0.95±0.04	0.95±0.03	–
13	1.13±0.18	0.98±0.04	0.98±0.04	1.5±1.1

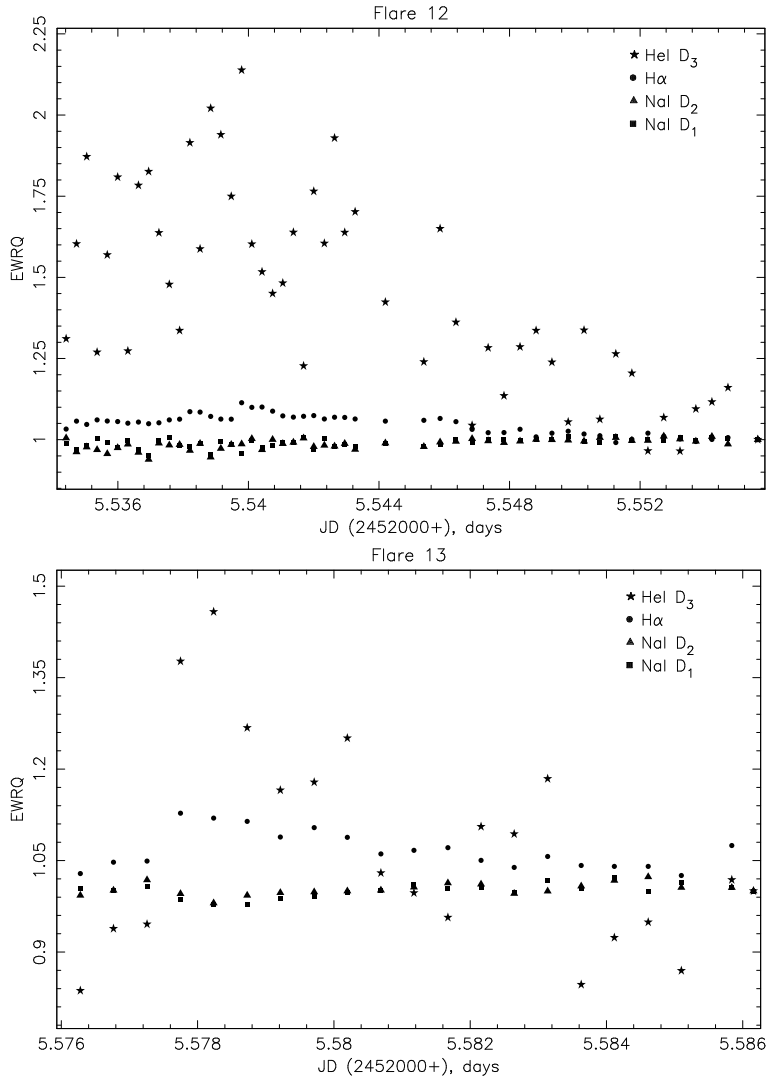

Figure 3.6: As Fig. 3.5 but for the flares detected using the R1200Y grating (lines: Hα, Na I D_1, Na I D_2, He I D_3).

the continuum near 8850 Å. This value is then transformed into a continuum surface flux of $F(8850\ \text{Å}) = 6.5 \times 10^5$ erg s^{-1}cm^{-2}Å^{-1}, using 0.44 $R_\odot$ for the radius and 0.203 arcsec for the parallax. Direct scaling from the flux-calibrated spectrum of AD Leo, shown by Pettersen & Hawley (1989), has allowed us to estimate the continuum surface fluxes near the emission lines of interest. We multiply this continuum value by the measured EW to determine the line surface flux. The absolute fluxes of the Balmer lines at the different flare maxima ($F_{\max}$) are listed in Table 3.5. These values will be used in § 3.4 to calculate the Balmer decrements. Note that each $F_{\max}$ only shows the contribution of the flare to the surface flux (the contribution of the quiescent state has been subtracted). Since our aim is to isolate the contribution of the flares from the total emission, we have chosen the quiescent state for each of them as a pseudo-quiescent, that is the minimum emission level just before or after the flare. In this way, variations generated by other processes,

Table 3.5: Surface fluxes of the Balmer lines at flare maximum ($F_{\max}$). The contribution of the quiescent state has been subtracted. Flares with no maximum data in any line have been omitted.

Flare	$F_{\max}$ (10^5 erg s^{-1}cm^{-2})							
	Hα	Hβ	Hγ	Hδ	H_8	H_9	H_{10}	H_{11}
1	–	0.90	0.64	0.56	0.29	0.23	0.109	0.070
2	–	1.82	1.10	0.90	0.47	0.33	0.108	0.105
3	–	0.34	0.19	0.15	0.08	0.053	0.011	0.013
4	–	0.70	0.52	0.41	0.22	0.17	0.120	0.079
5	–	0.34	0.23	0.19	0.10	0.04	0.079	0.061
6	–	1.19	0.70	0.62	0.32	0.16	0.084	0.040
7	–	0.94	0.62	0.43	0.19	0.25	0.076	0.090
8	–	0.74	0.48	0.42	0.16	0.14	0.072	0.053
9	–	0.57	0.27	0.30	0.11	0.11	0.070	0.036
11	–	0.35	0.07	0.18	0.08	0.03	0.050	0.010
12	1.10	–	–	–	–	–	–	–
13	1.40	–	–	–	–	–	–	–

which can contribute to the observed emission, are not taken into account. Even if these processes were magnetic reconnections within the same active region, assuming that the solar flare model is also applicable to the stellar case, the new emitting plasma would be placed in a different post-flare loop (Cargill & Priest 1983; Forbes & Malherbe 1986). Therefore, to a first approximation, its physical properties (see § 3.4) could be studied separately.

We have also converted the absolute fluxes into luminosities (L). Table 3.6 lists the contribution of each flare to the energy released in the Balmer lines. The released energy has been calculated by numerically integrating the luminosity from the beginning to the end of the flare and subtracting the contribution of its corresponding pseudo-quiescent state. The energy released during the impulsive and gradual decay phases, which has been calculated in the same way, is given as well.

3.3.4 Line profiles and asymmetries

This section is focused on the Balmer series and Ca II H & K lines. The intermediate spectral resolution of the observations has not allowed us to study the profile of the He I and Na I lines because of their low intensity.

We have plotted the temporal evolution of the observed line profiles during the detected flares (see the examples given in Fig. 3.7). No evidence for line-shifts has been found. However, the reported flares may be too weak to measure line-shifts using the available spectral resolution (see § 3.2). It seems that flares affect the core of the lines before the wings. The emission in both of them (core and wings) increases during the impulsive phase, shows the largest value when the $EWRQ$ of the line reaches the maximum,

Table 3.6: Energy released in the Balmer lines during each flare phase. The total released energy is also shown. The contribution of the quiescent state has been subtracted. We have omitted the flares with no data about their beginning, maximum and end.

Flare	Phase	Released energy (10^{29} erg)							
		Hα	Hβ	Hγ	Hδ	H_8	H_9	H_{10}	H_{11}
1	Impulsive	–	2.5	1.2	1.6	0.8	0.7	0.3	0.2
	Gradual	–	–	–	–	–	–	–	–
	Total	–	–	–	–	–	–	–	–
2	Impulsive	–	3.3	2.3	1.4	0.9	0.9	0.2	0.3
	Gradual	–	4.9	3.1	2.0	1.2	1.2	0.4	0.5
	Total	–	8.2	5.4	3.4	2.2	2.1	0.6	0.7
3	Impulsive	–	1.2	0.7	0.7	0.3	0.2	0.1	0.0
	Gradual	–	–	–	–	–	–	–	–
	Total	–	–	–	–	–	–	–	–
4	Impulsive	–	1.9	1.3	0.9	0.6	0.5	0.4	0.3
	Gradual	–	2.2	1.6	0.6	0.9	0.5	0.5	0.5
	Total	–	4.1	3.0	1.5	1.5	1.1	0.9	0.8
5	Impulsive	–	0.6	0.2	0.3	0.2	0.1	0.3	0.2
	Gradual	–	1.0	0.6	0.4	0.2	0.1	0.4	0.2
	Total	–	1.5	0.8	0.7	0.4	0.2	0.7	0.4
6	Impulsive	–	1.5	0.7	0.9	0.5	0.2	0.1	0.0
	Gradual	–	6.2	3.3	3.1	1.8	1.0	0.3	0.1
	Total	–	7.7	3.9	4.0	2.3	1.2	0.4	0.1
7	Impulsive	–	1.8	1.2	1.1	0.4	0.5	0.2	0.2
	Gradual	–	5.4	3.4	3.2	1.3	0.8	0.6	0.6
	Total	–	7.2	4.6	4.4	1.7	1.2	0.8	0.9
8	Impulsive	–	2.0	1.3	1.0	0.4	0.4	0.2	0.1
	Gradual	–	–	–	–	–	–	–	–
	Total	–	–	–	–	–	–	–	–
9	Impulsive	–	0.6	0.4	0.3	0.0	0.0	0.1	0.0
	Gradual	–	1.5	0.9	0.7	0.1	0.1	0.3	0.2
	Total	–	2.1	1.3	1.0	0.1	0.1	0.5	0.2
11	Impulsive	–	0.2	0.1	0.1	0.0	0.0	0.0	0.0
	Gradual	–	1.8	0.6	1.2	0.2	0.2	0.4	0.1
	Total	–	2.0	0.7	1.3	0.2	0.2	0.5	0.1
12	Impulsive	3.1	–	–	–	–	–	–	–
	Gradual	10.3	–	–	–	–	–	–	–
	Total	13.4	–	–	–	–	–	–	–
13	Impulsive	1.0	–	–	–	–	–	–	–
	Gradual	6.5	–	–	–	–	–	–	–
	Total	7.5	–	–	–	–	–	–	–

and decreases during the gradual decay. The emission in the wings of the Ca II H & K lines hardly rises during the observed flares, being only noticeable during the strongest ones (see Fig. 3.7). In fact, their broadening is negligible even at flare maximum. If the flare is too weak, as is the flare 5, the profile of the Balmer lines shows the same behaviour as that found for the Ca II H & K lines. In contrast, when the released energy is high enough to produce changes in the wings of the Balmer series (flares 2, 6 and 7), the core of these lines seems to rise to a constant value (which is independent of the $EWRQ_{\max}$) whereas the emission in the wings depends on the flare energy. Table 3.7 lists the width at the base of the lines of interest during the quiescent state and the maximum of the strongest observed flare (flare 2). The fact that the width of the Ca II lines is much less sensitive to flares than that of the Balmer lines suggests that the broadening may be due to the Stark effect (Byrne 1989; Robinson 1989). Nevertheless, mass motions can also be present (see below).

Figure 3.8 shows, as an example, the bisector of the Hβ and Ca II K lines during flare 2. The bisector of a line is defined as the middle points of the line profile taking points of equal intensity on both sides of the line (Toner & Gray 1988; López-Santiago et al. 2003).

The Balmer lines are broadened during the early-flare phases and the broadening decreases with flare evolution (see Fig. 3.7). Although the emission rises in both wings of the Balmer lines, the observed enhancement and broadening are larger in the red wing. Therefore the Balmer lines show a red asymmetry during the detected flares, and the largest asymmetry is observed at flare maximum (see also the behaviour of the bisectors given in Fig. 3.8). The stronger the flare (flares 2 and 6) the greater this asymmetry is. The red asymmetry is also stronger in higher members of the Balmer series. We have used a two-Gaussian (narrow=N and broad=B) fit to model the Balmer lines at flare maxima. The B component appears red-shifted with respect to N. For example, at the maximum of flare 2 the distance between both components increases from 0.4 Å in the case of Hβ to 1.5 Å in H_8. Doyle et al. (1988) observed a similar effect during a flare on YZ CMi, finding that Hγ and Hδ showed symmetrically broadened profiles while H_8 and H_9 showed predominantly red-shifted material. They suggested that within an exposure time such as those used in this work (see Table 3.1) several downflows, corresponding to different flare kernels that brighten successively one after another, may be present in the stellar atmosphere. Each downflow would produce a red-shifted contribution to the Balmer lines, which would be larger for higher members of the Balmer series (see § 3.3.2). In addition, a smaller red asymmetry in the Balmer lines is also observed during the quiescent state of AD Leo.

The Ca II H & K lines are not usually broadened and do not show any asymmetry, except the case of the strongest flare, where slight variations are observed (see Figs. 3.7 and 3.8).

There are several interpretations for the asymmetries. Broad Balmer emission wings have been observed during flares produced by very different kinds of stars, showing blue or red asymmetries (Doyle et al. 1988; Phillips et al. 1988; Eason et al. 1992; Houdebine et al. 1993; Gunn et al. 1994a; Abdul-Aziz et al. 1995; Abranin et al. 1998; Berdyugina et al. 1998; Montes et al. 1999; Montes & Ramsey 1999; López-Santiago et al. 2003) or no obvious line asymmetries (Hawley & Pettersen 1991). Broadened profiles and red asymmetries are important constraints on flare models (Pallavicini 1990). They can be

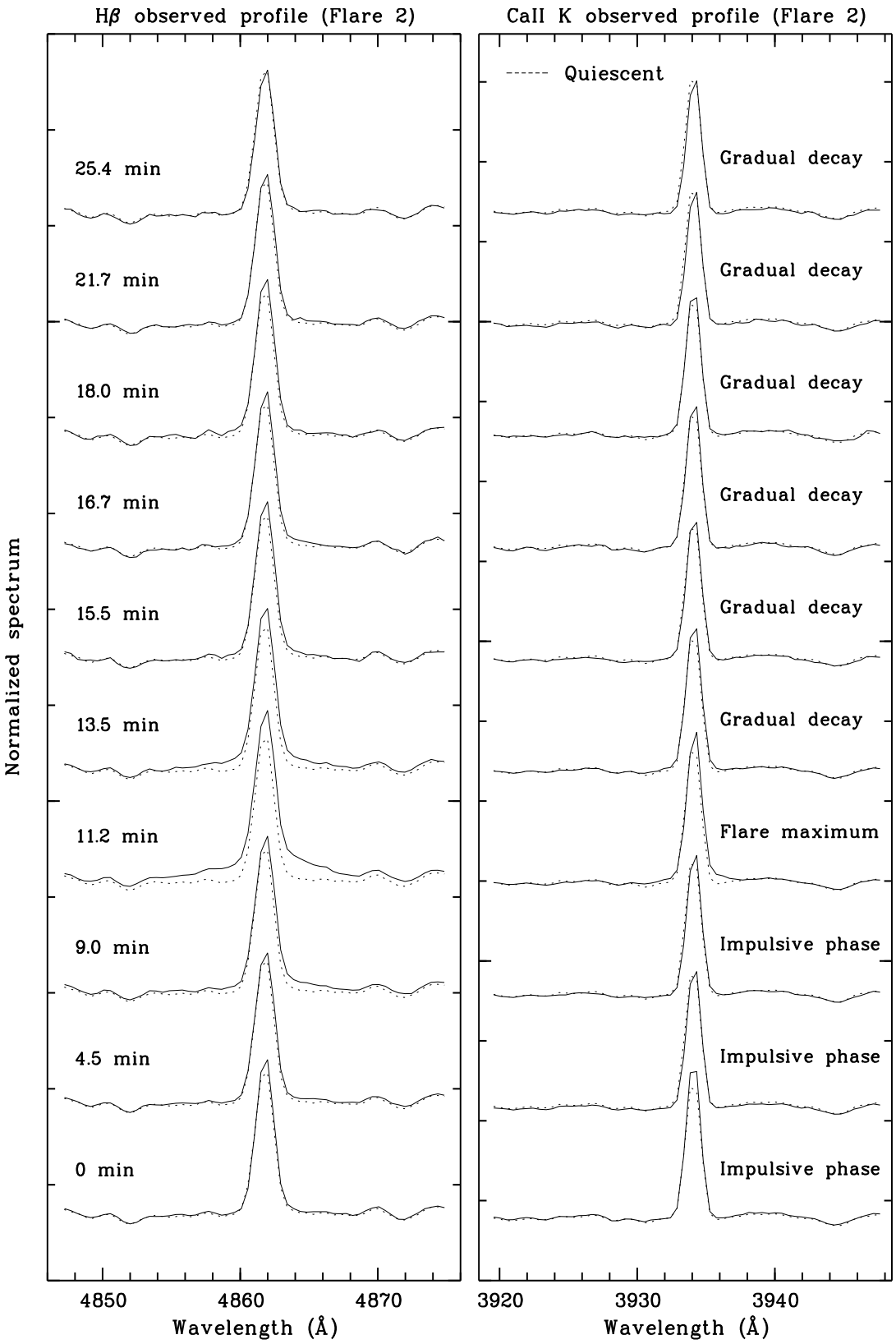

Figure 3.7: Evolution of the H_β (left) and Ca II K (right) line profiles (solid line) during the strongest observed flare (flare 2), compared with the quiescent state (dotted line).

Table 3.7: Width at the base of the chromospheric lines in the quiescent state and at the maximum of flare 2.

Line	Width at the base of the line	
	Quiescent state	Maximum of flare 2
Hβ	5±1	13±1
Hγ	4±1	6±1
Hδ	4±1	9±1
He I 4026 Å	1±1	1±1
Ca II H + Hϵ	4±1	6±1
Ca II K	3±1	5±1
H_8	3±1	6±1
H_9	3±1	5±1
H_{10}	3±1	3±1
H_{11}	3±1	5±1

attributed to plasma turbulence or mass motions in the flare region (see Montes et al. 1999; Fuhrmeister et al. 2005, and references therein). In solar flares, most frequently, a red asymmetry is observed in chromospheric lines. Taking into account that the flares reported in this work are like the most typical solar flares – non white-light flares – it was expected to find red asymmetries like those observed. However, evidence of blue asymmetries has been reported during solar flares (Heinzel et al. 1994). Red asymmetries often have been interpreted as the result of chromospheric downward condensations (CDC) (see Canfield et al. 1990, and references therein). Recent line profile calculations (Gan et al. 1993; Heinzel et al. 1994; Ding & Fang 1997) show that a CDC can explain both blue and red asymmetries. On the other hand, evidence of mass motions has been reported during stellar flares. In particular, a large enhancement in the far blue wings of Balmer lines during the impulsive phase of a stellar flare was interpreted as high velocity mass ejection (Houdebine et al. 1990) or high velocity chromospheric evaporation (Gunn et al. 1994b), whereas red asymmetries in Balmer lines were reported by Houdebine et al. (1993) as evidence of CDC.

The small red asymmetry observed in the Balmer series during the quiescent state therefore can be interpreted as multiple CDC in the stellar atmosphere. These CDC may be produced by unresolved continuous low energy flaring.

3.4 Balmer decrement line modeling

Balmer decrements (flux ratio of higher members to Hγ) frequently have been used to derive plasma densities and temperatures in the chromosphere of flare stars (Kunkel 1970; Gershberg 1974; Katsova 1990). Jevremović et al. (1998) developed a procedure (BDFP hereafter) to fit the Balmer decrements in order to determine some physical parameters in the flaring plasma. García-Alvarez et al. (2002) used the BDFP to obtain a detailed trace

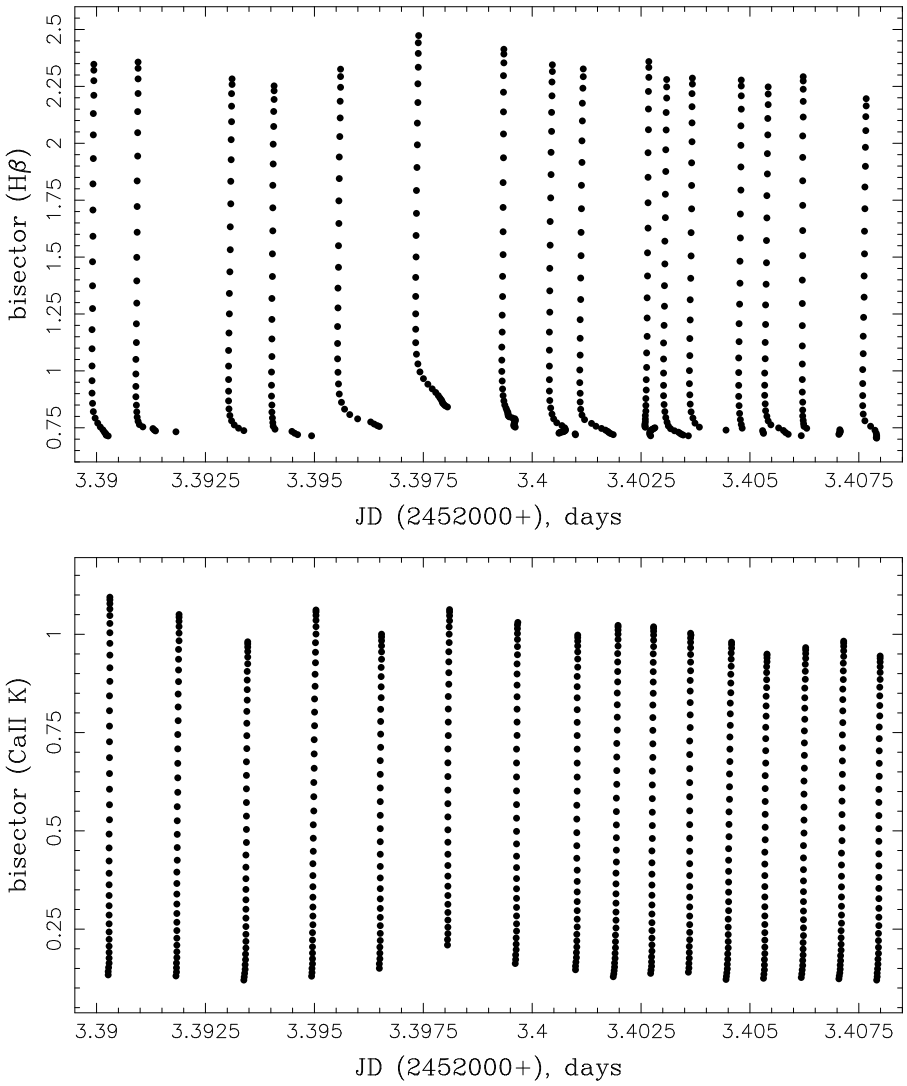

Figure 3.8: Evolution of the bisector of the H_β (top) and Ca II K (bottom) lines during the strongest flare (flare 2). Note that only the minimum value of each bisector is placed on the *JD* in which its respective spectrum was taken.

of physical parameters during several flares.

The BDFP is based on the solution of the radiative transfer equation. It uses the escape probability technique (Drake 1980; Drake & Ulrich 1980) and a simplified picture of the flaring plasma as a slab of hydrogen with an underlying thermal source of radiation which causes photoionization. This source represents a deeper layer in the stellar atmosphere, which is exposed to additional heating during flares. For a detailed description of the physical assumptions made by the BDFP, see § 4.1 of García-Alvarez et al. (2002). The BDFP minimizes the difference between the observed and calculated Balmer decrements using a multi-directional search algorithm (Torczon 1991, 1992). This allows us to find the best possible solution for the Balmer decrements in a four dimensional parameter space, where the parameters are: electron temperature (T_e), electron density (n_e),

Table 3.8: Physical parameters obtained for the observed flares. The area and stellar surface percentage covered by these flares are also shown.

Flare	Date	UT	$\log \tau_{Ly\alpha}$	$\log n_e$	$\log T_e$	$\log T_{us}$	Area ($\times 10^{19}$ cm^2)	Surface (%)
1	03/04/01	00:30	3.71	13.75	4.31	4.13	1.17	0.40
2	03/04/01	21:32	4.62	13.79	4.07	3.99	6.79	2.30
3	04/04/01	00:55	4.18	14.22	4.09	3.90	1.45	0.49
4	04/04/01	01:36	3.78	13.95	4.30	3.98	0.89	0.30
5	04/04/01	21:11	4.54	13.79	4.12	4.02	0.76	0.26
6	04/04/01	22:08	4.43	14.12	4.07	4.04	3.14	1.07
7	04/04/01	23:41	4.41	14.39	4.09	4.02	2.13	0.72
8	05/04/01	01:18	4.15	13.78	4.17	3.98	2.12	0.72
9	05/04/01	02:25	3.60	13.88	4.38	4.09	0.36	0.12

optical depth in the Lyα line ($\tau_{Ly\alpha}$), and temperature of the underlying source or background temperature (T_{us}). Although the temperature of the underlying source could be a free parameter in our code, we have fixed a lower limit at 2500 K for numerical stability reasons. The best solution for the Balmer decrements allows us to calculate the effective thickness of the slab of hydrogen plasma and the total emission measure per unit volume (see expressions given by Drake & Ulrich 1980). With these quantities we are also able to determine the surface area of the emitting plasma – volume/thickness – taking into account that the volume is the ratio of the observed flux in the Hβ line to the total emission measure (also in this line) per unit volume.

3.4.1 Physical parameters of the observed flares

We apply the BDFP to the flares observed on AD Leo. The Balmer decrements for Hγ, Hδ, H_8, H_9 and H_{10} have been calculated at each flare maximum using the flare-only fluxes given in Table 3.5. We do not include higher Balmer lines due to both the difficulty in assigning their local continuum level and the very low SNR in their spectral region.

Figure 3.9 shows the observed and fitted Balmer decrements at the maximum of the detected flares. The strength of an optical flare is related to the slope of the fit solution for the Balmer decrements (García-Alvarez 2003): shallower slopes mean stronger flares. The results after applying the BDFP are listed in Table 3.8. The flares 3, 6 and 7 have a relatively high electron density ($n_e > 1 \times 10^{14}$ cm^{-3}) compared with that found for the other flares (6×10^{13} cm$^{-3} < n_e < 9 \times 10^{13}$ cm^{-3}). The flare 3 also has the lowest background temperature ($T_{us} \sim 8000$ K) which means that the ionization balance in this flare is even less radiatively dominated than in the other ones (9500 K $< T_{us} <$ 13500 K). The electron temperature of the observed flares ranges from 12000 K to 24000 K. Taking into account that H_{10} seems to be out of the trend followed by the other Balmer decrements on flares 2 and 3 (see Fig. 3.9) we have also run the BDFP rejecting this point, obtaining no significant variations in the results (the logarithmic values of the physical parameters

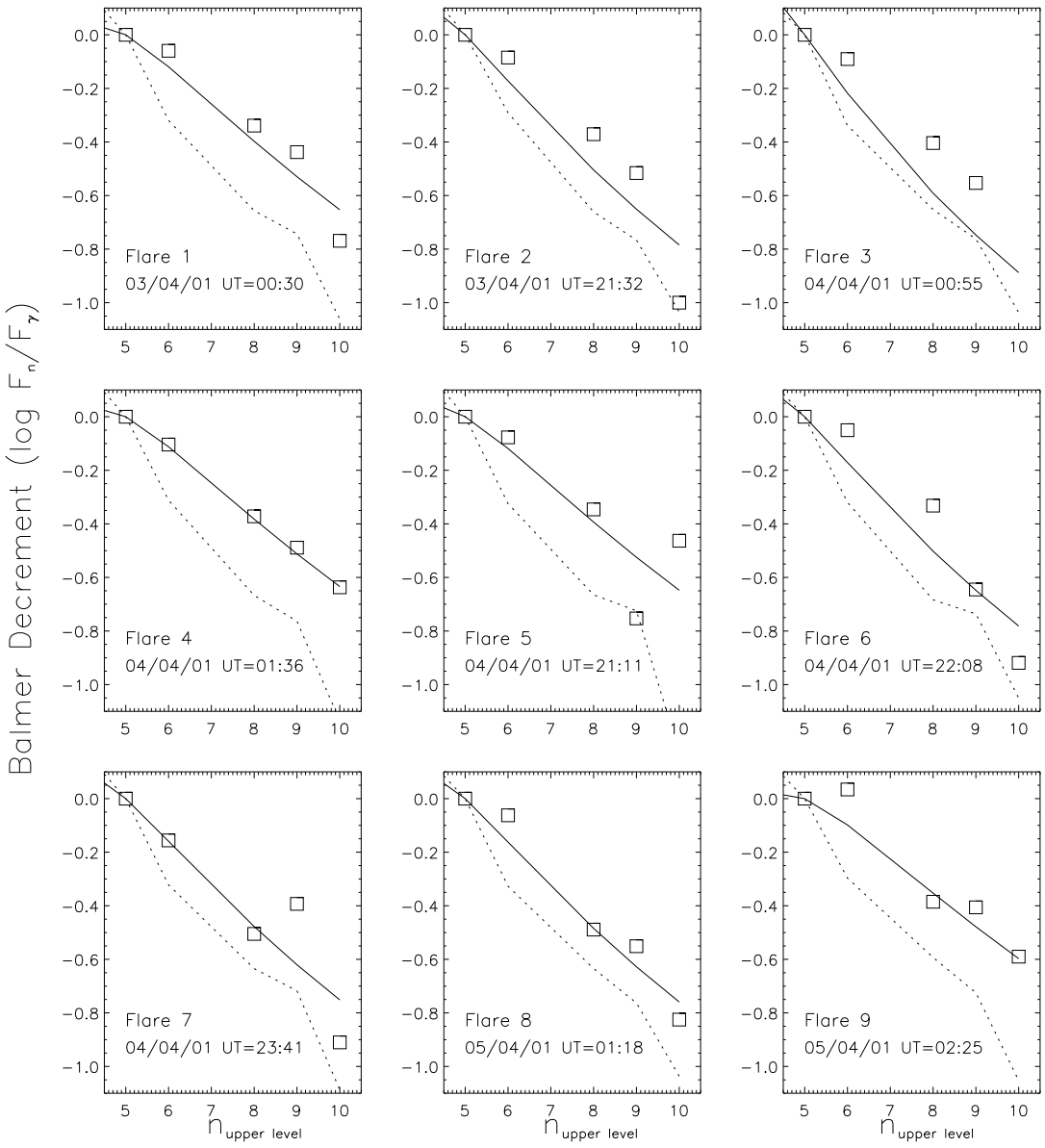

Figure 3.9: Observed Balmer decrements (squares) and optimum computed fits (solid line) at the maximum of the observed flares. The pseudo-quiescent state for each flare, as defined in § 3.3.3, is plotted as reference (dotted line). Note that the Balmer decrement for H_{10} is out of the plotted region in flare 3, but it has been taken into account in the fit.

given in Table 3.8 change by a mean of 5 %).

We have used the fit solutions to calculate the surface area covered by the flaring plasma. The values, which are between 3.6×10^{18} cm^2 and 6.8×10^{19} cm^2, are shown in Table 3.8. We find that all the observed flares cover less than 2.3 % of the projected stellar surface (πR^2).

All the obtained physical parameters are consistent with previously derived values for stellar flares. These flares are also similar in size and strength to those analysed in previous

works based on the same code (García-Alvarez 2003; García-Alvarez et al. 2002).

3.5 Discussion and conclusions

The star AD Leo has been monitored with high temporal resolution during 4 nights (2 – 5 April 2001). More than 600 intermediate resolution spectra have been analysed in the optical wavelength range. Although large variations have not been observed, we have found frequent short (duration between 14 ± 1 and 31 ± 3 min) and weak (released energy in Hβ between 1.5×10^{29} and 8.2×10^{29} erg) flares. Most of these flares are even weaker than those observed on AD Leo by Hawley et al. (2003). All the detected flares have been inferred from the variation in the EW of different chromospheric lines, which were measured using a very accurate method. Given that the continuum does not change during these events, they can be classified as non white-light flares, which so far represent the kind of flares least known on stars.

The observed flare activity is > 0.71 flares/hour, which is slightly larger than the values that other authors obtained for this star by photometry. As far as we know, it is the first time that such a high flare frequency is inferred from the variation of the chromospheric lines. AD Leo seems to be continuously flaring since we have detected 14 moderate flares and a great number of smaller events that appear superimposed on them. Given that the energy distribution of flares was found to be a power law (Datlowe et al. 1974; Lin et al. 1984) of the form $dN/dE = kE^{-\alpha}$ – where dN is the number of flares (per unit time) with a total energy (thermal or radiated) in the interval $[E, E + dE]$, and α is greater than 0 – we can expect very weak flares occurring even more frequently than the observed ones. Therefore our results can be interpreted as additional evidence of the important role that flares can play as heating agents of the outer atmospheric stellar layers (Güdel 1997; Audard et al. 2000; Kashyap et al. 2002; Güdel et al. 2003; Arzner & Güdel 2004).

A total of 14 flares have been studied in detail. The Balmer lines allow us to distinguish two different morphologies: some flares show a gradual decay much longer than the impulsive phase while another ones are less impulsive. This resembles the two main types of solar flares (eruptive and confined) described by Pallavicini et al. (1977). However, the Ca II H & K lines always show the same behaviour and their evolution is less impulsive than that found for the Balmer lines. The two maxima and/or weak peaks, observed sometimes during the detected flares, can be interpreted as the succession of different magnetic reconnection processes, which would be caused as consequence of the disturbance produced by the original flare, as Kopp & Pneuman (1976) suggested for the Sun. The Ca II H & K lines reach the flare maximum after the Balmer series. It seems that the time delay is higher when the impulsive phase of the Balmer lines is shorter. The moment at which a line reaches its maximum is related to the temperature that characterizes the formation of the line and, therefore, is also related to the height where the line is formed. During the detected flares, the relative increase observed in the emission of the Balmer lines is greater for lower wavelengths. We have also found that not only are the detected flares like the most typical solar flares (non white-light flares), but the asymmetries observed in chromospheric lines (red asymmetries) are also like the most frequent asymmetries observed in the Sun during flares. The detected broad Balmer emission wings

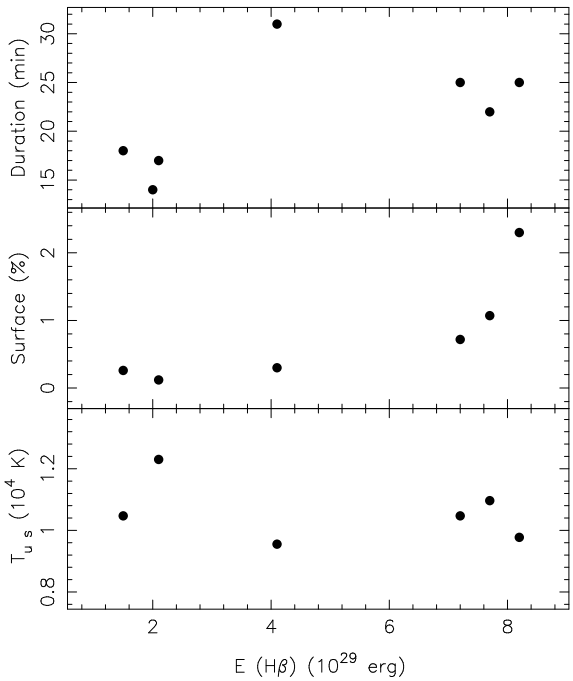

Figure 3.10: Flare duration, stellar surface and temperature of the underlying source at flare maximum vs. energy released in Hβ during the detected flares.

and red asymmetries can be attributed to plasma turbulence, mass motions or CDC. The Ca II H & K lines seem to be less affected by flare events and their broadening is negligible. A small red asymmetry in the Balmer series is also observed during the quiescent state, which could be interpreted as multiple CDC probably due to continuous flaring of very low energy.

We have used the Balmer decrements as a tracer of physical parameters during flares by using the model developed by Jevremović et al. (1998). The physical parameters of the flaring plasma (electron density, electron temperature, optical thickness and temperature of the underlying source), as well as the covered stellar surface, have been obtained. The electron densities found for the analysed flares (6×10^{13} cm^{-3} – 2×10^{14} cm^{-3}) are in general agreement with those that other authors find by using semi-empirical chromospheric modeling (Hawley & Fisher 1992a,b; Mauas & Falchi 1996). The electron temperatures are between 12000 K and 24000 K. The temperature of the background source ranges from 8000 K to 13500 K. All the obtained physical parameters are consistent with previously derived values for stellar flares. The areas – no larger than 2.3 % of the projected stellar surface – are comparable with the size of other solar and stellar flares (Tandberg-Hanssen & Emslie 1988; García-Alvarez 2003; García-Alvarez et al. 2002).

We have also analysed the relationships between the flare parameters. The released energy is correlated with the flare duration and the area covered by the flaring plasma, but not with the temperature of the underlying source (see Fig. 3.10). These results are in general agreement with those found by Hawley et al. (2003) using only 4 flares and a different method for obtaining the physical parameters. We have found a clear relation

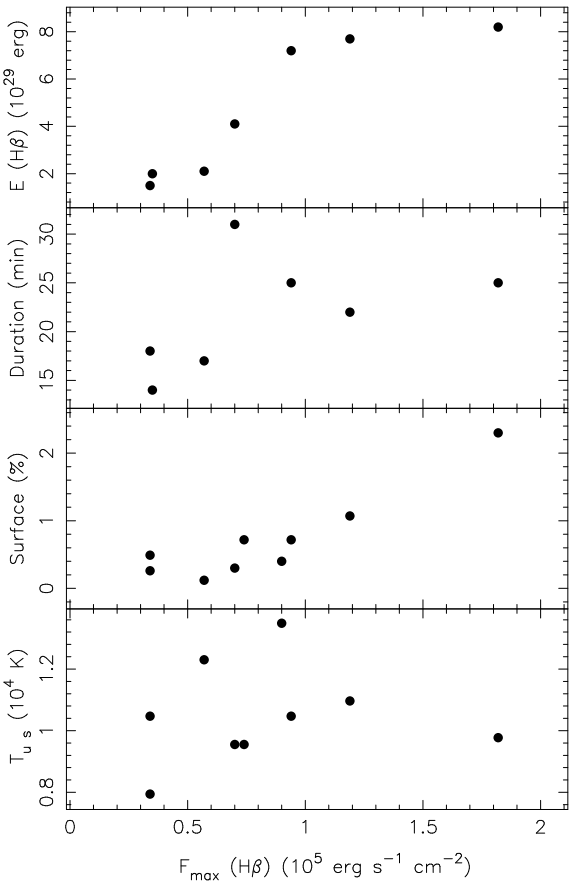

Figure 3.11: As Fig. 3.10 but vs. the flux emitted in Hβ at flare maximum. The top panel has been added to show the relation between this flux and the energy released in Hβ.

between the released energy and the flux at flare maximum (see Fig. 3.11). Also, the higher the flux, the longer the flare. This flux is also correlated with the area covered by the emitting plasma at flare maximum, but not with the temperature of the underlying source (Fig. 3.11). No correlations between the area, temperature and duration have been found: i.e. these parameters seem to be independent. The magnetic geometry seems to be a very important factor in flares: firstly, the flare duration can be related to the loop length, as in X-rays (see review by Reale 2002), in the sense that a fast decay implies a short loop and a slow decay a large loop; and secondly, the flare area can be related to the loop width, because the surface covered by the Balmer emitting plasma would be the projected area of the flaring loops. On the other hand, the temperature of the underlying source could be related to the depth of the layer reached by the flare accelerated particles, which is also related to the energy released through magnetic reconnection. For explaining the fact that the temperature of the underlying source seems to be well-defined and independent of the flare energy (see Figs. 3.10 and 3.11), we suggest that larger energies may imply more energetic particles and therefore larger depths, but not necessarily higher temperatures.

This work has extended the current number of stellar flares analysed using high temporal resolution and good quality spectroscopic observations. However, there is still a

need for new data of this type to trace the behaviour of the physical parameters throughout these events. This will help us to understand the nature of flares on dMe stars. Also, higher spectral resolution is required to better study the changes that take place in stellar atmospheres during flares.

Chapter 4

X-ray flares on the UV Ceti-type star CC Eridani: a "peculiar" time-evolution of spectral parameters*

I. Crespo-Chacón[1,2], G. Micela[1], F. Reale[1,3], M. Caramazza[1],
J. López-Santiago[1,2], I. Pillitteri[3]

[1] Osservatorio Astronomico di Palermo, Piazza del Parlamento 1, I-90134 Palermo, Italy
[2] Departamento de Astrofísica y Ciencias de la Atmósfera, Facultad de Ciencias Físicas, Universidad Complutense de Madrid, E-28040 Madrid, Spain
[3] Dip. di Scienze Fisiche e Astronomiche – Sez. di Astronomia – Università di Palermo, Piazza del Parlamento 1, I-90134 Palermo, Italy

Originally published in Astronomy and Astrophysics (A&A) **471**, 929-939 (2007)

Received 3 April 2007 / Accepted 7 June 2007

Abstract

Context. Weak flares are supposed to be an important heating agent of the outer layers of stellar atmospheres. However, due to instrumental limitations, only large X-ray flares have been studied in detail until now.
Aims. We used an XMM-Newton observation of the very active BY Dra–type binary star CC Eri in order to investigate the properties of two flares that are weaker than those typically studied in the literature.
Methods. We performed time-resolved spectroscopy of the data taken with the EPIC-PN CCD camera. A multi-temperature model was used to fit the spectra. We inferred the size of the flaring loops using the density-temperature diagram. The loop scaling laws were applied for deriving physical parameters of the flaring plasma. We also estimated the number of loops involved in the observed flares.

*Based on observations obtained with XMM-Newton, an ESA science mission with instruments and contributions directly funded by ESA Member States and NASA.

Results A large X-ray variability was found. Spectral analysis showed that all the regions in the light curve, including the flare segments, are well-described by a 3-T model with variable emission measures but, surprisingly, with constant temperatures (values of 3, 10 and 22 MK). The analysed flares lasted $\sim$ 3.4 and 7.1 ks, with flux increases of factors 1.5 – 1.9. They occurred in arcades made of a few tens of similar coronal loops. The size of the flaring loops is much smaller than the distance between the stellar surfaces in the binary system, and even smaller than the radius of each of the stars. The obtained results are consistent with the following ideas: (i) the whole X-ray light curve of CC Eri could be the result of a superposition of multiple low-energy flares, and (ii) stellar flares can be scaled-up versions of solar flares.

Key words. X-rays: stars – Stars: coronae – Stars: activity – Stars: flare – Stars: late-type – Stars: individual: CC Eri

4.1 Introduction

Solar-like stars (main sequence stars with spectral types from F to early M) have radiative cores and convective outer envelopes. Convection, together with differential rotation, generates a magnetic dynamo (see Parker 1975, and references therein) that is responsible of the formation of the corona (see Favata & Micela 2003; and Güdel 2004, for two extensive reviews about stellar coronal astronomy). Magnetic activity similar to that observed on the Sun is typically detected on these stars, showing variability through all the electromagnetic spectrum. The activity level of a star is frequently measured in terms of its coronal X-ray luminosity $L_{\rm X}$. Using data collected by the ROSAT satellite, Schmitt et al. (1995) and Schmitt (1997) found that solar-like stars present X-ray luminosities (integrated over the 0.1-2.4 keV energy band) in the range $25.5 \lesssim \log L_{\rm X}(\mathrm{erg\ s^{-1}}) \lesssim 29.5$. This luminosity is correlated with the stellar rotation rate (Pallavicini et al. 1981). Walter (1982) noticed that a single power law dependence between $L_{\rm X}/L_{\rm bol}$ and the angular velocity was unable to reproduce all the observed data, and proposed to replace it by either a broken power law or an exponential relationship. This result later led to the concept of saturation of stellar activity at high rotation rates (Vilhu 1984; Vilhu & Walter 1987). Rotational velocity, and therefore activity, decreases with age because of the angular momentum losses due to the magnetised stellar wind (Rengarajan 1984; Pace & Pasquini 2004). However, short-period binaries can maintain high rotation rates since they are synchronized by tidal coupling.

Flares are the most extreme evidence of magnetic activity in stellar atmospheres. Frequent flaring is found on late K and M dwarfs in the solar neighbourhood (the so-called UV Ceti-type stars – see their general properties in Pettersen, 1991). Similarities between solar flares and those observed on UV Ceti-type stars suggest that they are produced by the same basic physical mechanisms. Flares are supposed to be the result of the energy release from magnetic field reconnection in the lower corona (e.g., Kopp & Pneuman 1976). In consequence, electrons and ions are accelerated and gyrate downward along the magnetic field lines, producing synchrotron radio emission. Bremsstrahlung radiation is emitted in hard X-rays (> 20 keV) when these ionized beams collide with the denser

material of the chromosphere. At the same time, the gas in the affected chromospheric region is heated (optical and UV radiation is then emitted) and evaporated. Thus, the density and temperature of the newly formed coronal loops increase, emitting in soft X-ray and extreme UV wavelengths. Recent evidence in favour of this scenario was given by Mitra-Kraev et al. (2005) and Smith et al. (2005).

A recurrent idea in the literature is that flares are the main heating agent of the outer stellar atmospheres (e.g., Audard et al. 2000), so that the observed "quiescent" emission would be the result of a superposition of multiple small flares (named "nano-flares"). The distribution law that gives the number of flares dN within an energy-interval $[E, E + dE]$ allows us to estimate the energy budget of the corona. In particular, solar flares are distributed following a power law (Datlowe et al. 1974; Lin et al. 1984; Dennis 1985), that is

$$\frac{dN}{dE} = k_1 E^{-\alpha}, \tag{4.1}$$

where k_1 is a constant and α is the power-law index. For $\alpha > 2$, an extrapolation of Eq. (4.1) to flare energies below the detection threshold would be sufficient to account for the luminosity of the quiescent corona. For this reason, it is crucial to investigate the validity of such an extrapolation (Hudson 1991), as well as the value of α on magnetically active stars. For the Sun, values of α between 1.5 and 2.6 were reported (Crosby et al. 1993; Porter et al. 1995; Krucker & Benz 1998). However, a later study carried out by Aschwanden et al. (2000) suggests the insufficiency of nano-flares to heat the solar corona. On the other hand, for active stars, Collura et al. (1988) and Osten & Brown (1999) found $\alpha \approx 1.5-1.6$, while other authors have reported $\alpha > 2$ (Audard et al. 1999, 2000; Kashyap et al. 2002; Güdel et al. 2003). Therefore, it is still unclear if Eq. (4.1) can be extrapolated from large observable flares towards the weakest ones in order to support the flare-heating hypothesis.

While flare stars have been studied in the optical during more than half a century, the first sizeable sample of X-ray flares was only compiled after the launch of the *Einstein* Observatory (Haisch 1983). Later, Pallavicini et al. (1990) presented the results of a comprehensive survey of X-ray observations of flare stars carried out with the EXOSAT Observatory. However, until recent years, and due to instrumental limitations, only large X-ray flares could be studied in detail. At the present time, the great sensitivity, wide energy range, high energy resolution, and continuous time coverage of the EPIC (European Photon Imaging Cameras) detectors – on-board the XMM-Newton satellite – also enable the detection and analysis of smaller flares. UV Ceti-type flare stars are specially indicated for this purpose because of its proximity. For all these reasons, we decided to carry out the present study of the X-ray flares detected on the UV Ceti-type star CC Eri using the XMM-Newton satellite.

CC Eri (HD 16157) is a spectroscopic binary star (BY Dra-type) located in the immediate solar neighbourhood, at a distance of 11.51 ± 0.11 pc (from Hipparcos, Perryman et al. 1997). This is a SB2 system (Strassmeier et al. 1993) which consists of a K7.5Ve primary and a M3.5Ve secondary (Amado et al. 2000), with mass ratio ≈ 2 (Evans 1959; Amado et al. 2000). The photometric period – 1.56 days – results to be equal to that of the orbital motion (Evans 1959; Bopp & Evans 1973; Bopp & Fekel 1977). Thus, the syn-

chronization due to the tidal lock makes the primary component to be one of the fastest rotating late K dwarfs in the solar vicinity. Using kinematical criteria, the age of the system was estimated to be 9.16 Gyr (Demircan et al. 2006). Busko et al. (1977) and Amado et al. (2000) found that the chromospheric emission of CC Eri varies in antiphase with its optical continuum, suggesting the presence of active emission regions associated with starspots. Besides, its quiescent radio emission is polarized at the 10 - 20 % level (Osten et al. 2002; Slee et al. 2004), indicating large-scale ordering in the stellar magnetic field. CC Eri presents a strong flare activity over a wide range of energies (Busko & Torres 1976, 1978; Caillault et al. 1988; Byrne et al. 1992; Güdel 1992; Pan & Jordan 1995; Amado et al. 2000; Osten et al. 2002; Slee et al. 2004). First X-ray detections of CC Eri were done with HEAO1, showing $\log L_X(\mathrm{erg\ s^{-1}}) \approx 29.26$ in the 2 – 20 keV band (Tsikoudi 1982), *Einstein*, which measured $\log L_X(\mathrm{erg\ s^{-1}}) \approx 29.51$ in the 0.15 – 4.5 keV range (Caillault 1982), and EXOSAT, that observed $\log L_X(\mathrm{erg\ s^{-1}}) \approx 29.62$ in the 0.04 – 2 keV interval (Pallavicini et al. 1988). However, since none of these observations lasted very long, little information on the temporal and spectral variation of the source in X-rays was available. Pan & Jordan (1995) observed and analysed for the first time an X-ray flare on CC Eri, using ROSAT observations. They measured a quiescent luminosity $\log L_X(\mathrm{erg\ s^{-1}}) \approx 29.40$ in the 0.17 – 2 keV band. The flare had an e-folding rise and decay times of about 1 h (or less) and 2 h, respectively, and the emission was enhanced by a factor greater than 2. A 2-T model gave an adequate description to all the ROSAT spectra and showed the presence of high-temperature plasma ($\sim$ 10 MK) even during the time-intervals where no flare activity was detected. This is consistent with the results obtained for the quiescent emission of M-dwarfs using data from the EXOSAT ME and *Einstein* IPC (e.g., Pallavicini et al. 1990; Schmitt et al. 1990). All the X-ray luminosities measured for CC Eri are similar and place this binary star among the most active ones. This is clearly noticed when comparing the quiescent X-ray luminosity obtained for CC Eri from the data analysed in this work ($L_{\mathrm{X,\ 0.1-2.4\ keV}} \approx 3.7 \times 10^{29}$ erg s^{-1}) with the cumulative X-ray luminosity distribution functions found by Schmitt et al. (1995) for low-mass stars in the solar neighbourhood.

In this paper, we present the study of an XMM-Newton observation of CC Eri, which, for the first time, reveals details about the behaviour of the parameters that characterized the plasma during two flares weaker than those typically analysed in other active dM stars. Technical information about the observation and details of the data analysis is given in § 4.2. In § 4.3 we describe the light curve and the different kinds of variations observed. The time-resolved study of spectral parameters is presented in § 4.4, where we also estimate the size of the flaring loops. Finally, in § 4.5, we discuss and interpret the results in the context of solar and stellar flares.

4.2 Observations and data analysis

The observation of CC Eri analysed in this work was performed with the XMM-Newton satellite on August, 8, 2003 (PI: H. Kay, ID: 0148790101) during revolution 0671. The XMM-Newton satellite owns the most sensitive soft X-ray detector system presently available: the EPIC instrument. It consists of three imaging and non-dispersive CCD-based

cameras: the twin MOS 1 and MOS 2, and the PN (Turner et al. 2001; Strüder et al. 2001). The wavelength range measured by the EPIC detectors allows one to obtain a reliable determination of properties of the hottest plasma components. For our timing and spectral analysis, we used only the data from the PN-CCD camera, that is more sensitive than the MOS detectors. This observation was done in the full frame mode with the thick filter. The exposure time of the image taken with EPIC-PN was 36.703 ks, that is, 0.27 times the orbital period of the binary star CC Eri.

We used the event file in the PPS data products, which was produced with the standard XMM-Newton Science Analysis System (SAS) software, version 5.4.2. The light curve and the spectra were obtained with standard tools of SAS. The PN responses were generated with the SAS RMFGEN and ARFGEN tasks. The spectral analysis was done with the X-ray spectral fitting package XSPEC V11.3.2 (Arnaud 1996, 2004).

Standard selection criteria were applied for filtering the data (see Ehle et al. 2004). We extracted events in the energy band between 0.5 – 10.0 keV that triggered only one or two detector pixels at the same time (PATTERN ≤ 4). Data below 0.5 keV were excluded to avoid residual calibration problems in the response matrices at soft energies. Nevertheless, since flares mainly affect hotter thermal components, the spectral region below 0.5 keV is not crucial for our analysis. In fact, we checked that no significant variations are found in the spectral parameters (see § 4.4.1) when the region 0.3 – 0.5 keV is included for fitting the spectra. The EPATPLOT task was used for confirming the existence of pile-up affecting the inner region of CC Eri. To lose the minimum number of counts as possible, we looked for and ignored the smallest region that allowed avoiding the pile-up effects during the whole observation. The X-ray light curve and spectra were therefore obtained with the events taken from an annulus with inner radius 12″ and outer radius 44″. On the other hand, background photons were extracted from a source-free region – a circle with a radius of 54.4″– placed at the same CCD as CC Eri.

4.3 The light curve

Figure 4.1 shows the source (background - subtracted) and background light curves of CC Eri as observed with the EPIC-PN detector for a temporal binning of 100 s and the filtering criteria given in § 4.2. Note that the background count-rate was scaled to the size of the source region. The dead-time correction was applied to both the source and background count-rates. A significant X-ray variability was found throughout the observation. The lowest activity level (L0 or *quiescent state* hereafter) was observed at the beginning. It was followed by a small flare (FA) where the stellar flux increased by a factor 1.3. Another two flares (FB and FC) with flux changes of factors 1.5 – 1.9, depending on the selected reference level, were also observed. The maxima of these two flares were separated by 5 hours. In addition, the stellar emission between these two events was also variable – two different activity levels (L1 and L2) were identified – and higher than that observed during the quiescent state. The start and end times of the main selected periods are summarized in Table 4.1. FA, FB and FC radiated in the 0.5 – 10.0 keV band a total energy of 0.08, 0.75 and 1.5×10^{33} erg, respectively.

In terms of relative increasing of flux with respect to the quiescent level, the strength

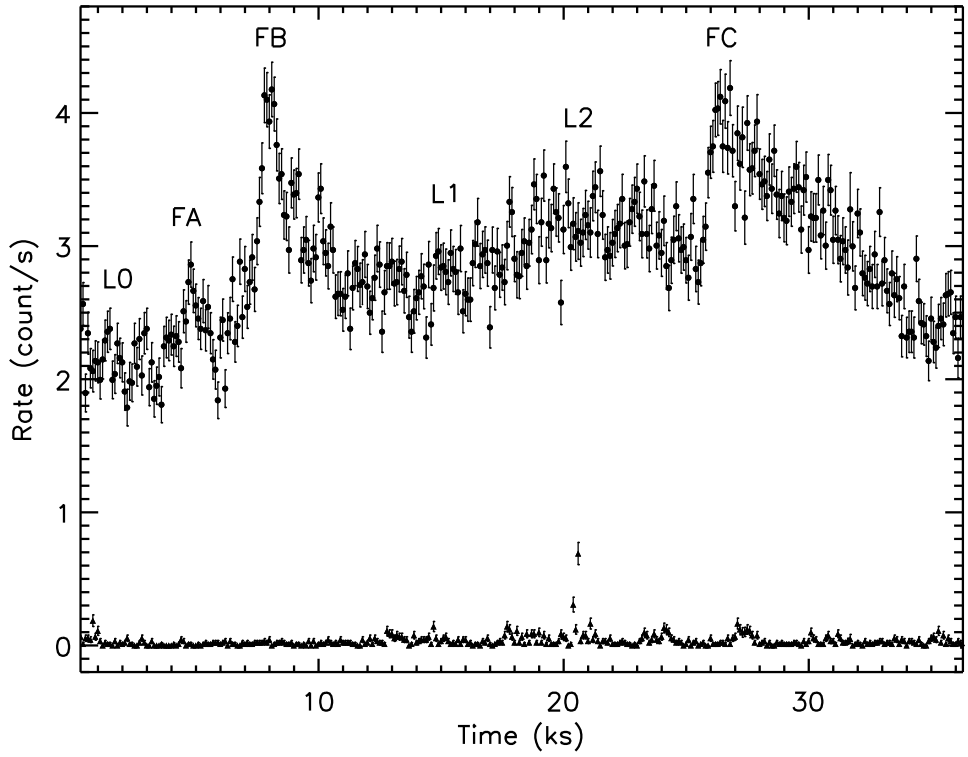

Figure 4.1: Source (upper region) and background (lower region) light curves of CC Eri as observed with the EPIC-PN detector for the energy band 0.5 – 10.0 keV and a temporal binning of 100 s. The labels FA, FB and FC refer to the detected flares while L0, L1 and L2 designate different emission levels where no clear flare activity was observed.

of the detected flares is somewhat smaller than the typical values analysed on active low-mass stars. For instance, Robrade & Schmitt (2005) found flux increases of factors 2 – 3 in flares produced by EQ Peg, AT Mic, AD Leo and EV Lac. All of them can be considered as moderate flares in view of the flux increases (10 – 300 times the quiescent state value) that Favata et al. (2000c), Katsova et al. (2002), and Güdel et al. (2004) observed respectively on EV Lac, EQ Peg and Prox Cen. The detected flares are even a little bit weaker than that observed by Pan & Jordan (1995) on the same star, CC Eri, which showed a ratio between the peak and minimum fluxes larger than a factor of 2. However, in absolute terms, the peak X-ray luminosity of the analysed flares is large compared to that of the brightest solar flares.

Table 4.2 lists the duration of the rising and decay phases of the observed flares. Since the behaviour of these two phases can be well-described by an exponential law, their duration was respectively estimated as the $1/e$ rise time ($\tau_{\rm R}$) or $1/e$ decay time ($\tau_{\rm D}$). The values of $\tau_{\rm R}$ and $\tau_{\rm D}$ were therefore determined from a least-squares fit to the corresponding data by an exponential function of the form $R = A_0 e^{(t-t_{\rm max})/\tau} + R_{\rm base}$; where R is the count-rate, $R_{\rm base}$ is the count-rate in the quiescent state (L0 in this case), A_0 is the amplitude at the flare maximum, t is the time, $t_{\rm max}$ is the time at the flare maximum, and τ is $\tau_{\rm R}$ or - $\tau_{\rm D}$. Note in Fig. 4.1 that flare FC could have a larger or shorter decay time, depending on the value considered for $R_{\rm base}$ (i.e., equal to that of L0 or, on the contrary, L1), but being

Table 4.1: Time-intervals of the main activity levels detected on CC Eri (see Fig. 4.1).

Activity level	Time-interval (ks after the observation starts)
L0	0.0 – 3.6
FA	3.6 – 5.6
FB	5.6 – 12.9
L1	12.9 – 17.7
L2	17.7 – 23.7
FC	23.7 – 36.7

Table 4.2: Duration of the rising (τ_R) and decay (τ_D) phases of the flares observed on CC Eri.

Flare	τ_R (s)	τ_D (s)
FA	400	580
FB	570	2850
FC	1100	5960

always greater than 50 minutes. Using data collected by the LE experiment on EXOSAT, Pallavicini et al. (1990) found two different types of flares in a sample of 32 M dwarf stars, i.e., *impulsive flares* and *long decay flares*, similar to the ones observed on the Sun (Pallavicini et al. 1977). Those in the first group are reminiscent of solar *compact* flares, showing rise times of a few minutes and decay times of tens of minutes; and those in the second group, with decay times of the order of ≈ 1 hour or longer, are reminiscent of solar long-duration *2-ribbon* flares. Thus, FA can be classified as an impulsive flare and FC as a long decay one. However, the classification of flare FB is unclear since its decay time is in the limit range between the two types. As discussed by Pallavicini (1988) and Poletto et al. (1988), these morphological differences may indicate real physical differences in the energy release process, as it also appears to happen for solar compact and 2-ribbon flares (Pallavicini et al. 1977; Priest 1981). In particular, in compact flares energy is probably released only during the impulsive phase, whereas in 2-ribbon flares a prolonged energy release is apparently required to explain their long decay times. Regarding this point, it is interesting to note the peaks observed in the light curve during the decay of flare FB, which are probably related to different magnetic reconnection processes (superposed flare-type events).

4.3.1 Searching for short-term variability

There are three long intervals in the light curve of CC Eri (L0, L1 and L2) that have been supposed to have a constant emission level. In this section we make use of the method

given by Marino et al. (2000) to test whether small changes within each one of these time regions (see Fig. 4.1) can be considered further short-term stellar variability or, on the contrary, are compatible with statistical fluctuations.

Assuming that during the intervals L0, L1 and L2 the star has a constant count-rate equal to the mean count-rate characteristic of each one of these regions ($R_{\rm m}$[Li]), we computed the net counts expected ($c_{\rm exp,\ bin}$[Li]) in the used temporal bin (100 s). For every interval, we generated a set of simulated data with the N Poisson distribution centered on $c_{\rm exp,\ bin}$[Li], which represents possible outcomes from the observations if the source had a constant count-rate equal to the mean count-rate of the interval. Each set consisted of 1000 of such simulations. We then calculated the cumulative distribution function (CDF[2]) of the count-rates observed within the interval, as well as of each one of these simulations. The set of the CDF's obtained for the simulations allowed us to evaluate the spread introduced by statistical fluctuations.

In Fig. 4.2 we have plotted the CDF of the intervals L0, L1 and L2. All of them are compared with their corresponding simulations for a constant source with count-rate equal to $R_{\rm m}$[Li] (dashed area). In all the three cases the CDF of the observed count-rates is contained within the space occupied by the CDF's of the simulations. Therefore, statistical fluctuations can account for the observed spread and possible short-term variability on CC Eri cannot be distinguished from noise in these regions. However, when the analysis is done for the three intervals (L0, L1 and L2) altogether, significant differences between the observations and simulations are found (see Fig. 4.3). In fact, the same happens when the analysis is separately done for L0 and L1, or L1 and L2. The difference between the emission from L0, L1 and L2 is therefore due to stellar variability and cannot be explained only by statistical fluctuations.

The same type of study can also be used to quantify the variations found in the complete light curve of CC Eri (Fig. 4.4). Since in this case we were looking for changes relative to the quiescent emission, we chose as reference level the mean count-rate measured for the quiescent state, i.e. $R_{\rm m}$[L0]. If the duration of the observation were long enough, the CDF could be considered as the fraction of time that the star spends with a count-rate greater than, or equal to, a given value. The tail of the CDF at rate $\gtrsim 3$ count/s is produced by the two strongest detected flares (FB and FC). The rest of the CDF not consistent with the simulations accounts for the other kind of variability observed at different time scales on the light curve of CC Eri.

In addition, we analysed FA to confirm that the emission within this time-interval was not constant. We obtained that the part of the CDF at the highest count-rates of FA is out of the simulations. Therefore, FA is probably a flare-event. However, the current instrumentation did not allow us to carry out a time-resolved study of the different phases of FA due to the low strength and shortness of this flare.

[2]The cumulative distribution function (CDF) represents the probability of observing a number of counts – in the chosen temporal bin – greater than, or equal to, a given value.

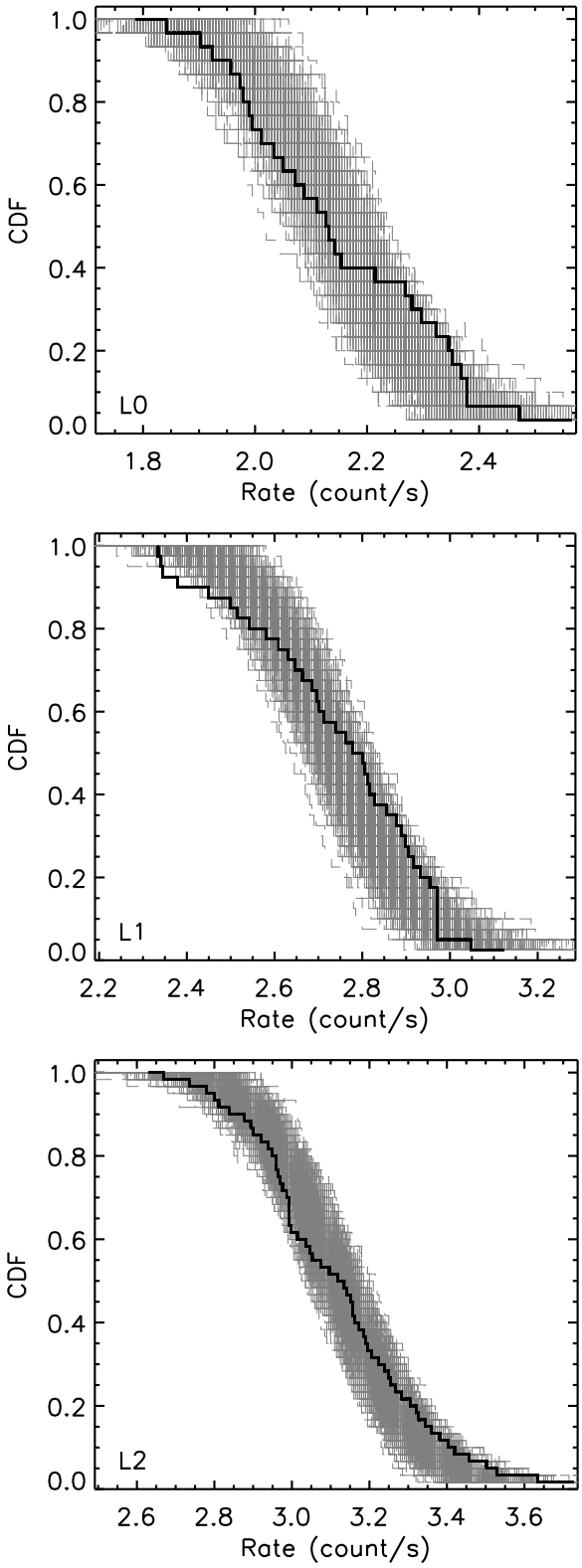

Figure 4.2: Cumulative distribution function of the count-rates observed in the regions L0, L1 and L2 (solid black line) compared to those simulated by supposing a constant source with count-rate equal to the mean value ($R_{\rm m}$[Li]) in the given region (dashed area).

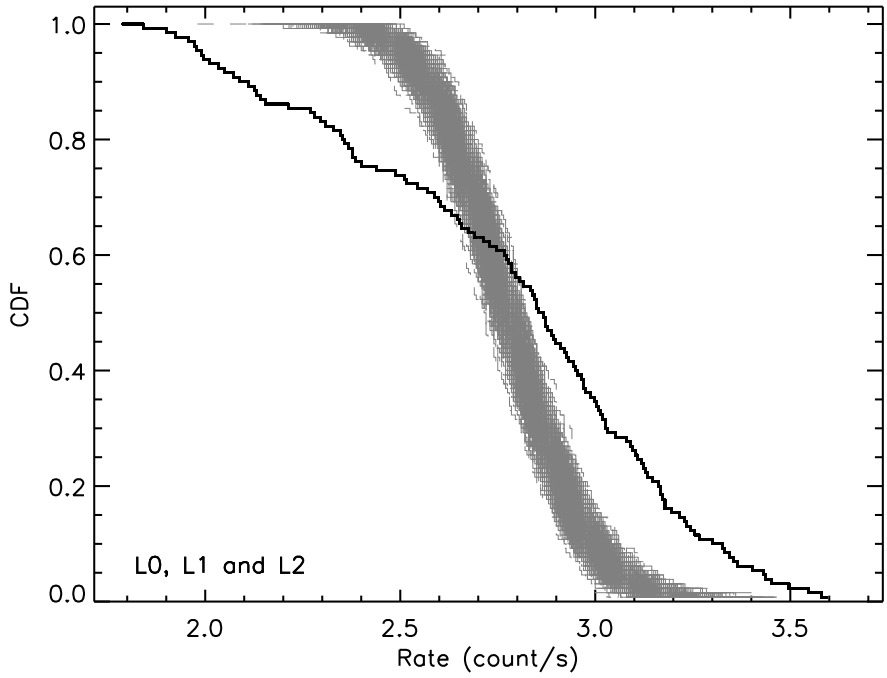

Figure 4.3: Cumulative distribution function of the observed count-rates obtained for L0, L1 and L2 altogether (solid black line) compared to those simulated by supposing a constant source with count-rate equal to the mean value of these three regions (dashed area).

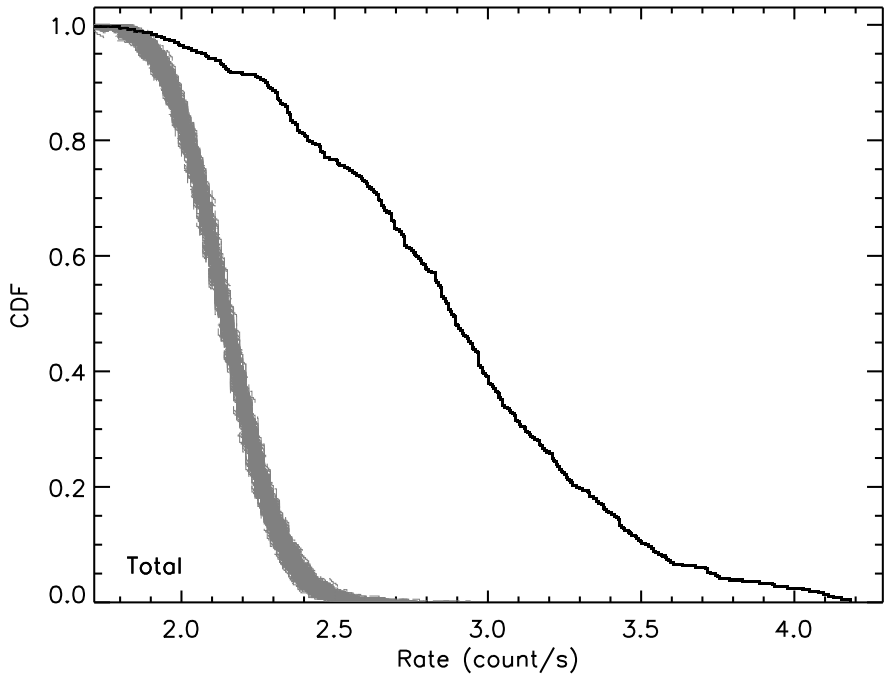

Figure 4.4: Cumulative distribution function of the count-rates detected in the whole observation of CC Eri (solid black line) compared to those simulated by supposing a constant source with count-rate equal to the quiescent value (dashed area).

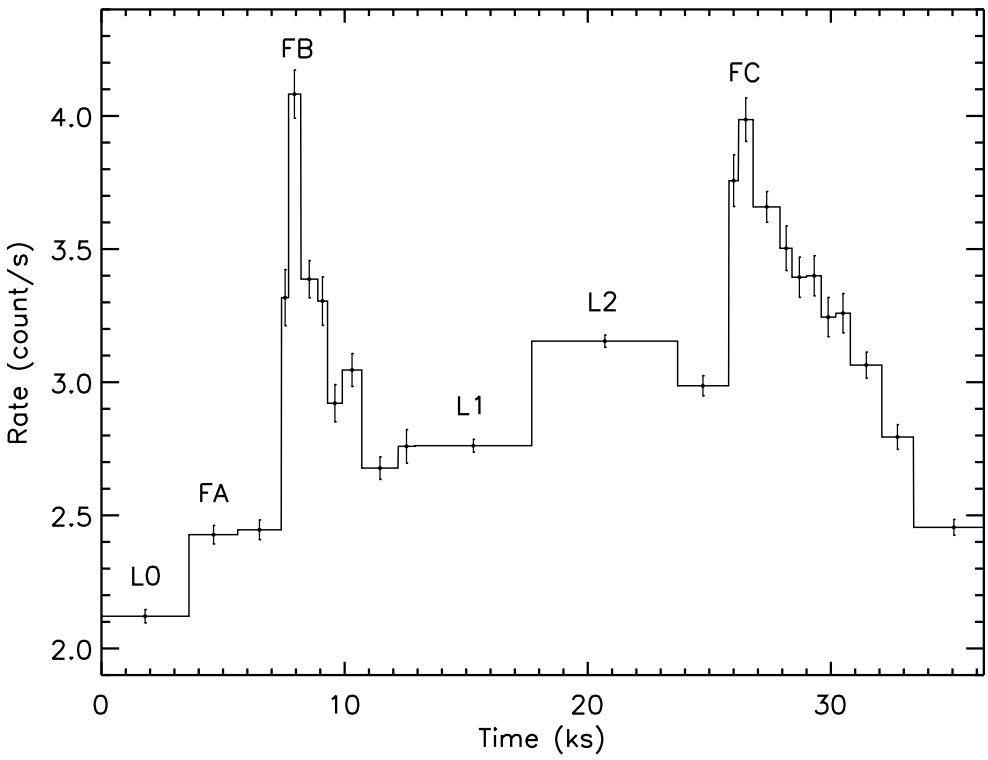

Figure 4.5: Rebinned light curve of CC Eri for the energy band 0.5 – 10.0 keV.

4.4 Spectral analysis

In this section we carry out a time-resolved study of coronal properties (temperature, emission measure and metal abundance) through the whole observation of CC Eri.

With this scope, and taking the variability pattern in the light curve into account, the total observing time was split in several time-intervals with approximately constant count-rate. All the intervals were chosen in order to have enough signal to perform a reliable spectral analysis. Most of the spectra have at least 2000 counts. However, the spectrum extracted for the rising phase of both FB and FC was taken with less photons ($\gtrsim$ 1000 counts) for avoiding to mix this region with the flare maximum. The rebinned light curve of CC Eri is shown in Fig. 4.5. We obtained the spectra of all these intervals following the filtering criteria given in § 4.2. Every spectrum was binned to provide at least 8 counts per spectral bin. Bad channels were always excluded.

We modeled the spectra by using the Astrophysical Plasma Emission Code (APEC, Smith et al. 2001a) included in the XSPEC software. APEC calculates spectral models for hot, optically thin plasmas using atomic data stored in the Astrophysical Plasma Emission Database (APED, Smith et al. 2001b). The APED files contain atomic data such as collisional and radiative rates, recombination cross sections, dielectronic recombination rates, and satellite line wavelengths, which constitute the relevant information for calculating both the continuum and line emission. Interstellar absorption was taken into account by using the photoelectric cross sections of Morrison & McCammon (1983), also available in XSPEC. Despite the generally satisfactory results of using the χ^2 minimization technique

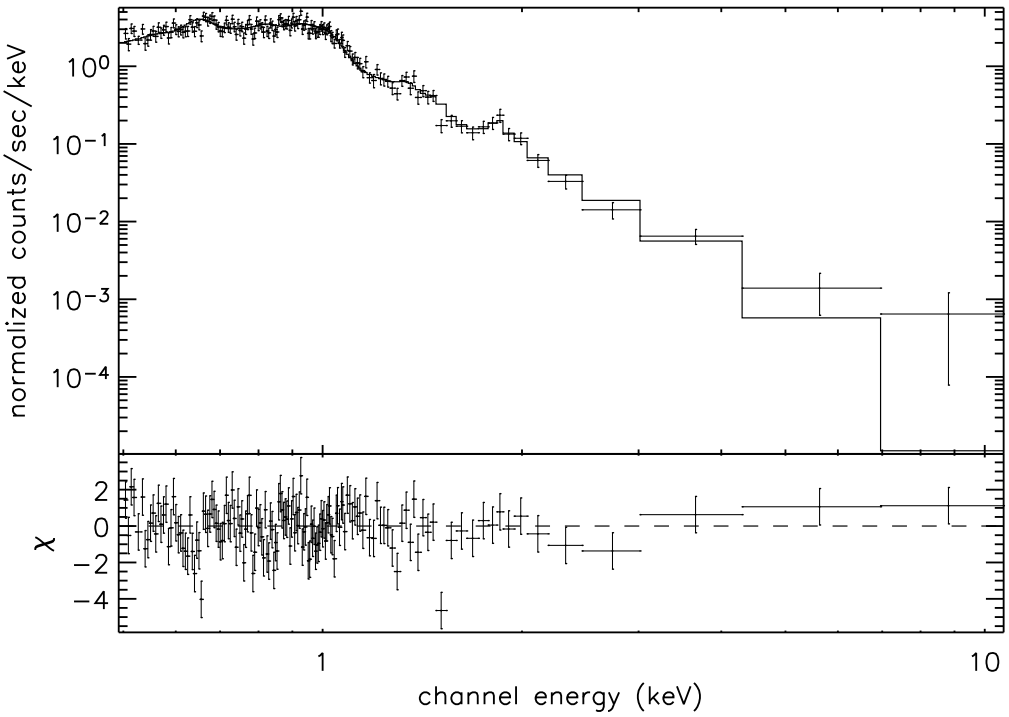

Figure 4.6: X-ray spectrum of the quiescent state of CC Eri (L0). The best fit (2-T APEC model) is also shown with a solid line.

for obtaining the best fitted model, it runs into problems when the number of events is small. For this reason, our fit procedure was based on the Cash's C statistic minimization (Nousek & Shue 1989), which gives better fits in the low-count regime (note also that the C statistic is equivalent to χ^2 in the limit of large number of counts). Unfortunately, for the C statistic there exists no method analogous to that of the reduced χ^2 value ($\chi^2_{\rm red}$) with which we can measure the goodness of the fit. We can determine the best parameters by minimizing the function, but we have no criteria for rejecting the model. Therefore, for giving an idea of the goodness of our fits we show the reduced χ^2 value generated by each model (obtained through C statistic minimization) and its corresponding data set. The errors associated with the fitted parameters were calculated for a confidence level of 2.706 σ.

A 2-T model was needed to describe the shape of the coronal spectrum of the quiescent state (L0, see Fig. 4.6). Leaving all the parameters as free variables, and taking the same global abundance (scaled on the solar photospheric values of Anders & Grevesse 1989) for all the temperature components, we obtained the following results: the hydrogen column density ($N_{\rm H}$) of the intervening interstellar medium is negligible in the studied wavelength range, as expected due to the proximity of CC Eri; the global coronal abundance is $Z/Z_\odot = 0.33^{+0.10}_{-0.07}$; the temperatures are $KT_1 = 0.301^{+0.011}_{-0.011}$ keV and $KT_2 = 0.927^{+0.034}_{-0.036}$ keV; and the emission measures for these thermal components are $EM_1 = 1.69^{+0.35}_{-0.31} \times 10^{52}$ cm^{-3} and $EM_2 = 1.50^{+0.30}_{-0.26} \times 10^{52}$ cm^{-3}, that is, $EM_2/EM_1 \approx 0.9$. These values give the best possible fit to the data using the C statistic, corresponding to a $\chi^2_{\rm red} \approx 1.44$.

4.4.1 Time-resolved study of spectral parameters

We carried out the spectral analysis of all the time-intervals showed in Fig. 4.5 to examine the influence of the observed flares on the temperatures and emission measures of the plasma. Reale et al. (2001) converted X-ray data of a sample of solar flares into the same format and framework as stellar X-ray data, in the perspective to use them as templates for interpreting stellar flares. They found that synthesized stellar-like spectra of solar flares (previously subtracted by the quiescent "background" spectrum) are generally well-fitted with a single thermal component (1-T model) at a temperature close to that of the maximum of the $EM(T)$ distribution. However, two thermal components are sometimes needed to fit the data during the decay, probably due to a rapid variation of the plasma temperature within this phase. In fact, they detected deviations from the isothermal description for the flares with no significant sustained heating. Consequently, our first approach consisted on using a 3-T model to fit each observed spectrum, fixing all the parameters of the first two components at their quiescent values, whereas the temperature and emission measure of the third component (which describes the flaring plasma) were free to vary. Generally, the statistics did not allow to constrain the abundance of the additional APEC component. Therefore, it was assumed to be equal to the global abundance obtained for the quiescent state in order to avoid unphysical solutions. Results showed that this model failed to reproduce the observed data under the considered assumptions. A systematic excess at high energies appeared in the residuals, and the temperature of the hottest component resulted to be very similar to that of the second one. This suggested us that the emission measure of the second component may be changing (note that we fixed it at its quiescent value), and therefore the third component was trying to compensate its enhancement providing a temperature lower than that required to fit the high-energy region of the spectra. For these reasons, we decided to perform a self-consistent analysis by fitting the data using an "iterative" procedure, which is described below.

Each spectrum was fitted with a 3-T model, taking the same global abundance for all the thermal components and fixing it at its quiescent value. The first iteration was done leaving all the temperatures and emission measures as free parameters. Results for the temperature of the coolest component (KT_1) were plotted versus time (Fig. 4.7a) and count-rate (Fig. 4.8a). No change in KT_1 was noticed. Moreover, the normalized histogram of the time-weighted values of KT_1 (Fig. 4.9a) showed an approximately Gaussian distribution peaked at the temperature of the coolest component of the 2-T model that described the quiescent state. A Gaussian fit provided the mean temperature of the distribution, together with its uncertainty (standard deviation), that is

$$\overline{KT}_1 = 0.296 \pm 0.016 \text{ keV}.$$

This value can be considered the best estimation for the temperature of the coolest component. Since $\overline{KT}_1$ was constant during the observation, we fixed it and computed the fits again (second iteration) allowing variations in the other two temperatures and in the emission measure of all the three thermal components. No change was then detected in KT_2 (see Figs. 4.7b and 4.8b). This temperature also appeared to be uniform throughout the observation. Using a Gaussian distribution to fit the normalized histogram of the

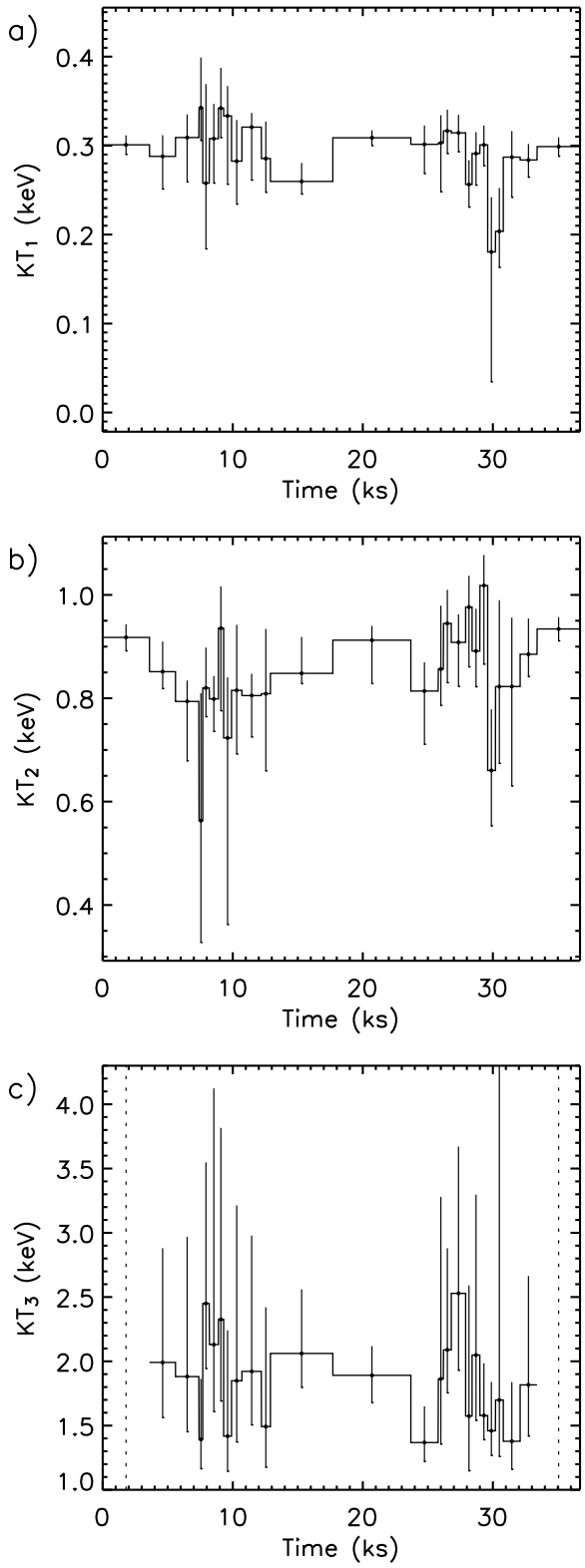

Figure 4.7: Time-evolution of the coronal temperatures obtained with the 3-T model. In the KT_3 panel, a dashed line marks the time-segments for which this temperature could not be constrained (see text). Note that the time-resolution is the same as that shown in Fig. 4.5.

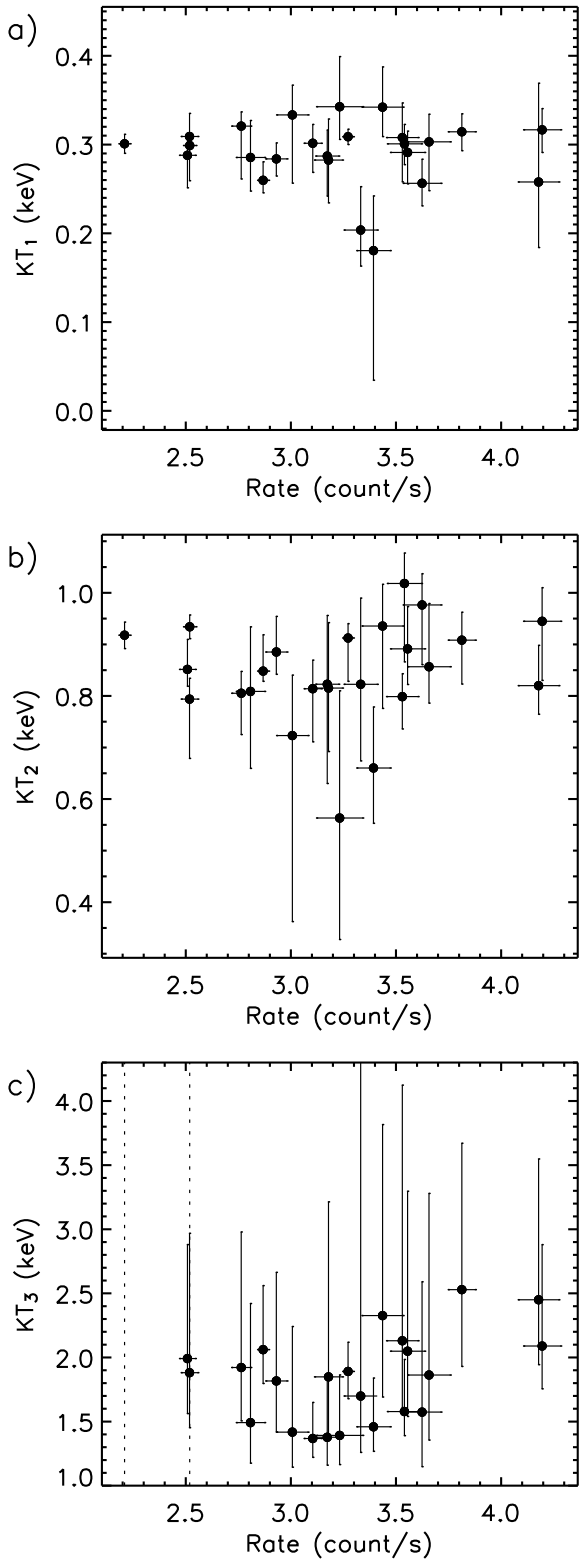

Figure 4.8: Coronal temperatures (obtained with the 3-T model) vs. count-rate. In the KT_3 panel, a dashed line marks the time-segments for which this temperature could not be constrained (see text). Note that no significant changes in the temperature values are observed even at flare maxima (points with the highest count-rates).

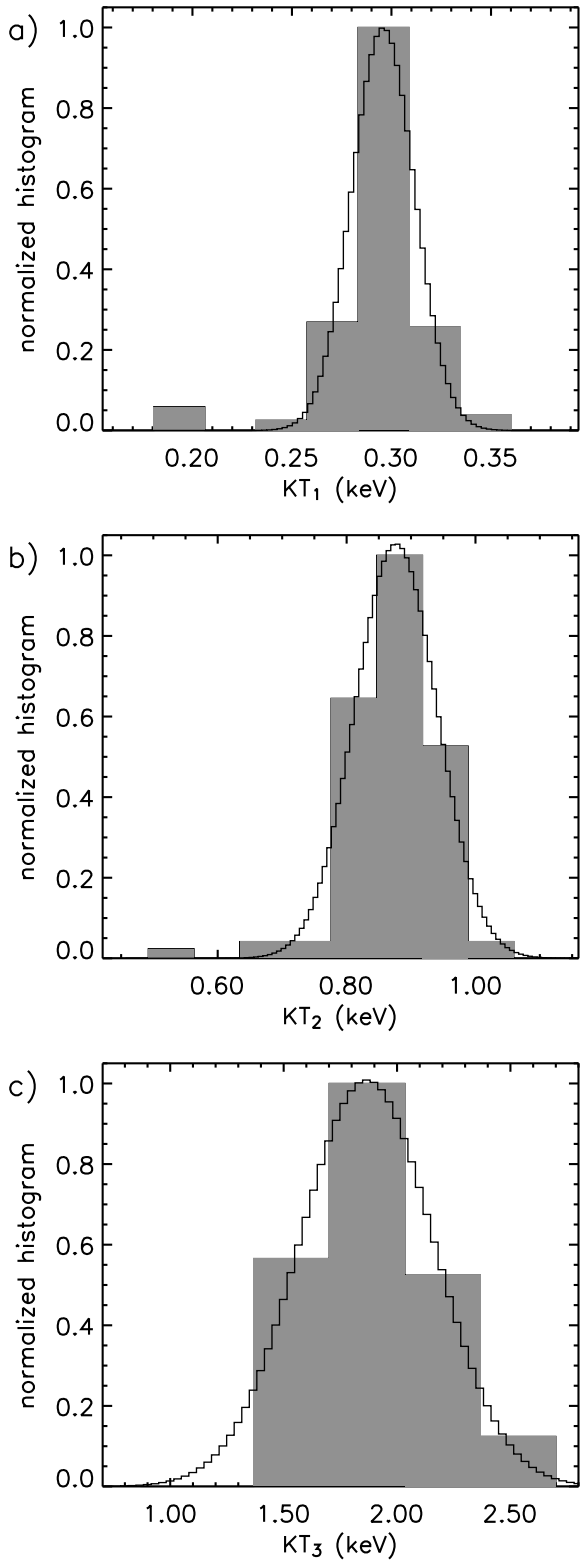

Figure 4.9: Distribution of the three temperatures that characterize the corona of CC Eri during the XMM-Newton observation. The corresponding Gaussian fits are also plotted.

time-weighted values of this parameter (Fig. 4.9b), we obtained

$$\overline{KT}_2 = 0.88 \pm 0.06 \text{ keV},$$

which is clearly consistent with the temperature of the hottest component of the 2-T model that described the quiescent state. In addition to $\overline{KT}_1$, $\overline{KT}_2$ was also fixed in the model and the fits were repeated (third iteration) leaving free the temperature of the hottest component and the three emission measures. Figures 4.7c and 4.8c show the values obtained for KT_3 versus time and count-rate, respectively. It was not possible to constrain this temperature for the segments with an emission level equal or very similar to that of the quiescent state (first and last time-intervals). However, we cannot discard the existence of a little amount of hotter material during these time-intervals, with a contribution not strong enough to be detected. No clear pattern was detected in the time-evolution of KT_3 during the observed flares (see Fig. 4.7c). In fact, the most surprising result is that no significant enhancement in this temperature was found during any phase of the observed flares when comparing them with non-flaring intervals (see also Fig. 4.8c). Furthermore, when accounting for the calculated uncertainties, all the values of KT_3 are compatible with the average value obtained by fitting a Gaussian distribution to the normalized histogram of the time-weighted values of KT_3 (Fig. 4.9c), as occurred for the other two temperatures, that is

$$\overline{KT}_3 = 1.87 \pm 0.30 \text{ keV}.$$

Therefore, we fixed the three temperatures ($\overline{KT}_1$, $\overline{KT}_2$ and $\overline{KT}_3$) and computed the last iteration leaving all the emission measures as free parameters when doing the fits. Results of the best-fitting models are given in Table 4.3 (note that the first and last time-intervals were also fitted with the same model). All the calculated fits can be considered good-quality models in terms of the χ^2_{red} test statistic. The time-evolution of the three emission measures is plotted in Fig. 4.10. Figure 4.11 complements this figure giving the emission measure of each component versus the count-rate.

Our analysis shows that the occurrence of flares may be explained with the increasing of the emission measures related to the hottest temperatures, and in particular to the third one, while the dominant temperatures remain unchanged.

4.4.2 Loop modeling

Although stellar flares are not spatially resolved, we can infer the size of these structures by assuming that they are produced by the same basic physical mechanisms as solar flares and using flare loop models (see Kopp & Poletto 1984; White et al. 1986; Poletto et al. 1988; van den Oord & Mewe 1989; Pallavicini et al. 1990; Serio et al. 1991; Hawley et al. 1995; Reale et al. 1997; or the review given by Reale 2002, for an extensive discussion and comparison of these methods). Under the hypothesis of flares occurring inside closed coronal structures, and assuming that the heat pulse is released at the beginning of the flare, the decay time of the X-ray emission scales with the length of the loop which confines the flaring plasma. However, the presence of significant heating during the de-

Table 4.3: Results derived from the time-resolved spectral analysis after fixing the hydrogen column density, the global coronal abundance, and the different temperatures (see text in § 4.4.1). Columns show: (1) label referring to the time-region where the spectrum is included (see Figs. 4.1 and 4.5); (2) time-coverage; (3), (4) and (5) emission measures, from the coolest (EM_1) to the hottest (EM_3) thermal components; (6) reduced χ^2 and degrees of freedom; (7) and (8) X-ray flux and luminosity in the 0.5 – 10.0 keV band.

[1]Region	[2]$\text{Time}_{\text{start}} - \text{Time}_{\text{end}}$ (ks)	[3]EM_1 (10^{52} cm^{-3})	[4]EM_2 (10^{52} cm^{-3})	[5]EM_3 (10^{52} cm^{-3})	[6]χ^2_{red} (d.o.f)	[7]f_{X} (10^{-11}erg cm^{-2} s^{-1})	[8]log L_{X}(erg s^{-1})
L0	0.0 – 3.6	$1.63^{+0.09}_{-0.09}$	$1.43^{+0.08}_{-0.08}$	$0.10^{+0.08}_{-0.08}$	1.44 (150)	1.52	29.38
FA	3.6 – 5.6	$1.58^{+0.13}_{-0.13}$	$1.58^{+0.12}_{-0.12}$	$0.42^{+0.11}_{-0.11}$	1.11 (209)	1.77	29.45
FB	5.6 – 7.4	$1.67^{+0.14}_{-0.14}$	$1.54^{+0.12}_{-0.12}$	$0.42^{+0.12}_{-0.12}$	0.97 (200)	1.78	29.45
FB	7.4 – 7.7	$1.92^{+0.38}_{-0.37}$	$1.69^{+0.37}_{-0.35}$	$1.17^{+0.41}_{-0.39}$	0.96 (85)	2.39	29.58
FB	7.7 – 8.2	$1.55^{+0.32}_{-0.31}$	$2.33^{+0.31}_{-0.30}$	$2.05^{+0.34}_{-0.35}$	0.87 (161)	3.17	29.70
FB	8.2 – 8.9	$2.00^{+0.26}_{-0.25}$	$2.13^{+0.24}_{-0.24}$	$0.92^{+0.25}_{-0.24}$	0.97 (98)	2.55	29.61
FB	8.9 – 9.3	$1.60^{+0.33}_{-0.32}$	$1.76^{+0.31}_{-0.30}$	$1.65^{+0.36}_{-0.35}$	1.02 (111)	2.61	29.62
FB	9.3 – 9.9	$1.81^{+0.26}_{-0.25}$	$1.97^{+0.24}_{-0.24}$	$0.50^{+0.25}_{-0.23}$	0.89 (114)	2.14	29.53
FB	9.9 – 10.7	$1.95^{+0.23}_{-0.22}$	$1.92^{+0.21}_{-0.21}$	$0.70^{+0.22}_{-0.21}$	1.21 (166)	2.27	29.56
FB	10.7 – 12.2	$1.71^{+0.16}_{-0.15}$	$1.64^{+0.14}_{-0.14}$	$0.63^{+0.15}_{-0.14}$	1.19 (200)	1.98	29.50
FB	12.2 – 12.9	$1.95^{+0.23}_{-0.23}$	$1.61^{+0.22}_{-0.21}$	$0.54^{+0.23}_{-0.22}$	0.95 (147)	1.99	29.50
L1	12.9 – 17.7	$1.78^{+0.09}_{-0.09}$	$1.67^{+0.08}_{-0.08}$	$0.69^{+0.09}_{-0.09}$	1.22 (275)	2.06	29.51

Table 4.3: Continuation.

[1]Region	[2]$\text{Time}_{\text{start}} - \text{Time}_{\text{end}}$ (ks)	[3]EM_1 (10^{52} cm^{-3})	[4]EM_2 (10^{52} cm^{-3})	[5]EM_3 (10^{52} cm^{-3})	[6]χ^2_{red} (d.o.f)	[7]f_{X} (10^{-11}erg cm^{-2} s^{-1})	[8]log L_{X}(erg s^{-1})
L2	17.7 – 23.7	$1.81^{+0.08}_{-0.08}$	$1.94^{+0.08}_{-0.08}$	$0.92^{+0.09}_{-0.09}$	1.06 (264)	2.37	29.57
FC	23.7 – 25.8	$1.89^{+0.14}_{-0.14}$	$1.98^{+0.13}_{-0.13}$	$0.55^{+0.14}_{-0.14}$	1.36 (234)	2.20	29.54
FC	25.8 – 26.2	$2.12^{+0.35}_{-0.33}$	$2.22^{+0.31}_{-0.32}$	$0.91^{+0.33}_{-0.32}$	0.99 (121)	2.64	29.62
FC	26.2 – 26.8	$2.12^{+0.30}_{-0.29}$	$2.07^{+0.27}_{-0.27}$	$1.95^{+0.31}_{-0.30}$	1.12 (175)	3.16	29.70
FC	26.8 – 27.9	$1.86^{+0.21}_{-0.21}$	$2.14^{+0.21}_{-0.20}$	$1.44^{+0.23}_{-0.23}$	1.12 (184)	2.81	29.65
FC	27.9 – 28.4	$1.95^{+0.30}_{-0.29}$	$2.15^{+0.29}_{-0.28}$	$1.08^{+0.32}_{-0.30}$	0.91 (142)	2.64	29.62
FC	28.4 – 29.0	$2.33^{+0.28}_{-0.27}$	$1.91^{+0.25}_{-0.25}$	$1.00^{+0.27}_{-0.26}$	0.82 (155)	2.57	29.61
FC	29.0 – 29.6	$2.21^{+0.28}_{-0.27}$	$1.62^{+0.25}_{-0.25}$	$1.47^{+0.28}_{-0.27}$	1.19 (160)	2.63	29.62
FC	29.6 – 30.2	$1.89^{+0.28}_{-0.27}$	$1.98^{+0.27}_{-0.26}$	$0.99^{+0.28}_{-0.27}$	0.99 (156)	2.47	29.59
FC	30.2 – 30.8	$2.00^{+0.27}_{-0.27}$	$2.07^{+0.26}_{-0.25}$	$0.69^{+0.27}_{-0.26}$	0.96 (149)	2.38	29.58
FC	30.8 – 32.1	$2.15^{+0.19}_{-0.19}$	$1.90^{+0.18}_{-0.17}$	$0.54^{+0.18}_{-0.17}$	1.05 (148)	2.24	29.55
FC	32.1 – 33.4	$2.00^{+0.17}_{-0.17}$	$1.73^{+0.16}_{-0.15}$	$0.53^{+0.16}_{-0.15}$	1.15 (190)	2.08	29.52
FC	33.4 – 36.7	$1.82^{+0.10}_{-0.10}$	$1.67^{+0.09}_{-0.09}$	$0.12^{+0.09}_{-0.09}$	1.73 (139)	1.74	29.44

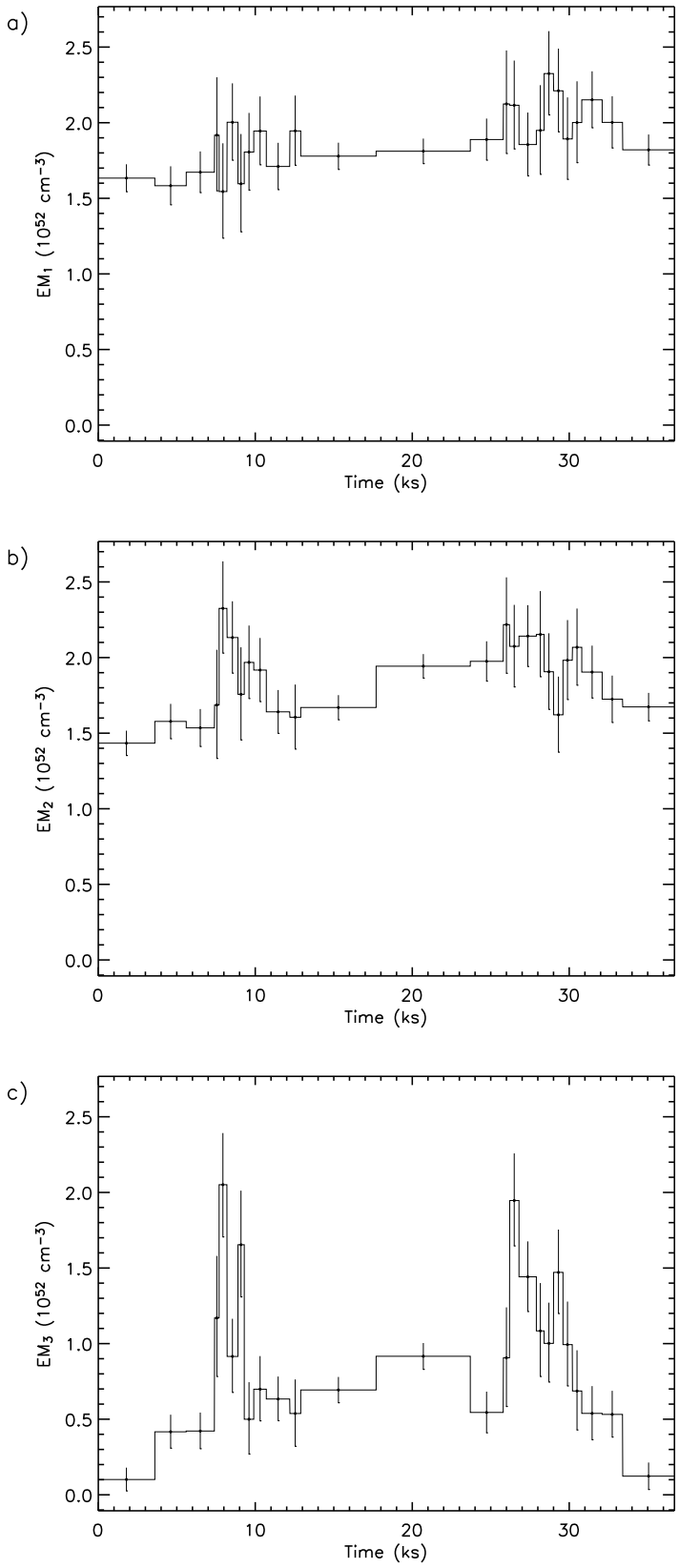

Figure 4.10: Time-evolution obtained for the emission measure of the three thermal components. Note that the time-resolution is the same as that shown in Fig. 4.5.

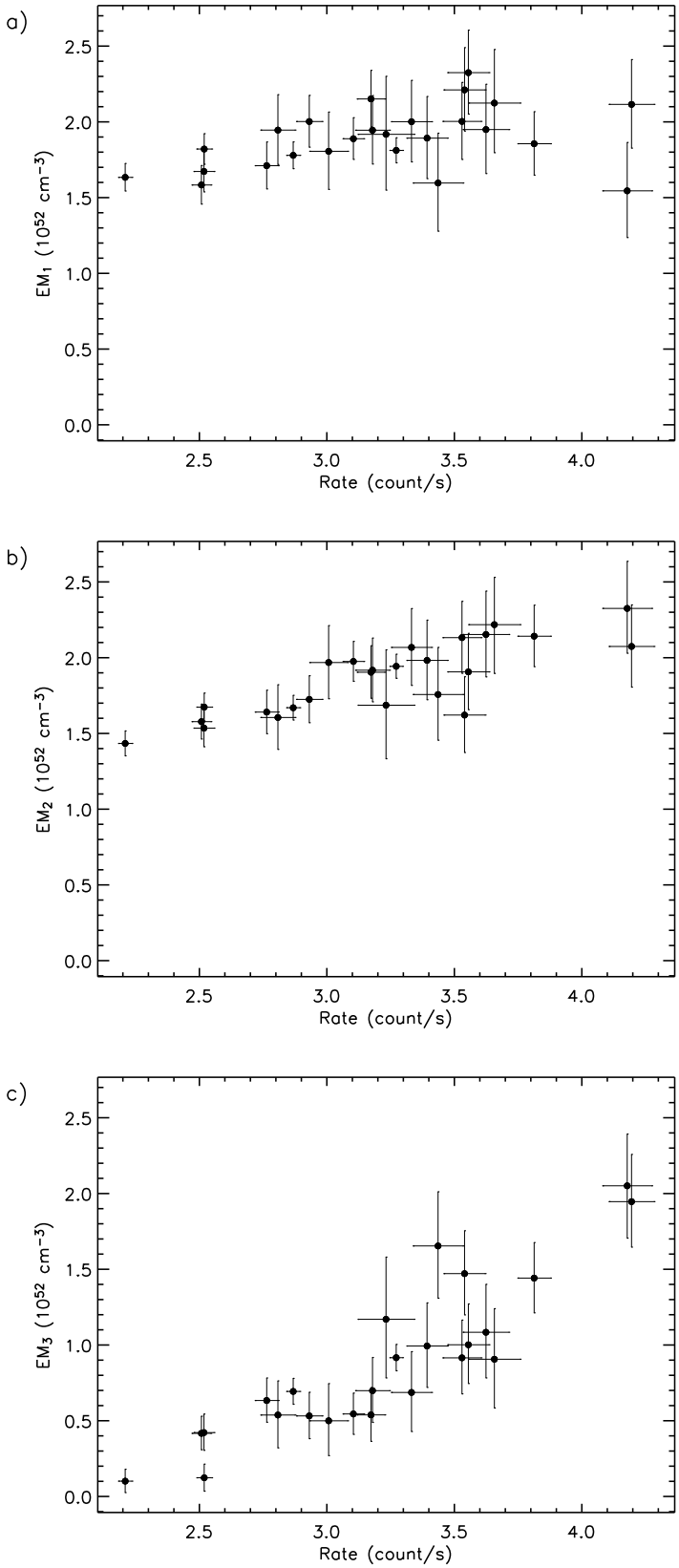

Figure 4.11: Emission measure of the three thermal components vs. count-rate.

cay would slow down this phase and, therefore, the size of the flaring loop would be overestimated. It was shown that the slope (ζ) of the path of the flare decay in the density-temperature ($\log n_{\rm F} - \log T_{\rm F}$) plane mainly depends on the heating decay time (Jakimiec et al. 1992; Sylwester et al. 1993; Reale et al. 1997). Reale et al. (1997) derived an empirical formula using hydrodynamic simulations of single semi-circular flaring loops with constant cross-section, and including the effect of the heating in the decay:

$$L = \frac{\tau_D \sqrt{T_{\rm max}}}{3.7 \times 10^{-4} F(\zeta)} \qquad F(\zeta) \geq 1 \tag{4.2}$$

where L is the loop half-length (in cm), $T_{\rm max}$ the loop maximum temperature (in K), τ_D the e-folding decay time derived from the light curve (in seconds), and $F(\zeta)$ a non-dimensional factor (larger than one) which accounts for the heating in the decay. The slope of the decay path in the density-temperature diagram is maximum (~ 2) if the heating is negligible during the decay, and minimum (~ 0.5) if the heating dominates this phase (Jakimiec et al. 1992). Equation (4.2) was successfully tested on resolved solar flares observed with Yohkoh/SXT (Reale et al. 1997) and has been further extended and applied to several stellar flares observed with a wide variety of detectors (Reale & Micela 1998; Favata et al. 2000a,b,c, 2001; Maggio et al. 2000; Güdel et al. 2001; Stelzer et al. 2002; Briggs & Pye 2003; Reale et al. 2004; Pillitteri et al. 2005; Franciosini et al. 2007). The correction factor $F(\zeta)$ needs to be calibrated for each detector, since it depends on the spectral bandpass and resolution. For EPIC-PN observations, the expression given by Reale (2007) has to be used:

$$F(\zeta) = \frac{c_a}{\zeta - \zeta_a} + q_a \tag{4.3}$$

where $c_a = 0.51$, $\zeta_a = 0.35$, $q_a = 1.36$. Equation (4.3) can be used for slopes in the range $0.35 < \zeta \leq 1.6$.

For stellar flares the density can rarely be directly measured. Nevertheless, since reasonably the soft X-ray flare volume is approximately constant during the flare development, the square root of the emission measure can be used as a proxy for the density (note that $EM_{\rm F} = \int n_{\rm e} n_{\rm H}\, dV_{\rm F} \approx n_{\rm F}^2 V_{\rm F}$ for a totally ionized hydrogen plasma).

As described in § 4.4.1, the analysed flares (FB and FC) only involve the two hottest components of the 3-T model used to fit the spectra. We obtained the flare contribution of each one of these components to the total emission measure ($EM_{2,\rm F}$ and $EM_{3,\rm F}$) by simply subtracting from EM_2 and EM_3 their corresponding value measured for the quiescent state (L0). Therefore, the total emission measure of the flaring plasma ($EM_{\rm F}$) is given by the sum of $EM_{2,\rm F}$ and $EM_{3,\rm F}$. A mean temperature of the flaring plasma ($T_{\rm F}$) was also calculated for each spectrum as a weighted average of the temperature of the two hottest components in the 3-T model, where the respective weights were $EM_{2,\rm F}/EM_F$ and $EM_{3,\rm F}/EM_F$. The resulting $\log EM_{\rm F}^{1/2} - \log T_{\rm F}$ diagram is plotted in Fig. 4.12 for the decay of FB and FC. A linear fit to the data provided a slope of $\zeta = 0.18 \pm 0.27$ for FB and $\zeta = 0.45 \pm 0.08$ for FC, indicating the presence of sustained heating during the decay of both flares. Since the slope for FB is compatible with the lower asymptotic value for which Eq. (4.3) can be applied, we obtained an upper limit for the loop half-length of this flare by using $\zeta = 0.45$. The maximum temperature in the flaring loop ($T_{\rm max}$) can

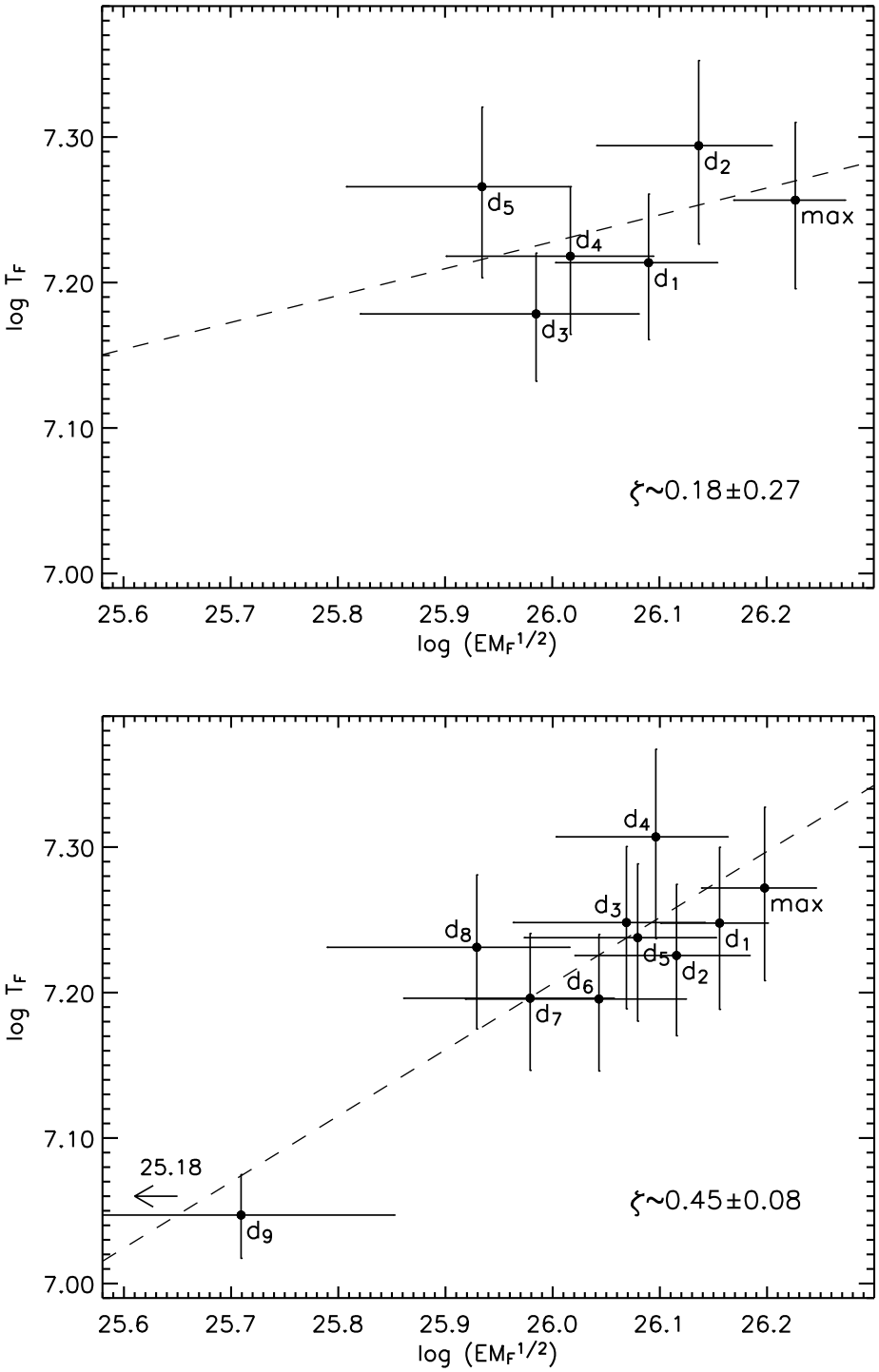

Figure 4.12: Density–temperature (log $n_{\rm F}$ – log $T_{\rm F}$) diagram of the variable component (see text) for the decay phase of flares FB (top panel) and FC (bottom panel). $EM_{\rm F}^{1/2}$ has been used as a proxy for the density. Numbers indicate the time-evolution of the values. The point at the flare maximum (max) is also plotted. For each flare, the dashed line shows the best linear fit to the decay data. The derived slopes (ζ) are also given.

be derived from the maximum observed temperature ($T_{\rm F,max}$). The observed temperature is a kind of average temperature of the flaring loop, which is therefore lower than the loop maximum temperature. The relationship between $T_{\rm max}$ and $T_{\rm F,max}$ depends on the instrumental response. For EPIC-PN, Reale et al. (2004) reported:

$$T_{\rm max} = 0.184 T_{\rm F,max}^{1.130} \tag{4.4}$$

Thus, $T_{\rm max}$ resulted to be 32×10^6 K for FB, and 30×10^6 K for FC, with uncertainties of 16 %.

Using the quantities given above, the values of τ_D shown in Table 4.2, and Eqs. (4.2) and (4.3), we obtained $L < 7 \times 10^9$ cm for the half-length of the loop involved in the flare

Table 4.4: Parameters derived for flares FB and FC.

	Flare FB	Flare FC
[a] $\tau_{\rm D}$ (s)	2850	5960
[b] $L_{\rm X,max}$ (10^{29} erg s^{-1})	2.6	2.6
[c] $E_{\rm X,tot}$ (10^{33} erg)	0.75	1.5
[d] ζ	0.18 ± 0.27	0.45 ± 0.08
[e] $T_{\rm max}$ (10^6 K)	32 ± 5	30 ± 5
[f] L (10^9 cm)	< 7	14 ± 8
[g] p (10^3 dyn cm^{-2})	> 1.7	0.74 ± 0.34
[h] $n_{\rm e}$ (10^{11} cm^{-3})	> 2.0	0.88 ± 0.43
[i] $V_{\rm F}$ (10^{30} cm^3)	< 0.7	3.2
[j] $E_{\rm H}$ (erg s^{-1} cm^{-3})	> 3.7	∼ 0.8
[k] $N_{\rm loops}$	∼ 38	∼ 19
[l] B (G)	> 210	> 140

[a] e-folding decay time derived from the light curve.

[b] Luminosity at the flare peak (0.5 – 10.0 keV band).

[c] Total radiated energy (0.5 – 10.0 keV band).

[d] Slope of the decay path in the density-temperature diagram (see details in § 4.4.2).

[e] Maximum temperature in the loop at the flare peak (see § 4.4.2).

[f] Half-length of the flaring loops (see § 4.4.2).

[g] Maximum pressure in the loop at the flare peak (estimated from the loop scaling laws given by Rosner et al. 1978).

[h] Maximum electron density in the loop at the flare peak. We have assumed a totally ionized hydrogen plasma (i.e., $p = 2 n_{\rm e} k T_{\rm max}$).

[i] Volume of the flaring region (note that $EM_{\rm F} \approx n_{\rm e}^2 V_{\rm F}$ for a totally ionized hydrogen plasma).

[j] Heating rate per unit volume at the flare peak (estimated from the loop scaling laws given by Rosner et al. 1978).

[k] Number of loops needed to fill the flare volume. We have assumed a loop aspect $r/L = 0.1$ for a single loop.

[l] Magnetic field ($p \leq p_B = B^2/8\pi$).

FB, and $L \approx (14 \pm 8) \times 10^9$ cm for that involved in FC.

4.5 Discussion and conclusions

We have presented a detailed study of the X-ray variability that the binary star CC Eri showed during an XMM-Newton observation. The great sensitivity of the EPIC-PN CCD camera allowed us to perform time-resolved spectroscopy of two flares weaker (flux increases of factors 1.5 – 1.9) than those typically analysed in the literature. The maximum luminosity of these flares in the 0.5 – 10.0 keV band was $\approx 2.6 \times 10^{29}$ erg/s.

Results show that, during the analysed observation, the corona of CC Eri is well-described by a 3-T model with constant temperatures (values of 3, 10 and 22 MK) and time-variable emission measures. The emission measure of the coolest component (EM_1) ranges between 1.6 – 2.3 $\times$ 10^{52} cm^{-3}, the one of the second component (EM_2) between 1.4 – 2.3 $\times$ 10^{52} cm^{-3}, and that of the hottest component (EM_3) varies between 0.1 – 2.1 $\times$ 10^{52} cm^{-3}. That is, EM_1 reaches 1.4 times the value measured for the quiescent state, EM_2 varies up to a factor of 1.6, and EM_3 increases up to 21 times its quiescent value. Therefore, the hottest component dominates the X-ray variability observed on CC Eri (see also Fig. 4.10). The changes in the emission measure of the coolest component could be due to the variable aspect of the binary during its orbital motion. However, the changes in the emission measure of the two hottest components are clearly correlated with the variations observed in the light curve during the detected flares (see Figs. 4.10 and 4.11). The results obtained for the two hottest components resemble those reported by Reale et al. (2001) for a sample of solar flares that covered a wide range of intensities and physical conditions. They found that the $EM(T)$ distribution of all the flares in the sample follows a common evolution path: it starts low but already at a relatively high temperature ($\sim 10^7$ K independently of the flare intensity), it grows toward higher EM values during the rising phase and then decreases during the decay, maintaining always a more or less constant shape and peak temperature. In other words, they found that the height of the $EM(T)$ distribution is clearly variable during the different phases of solar flares, while the width and peak temperature of the distribution suffer from much smaller changes. As far as we are concerned, this is the first time that no evident temperature variations are observed in a time-resolved study of stellar flares (see Figs. 4.7 and 4.8). Besides, the fact that the temperatures that characterize the flaring plasma coincide with those of the quiescent state is consistent with a recurrent idea in the literature, that is: the quiescent emission of magnetically active stars may be produced, to a large fraction, by continuous flaring activity (see § 4.1 and references therein). Thus, the light curves of multiple small flares overlap, and only larger flares stand out from the quiescent level. Besides, without temperature variations, differences in the emission measure between time-intervals with diverse count-rate, such as those observed for L0, L1 and L2 (see Fig. 4.1 and Table 4.3), can be identified with differences in the total coronal volume occupied by the flaring plasma. Density variations may also account for the changes in emission measure. However, we expect that, if they were significant, they would be driven by local heating injections or leaks, and therefore coupled to temperature variations but, as discussed above, temperature variations are not detected.

The slope of the path in the density-temperature diagram indicates the presence of significant heating during the decay of the analysed flares, and leads to an upper limit of 7 and 14×10^9 cm, respectively, for the half-length of the flaring loops. From the orbital solution of CC Eri (Amado et al. 2000) and the stellar radius of its components, we obtain a minimum distance between their surfaces of $\sim 1.4 \times 10^{11}$ cm. Even the largest loops involved in the detected flares only cover ~ 10 % of this distance. Therefore, it is likely that the flaring loops are included all in the corona of one of the stars, and do not result from the magnetic fields bridging the two stars. In addition, bearing the spectral type of the stellar components of CC Eri in mind, the ratio between the half-length of the flaring loops and the stellar radius (R_*) would be 0.1 and 0.3 if the flares were produced by the K7.5Ve star, or 0.2 and 0.4 if they were produced by the M3.5Ve star. In both cases, the loop height above the stellar surface ($2L/\pi$ for vertical loops with semi-circular geometry) is about $0.1 - 0.3\ R_*$, implying a relatively compact flaring corona. These results are in agreement with the loop half-lengths derived for other Me dwarfs ($L \leq 0.5\ R_*$; Favata & Micela 2003).

Assuming that at the flare peak the flaring loop is not far from a steady-state condition, and given that the derived loop half-lengths are significantly smaller than the pressure scale height[3], we can apply the so-called RTV scaling laws (Rosner et al. 1978). These relationships link the pressure (p) and the heating rate per unit volume ($E_{\rm H}$) with the loop half-length and the loop maximum temperature. Table 4.4 lists all these quantities for the observed flares. We have also estimated the electron density under the assumption of a totally ionized hydrogen plasma, obtaining $n_{\rm e} \sim 10^{11}$ cm^{-3}. This is compatible with values expected for a plasma in coronal conditions. In order for the electron density to be consistent with the $EM_{\rm F}$ measured at the peak of the analysed flares, the flaring volumes should be as large as 10^{30} cm^3. From the pressure of the flaring plasma (see Table 4.4), we infer that the minimum magnetic field required to confine the plasma at the flare peak is ~ 210 G for FB and ~ 140 G for FC.

To satisfy the energy balance relation for the flaring region as a whole, the maximum X-ray luminosity must be lower than the total input energy rate at the flare peak ($H = E_{\rm H} V_{\rm F}$). The rest of the input energy is used for thermal conduction, kinetic energy and radiation at lower frequencies. From the analysis of a large optical flare on the M3.5Ve star AD Leo, Houdebine et al. (1993) concluded that the total kinetic energy during the event was of the same order as the radiated energy. For both FB and FC, we obtain that $L_{\rm X,max}$ is about 10 % of H, compatible with the X-ray radiation being only one of the energy loss terms during the detected flares. This value is in agreement with those reported for solar flares, where the soft X-ray radiation at the peak only accounts for $10 - 20$ % of the total energy budget (Wu et al. 1986). Reale et al. (2004) found a similar percentage (~ 15 %) for a flare observed on the M5.5Ve star Proxima Centauri, while Favata et al. (2000c) estimated a higher value (~ 35 %) for an extreme X-ray flare detected on the M3.5Ve star EV Lac.

If the detected flares were produced by a single loop, its aspect ($\beta = r/L$, where r is the radius of the loop cross-section derived from the volume and loop length) should be 0.6 for

[3]The pressure scale height is defined as $h_{\rm p} = 2kT_{\rm max}/(\mu g)$, where μ is the average atomic weight and g is the surface gravity of the star. Therefore, $h_{\rm p} \approx 5000 T_{\rm max}/(g/g_\odot)$. Taking the spectral type of the stellar components of CC Eri into account, $h_{\rm p} \geq 7 \times 10^{10}$ cm for both FB and FC.

FB and 0.4 for FC. Such a large cross-section is not observed on solar coronal loops, for which typical values of β are in the range 0.1 – 0.3. Therefore, we suggest a more realistic scenario consisting on flaring structures made up of several similar loops. Assuming $\beta = 0.1$, FB and FC occur in arcades composed of $\sim$ 38 and 19 loops, respectively. Similar structures are also observed to flare on the Sun. For example, the Bastille day flare (2000 July 14) is an intense solar flare (GOES class X6) that occurred on a curved arcade with some 100 post-flare loops (Aschwanden & Alexander 2001; Reeves & Warren 2002). Stellar analogues have been proposed for the Me dwarf Proxima Centauri, where the best description for a flare analysed by Reale et al. (2004) shows the presence of an arcade made up of $\sim$ 5 loops; and also for the younger ($\sim$ 100 Myr) G9 dwarf ZS 76, where Pillitteri et al. (2005) estimated 20 – 30 loops for the flaring arcades. Therefore, we conclude that events like solar arcade flares may be a common phenomenon on stars, in wide generality.

Chapter 5

A detailed study of the rise phase of a long duration X-ray flare in the young star TWA 11B

J. López-Santiago[1], I. Crespo-Chacón[1], G. Micela[2], F. Reale[3,2]

[1] Departamento de Astrofísica y Ciencias de la Atmósfera, Facultad de Ciencias Físicas, Universidad Complutense de Madrid, E-28040 Madrid, Spain

[2] Osservatorio Astronomico di Palermo, Piazza del Parlamento 1, I-90134 Palermo, Italy

[3] Dip. di Scienze Fisiche e Astronomiche – Sez. di Astronomia – Università di Palermo, Piazza del Parlamento 1, I-90134 Palermo, Italy

Originally published in Astrophysical Journal (ApJ) **712**, 78-87 (2010)

Received 23 April 2009 / Accepted 2 February 2010

Abstract

We analysed a long duration flare observed in a serendipitous *XMM-Newton* detection of the M star CD-39 7717B (TWA 11B), member of the young stellar association TW Hya ($\sim$ 8 Myr). Only the rise phase (with a duration of $\sim$ 35 ks) and possibly the flare peak were observed. We took advantage of the high count-rate of the X-ray source to carry out a detailed analysis of its spectrum during the whole exposure. After a careful analysis, we interpreted the rise phase as resulting from the ignition of a first group of loops (event A) which triggered a subsequent two-ribbon flare (event B). Event A was analysed using a single-loop model, while a two-ribbon model was applied for event B. Loop semi-lengths of $\sim 4R_*$ were obtained. Such large structures had been previously observed in very young stellar objects ($\sim$ 1 – 4 Myr). This is the first time that they have been inferred in a slightly more evolved star. The fluorescent iron emission line at 6.4 keV was detected during event B. Since TWA 11B seems to have no disk, the most plausible explanation found for its presence in the X-ray spectrum of this star is collisional- or photo-ionization. As far as

we are concerned, this is only the third clear detection of Fe photospheric fluorescence in stars other than the Sun.

Key words. Stars: activity – Stars: coronae – Stars: flare – Stars: individual (CD-39 7717B, TWA 11B) – Stars: pre-main sequence

5.1 Introduction

Among all the processes manifested in stellar coronae, flares are the most energetic ones. They are supposed to be the result of the energy release from magnetic field reconnection in the lower corona (e.g., Kopp & Pneuman 1976). As a consequence, electrons and ions in the reconnection region are accelerated downward, along the magnetic field lines, toward lower atmospheric layers. When they reach the upper chromosphere, the local gas is heated and evaporated into the new-formed magnetic loops. Thus, the density and temperature of these loops increase, causing intense emission of soft (< 10 keV) X-rays.

Stellar flares have been observed in almost all the H-R diagram (see Vaiana et al. 1981, for a review). However, they are more frequent in late-type stars, where they present a large variety of sizes and durations. In late-K and M dwarfs (the so-called UV Ceti-type stars; see Pettersen 1991, for a description of their main properties), moderate flares are frequently observed. During such events, the X-ray flux usually increases by a factor of $2 - 4$ (e.g., Robrade & Schmitt 2005). Giant flares, in which the X-ray flux increases from dozens to hundreds times the quiescent state value, have been detected in some M dwarfs such as EV Lac (Favata et al. 2000c), EQ Peg (Katsova et al. 2002), and Prox Cen (Güdel et al. 2004). The duration of those flares is of the order of a few kiloseconds, even in the more energetic ones. For instance, the giant flare observed in EV Lac lasted $\sim$ 5 ks. Long-duration flares are more common in pre-main-sequence stars than in the UV Ceti-type ones. For example, during the 13 days observing run of the ORION Nebula Complex (ONC) by *Chandra*, at least 19 flares with durations above half a day were detected (Favata et al. 2005). Long-duration flares were also observed in the Taurus star-forming complex (Franciosini et al. 2007; Stelzer et al. 2007). The longer duration of these events is usually attributed to the presence of larger coronal structures in young stars.

The *XMM-Newton* and *Chandra* missions have contributed enormously to the understanding of the processes involved in the X-ray emission of late-type stars. In particular, the improved temporal and spectral resolutions, together with the development of theoretical models (e.g., Kopp & Poletto 1984; Poletto et al. 1988; Serio et al. 1991; Güdel et al. 1999; Reale et al. 2004; Reale 2007), have provided us with powerful tools for investigating coronal flares. Detailed diagnostics of X-ray flares have been carried out by different authors. Favata et al. (2005) determined general properties of flaring loops, in terms of temperature and semi-length, for young stellar objects in the ONC. From their analysis, the authors inferred loop semi-lengths comparable to the stellar radius in some cases. They speculated that these large structures are connected with the protoplanetary disk and are, in fact, the same structures that channel the plasma producing accretion. A similar work was done for the Taurus star-forming region (Franciosini et al. 2007), where

the authors remarked that some coronal loops extended up to a distance comparable with the stellar radius (see also Giardino et al. 2004). Studies for more evolved stars were done by, e.g., Reale et al. (2004), Crespo-Chacón et al. (2007), and Testa et al. (2007), who found flaring loops with semi-lengths of $\sim 0.2 - 0.5\ R_\star$ (i.e., a relatively compact flaring corona).

In the works presented in the previous paragraph, the diagnostic of X-ray flares was done using the procedure described by Reale et al. (1997, 2004) to model the decay phase, which assumes the flare to be produced in a single loop where heating does not entirely drive the flare decay. Reale (2007) extended this method to the rise phase and compared the parameters determined in this way with those obtained by analysing the decay phase for three stellar flaring loops (see also Pan et al. 1997), finding a good agreement between them. On the other hand, the solar two-ribbon model developed by Kopp & Poletto (1984), or its stellar version (Poletto et al. 1988), should be used when heating totally drives the flare evolution (Reale 2002, 2003). In this model, the reconnection energy is supposed to be dissipated immediately after being released. Kopp & Poletto (1984) assumed that only a fraction of the magnetic energy released by the reconnection process is used to supply the thermal energy of the newly formed flare loops. Poletto et al. (1988) assumed that a factor of 10 % of this thermal energy escapes into the X-ray regime, as suggested by detailed studies of solar flares (Canfield et al. 1980). We also refer the reader to Güdel et al. (1999), who included time-dependent conductive and radiative losses in the X-ray corona self-consistently.

In this work, we analyse an *XMM-Newton* serendipitous observation of the young M-type star TWA 11B in which the X-ray emission suffered a continuous increase during approximately 35 ks. The duration and statistics of the observed rise have allowed us (1) to carry out a detailed spectral time analysis and (2) to derive properties of the star's magnetic configuration by using both the single-loop and the two-ribbon flare models described above.

5.2 Observation and data treatment

The *XMM-Newton* observation (ID 0006220201) was performed in the revolution 197, between 2001 January 4 and 5, for a total duration of 43 ks. The field is centered on the coordinates $\alpha_{2000} = 12^{\rm h}35^{\rm m}34^{\rm s}$ and $\delta_{2000} = -39^\circ54'55''$ (the main target being the Seyfert 2 galaxy NGC 4507). The EPIC cameras were operated in Full Frame mode using the Thick filter. Our target is situated 5.18 arcmin at the northeast of the central source, in the field of view of both the MOS and PN detectors. The EPIC-*XMM* source coincides with the position of the optical counterpart of TWA 11B. The primary star, TWA 11A (an A0-type star), is situated at $\sim$ 8 arcsec from TWA 11B. Although none X-ray emission is expected from an A0 star, we investigated the possibility that the primary star produced some X-rays that could affect our results. We studied a serendipitous detection of HETG *Chandra* of the source (Observation ID 2150). In this 140 ks exposure *Chandra* observation, the X-ray source is clearly identified with TWA 11B (see Fig. 5.1), while none X-ray emission coming from TWA 11A is detected. Therefore, we are confident that the X-ray emission detected in the *XMM-Newton* observation comes only from the M

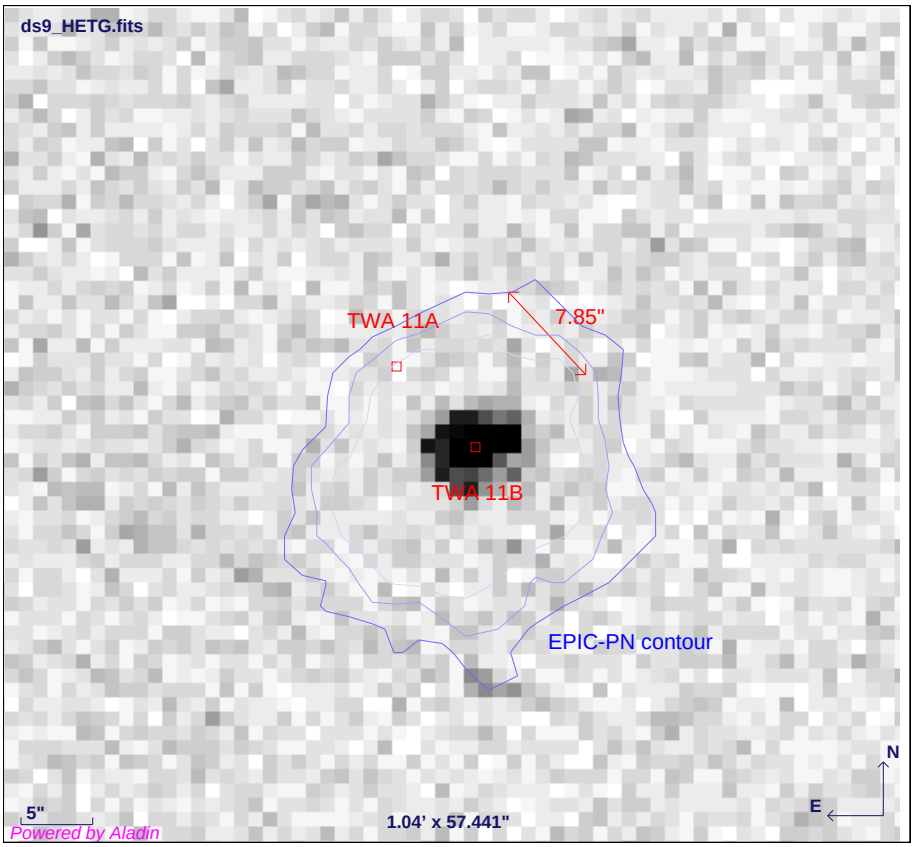

Figure 5.1: *Chandra* HETG serendipitous detection of TWA 11B. The position of the optical counterparts of TWA 11A and TWA 11B is marked. Contours of the PSF observed in the *XMM-Newton* EPIC exposure are overplotted.

star TWA 11B.

The data reduction followed the standard operating procedure. We used the version 7.1.0 of the *XMM-Newton* Science Analysis System (SAS) to derive a table of calibrated events in the energy range 0.3 – 10.0 keV. To extract the events, we chose a radius of 30 arcsec, which is slightly larger than the 3σ level of the source's point-spread function (PSF). This assures us to lose less than 1% of the counts from the source. Different filters were applied to eliminate bad events and noise. Note that the observation was neither affected by pile-up nor by high flaring background periods.

The X-ray light curve (Fig. 5.2) showed a total increase in the star's count-rate of a factor of 4.2 from the lower level (≈ 0.25 counts s^{-1}) to the maximum observed emission. Similar relative increases in flux were previously reported in flares from other stars (e.g., Robrade & Schmitt 2005). A first increase in the light curve is observed 5 ks after the beginning of the observation, reaching a local maximum only 5 ks later. After a brief decrease, the count-rate continues increasing until reaching the global maximum in the light curve (this happened 37 ks after the beginning and only 3 ks before the end of the observation). The total duration of the enhancement is 32 ks ($\approx$ 9 hr).[1] Note that the

[1]The rotation period of TWA 11B is not known. Scholz et al. (2007) measured a projected rotational

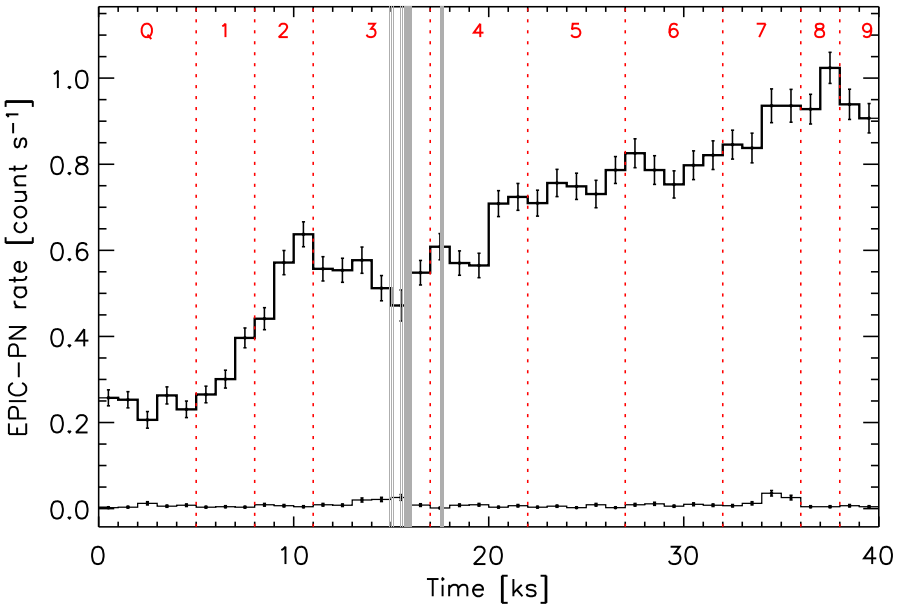

Figure 5.2: EPIC-PN light curve of TWA 11B in the energy range 0.3 – 10.0 keV. The curve was binned to a 1 ks time resolution. The event list was corrected for bad events and noise. The exposure was also corrected of live-time and good-time intervals. The gray segments mark the periods in which the instrument was turned off. The continuous line at the bottom is the background light curve. The time blocks used in the spectral analysis are plotted as dashed vertical lines.

observed maximum may or may not be the flare peak. In the latter case, the duration of the rise phase would be even longer.

In Fig. 5.3 we plot the evolution of the hardness ratio, which is a tracer of the temperature evolution, during the observation. Here, the soft energy band is defined as the range 0.3 – 0.8 keV and the hard energy band as 0.8 – 4.5 keV. Fig. 5.3 shows that the mean coronal temperature reached a maximum at $t \sim 7$ ks, maintained high with significant fluctuations during approximately the next 27 ks of exposure, and then it began to decrease gradually.

Overall, the rise phase is unusually long compared with those observed in other stars (e.g., Pan et al. 1997; Güdel et al. 1999; Reale 2002; Robrade & Schmitt 2005; Reale 2007; Crespo-Chacón et al. 2007). To date, so long rise phases have been observed only in some T Tauri stars (Favata et al. 2005; Giardino et al. 2006; Franciosini et al. 2007), some of them with accretion disks, and several RS CVn systems (Testa et al. 2007; Nordon & Behar 2007). In such stars, the relative increase in flux ranges from a factor 3 (V410 Tau; Franciosini et al. 2007) to a factor 10 (V892 Tau; Giardino et al. 2004) with rise-phase times from 8 to 55 ks. TWA 11B is a weak-line T Tauri M2.5 star with an age of $\sim$ 8 Myr (estimated from its membership in the TW Hya Association). While it shows no

velocity $v \sin i = 12.11 \pm 0.93$ km s^{-1}, which leads to an upper limit in the rotational period of 2.7 days. Thus, the observation cover, at least, 17% of the rotational period of the star. Nevertheless, no indication of occultation of the flaring region is observed.

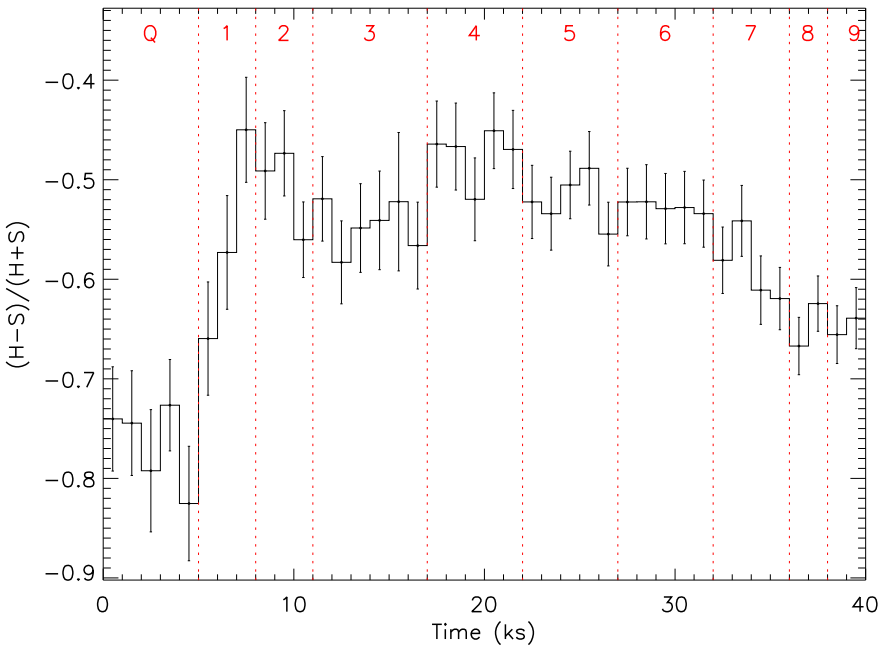

Figure 5.3: Hardness ratio evolution of TWA 11B during the observation with EPIC-PN. The time blocks used in the spectral analysis are plotted as in Fig. 5.2 for clarity.

signatures of an accretion disk (near-infrared color excess or strong Hα emission; Stauffer et al. 1995), it is still contracting. Thus, physical conditions in its atmosphere should be more similar to those of sub-giant stars than of the main-sequence ones. This may be the reason why long duration rise phase flares are observed in both T Tauri stars and RS CVn systems.

A more detailed inspection of the light curve shows that the emission increased faster initially, it had a well-defined local maximum at $t \approx 10$ ks, and then it grew again, but more gradually this time, until the end of the observation. At the very end, there is a hint that the emission stopped increasing. Such a long rise phase suggests that we observed an uninterrupted sequence of flare events involving an extended coronal region. However, the faster initial rise and the local emission peak – coupled with the earlier hardness ratio peak – resembles the evolution of a self-standing flaring episode possibly occurring (at least during these initial stages) in a single loop (e.g., Reale 2007), whose decay merged with the ignition of the later overlapping events. Fig. 5.4 demonstrates that this peak is indeed significative and cannot be attributed to the effect of noise in the light curve. This figure shows the cumulative distribution of counts for 200 simulated constantly increasing light curves[2] (for $t \geq 5$ ks) with Poissonian noise (shadowed region) together with the cumulative distribution of counts observed during the rise (continuous line). Clearly, the simulations do not reproduce the observed distribution of counts for the first peak in the light curve. The differences are high enough to justify the treatment of this event as

[2]Constantly increasing light curves have been chosen for the simulations since the global enhancement mostly shows a linear pattern.

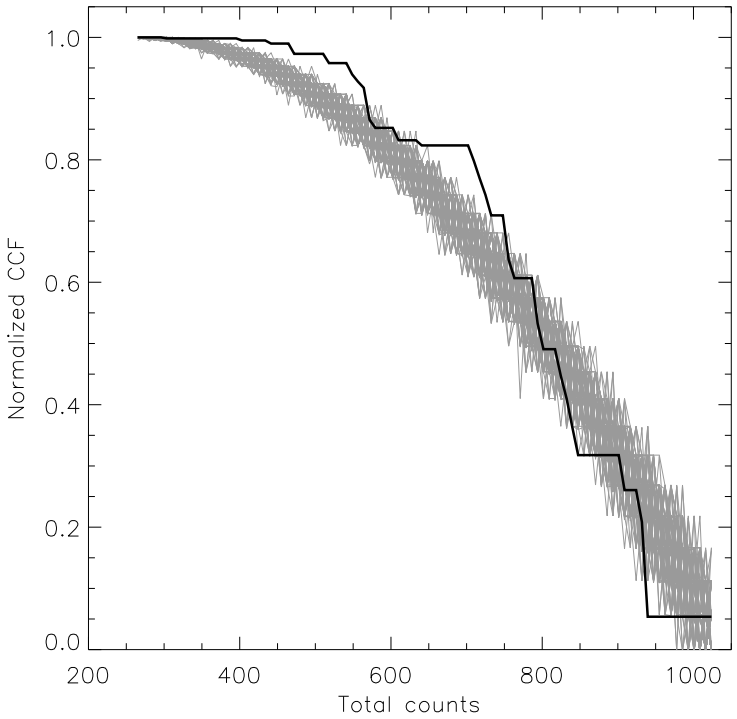

Figure 5.4: Normalized cumulative distribution of counts in the light curve of TWA 11B for $t \geq 5$ ks (continuous line). The shadowed region contains cumulative curves of 200 simulated constantly increasing light curves (also for $t \geq 5$ ks) with Poissonian noise.

independent. In the following, we work under this hypothesis.

The large number of counts collected from the source in the EPIC cameras allowed us to divide the observation in several time intervals with enough signal to perform a reliable spectral analysis (≥ 1000 counts in the quiescent and intervals 1 and 2, and ≥ 2000 counts in the remainder intervals after background subtraction[3]). This permitted (1) to investigate the nature of the processes taking place in our target and (2) to derive physical properties of it.

5.3 Spectral analysis

For the spectral analysis, the observation was split into 10 time intervals (vertical dashed lines in Fig. 5.2). These intervals sample different features in the light curve. We used the XSPEC spectral fitting package (Arnaud 1996, 2004) in the PN, MOS1, and MOS2 detectors simultaneously. We adopted the Astrophysical Plasma Emission Code (APEC, Smith et al. 2001a) included in the XSPEC software. APEC calculates spectral models for hot, optically thin plasmas using the Astrophysical Plasma Emission Database (APED, Smith et al. 2001b), that contains the relevant atomic data for calculating both the continuum and

[3]Intervals 1 and 2 have been studied separately to investigate the evolution of the parameters of the flaring plasma in its very first phases.

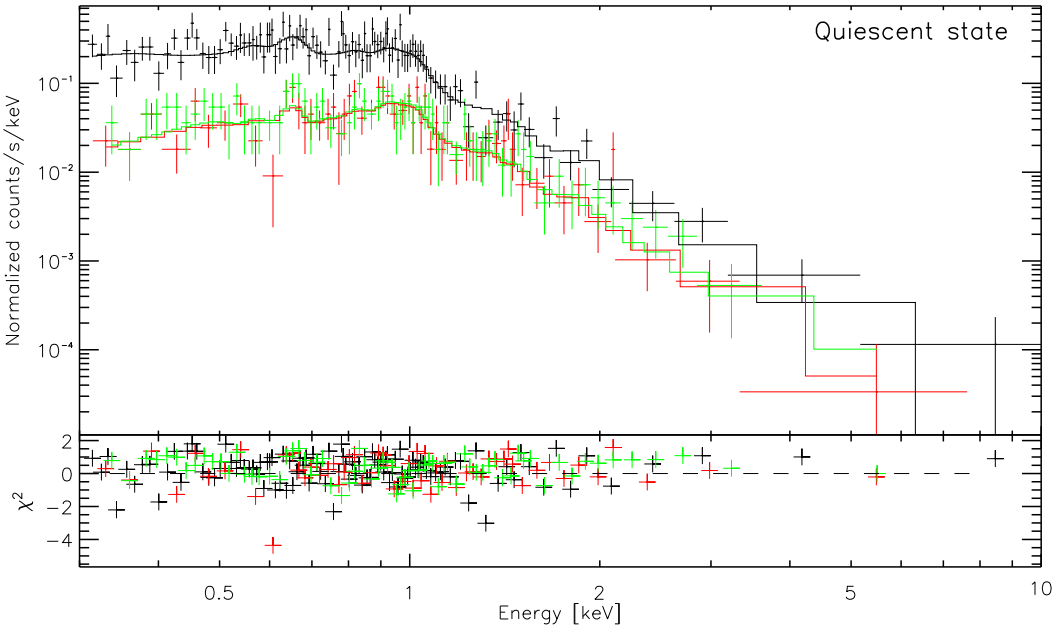

Figure 5.5: Observed EPIC-PN and MOS spectra of TWA 11B during the quiescent state (marked with Q in Fig. 5.2).

line emission. Interstellar absorption was taken into account using the interstellar photoelectric absorption cross-sections of Morrison & McCammon (1983), also available in XSPEC.

5.3.1 Quiescent state

The lowest (constant) count-rate level, found at the beginning of the observation, is assumed to be the quiescent state. The X-ray luminosity of the star during this lapse of time (assuming the same distance than the primary $d = 67 \pm 3$ pc) is $\log L_{\rm X}[{\rm erg\,s^{-1}}] = 29.35$, corresponding to $\log(L_{\rm X}/L_{\rm bol}) = -3.1$. These values are typical of both pre-main-sequence star members of young stellar associations (e.g., Kastner et al. 2003) and older field M dwarfs showing high X-ray activity (Robrade & Schmitt 2005; Crespo-Chacón et al. 2007). The best fit to the X-ray quiescent spectrum (Fig. 5.5) is given by a plasma model with two equally weighted thermal components (the output parameters of this fit are summarized in Table 5.1). Although high uncertainties are obtained for the hydrogen column density in our fit, the value of $N_{\rm H}$ obtained by us is very similar to that determined for other members of the TW Hya Association (e.g., Stelzer & Schmitt 2004; Argiroffi et al. 2005). Besides, the interstellar extinction was found to be negligible in the general direction of TW Hya (Rucinski & Krautter 1983).

Table 5.1: Output parameters from fitting the X-ray EPIC spectra of the quiescent state with a $2T$ model.

$N_{\rm H}$	=	$1.7^{+2.6}_{-1.7} \times 10^{20}$ cm^{-2}
Z	=	$0.17^{+0.08}_{-0.06}$ $Z_{\odot}$
kT_1	=	$0.27^{+0.03}_{-0.03}$ keV
EM_1	=	$2.2^{+1.4}_{-0.8} \times 10^{52}$ cm^{-3}
kT_2	=	$0.98^{+0.08}_{-0.08}$ keV
EM_2	=	$2.2^{+0.6}_{-0.5} \times 10^{52}$ cm^{-3}
$\chi^2_{\rm red}$ (d.o.f.)	=	0.86 (176)

5.3.2 Flaring state

Synthesized stellar-like spectra of solar flares (previously subtracted by the quiescent "background" spectrum) are generally well fitted with a single thermal component ($1T$ model, see Reale et al. 2001). Consequently, to analyse physical properties of the flaring plasma in our observation, we first subtracted the spectrum of the quiescent state from the observed spectrum in each time interval. Then we fitted a $1T$ model, leaving its temperature ($kT_{\rm F}$) and emission measure ($EM_{\rm F}$) as free parameters. The values of the column density ($N_{\rm H}$) and abundance (Z) were fixed to those derived for the quiescent state. With this technique, we interpret that the coronal spectrum during the flare results from adding to the quiescent spectrum a third thermal component, which is ascribed to heated material filling the flaring loops (Reale et al. 2001; Crespo-Chacón et al. 2007). Models with additional temperature components were checked, but did not improve the fit results significantly.

Results from spectral fitting are given in Table 5.2. As expected from the hardness ratio evolution (Fig. 5.3), the temperature peaked in time segment 1. Then, it decreased gradually but almost continuously until the end of the observation. On the other hand, the emission measure increased continuously from the beginning of the rise and starts to decrease only near the end of the observation.

Evolution of the emission measure distribution

In order to approximate physically more realistic continuous emission measure distributions (EMDs) of the plasma, we used a multi-temperature model as in Robrade & Schmitt (2005). In that work, the authors used a $6T$ model on a logarithmic, almost equidistant grid with temperatures fixed at 0.2, 0.3, 0.6, 1.2, 2.4, and 4.8 keV (which correspond to 2.3, 3.5, 7.0, 14.0, 28.0, and 56.0 MK), sampling those spectral regions where the *XMM-Newton* detectors are more sensitive. To fit our spectra, the values of $N_{\rm H}$ and Z were fixed to those previously determined for the quiescent state. Thus, the only variables are the emission measures. Note that in this case we are fitting each spectrum as a whole (i.e., the quiescent spectrum was not subtracted from the rest of the spectra). Results from

Table 5.2: Spectral results for the flaring component in each time segment of the light curve (except the quiescent time interval).

Time segment	Time interval (ks)	Central time (ks)	$kT_{\rm F}$ (keV)	$\rm EM_F$ (10^{52} cm^{-3})	$\chi^2_{\rm red}$ (d.o.f.)
1	5 – 8	6.5	8^{+60}_{-4}	$0.72^{+0.20}_{-0.17}$	1.05 (129)
2	8 – 11	9.5	$2.4^{+0.4}_{-0.3}$	$4.0^{+0.3}_{-0.3}$	0.87 (215)
3	11 – 17	14	$2.5^{+0.4}_{-0.3}$	$3.88^{+0.27}_{-0.28}$	1.08 (369)
4	17 – 22	19.5	$2.27^{+0.25}_{-0.27}$	$5.3^{+0.3}_{-0.3}$	0.87 (355)
5	22 – 27	24.5	$1.88^{+0.14}_{-0.14}$	$7.2^{+0.3}_{-0.3}$	0.89 (406)
6	27 – 32	29.5	$1.66^{+0.18}_{-0.08}$	$8.3^{+0.3}_{-0.3}$	1.03 (430)
7	32 – 36	34	$1.31^{+0.05}_{-0.05}$	$9.2^{+0.4}_{-0.4}$	0.97 (379)
8	36 – 38	37	$1.22^{+0.06}_{-0.06}$	$9.9^{+0.5}_{-0.5}$	1.01 (243)
9	38 – 41	39.5	$0.99^{+0.04}_{-0.04}$	$9.7^{+0.4}_{-0.4}$	0.86 (313)

applying this $6T$ model to our observation are shown in Table 5.3 and Fig. 5.6, and are summarized in the following items:

- The amount of plasma emitting at temperatures above 28 MK is negligible in the quiescent state.

- Plasma emitting at the highest temperatures ($\sim$ 56 MK) appears at the beginning of the first (faster) rise (time segment 1), while the rest of the EMD curve remains as in the quiescent state. Note that in this time segment we obtained the maximum temperature for the flaring component when fitting it with the $1T$ model (see first part of § 5.3.2 and Table 5.2).

- The only significant difference between the EMD of the quiescent state and that derived for time segment 2 (where the light curve of the first flare peaks) is an excess of plasma emitting at temperatures around 28 MK. We interpret it as the cooling of the material at higher temperatures that was detected in time segment 1 together with additional plasma evaporated after the temperature peak was reached in time segment 1 (note that the total emission measure of the flaring component in time segment 2 is higher than that measured in time segment 1, as it can also be seen in Table 5.2).

- The excess of plasma emitting in the region around 28 MK that was observed in time segment 2 continues cooling toward lower temperatures during time segment 3. At the same time, a high quantity of plasma appears again at the highest temperatures ($\sim$ 56 MK). This quantity is even larger than that measured in time segment 1 and is approximately coincident with the beginning of the second (more gradual) rise.

Table 5.3: Output parameters (emission measures, in units of 10^{52} cm^{-3}) from fitting the whole X-ray EPIC spectra to a 6T model with temperatures fixed at 0.2, 0.3, 0.6, 1.2, 2.4, and 4.8 keV. EM'_1 is the emission measure corresponding to the thermal component of 0.2 keV, EM'_2 is that of 0.3 keV, and so on. Uncertainties are calculated for a 2.7σ confidence level.

Time Interval	EM'_1	EM'_2	EM'_3	EM'_4	EM'_5	EM'_6
Quiescent	$1.00^{+0.88}_{-0.91}$	$1.00^{+1.28}_{-1.00}$	$0.77^{+0.61}_{-0.59}$	$1.63^{+0.26}_{-0.28}$	$0.00^{+.....}_{-0.00}$	$0.00^{+0.09}_{-0.00}$
1	$0.66^{+0.80}_{-0.66}$	$0.59^{+1.51}_{-0.59}$	$0.75^{+0.63}_{-0.75}$	$1.85^{+0.63}_{-0.72}$	$0.00^{+1.04}_{-0.00}$	$0.85^{+0.29}_{-0.30}$
2	$0.13^{+1.24}_{-0.13}$	$2.14^{+0.96}_{-2.14}$	$0.31^{+1.15}_{-0.31}$	$2.12^{+1.15}_{-0.97}$	$3.70^{+0.66}_{-2.17}$	$0.00^{+1.23}_{-0.00}$
3	$1.31^{+0.61}_{-1.09}$	$0.22^{+1.58}_{-0.22}$	$2.04^{+0.48}_{-0.78}$	$2.73^{+0.54}_{-0.60}$	$0.00^{+0.61}_{-0.00}$	$1.91^{+0.29}_{-0.28}$
4	$0.85^{+0.98}_{-0.84}$	$1.88^{+0.88}_{-1.88}$	$0.01^{+0.92}_{-0.01}$	$4.48^{+0.92}_{-0.88}$	$1.32^{+1.86}_{-1.32}$	$1.48^{+1.39}_{-1.08}$
5	$0.54^{+1.07}_{-0.54}$	$2.42^{+2.40}_{-2.11}$	$0.62^{+1.02}_{-0.62}$	$5.19^{+1.17}_{-0.60}$	$1.69^{+1.89}_{-1.69}$	$1.41^{+1.06}_{-1.07}$
6	$0.92^{+1.20}_{-0.92}$	$1.94^{+1.14}_{-1.94}$	$0.96^{+1.04}_{-0.96}$	$5.41^{+1.08}_{-1.22}$	$2.53^{+1.01}_{-2.17}$	$1.01^{+1.22}_{-1.01}$
7	$1.26^{+1.46}_{-1.24}$	$1.36^{+2.32}_{-1.36}$	$1.30^{+1.06}_{-1.25}$	$8.35^{+1.24}_{-1.49}$	$0.86^{+1.75}_{-0.86}$	$0.58^{+0.82}_{-0.58}$
8	$2.64^{+1.17}_{-2.64}$	$0.25^{+4.07}_{-0.25}$	$3.39^{+1.01}_{-2.00}$	$8.17^{+1.38}_{-2.07}$	$0.09^{+2.40}_{-0.09}$	$0.81^{+0.60}_{-0.81}$
9	$1.38^{+1.32}_{-1.38}$	$0.83^{+2.90}_{-0.83}$	$4.08^{+1.08}_{-1.66}$	$8.39^{+0.98}_{-1.02}$	$0.00^{+0.82}_{-0.00}$	$0.23^{+0.40}_{-0.23}$

- During time segments 4 – 7, the amount of plasma emitting at the highest temperatures remains still high, while a large excess of material (compared to the quiescent state) appears also between 7 and 28 MK (reaching the maximum always at a temperature $\approx$ 14 MK). The existence of intense, sustained heating is needed to explain the maintenance of plasma at temperatures around 56 MK. The evolution of the rest of the EMD curve can be interpreted as the cooling of the continuously new appearing very hot plasma together with heated material that evaporates from lower layers and fills the flaring loops.

- During time segments 8 and 9 the emission at temperatures $\gtrsim$ 28 MK turns back to the level found at the quiescent state, which is an indication of the strong heating not being present any more. However, the height of the maximum in the EMD curve is even larger than in the previous time segments, appearing also excess emission at even lower temperatures (down to $\sim$ 3 MK).

5.4 Flare modeling

Results from § 5.2 and § 5.3 support the idea of the observed rise ($t \geq 5$ ks) being the consequence of two separate flare events: the first more impulsive one (event A) starting in time segment 1, followed by a more gradual energy release (event B) having a beginning that is merged with the decay phase of event A and becoming dominant at the end of time segment 3. But, what kind of magnetic structures is producing each one of these events? According to Reale (2007), multiple loop structures can be involved in a flare,

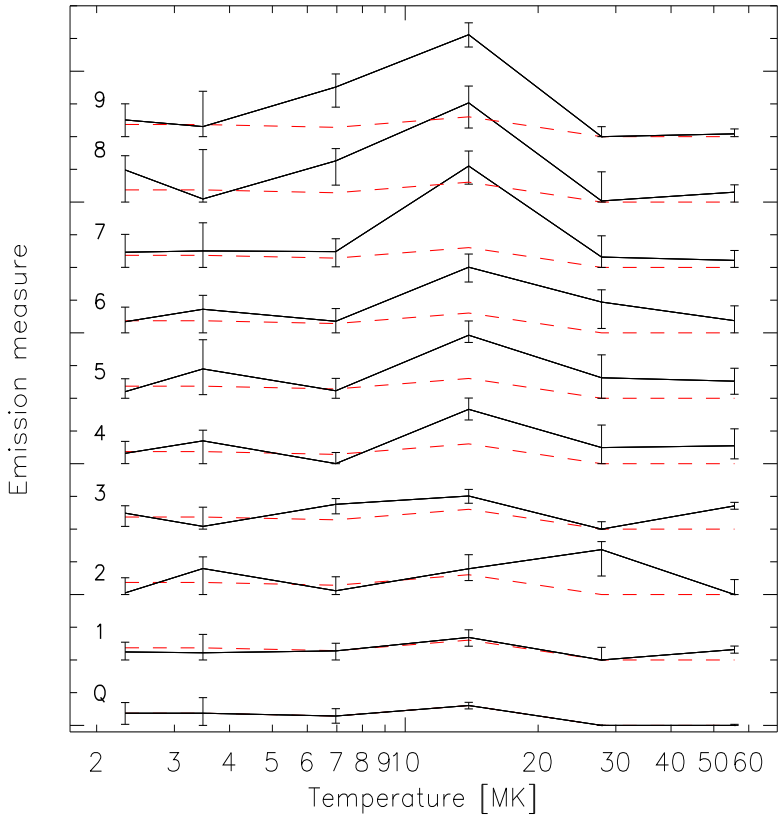

Figure 5.6: EMDs as derived with the 6T model. The curves are shifted in the y-axis to better observe the flare evolution in time. Each one of the EMDs (shown as continuous lines) is labeled with the same number as its corresponding time segment (see Table 5.2). The quiescent is marked as Q. For comparison, the EMD of the quiescent state is also overplotted as a red, dashed line at the same zero level than each one of the rest EMDs.

but this frequently occurs only in its late phases. The initial phases of an X-ray flare are usually quite localized and one can reasonably assume the presence of a single dominant loop (e.g., Aschwanden & Alexander 2001; Reale et al. 2004). This assumption is realistic enough in most of the observed rise phases, where the impulsive heating typically involves a dominant loop (while later residual heating may be released in other similar adjacent loops). The clear evidence of a delay between the temperature peak and the density peak is consistent with a single-loop model, at least until the moment in which this maximum density is reached. This delay is often observed both in solar flares (e.g., Sylwester et al. 1993) and in stellar flares (e.g., van den Oord et al. 1988; van den Oord & Mewe 1989; Favata et al. 2000c; Maggio et al. 2000; Stelzer et al. 2002), even in very long ones (Favata et al. 2005; Getman et al. 2008). The presence of this delay is indeed a signature of a relatively short heat pulse (the larger the delay, the shorter the heat pulse is) and of the coherent hydrodynamic evolution of plasma confined in a loop. Arcades and two-ribbon flares are instead characterized by strong and/or lasting heating (Kopp &

Poletto 1984) and/or irregular light curves (Aschwanden & Alexander 2001; Reale et al. 2004). Thus, event A is likely characterized (or dominated) by a single flaring loop since its ignition occurs only at time segment 1 (as suggested by the plasma appearing at very high temperatures in its corresponding EMD, see § 5.3.2) and shows a delay between the temperature peak and the density peak reached by the flaring plasma in it (see Table 5.2). Event B is probably triggered by event A. The evolution of the whole EMD during event B evidences continuous, but decreasing in efficiency, heating of material and is consistent with event B being a two-ribbon flare. In § 5.4.2, we demonstrate that the light curve of event B is indeed well-reproduced by a two-ribbon flare model. Continual reconnections in an arcade may also be responsible for event B. However, in this case one would expect a more irregular pattern in the light curve than that observed in Fig. 5.2, and the EMD evolution would not necessarily point to a kind of heating that is decreasing in efficiency with time, as we have observed.

5.4.1 Event A: the single-loop flare

We used the results from fitting the spectra with the $1T$ model (see § 5.3), given in Table 5.2, to determine the length of the loop involved in event A. For the temperature in time segment 1, we used $kT = 4$ keV (the lower limit from the fit) since its upper limit is undetermined (see Table 5.2).

For this event, the complete rise phase is observed and instead we miss satisfactory information from the decay phase. A complete theoretical analysis of the rise phase of a flare occurring in a single loop is given by Reale (2007). The author showed that the loop half-length (L) can be determined from the maximum temperature reached by the flaring plasma (T_0) and the temperature and time in which the density peaks (T_M and t_M, respectively) by

$$L \approx 3 \times 10^{5/2} t_\mathrm{M} \frac{T_0^{5/2}}{T_\mathrm{M}^2}, \tag{5.1}$$

where all the parameters are given in c.g.s. units. The maximum temperature (T_0) is related to the temperature measured for the flaring component by spectral fitting (T_obs). For the EPIC instrument,

$$T_0 = 0.13 T_\mathrm{obs}^{1.16}. \tag{5.2}$$

For event A, the maximum temperature and maximum emission measure were reached in the time segments 1 and 2, respectively. For a single-loop description, the (square root of the) emission measure becomes a good proxy of the density, because the loop volume presumably does not change much during the event. In this case, from Eq. 5.1 we obtain a loop half-length $L = 1.8 \pm 0.3 \times 10^{11}$ cm, i.e., $\sim 4 \pm 1\ R_\star$ (assuming a stellar radius $R_\star = 0.64\ R_\odot$ – from the pre-main-sequence models of Siess et al. 2000, for an M2.5 star with 8 Myr, such as TWA 11B is supposed to be). Although this value is relatively large, similar loop sizes have already been derived for young stars in star-forming regions (Favata et al. 2005; Franciosini et al. 2007). As far as we are concerned, this would be the first time that such a relatively long loop is detected in a star older than 3 – 4 Myr.

Table 5.4: Parameters of the flaring loop involved in event A, derived as in Reale (2007). We have assumed a semi-circular geometry.

Parameter	Units	Value
$n_{\rm M}$	10^{10} cm^{-3}	2.0 ± 0.7
$n_{\rm avg}$	10^{10} cm^{-3}	4.1 ± 0.7
V	10^{31} cm^{3}	2.3 ± 0.8
A	10^{20} cm^{2}	0.6 ± 0.2
r	10^{10} cm	0.4 ± 0.1
L	10^{11} cm	1.8 ± 0.3

This loop would fill a volume $V \approx 2.3 \times 10^{31}$ cm^3 (see Reale 2007, for further details on the relations used for determining this quantity). Assuming a semi-circular geometry, its aspect (r/L, with r being the loop cross-section) would be of the order of 2 %, which is quite lower than that observed in the Sun ($\sim$ 10 %), but compatible with the results in Favata et al. (2005). In Table 5.4, we summarize the main parameters of the loop involved in event A, i.e., those already mentioned and maximum density at the loop apex ($n_{\rm M}$), average density in the loop when the maximum density is reached at the apex ($n_{\rm avg}$) and the cross-sectional area of the loop (A). Such parameters were determined with the relations given in Reale (2007).

Comparing our results with those obtained by Reale (2007) for events observed in Algol, AB Dor, and Prox Cen, we conclude that (1) our densities seem to be similar to those determined in the Algol and Prox Cen flares and that (2) the loop volume and its subtended area are of the same order of magnitude as those found for Prox Cen, another M star. Note that the largeness of some of the errors shown in Table 5.4 is a consequence of the propagation of errors in the equations.

For the sake of completeness, we made the exercise to repeat the same analysis to the entire flare event (A+B) as if it all occurred in a single loop. For a flare temperature peaking in time segment 1 ($t_0 \approx 6.5$ ks), and the density peaking in time segment 8 ($t_{\rm M} \approx 37$ ks), using Eq. 5.1, we obtained $L = 1.3 \times 10^{13}$ cm, i.e. $L \sim 260 R_\star$. Obviously, such a long loop would be easily destroyed by the stellar rotation. Clearly, this result makes no sense.

5.4.2 Event B: the two-ribbon flare

For the study of event B, we used the two-ribbon flare model by Kopp & Poletto (1984) extended to the stellar case (Poletto et al. 1988). This model supposes that a disruptive event opens a loop arcade, being the open field lines then driven toward a radial neutral sheet (above the magnetic neutral line) where they reconnect at progressively higher altitudes. Thus, the continuous heating provided by these reconnections is capable of reproducing the temporal profile of the energy rate released during both the rise and decay phases of a two-ribbon flare. By analogy to that observed on the Sun, the model considers that the

arcade of loops is extended along the east–west direction (i.e., axial symmetry around the polar axis is assumed). It also assumes that the magnetic field is potential between the stellar surface and the location of the neutral line and extends radially outward from there. The magnetic field in the meridional planes of the arcade can therefore be expressed in terms of a single lobe of a Legendre polynomial of degree n. Note the following:

i Each lobe is latitudinally bounded by radial magnetic fields.

ii The arcade corresponds to one lobe axisymmetrically continued over some longitude in the east–west direction.

iii Through an appropriate choice of n, one can find a lobe placed in the range of latitudes covered by the active region. However, as spatial information is available only for the Sun, stellar flaring regions are generally assumed to be centered on the equator for odd n and to end at the equator for even n.

iv As stellar observations cannot provide any information on the time-dependent rise of the neutral point, it is assumed to mimic the solar case. Thus, it follows an exponential law of the form given by Eq. 5.3, where y is the height of the neutral point (in units of $R_\star$, measured from the star's center), t is the time (measured from the beginning of the two-ribbon flare, $t_{\rm ini}$), t_0 is a time constant, and $H_{\rm m}$ is the maximum height reached by the reconnection point during its upward movement (measured from the star's surface). $H_{\rm m}$ is typically chosen to be equal to the latitudinal extent of the arcade, which is in turn linked with n (see Eqs. 5.4 and 5.5):

$$y = 1 + \frac{H_{\rm m}}{R_\star}(1 - e^{-\frac{t}{t_0}}) \tag{5.3}$$

$$H_{\rm m} \approx \frac{\pi}{n + 1/2} R_\star \qquad \text{for } n > 2 \tag{5.4}$$

$$H_{\rm m} \approx \frac{\pi}{2} R_\star \qquad \text{for } n = 2 \tag{5.5}$$

Under all these assumptions, the rate of magnetic energy released by the reconnecting arcade per radian of longitude (dE/dt) can be expressed as

$$\frac{dE}{dt} = \frac{1}{8\pi} 2n(n+1)(2n+1)^2 R_\star^3 B_{\rm m}^2 \times \frac{I_{1,2}(n)}{P_n^2(\theta_{1,2})} \frac{y^{2n}[y^{2n+1} - 1]}{[n + (n+1)y^{2n+1}]^3} \left(\frac{dy}{dt}\right), \tag{5.6}$$

where $I_{1,2}(n) = \int P_n^2(\theta) {\rm d}(\cos\theta)$ evaluated between the latitudinal borders of the lobe, $P_n(\theta)$ is the Legendre polynomial of degree n, θ is the co-latitude, $\theta_{1,2}$ is the co-latitude of either boundary of the lobe, and $B_{\rm m}$ is the maximum surface magnetic field in the active region. The factor $B_{\rm m}^2$ merely defines the normalization of the energy release light curve, while t_0 and n determine its shape. As Eq. 5.6 is given per radian of longitude, a length (l) must be assumed for the arcade in order to calculate its total energy-release rate. Solar two-ribbon flares occur in loop arcades whose length is typically about 1.5 times their width ($l \approx 1.5 H_{\rm m}$). In our study, we adopted this ratio for any given n.

Since, in the view of many authors, the initiation process for the flare itself might be the result of a more rapid (nearly explosive) reconnection than the reconnection process about which Kopp & Poletto (1984) and Poletto et al. (1988) speak, they stressed that their model is applicable only after the initial flare trigger mechanism is terminated. In fact, the model seems not to be able to describe the time of impulsive heating and steeply increasing temperatures. However, the impulsive phase typically ceases before reaching the 50 % flare peak level in the soft X-ray bandpass commonly used for stellar observations. At this time in our observations, the temperature is gradually decreasing. Hence, the model is applicable from time segment 4 of the light curve to the end of our observations (time segment 3 is rejected also for avoiding possible contamination from the decay of event A).

In order to apply the described model, the photospheric magnetic field in the flaring region (from which $B_{\rm m}$ can be determined) and its latitudinal location and size (which dictate n) should be known. In the solar case, observations provide all these data, whereas in the stellar case, at best, they can only be inferred indirectly. Since we are unaware of the location, size, and magnetic field strength of the active region that we are studying, we treated n and $B_{\rm m}$ as free parameters to be determined from the best fit of the model to the observations.

We created a grid of values for the free parameters n, t_0, and $t_{\rm ini}$ to fit event B with the two-ribbon flare model (the lower limit of $t_{\rm ini}$ was fixed at the beginning of the whole enhancement because of obvious physical reasons). For each set of these parameters, we determined the $B_{\rm m}$ that best fit the data by minimizing the χ^2 value, which is defined as

$$\chi^2 = \sum_{i=1}^{N} \left(\frac{L_{{\rm mod},i} - L_{{\rm obs},i}}{\Delta L_{{\rm obs},i}} \right)^2 , \tag{5.7}$$

where $L_{\rm mod}$ is the expected luminosity from the model ($L_{\rm mod} = f \cdot q \cdot l \cdot dE/dt$), $L_{\rm obs}$ is the observed luminosity, $\Delta L_{\rm obs}$ is the error in the observed luminosity, and N is the number of time intervals with which we fitted the two-ribbon model (from time segment 4 to 9). Following the solar analogy (Canfield et al. 1980, see § 5.1), we assumed the measured radiative losses in the X-ray band to be $\approx$ 10 % of the thermal energy generated as consequence of magnetic reconnections, that is $f \approx 0.1$ (see Poletto et al. 1988, for details). Actually, only a fraction ($q < 1$) of the liberated magnetic energy is indeed used to heat the plasma (thermal energy that is subsequently lost via radiation and conduction), while the rest is transformed into mechanical energy, into fast particles ejected from the corona, etc. At this point, we want to notice that we did not find a unique solution corresponding to a single set of parameters, but a number of solutions producing a good fit ($\chi^2 \sim 1$).

In Table 5.5, we show the two-ribbon flare parameters for some of the good fits we have obtained. We plot these results together with the observations in Fig. 5.7. Other good fits were found also for larger values of n (i.e., active regions with smaller width and, therefore, shorter loops), but note that a smaller active region needs higher surface magnetic fields for reproducing a given energy-release rate. Thus, loop systems that reach larger altitudes – i.e., small values of n – may be more realistic in our case, although other loop configurations cannot be excluded (see § 5.5).

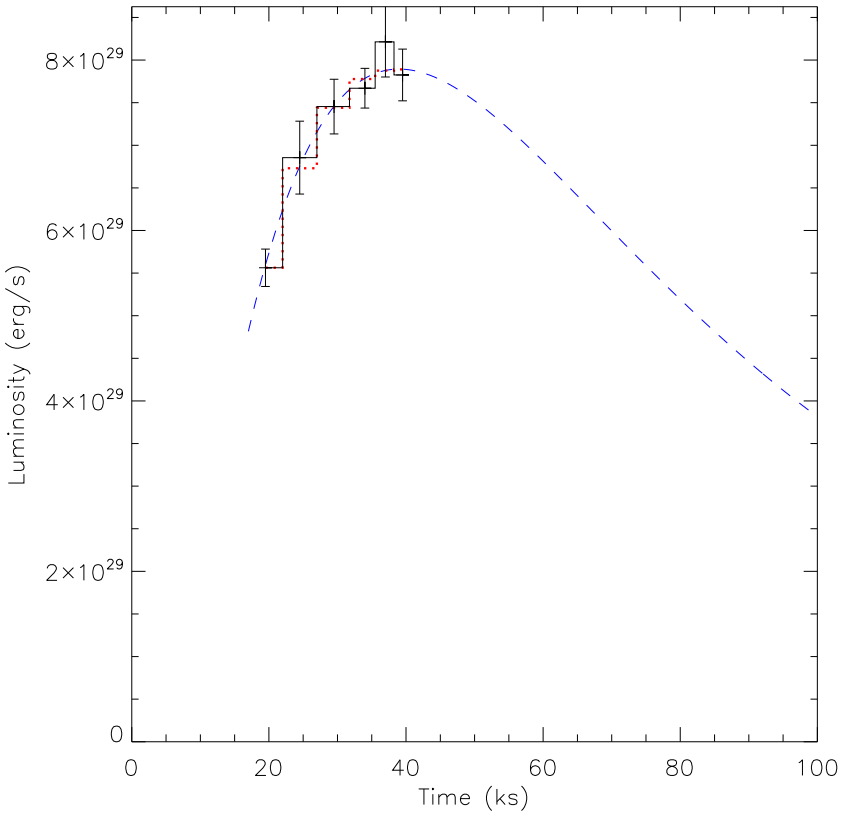

Figure 5.7: Best fit to the observations using the two-ribbon model for $n = 2$ (see Table 5.5). Note that each set of parameters in Table 5.5 produces similar results in the fitted region while having different slopes in the previous part and in the decay. The light curve segments used to fit the two-ribbon model (time segments 4 – 9, see also Fig. 5.2) is shown with a solid line. The dashed line is the model. We have also plotted the average values of the model in each time interval during event B (dotted line) for a clearer comparison between the observed light curve and the model.

The values given in Table 5.5 for the maximum surface magnetic field were determined assuming that all the magnetic energy is used to heat the plasma that fills the flaring loops ($q = 1$). Kopp & Poletto (1984) used $q = 0.003$ for a solar flare. On the other hand, during the analysis of a stellar flare, Güdel et al. (1999) found acceptable solutions with $q < 0.05$ for $n = 2$ and $q \approx 0.01 - 0.02$ for $n = 3 - 4$. For event B we found that small values of q ($\sim 0.01 - 0.02$) imply very strong photospheric magnetic fields in the flaring region ($B_{\rm m} \approx 3 - 18$ kG). Using $q = 0.05$, we obtained $B_{\rm m} \approx 2$ kG for $n = 2$ and $B_{\rm m} \approx 3 - 8$ kG for $n = 3 - 10$.

5.5 The fluorescent Fe 6.4 keV line

During the inspection of the X-ray spectrum in the different time intervals, we observed a feature (excess emission not reproduced by the plasma model) close to the Fe K_α line

Table 5.5: Two-ribbon flare parameters resulting from fitting the model to the observed energy release rate from event B.

Polynomial degree	2	3	5	10
Region width [deg]	90°	53°	33°	17°
$H_{\rm m}$ [$R_\star$]	1.57	0.90	0.57	0.30
$L_{\rm m}{}^a$ [$R_\star$]	2.46	1.41	0.89	0.47
$t_{\rm ini}$ [ks]	7.0	6.5	6.0	5.5
t_0 [ks]	247	192	183	174
$B_{\rm m}\sqrt{q}$ [G]	440	730	1050	1830
$v_{\rm rise}$ [km s^{-1}]	2.8	2.1	1.4	0.8
$N_{\rm e}$ [$\times 10^{10}$ cm^{-3}]	1.1	2.6	5.1	13.3
χ^2	1.02	1.02	1.04	1.04

[a] $L_{\rm m}$ is the loop semi-length determined from $H_{\rm m}$ assuming a semi-circular geometry.

at redder wavelengths. We identified this feature as the Fe fluorescent line at 6.4 keV. It was noticeable only during the time segments 4 – 9, while it was neither in time segments 1 – 3 nor in the quiescent state (see Fig. 5.8). Unfortunately, we could not monitor the time variation of this emission line since the individual spectra of each time interval have no counts enough for accurately fitting the line. Thus, to quantify the excess emission at 6.4 keV in our observations, we performed spectral fitting using an interstellar absorbed $3T$-plasma model and an additional Gaussian line component at 6.4 keV. We fitted, on the one hand, the spectrum integrated from the quiescent to time segment 3 (inclusive) and, on the other hand, the spectrum integrated from time segment 4 – 9 (inclusive). The Gaussian flux obtained in this way for the former spectrum is zero. The best-fit results are shown in Table 5.6. Note that we left free only the temperature and the emission measure of the third (hottest) thermal component and the Gaussian, while the rest of the parameters were fixed to the values obtained for the quiescent state (Table 5.1).

In the past, fluorescent Fe emission were commonly observed in classical T Tauri stars and protostars (Tsujimoto et al. 2005; Favata et al. 2005; Giardino et al. 2007; Sciortino 2008), where it has been attributed to the incidence of X-ray emission onto the protoplanetary disk or into the circumstellar gas surrounding very young objects. However, the Fe 6.4 keV line has been observed also in the giant star HR 9024 (Testa et al. 2008) and the RS CVn system II Peg (Osten et al. 2007). In the case of HR 9024, the authors attributed its presence to the incidence of hard X-rays onto the photosphere, in concordance with what is observed in the Sun. In II Peg, the excitation mechanism was ascribed to electron impact ionization of photospheric Fe.

In our observation, we do not have enough statistics to perform a robust analysis of the fluorescent line. Nevertheless, some constraints can be given. On the one hand, the line is not observed during the first event. This may be consistent with the scenario of the

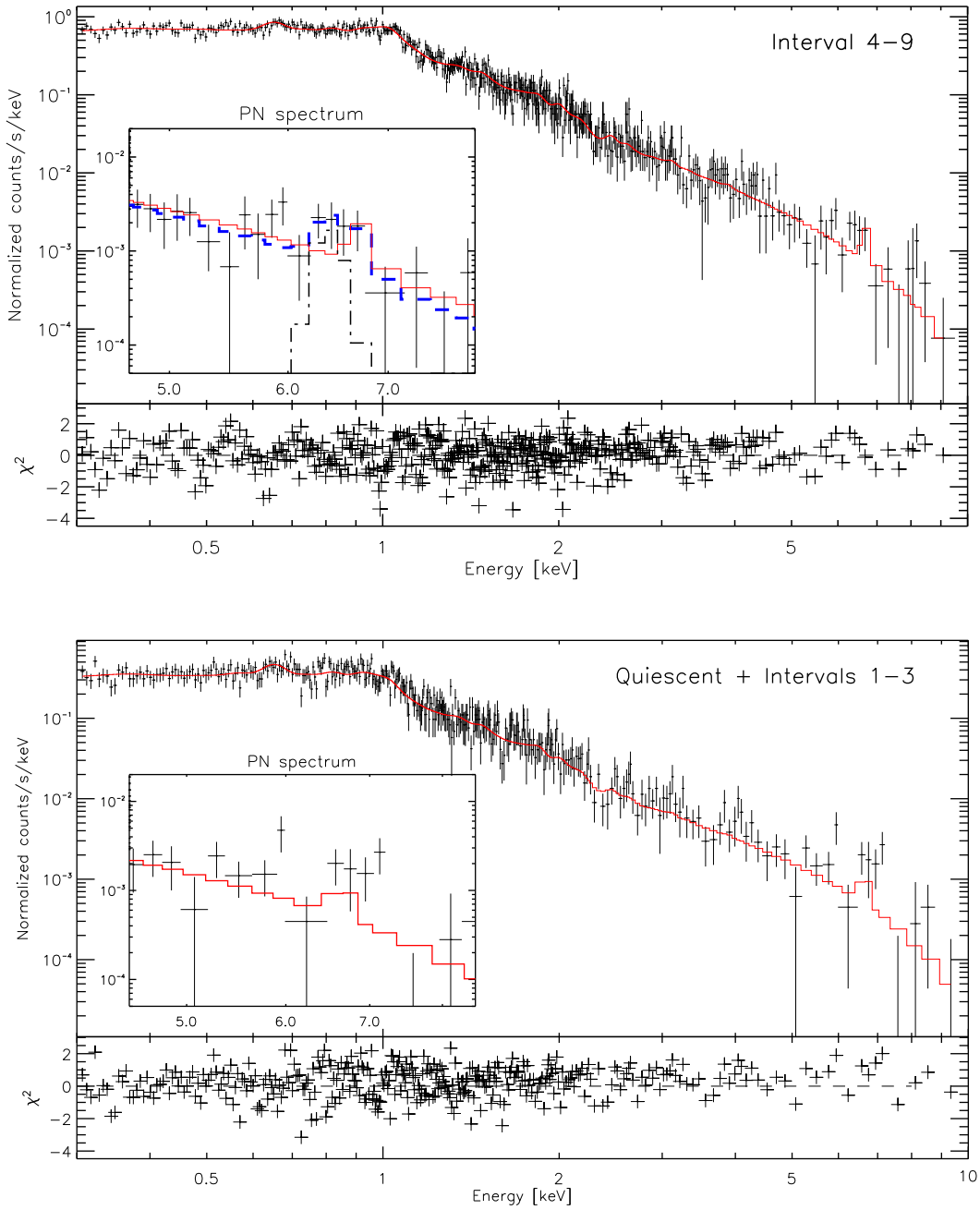

Figure 5.8: Top: PN spectrum of TWA 11B integrated in the time segments 4 – 9, with the clear excess emission in 6.4 keV. The (red) continuous line is the fitted 3T model. In the small window, the (blue) dashed-line is the fitted 3T model + Gaussian component. The Gaussian component is also plotted as a dot-dashed line. Bottom: same as figure in the top but integrated in the time segments 1 – 3 plus quiescent. Here, the excess emission in 6.4 keV is clearly not present.

long loop for this event. The efficiency of the fluorescence decreases with the distance of the X-ray source to the photosphere (e.g., Drake et al. 2008). Therefore, if the fluorescent

Table 5.6: Best-fitting values ($3T$ plasma model + Gaussian) for the spectrum integrated in the time segments 4 – 9. Only the temperature and the emission measure of the third thermal component and the Gaussian are listed because the remaining parameters were fixed to the values estimated for the quiescent state. The given $\chi^2_{\rm red}$ and d.o.f. values refer to the total fit.

kT_3 (keV)	=	$2.02^{+0.13}_{-0.12}$
EM_3 (10^{52} cm^{-3})	=	$4.7^{+0.3}_{-0.3}$
Gaussian central energy (keV)	=	$6.4^{+0.9}_{-0.6}$
Gaussian flux (10^{-6} ph cm^{-2} s^{-1})	=	$0.9^{+0.7}_{-1.3}$
Gaussian σ (eV)	=	$9.7^{+0.6}_{-9.7}$
$\chi^2_{\rm red}$ [d.o.f.]	=	0.96 [499]

line were produced by photoionization, it should not be observed during flares occurring in long loops. On the other hand, the presence of the line during the second event could be indicative of a not very high loop system, if it were produced by photoionization. In contrast, if the line were produced by collisional ionization, there would be none constraint to the loop height. A result in favour with the non-photoionization nature of the fluorescence line is shown in Czesla & Schmitt (2007). In their study, the authors modeled the illuminating input spectrum and obtained line fluxes below the observations. With our data, the collisional production of the fluorescence line cannot be discarded.

5.6 Final remarks and conclusions

In this paper, we analysed the long rise phase of a flare observed in *XMM-Newton* archive data of the $\sim$ 8 Myr old star TWA 11B. The analysis of the light curve, of the hardness-ratio curve, and of the time-resolved spectra consistently indicates that probably the flare first involved mainly a single loop and then propagated to a loop arcade becoming a proper two-ribbon flare. We split our analysis into three parts: the quiescent state, the single-loop flare (event A), and the two-ribbon system (event B). Event A was studied with the analysis described in Reale (2007). For event B, we used the stellar version of the Kopp & Poletto (1984)'s solar two-ribbon flare model that is able to provide some limited information about the late flaring structures.

For the single loop, we obtained a semi-length of approximately $1.8 \pm 0.3 \times 10^{11}$ cm ($\sim 4 \pm 1$ R$_\star$), with a volume $V = 2.3 \times 10^{31}$ cm^3 and a cross-section $r/L \sim 2\%$. These values are comparable to those found by Favata et al. (2005) in Orion members. This fact makes us suggest that large and thin loops are common in young active stars. For the two-ribbon system, different results consistent with the observed data were found. Good fits ($\chi^2 \sim 1$) were obtained for both small and large values of n (i.e., for high and short loop arcades). Bearing the semi-length of the first loop in mind, the more realistic scenario for the two-ribbon system is that with long loops. In any case, the estimated values of the

maximum surface magnetic field in the flaring region result to be quite strong, reaching 2 – 8 kG when a large fraction of the liberated magnetic energy ($q = 0.05$) is assumed to heat the plasma, and up to 18 kG when $q \sim 0.01$.

During the inspection of the X-ray spectrum, we observed the Fe fluorescent line at 6.4 keV during the time in which the two-ribbon system evolved (time segments 4 – 9). The absence of the line during the first event may be consistent with the long loop scenario for event A. In contrast, the detection of the fluorescence line during the second event could be indicative of a not very high loop system involved in the two-ribbon flare, if the line were produced by photoionization. Otherwise, there would be none constraint to the loop system height.

Chapter 6

Summary, discussion and conclusions

6.1 Summary and discussion

In this Ph.D. Thesis we have studied flares on main- and pre-main-sequence M-type stars by using observations in different wavelength ranges in order to analyse their effects at different layers of stellar atmospheres. In particular, optical and X-ray spectra have been used so that we can investigate how flares respectively affect the chromosphere and the corona of stars. By using theoretical models, we have been able of estimating physical properties of flaring plasma as well as sizes of flaring loops. We have discussed and interpreted the results in the context of solar and stellar flares reported so far.

We have studied in depth flares on two different UV Ceti-type stars and on a pre-main-sequence M-type star. In particular, we have analysed chromospheric flares on the fast rotating M3Ve star AD Leo (Chapter 3); and coronal flares on the spectroscopic K7.5Ve+M3.5Ve binary system CC Eri (Chapter 4), and also on the 8 Myr old, weak-line T Tauri M2.5 star TWA 11B (Chapter 5), which is still contracting but shows no signatures of being surrounded by an accretion disk. The main aspects of these works are summarized in the following lines.

i The star **AD Leo** was spectroscopically monitored with high temporal resolution during 4 nights. More than 600 intermediate resolution, optical spectra have been studied. With this work for AD Leo we have considerably extended the existing sample of stellar flares analysed with good quality spectroscopy in the optical range. In particular:

- We detected frequent short (duration between 14 ± 1 and 31 ± 3 min) and weak (released energy in Hβ between 1.5×10^{29} and 8.2×10^{29} erg) flares. The continuum flux did not change during these events. A total of 14 flares were inferred from the evolution of the *EW* of different chromospheric lines (Balmer series from Hα to H_{11}, the Ca II H & K and Na I D_1 & D_2 doublets, as well as the He I D_3 and He I 4026 Å lines). These events are therefore classified as non white-light flares. Even though this kind of flare is the most typical in the Sun, very few such events had been previously detected in stars (see Butler et al. 1986; Houdebine 2003).

- The results shown in Appendix A for 10 additional UV Ceti-type stars (spectral types from K7 to M4) confirm that the kind of variability detected in AD Leo (frequent non white-light flares) appears to be a common phenomenon among this type of stars.
- The observed flare frequency is very high. Sometimes new flares take place when others are still active. We have measured more than 0.71 flares/hour. This value is slightly larger than the values that other authors obtained for this star by photometry. As far as we know, it is the first time that such a high flare frequency is inferred from the variation of the chromospheric lines. Thus, given that all the detected flares are non white-light flares, we conclude that non white-light flares may be more frequent on stars than white-light flares, as observed on the Sun. Bearing in mind the energy distribution of flares reported by Datlowe et al. (1974) and Lin et al. (1984), we can expect very weak flares occurring even more frequently than the observed ones. Therefore our results can be interpreted as additional evidence of the important role that flares can play as heating agents of the outer atmospheric stellar layers (Güdel 1997; Audard et al. 2000; Kashyap et al. 2002; Güdel et al. 2003; Arzner & Güdel 2004). This idea may be supported by the outcome of our study on the chromospheric flux-to-flux relationships reported in Appendix B. We show that not all the M-type stars, but only flare M dwarfs deviate systematically from the trend established by hotter active stars in some chromospheric flux-to-flux diagrams.
- The Balmer lines allow us to distinguish two different morphologies: some flares show a gradual decay much longer than the impulsive phase while another ones are less impulsive. This resembles the two main types of solar flares (eruptive and confined) described by Pallavicini et al. (1977). The evolution of the Na I D_1 & D_2, He I D_3 and He I 4026 Å lines is quite similar to that of the Balmer series. This behaviour is less clear for the He I lines because of the higher uncertainty in their values. On the contrary, the Ca II H & K lines always show the same pattern and their evolution is less impulsive than that found for the Balmer lines.
- The two maxima and/or additional weak peaks, observed sometimes during the detected flares, can be interpreted as the succession of different magnetic reconnection processes (decreasing in efficiency), which would be consequence of the disturbance produced by the original flare, as Kopp & Pneuman (1976) suggested for the Sun. The Ca II H & K lines reach the flare maximum after the Balmer series. The shorter the impulsive phase of the Balmer lines is, the larger the time delay observed between these maxima. The moment at which a line reaches its flare peak is related to the line formation temperature and therefore depends on the height where the line is formed. According to the line formation models in stellar atmospheres, the Ca II H & K lines are formed at deeper and cooler layers than the Balmer series. Therefore, the gas that is heated and evaporated into the newly formed loop after magnetic reconnection (Cargill & Priest 1983; Forbes & Malherbe 1986) cools

and reaches the formation temperature of the Balmer series before the one of the Ca II H & K lines.

- During the detected flares, the relative increase observed in the emission of the Balmer lines is greater for lower wavelengths.
- It seems that flares affect the core of the lines before the wings.
- We have found red asymmetries in the Balmer lines during the detected flares. Red asymmetries are typically observed in solar flares. The Ca II H & K lines seem to be less affected by flare events and their broadening is negligible. The fact that the width of the Ca II lines is much less sensitive to flares than that of the Balmer lines suggests that the broadening may be due to the Stark effect (Byrne 1989; Robinson 1989). Nevertheless, the detected broad Balmer emission wings and red asymmetries can also be attributed to plasma turbulence, mass motions or CDC. A small red asymmetry in the Balmer series is also observed during the quiescent state, which could be interpreted as multiple CDC probably due to unresolved continuous low energy flaring.
- We have used the Balmer decrements as a tracer of physical parameters at the peak of the detected flares. The physical parameters of the flaring plasma and the covered stellar surface have been obtained by applying the procedure developed by Jevremović et al. (1998), which is based on the solution of the radiative transfer equation by assuming a simplified picture of the chromospheric flaring plasma as a slab of hydrogen with an underlying thermal source of radiation which causes photoionization. During the analysed flares, the chromospheric flaring plasma reach electron densities in the range 6×10^{13} cm^{-3} – 2×10^{14} cm^{-3} and electron temperatures between 12000 K and 24000 K; while the temperature of the background source ranges from 8000 K to 13500 K. All the obtained physical parameters are consistent with previously derived values for stellar flares. The areas – no larger than 2.3 % of the projected stellar surface – are comparable with the size of other solar and stellar flares (Tandberg-Hanssen & Emslie 1988; García-Alvarez 2003; García-Alvarez et al. 2002).
- We have also analysed the relationships between the flare parameters:
  - The released energy is correlated with the flare duration and the area covered by the flaring plasma, but not with the temperature of the underlying source. These results are in general agreement with those found by Hawley et al. (2003) using only 4 flares and a different method for obtaining the physical parameters.
  - We have found a clear relation between the released energy and the flux at flare maximum. Also, the higher the flux, the longer the flare. This flux is also correlated with the area covered by the emitting plasma at flare maximum, but not with the temperature of the underlying source.
  - No correlations between the area, temperature and duration have been found: i.e. these parameters seem to be independent.

The magnetic geometry seems to be a very important factor in flares: firstly, the flare duration could be related to the loop length, as in X-rays (see review by Reale 2002), in the sense that a fast decay implies a short loop and a slow decay a large loop; and secondly, the flare area could be related to the loop width, because the surface covered by the Balmer emitting plasma would be the projected area of the flaring loops. On the other hand, the temperature of the underlying source could be related to the depth of the layer reached by the flare accelerated particles, which is also related to the energy released through magnetic reconnection. For explaining the fact that the temperature of the underlying source seems to be well-defined and independent of the flare energy, we suggest that larger energies may imply more energetic particles and therefore larger depths, but not necessarily higher temperatures.

ii For the binary star **CC Eri** we have studied in detail its X-ray variability during a 36 ks XMM-Newton observation, covering about a quarter of its orbital period. The great sensitivity of the EPIC-PN CCD camera allowed us to perform time-resolved spectroscopy of two flares (FB and FC) weaker than those typically analysed in the literature for stars other than the Sun. In brief:

- The maximum luminosity of these flares in the 0.5 – 10.0 keV band was about 2.6×10^{29} erg/s. That is, FB and FC showed a maximum flux increase of factors 1.5 – 1.9, depending on the selected reference level. In this band, the total energy emitted by FB and FC was ~ 0.75 and 1.5×10^{33} erg, respectively. FC reached its peak about 5 h after the peak FB.
- We have calculated coronal temperatures and emission measures by fitting the spectra using an iterative procedure and the Astrophysical Plasma Emission Code included in the XSPEC software (which calculates spectral models for hot, optically thin plasmas). During the observation, the corona of CC Eri is well-described by a 3-T model with constant temperatures of 3, 10 and 22 MK, and time-variable emission measures. The emission measure of the coolest component (EM_1) ranged between $1.6 - 2.3 \times 10^{52}$ cm^{-3}, the one of the second component (EM_2) between $1.4 - 2.3 \times 10^{52}$ cm^{-3}, and that of the hottest component (EM_3) varied between $0.1 - 2.1 \times 10^{52}$ cm^{-3}. That is, EM_1 reached 1.4 times the value measured for the quiescent state, EM_2 varied up to a factor of 1.6, and EM_3 increased up to 21 times its quiescent value. The changes in the emission measure of the coolest component could be due to the variable aspect of the binary during its orbital motion. The changes in the emission measure of the two hottest components are clearly correlated with the variations observed in the light curve during the detected flares. In fact, the hottest component dominates the X-ray variability observed on CC Eri.
- As far as we are concerned, this is the first time that no evident temperature variations are observed in a time-resolved study of stellar flares: the temperatures that characterize the flaring plasma coincide with those of the quiescent state and only the amount of material emitting at each one of these temperatures changes. Previous studies (Pallavicini et al. 1990; Schmitt et al. 1990)

reported that UV Ceti-type stars have coronal plasma at 10 MK even in its quiescent state, in conjunction with lower temperature ($T \sim 3 \times 10^6$ K) material, while F and G main-sequence stars have the 10 MK component either absent of very weak. Our results are therefore consistent with a recurrent idea in the literature, that is: the quiescent emission of at least UV Ceti-type stars may be produced, to a large fraction, by continuous flaring activity (see § 4.1 and references therein). Thus, the light curves of multiple small flares would overlap, and only larger flares would stand out from the quiescent level. Since no temperature variations are detected, differences in the emission measure between time-intervals with diverse count-rate are identified with differences in the total coronal volume filled by the flaring plasma. Density variations may also account for the changes in emission measure. However, we expect that, if they were significant, they would be driven by local heating injections or leaks, and therefore coupled to temperature variations but, as discussed above, temperature variations are not detected.

- The results obtained for the two hottest components resemble those reported by Reale et al. (2001) for a sample of solar flares that covered a wide range of intensities and physical conditions. They found that the $EM(T)$ distribution of all the flares in the sample follows a common evolution path: it starts low but already at a relatively high temperature ($\sim 10^7$ K independently of the flare intensity), it grows toward higher EM values during the rising phase and then decreases during the decay, maintaining always a more or less constant shape and peak temperature. In other words, they found that the height of the $EM(T)$ distribution is clearly variable during the different phases of solar flares, while the width and peak temperature of the distribution suffer from much smaller changes.

- According to Reale et al. (1997); Reale (2007) and Reale et al. (2004), the slope of the path in the density-temperature diagram indicates the presence of significant heating during the decay of the two analysed flares (FB and FC), and leads to an upper limit for the half-length of the flaring loops (L) of 7 and 14×10^9 cm, respectively. Bearing the spectral type of the stellar components of CC Eri in mind, the ratio between the half-length of the flaring loops and the stellar radius (R_*) would be 0.1 and 0.3 if the flares were produced by the K7.5Ve star, or 0.2 and 0.4 if they were produced by the M3.5Ve star. In both cases, the loop height above the stellar surface ($2L/\pi$ for vertical loops with semi-circular geometry) is about $0.1 - 0.3\ R_*$, implying a relatively compact flaring corona. These results are in agreement with the loop half-lengths derived for other Me dwarfs ($L \leq 0.5\ R_*$; Favata & Micela 2003).

- From the orbital solution of CC Eri (Amado et al. 2000) and the stellar radius of its components, we obtain a minimum distance between their surfaces of $\sim 1.4 \times 10^{11}$ cm. Even the largest loops involved in the detected flares only cover ~ 10 % of this distance. Therefore, it is likely that the flaring loops are included all in the corona of one of the stars, and do not result from the magnetic fields bridging the two stars.

- As the loop half-lengths are significantly smaller than the pressure scale height, we have assumed that the flaring loop is not far from a steady-state condition at the flare peak in order to apply the so-called RTV scaling laws (Rosner et al. 1978). Thus, we derive the pressure (p) and the heating rate per unit volume ($E_{\rm H}$) from the loop half-length and the loop maximum temperature. The values estimated for these quantities result to be 0.7 $\times 10^3$ dyn cm^{-2} and 0.8 erg s^{-1} cm^{-3} for FC. Larger values were obtained for FB, in which only a lower limit could be calculated for these parameters ($p > 1.7 \times 10^3$ dyn cm^{-2} and $E_{\rm H} > 3.7$ erg s^{-1} cm^{-3}).
- We have also estimated the electron density under the assumption of a totally ionized hydrogen plasma, obtaining $n_{\rm e} \sim 10^{11}$ cm^{-3}. This is compatible with values expected for a plasma in coronal conditions.
- In order for the electron density to be consistent with the $EM_{\rm F}$ measured at the peak of the analysed flares, the flaring volumes should be as large as 10^{30} cm^3.
- From the pressure of the flaring plasma, we infer that the minimum magnetic field required to confine the plasma at the flare peak is ~ 210 G for FB and ~ 140 G for FC.
- To satisfy the energy balance relation for the flaring region as a whole, the maximum X-ray luminosity must be lower than the total input energy rate at the flare peak ($H = E_{\rm H} V_{\rm F}$). The rest of the input energy is used for thermal conduction, kinetic energy and radiation at lower frequencies. For both FB and FC, we obtain that $L_{\rm X,max}$ is about 10 % of H, compatible with the X-ray radiation being only one of the energy loss terms during the detected flares. This value is in agreement with those reported for solar flares, where the soft X-ray radiation at the peak only accounts for 10 – 20 % of the total energy budget (Wu et al. 1986). Reale et al. (2004) found a similar percentage ($\sim$ 15 %) for a flare observed on the M5.5Ve star Proxima Centauri, while Favata et al. (2000c) estimated a higher value ($\sim$ 35 %) for an extreme X-ray flare detected on the M3.5Ve star EV Lac.
- If the detected flares were produced by a single loop, its aspect ratio ($\beta = r/L$, where r is the radius of the loop cross-section derived from the volume and the loop length, L) should be 0.6 for FB and 0.4 for FC. Such a large values of β are not observed on solar coronal loops, for which typical values of β are in the range 0.1 – 0.3. Therefore, for the flares detected on CC Eri we suggest a more realistic scenario consisting on flaring structures made up of several similar loops with aspect ratio comparable to that of solar loops. Assuming $\beta = 0.1$, FB and FC would occur in arcades composed of $\sim$ 38 and 19 loops, respectively. Similar structures are also observed to flare on the Sun. For example, the Bastille day flare (2000 July 14) is an intense solar flare (GOES class X6) that occurred on a curved arcade with some 100 post-flare loops (Aschwanden & Alexander 2001; Reeves & Warren 2002). Stellar analogues have been proposed for the Me dwarf Proxima Centauri, where the best description for a flare analysed by Reale et al. (2004) shows the presence of an arcade made up of ~ 5 loops; and also for the younger ($\sim$ 100 Myr)

G9 dwarf ZS 76, where Pillitteri et al. (2005) estimated 20 – 30 loops for the flaring arcades. Therefore, we conclude that events like solar arcade flares may be a common phenomenon on stars, in wide generality.

iii We have analysed an XMM-Newton serendipitous observation of the young M-type star **TWA 11B**, member of the young stellar association TW Hya (~8 Myr). The observation covered at least 17% of the rotational period of the star. The EPIC MOS and PN instruments detected a first weak increase in the light curve that reached a local maximum 1.4 hr after the rise started. After a brief decrease, the count rate continued increasing, but more gradually this time, until reaching the global maximum in the light curve just 0.8 hr before the end of the observation. The latter enhancement lasted approximately 9 hr and the star's count rate raised a factor 4.2 from the lower level. A full study of the recorded data (quiescent state in addition to both the moderate and the extremely long rises) has been performed:

- We have used the evolution of the hardness ratio as a tracer of the temperature evolution. Results show that the mean coronal temperature reached a maximum just before the local peak due to the first, moderate rise. Then it maintained high with significant fluctuations during approximately the next 7.5 hr of exposure. In this moment, just before the global maximum in the light curve, the mean coronal temperature began to decrease and continued diminishing gradually until the end of the observation. To date, so long rise phases have been previously observed only in some T Tauri stars, some of them with accretion disks, and several RS CVn systems. Such a long rise phase suggests that we are observing an uninterrupted sequence of flare events involving an extended coronal region. The faster initial rise and the local emission peak – coupled with the earlier hardness ratio peak – resembles the evolution of a self-standing flaring episode possibly occurring (at least during these initial stages) in a single loop, whose decay merged with the ignition of the later overlapping events.
- The large number of counts collected from the source in the EPIC cameras has allowed us to perform a reliable time-resolved spectral analysis. For this purpose, we have again used the Astrophysical Plasma Emission Code.
  - The quiescent state: the best fit to the X-ray quiescent spectrum is given by a plasma model with two equally weighted (emission measure around 2.2×10^{52} cm^{-3}) thermal components with temperatures of 0.27 and 0.98 keV.
  - The flaring state: for this state, two different approaches have been tested. In the first approach, we have obtained good fits by assuming that the coronal spectrum during the flare results from adding a third thermal component to the quiescent spectrum, which is ascribed to heated material filling the flaring loops. Results from these fits confirm those obtained for the temperature from the hardness ratio curve. In the second approach, we have obtained physically more realistic emission measure distributions (EMDs) by using a $6T$ model with free emission measures

and temperatures fixed on a logarithmic, almost equidistant grid. Plasma emitting at the highest temperatures ($\sim$ 56 MK) appears at the beginning of the first (faster) rise. When this first rise peaks, an excess of plasma emitting at temperatures around 28 MK is detected relative to the quiescent state. This excess is believed to result from the cooling of the material previously detected at higher temperatures, and possibly to additional evaporated plasma. Later, the excess of plasma emitting in the region around 28 MK continues cooling toward lower temperatures. At the beginning of the second (more gradual) rise, a high quantity of plasma appears again at the highest temperatures ($\sim$ 56 MK). During the following five hours, the amount of plasma emitting at these temperatures remains still high. Note that the existence of intense, sustained heating is needed to explain the maintenance of plasma at so high temperatures. Besides, a large excess of material (compared to the quiescent state) appears also between 7 and 28 MK. This is interpreted as the cooling of the continuously new appearing very hot plasma, together with new heated material that evaporates from lower layers and fills the flaring loops. When the global peak in the light curve is reached, the emission at temperatures greater than 28 MK turns back to the quiescent level, which is an indication of the strong heating not being present any more. However, the amount of material at medium temperatures is extremely high compared to that measured in the previous time segments. Again, this excess of plasma is believed to result from the cooling of the material previously detected at higher temperatures, and possibly to new evaporated plasma.

- The analysis of the light curve, of the hardness-ratio curve, and of the time-resolved spectra supports the idea of having two different flaring structures in the observation: the first more impulsive one (event A) responsible for the first, moderate rise and the first (local) peak; followed by a more gradual energy release (event B) having a beginning that is merged with the decay phase of event A and becoming dominant during the rest of the observation. The clear evidence of a delay between the temperature peak and the density peak is in fact consistent with a single-loop model, at least until the moment in which this maximum density is reached. Event B is probably triggered by event A. The evolution of the whole EMD during event B evidences continuous, but decreasing in efficiency, heating of material and is consistent with event B being a proper two-ribbon flare.

- Since only the rise and the peak of event A have been detected, we have used the theoretical analysis reported by Reale (2007) for single loops in order to determine several properties of the loop involved in this flare. With this method, the loop half-length is calculated from the maximum temperature reached by the flaring plasma and the temperature and time in which the density peaks. These quantities come from the $1T$ flare model (first approach referred above). The loop semi-length results to be $1.8 \pm 0.3 \times 10^{11}$ cm ($\sim 4 \pm 1\ R_\star$). Assuming a semi-circular geometry, the aspect ratio of this loop

would be of the order of 2%, which is quite lower than that observed in the Sun. Both the loop semi-length and the aspect ratio that we have obtained are comparable to values found by Favata et al. (2005) in star-forming regions. As far as we are concerned, this is the first time that such a relatively long loop is detected in a star older than 3 – 4 Myr.

- For event B, we used the two-ribbon flare model by Kopp & Poletto (1984) extended to the stellar case (Poletto et al. 1988). This model supposes that a disruptive event opens a loop arcade, being the open field lines then driven toward a radial neutral sheet where they reconnect at progressively higher altitudes. Thus, the continuous heating provided by these reconnections is capable of reproducing the temporal profile of the energy rate released during both the rise and decay phases of a two-ribbon flare. Since only the rise phase (and possibly the peak) of event B was detected, we have not found a unique solution corresponding to a single set of parameters, but a number of solutions producing a good fit. Good fits have been indeed obtained for both high and short loop arcades. Bearing the semi-length of the first loop in mind, the more realistic scenario for the two-ribbon system would be that with long loops. In any case, the estimated values of the maximum surface magnetic field in the flaring region result to be quite strong, reaching 2 – 8 kG when a large fraction of the liberated magnetic energy ($q = 0.05$) is assumed to heat the plasma, and up to 18 kG when $q \sim 0.01$.
- During the inspection of the X-ray spectrum, we observed the Fe fluorescent line at 6.4 keV during the time in which the two-ribbon system evolved. The absence of the line during the first event may be consistent with the long loop scenario for event A. In contrast, the detection of the fluorescence line during the second event could be indicative of a not very high loop system involved in the two-ribbon flare, if the line were produced by photoionization. Otherwise, there would be none constraint to the loop system height.

6.2 Conclusions

Main conclusions of this Ph.D. Thesis can be summarized in the following points:

- UV Ceti-type stars show frequent short (typical duration of 15 – 30 min), weak (released energy in Hβ of the order of 10^{29} – 10^{30} erg) optical flares that are noticeable in some chromospheric lines, specially in the Balmer series, and show no significant emission in white light.

- Non-white-light flares are more frequent on UV Ceti-type stars than white-light flares, as observed in the Sun. In particular, we detected more than 0.71 non-white-light flares per hour in a high-temporal resolution spectroscopic monitoring of AD Leo, while white-light flares were not detected at all during these observations.

- Non-white-light flares take place in small areas of the stellar surface of UV Ceti-type stars, covering less than 2 – 3 % of the projected stellar disk. These areas are comparable with the size of other solar and stellar flares (Tandberg-Hanssen & Emslie 1988; García-Alvarez 2003; García-Alvarez et al. 2002).

- In non-white-light flares, the released energy is correlated with the flare duration and the area covered by the flaring plasma, but not with the temperature reached in the underlying source. However, no correlations between the flare duration, area and temperature of the underlying source have been found. We suggest that larger released energies may imply more energetic particles that reach lower depths when moving down along the magnetic field lines, but they do not necessarily cause higher temperatures in the underlying source that catch them.

- In the UV Ceti-type star CC Eri, during both low/medium-energy flares and several "pseudo-quiescent" levels, we have detected significant changes in the amount of material at temperatures of 10 MK that are positively correlated with the flare emission level. We interpret this result as an evidence for non-resolved low-energy flaring activity being the origin of the plasma at 10 MK that is present even during the "quiescent" state of UV Ceti-type stars (Pallavicini et al. 1990; Schmitt et al. 1990). Thus, the light curves of multiple small flares would overlap, and only larger flares would stand out from the quiescent level.

- For the UV Ceti-type star CC Eri we find flaring loops with semi-lengths in the range 0.1 – 0.4 stellar radius, in agreement with the results reported for other Me dwarfs ($L \leq 0.5\ R_*$; Favata & Micela 2003), implying a relatively compact flaring corona for this kind of stars.

- For pre-main-sequence stars such as TWA 11B, the flaring structures appear to be quite complicated, with a mixture of very long (up to 4 stellar radius), thin (aspect ratio $\approx$ 2 %) single loops and compact arcades acting at the same time. Note that the aspect ratio of these large, single loops is much lower than that observed at the Sun ($\approx$ 10 %).

- In the UV Ceti-type star CC Eri we infer the presence of flaring arcades made up of 20 – 40 magnetic loops. Pillitteri et al. (2005) estimated 20 – 30 loops for the flaring arcades on the younger ($\sim$ 100 Myr) G9 dwarf ZS 76. Besides, in the pre-main-sequence M-type star TWA 11B we also detect a large two-ribbon flare. So we conclude that events like solar arcade flares (as the Bastille day flare – 2000 July 14) may be a common phenomenon on stars, in wide generality.

- In the UV Ceti-type star CC Eri, we found that the soft X-ray radiation at the flare peak only accounts for 10 % of the maximum heating rate. This value is in agreement with those reported for solar flares (10 – 20 %, Wu et al. 1986), is similar to the percentage estimated by Reale et al. (2004) for a flare on the M5.5Ve star Prox Cen (15 %), and is considerably smaller than the value determined by Favata et al. (2000c) for an extreme X-ray flare on the M3.5Ve star EV Lac.

- The magnetic field required to confine plasma in coronal loops of the UV Ceti-type star CC Eri is at least of the order of 100 G.

- The surface magnetic field in two-ribbon flares of the pre-main-sequence star TWA 11B appears to be quite strong, reaching 2 – 8 kG when a large fraction ($\sim$ 5 %) of the liberated magnetic energy is assumed to heat the plasma, and even larger if this fraction were smaller.

Chapter 7

List of publications

7.1 Papers in peer-reviewed journals

7.1.1 Refereed articles included in this thesis

1. ***"Analysis and modeling of high temporal resolution spectroscopic observations of flares on AD Leonis"***, Crespo-Chacón, I., Montes, D., García-Alvarez, D., Fernández-Figueroa, M. J., López-Santiago, J., & Foing, B. H., 2006, A&A, 452, 987.

2. ***"X-ray flares on the UV Ceti-type star CC Eridani: a "peculiar" time-evolution of spectral parameters"***, Crespo-Chacón, I., Micela, G., Reale, F., Caramazza, M., López-Santiago, J., & Pillitteri, I., 2007, A&A, 471, 929.

3. ***"A Detailed Study of the Rise Phase of a Long Duration X-Ray Flare in the Young Star TWA 11B"***, López-Santiago, J., Crespo-Chacón, I., Micela, G., & Reale, F., 2010, ApJ, 712, 78.

7.1.2 Other refereed articles

1. ***"High Temporal Resolution Spectroscopic Observations of the Flare Star V1054 Oph"***, Crespo-Chacón, I., Montes, D., Fernández-Figueroa, M. J., López-Santiago, J., García-Alvarez, D., & Foing, B. H., 2004, Ap&SS, 292, 697.

2. ***"Cool Stars: Chromospheric Activity, Rotation, Kinematic and Age"***, Montes, D., Crespo-Chacón, I., Gálvez, M. C., Fernández-Figueroa, M. J., López-Santiago, J., de Castro, E., Cornide, M., & Hernán-Obispo, M., 2004, Lecture Notes and Essays in Astrophysics, 1, 119.

3. ***"The Nearest Young Moving Groups"***, López-Santiago, J., Montes, D., Crespo-Chacón, I., & Fernández-Figueroa, M. J., 2006, ApJ, 643, 1160.

4. ***"LU Vel (GJ 375): A M3.5Ve Flare and Double-Lined Spectroscopic Binary"***, Montes, D., Gálvez, M. C., Fernández-Figueroa, M. J., & Crespo-Chacón, I., 2006, Ap&SS, 304, 367.

5. ***"A high-resolution spectroscopic survey of late-type stars: chromospheric activity, rotation, kinematics, and age"***, López-Santiago, J., Montes, D., Gálvez-Ortiz, M. C., Crespo-Chacón, I., Martínez-Arnáiz, R. M., Fernández-Figueroa, M. J., de Castro, E., & Cornide, M., 2010, A&A, 514, AA97.

6. ***"Effect of magnetic activity saturation in chromospheric flux-flux relationships"***, Martínez-Arnáiz, R., López-Santiago, J., Crespo-Chacón, I., & Montes, D., 2011, MNRAS, 414, 2629.

7. ***"Erratum: Effect of magnetic activity saturation in chromospheric flux-flux relationships"***, Martínez-Arnáiz, R., López-Santiago, J., Crespo-Chacón, I., & Montes, D., 2011, MNRAS, 417, 3100.

8. ***"The ultracool dwarf DENIS-P J104814.7-395606. Chromospheres and coronae at the low-mass end of the main-sequence"***, Stelzer, B., Alcalá, J., Biazzo, K., Ercolano, B., Crespo-Chacón, I., López-Santiago, J., Martínez-Arnáiz, R., Schmitt, J. H. M. M. Rigliaco, E., Leone, F., & Cupani, G., 2012, A&A, 537, A94.

7.2 Conference proceedings

1. ***"Spectroscopic monitoring with high temporal resolution of the flare star AD Leo"***, Crespo-Chacón, I., Montes, D., López-Santiago, J., Fernández-Figueroa, M. J., García-Alvarez, D., & Foing, B. H., 2003, Highlights of Spanish Astrophysics III, 468.

2. ***"EURD: extreme ultraviolet spectrograph for the observation of diffuse radiation"***, Morales, C., Gómez, J. F., Rodrigo, C., Montero-Castaño, M., Quintana-Lacaci, G., Crespo-Chacón, I., Bowyer, S., Edelstein, J., & Korpela, E. 2003, Highlights of Spanish Astrophysics III, 495.

3. ***"High Temporal Resolution Spectra of Flare Stars"***, Montes, D., Crespo-Chacón, I., Fernández-Figueroa, M. J., López-Santiago, J., García-Alvarez, D., & Foing, B. H., 2004, Stars as Suns: Activity, Evolution and Planets, 219, 910.

4. ***"High resolution spectra of flare M-dwarfs"***, Crespo-Chacón, I., Montes, D., López-Santiago, J., & Fernández-Figueroa, M. J., 2005, Proceedings of the SEA/JENAM, CD P15.

5. ***"From microflares to strong and long-duration flares"***, Montes, D., López-Santiago, J, Crespo-Chacón, I., & Fernández-Figueroa, M. J., 2005, Proceedings of the SEA/JENAM, CD P69.

6. ***"High temporal resolution spectroscopy of late-type rapid rotator stars"***, Hernán-Obispo, M., de Castro, E., Cornide, M., Crespo-Chacón, I., Gálvez, M. C., & López-Santiago, J., 2005, Proceedings of the SEA/JENAM, CD P37.

7. ***"Astronomy and astrophysics communication in the UCM Observatory"***, Crespo-Chacón, I., de Castro, E., Díaz, C., Gallego, J., Gálvez, M. C., Hernán-Obispo, M., López-Santiago, J., Montes, D., Pascual, S., Verdet, A., Villar, V., & Zamorano, J., 2005, EAS Publications Series, 16, 111.

8. ***"Teaching Astronomy in non-formal education: stars workshop"***, Hernán-Obispo, M., Crespo-Chacón, I., Gálvez, M. C., & López-Santiago, J. 2005, EAS Publications Series, 16, 209.

9. ***"High temporal resolution spectroscopic observations of UV Cet type flare stars"***, Crespo-Chacón, I., Montes, D., Fernández-Figueroa, M. J., & López-Santiago, J. 2005, 13th Cambridge Workshop on Cool Stars, Stellar Systems and the Sun, 560, 491.

10. ***"Analysis of high temporal resolution spectra of late-type rapid rotator stars: BD +201790"***, Hernán-Obispo, M., De Castro, E., Cornide, M., Crespo-Chacón, I., Gálvez, M. C., & López-Santiago, J., 2005, 13th Cambridge Workshop on Cool Stars, Stellar Systems and the Sun, 560, 647.

11. ***"A study on the flux-flux and activity-rotation relationships for late-type stars members of young stellar kinematic groups"***, López-Santiago, J., Montes, D., Fernández-Figueroa, M. J., Gálvez, M. C., & Crespo-Chacón, I. 2005, 13th Cambridge Workshop on Cool Stars, Stellar Systems and the Sun, 560, 775.

12. ***"Flare stars among K dwarfs members of young stellar kinematic groups"***, Montes, D., López-Santiago, J., Crespo-Chacón, I., & Fernández-Figueroa, M. J. 2005, 13th Cambridge Workshop on Cool Stars, Stellar Systems and the Sun, 560, 825.

13. ***"Criteria for spectral classification of cool stars using high-resolution spectra"***, Montes, D., Martínez-Arnáiz, R. M., Maldonado, J., Roa-Llamazares, J., López-Santiago, J., Crespo-Chacón, I., & Solano, E., 2007, Highlights of Astronomy, 14, 598.

14. ***"EUVE J0825-16.3 and EUVE J1501-43.6: Two dMe Double-Lined Spectroscopic Binaries"***, Montes, D., Crespo-Chacón, I., Gálvez, M. C., & Fernández-Figueroa, M. J. 2007, IAU Symposium, 240, 690

15. ***"Relationships between physical and observational parameters during flares on M-dwarfs"***, Crespo-Chacón, I., García-Alvarez, D., Montes, D., Fernández-Figueroa, M. J., López-Santiago, J., Jevremovic, D., & Foing, B. H., 2007, Highlights of Spanish Astrophysics IV, CD.

16. ***"'High resolution spectroscopic analysis of cool stars possible members of the AB Doradus moving group'***, Montes, D., López-Santiago, J., Crespo-Chacón, I.,

Martínez-Arnáiz, R. M., & Maldonado, J., 2007, Highlights of Spanish Astrophysics IV, CD.

17. ***"High resolution spectra of cool stars in the Virtual Observatory: Criteria for spectral classification"***, Montes, D., Martínez-Arnáiz, R. M., Maldonado, J., Roa-Llamazares, J., López-Santiago, J., Crespo-Chacón, I., Gálvez, M. C., & Solano, E., 2007, Highlights of Spanish Astrophysics IV, CD.

18. ***"Spectroscopic properties of UV Ceti-type stars"***, Crespo-Chacón, I., Montes, D., López-Santiago, J., & Fernández-Figueroa, M. J., 2007, 14th Cambridge Workshop on Cool Stars, Stellar Systems, and the Sun, CD.

19. ***"Weak X-ray flares on the BY Dra-type binary star CC Eri"***, Crespo-Chacón, I., Micela, G., Caramazza, M., Reale, F., López-Santiago, J., & Pillitteri, I., 2007, 14th Cambridge Workshop on Cool Stars, Stellar Systems, and the Sun, CD.

20. ***"High resolution spectroscopic analysis of cool stars possible members of nearby young moving groups"***, Montes, D., López-Santiago, J., Crespo-Chacón, I., Martínez-Arnáiz, R. M., & Maldonado, J., 2007, 14th Cambridge Workshop on Cool Stars, Stellar Systems, and the Sun, CD.

21. ***"Modeling the long duration rise phase of a flare detected on the M star TWA 11 B"***, Crespo-Chacón, I., López-Santiago, J., Reale, F., & Micela, G. 2009, 15th Cambridge Workshop on Cool Stars, Stellar Systems, and the Sun, 1094, 584.

22. ***"Weak Flares on M-Dwarfs"***, Crespo-Chacón, I., López-Santiago, J., Montes, D., Fernández-Figueroa, M. J., Micela, G., Reale, F., García-Álvarez, D., Caramazza, M., & Pillitteri, I., 2010, Highlights of Spanish Astrophysics V, 393.

23. ***"VizieR Online Data Catalog: A high-resolution spectroscopic survey of late-type stars: chromospheric activity, rotation, kinematics, and age"***, López-Santiago, J., Montes, D., Gálvez-Ortiz, M. C., Crespo-Chacón, I., Martínez-Arnáiz, R. M., Fernández-Figueroa, M. J., de Castro, E., & Cornide, M., 2010, VizieR Online Data Catalog, 351, 49097.

7.3 Book chapters

1. ***"El destino de los satélites"***, Pérez-Hoyos, S., & Crespo-Chacón, I., 2003, Crónicas del Sistema Solar (Equipo Sirius, Colección Milenium), 161 - 168.

2. ***"Mil mundos esperando: los planetas extrasolares"***, Crespo-Chacón, I., Fernández-Ramírez, C., & Pérez-Hoyos, S., 2003, Crónicas del Sistema Solar (Equipo Sirius, Colección Milenium), 219 - 225.

Bibliography

Abada-Simon, M., Lecacheux, A., Aubier, M., & Bookbinder, J. A. 1997, A&A, 321, 841

Abdul-Aziz, H., Abranin, E. P., Alekseev, I. Yu., et al. 1995, A&AS, 114, 509

Aboudarham, J., & Hénoux, J. C. 1986a, A&A, 168, 301

Aboudarham, J., & Hénoux, J. C. 1986b, A&A, 156, 73

Abranin, E. P., Alekseev, I. Yu., Avgoloupis, S., et al. 1998, Astron. Astrophys. Trans., 17, 221

Amado, P. J., Doyle, J. G., Byrne, P. B., et al. 2000, A&A, 359, 159

Anders, E., & Grevesse, N. 1989, Geochim. Cosmochim. Acta, 53, 197

Argiroffi, C., Maggio, A., Peres, G., Stelzer, B., & Neuhäuser, R. 2005, A&A, 439, 1149

Arnaud, K. 1996, in ASP Conf. Ser. 101, Astronomical Data Analysis Software and Systems V, ed. G. H. Jacoby & J. Barnes, 17

Arnaud, K. 2004, BAAS, 36, 934

Arzner, K., & Güdel, M. 2004, ApJ, 602, 363

Aschwanden, M. J. 2008, ApJ, 672, L135

Aschwanden, M. J., Tarbell, T. D., Nightingale, R. W., et al. 2000, ApJ, 535, 1047

Aschwanden, M. J., & Alexander, D. 2001, Sol. Phys., 204, 91

Aschwanden, M. J., & Parnell, C. E. 2002, ApJ, 572, 1048

Audard, M., Güdel, M., & Guinan, E. F. 1999, ApJ, 513, L53

Audard, M., Güdel, M., Drake, J. J., & Kashyap, V. L. 2000, ApJ, 541, 396

Avrett, E. H., Machado, M. E., & Kurucz, R. L. 1986, in The lower atmosphere of solar flares, ed. D. F. Neidig, 216

Balega, I., Bonneau, D., & Foy, R. 1984, A&AS, 57, 31

Barden, S. C. 1985, ApJ, 295, 162

Bastian, T. S. 1994, Space Sci. Rev., 68, 261

Bastian, T. S., Benz, A. O., & Gary, D. E. 1998, ARA&A, 36, 131

Benz, A. O. 2008, Living Reviews in Solar Physics, 5, 1

Benz, A. O., & Güdel, M. 2010, ARA&A, 48, 241

Berdyugina, S., Ilyin, I., & Tuominen, I. 1998, in ASP Conf. Ser. 154, The Tenth Cambridge Workshop on Cool Stars, Stellar Systems and the Sun, ed. R. A. Donahue & J. A. Bookbinder, 1477

Berghmans, D. 2002, in Solar Variability: From Core to Outer Frontiers, ed. A. Wilson, 501 – 508

Böhm-Vitense, E. 2007, ApJ, 657, 486

Bopp, B. W., & Evans, D. S. 1973, MNRAS, 164, 343

Bopp, B. W., & Fekel, F., Jr. 1977, AJ, 82, 490

Bopp, B. W., & Stencel, R. E. 1981, ApJ, 247, L131

Briggs, K. R., & Pye, J. P. 2003, MNRAS, 345, 714

Browning, M. K. 2008, ApJ, 676, 1262

Busko, I. C., & Torres, C. A. O. 1976, Informational Bulletin on Variable Stars, 1186, 1

Busko, I. C., Quast, G. R., & Torres, C. A. O. 1977, A&A, 60, L27

Busko, I. C., & Torres, C. A. O. 1978, A&A, 64, 153

Butler, C. J., Rodono, M., Foing, B. H., & Haisch, B. M. 1986, Nature, 321, 679

Byrne, P. B. 1989, Sol. Phys., 121, 61

Byrne, P. B., & McKay, D. 1990, A&A, 227, 490

Byrne, P. B., Agnew, D. J., Cutispoto, G., Kilkenny, D. W., Neff, J. E., & Panagi, P. M. 1992, Surface Inhomogeneities on Late-Type Stars, LNP, 397, 255

Caillault, J.-P. 1982, AJ, 87, 558

Caillault, J.-P., Drake, S., & Florkowski, D. 1988, AJ, 95, 887

Canfield, R. C., Cheng, C.-C., Dere, K. P., et al. 1980, in Solar Flares, ed. P. A. Sturrock, 451

Canfield, R. C., Kiplinger, A. L., Penn, M. J., & Wülser, J. P. 1990, ApJ, 363, 318

Caramazza, M., Flaccomio, E., Micela, G., Reale, F., Wolk, S. J., & Feigelson, E. D. 2007, A&A, 471, 645

Cargill, P. J. 1994, ApJ, 422, 381

Cargill, P. J., & Priest, E. R. 1983, ApJ, 266, 383

Cargill, P. J., & Klimchuk, J. A. 1997, ApJ, 478, 799

Carmichael, H. 1964, NASA Special Publication, 50, 451

Carrington, R. C. 1859, MNRAS, 20, 13

Chabrier, G., & Baraffe, I. 1997, A&A, 327, 1039

Chupp, E. L., Forrest, D. J., Higbie, P. R., Suri, A. N., Tsai, C., & Dunphy, P. P. 1973, Nature, 241, 333

Chupp, E. L. 1984, ARA&A, 22, 359

Chupp, E. L. 1987, Physica Scripta, T18, 5

Crespo-Chacón, I., Montes, D., Fernández-Figueroa, M. J., López-Santiago, J., García-Alvarez, D., & Foing, B. H. 2004, Ap&SS, 292, 697

Crespo-Chacón, I., Montes, D., Fernández-Figueroa, M. J., & López-Santiago, J. 2006, in SEA/JENAM 2004, The Many Scales in the Universe, ed. J. C. del Toro Iniesta et al., Session 3, CD-P15

Crespo-Chacón, I., Micela, G., Reale, F., et al. 2007, A&A, 471, 929

Collura, A., Pasquini, L., & Schmitt, J. H. M. M. 1988, A&A, 205, 197

Crosby, N. B., Aschwanden, M. J., & Dennis, B. R. 1993, Sol. Phys., 143, 275

Cully, S. L., Fisher, G. H., Hawley, S. L., & Simon, T. 1997, ApJ, 491, 910

Czesla, S., & Schmitt, J. H. H. M. 2007, A&A, 470, L13

Dahlburg, R. B., Klimchuk, J. A., & Antiochos, S. K. 2005, ApJ, 622, 1191

Datlowe, D. W., Elcan, M. J., & Hudson, H. S. 1974, Sol. Phys., 39, 155

Delfosse, X., Forveille, T., Perrier, C., & Mayor, M. 1998, A&A, 331, 581

Dennis, B. R. 1985, Sol. Phys., 100, 465

Demircan, O., Eker, Z., Karataş, Y., & Bilir, S. 2006, MNRAS, 366, 1511

Ding, M. D., Fang, C., Gan, W. Q., & Okamoto, T. 1994, ApJ, 429, 890

Ding, M. D., & Fang, C. 1996, A&A, 314, 643

Ding, M. D., & Fang, C. 1997, A&A, 318, L17

Ding, M. D., Fang, C., & Yun, H. S. 1999, ApJ, 512, 454

Ding, M. D., Liu, Y., Yeh, C.-T., & Li, J. P. 2003, A&A, 403, 1151

Donati-Falchi, A., Falciani, R., & Smaldone, L. A. 1985, A&A, 152, 165

Doschek, G. A. 1990, ApJS, 73, 117

Doschek, G. A., Mariska, J. T., & Sakao, T. 1996, ApJ, 459, 823

Doschek, G. A., & Warren, H. P. 2005, ApJ, 629, 1150

Doyle, J. G. 1987, MNRAS, 224, 1

Doyle, J. G., Butler, C. J., Bryne, P. B., & van den Oord, G. H. J. 1988, A&A, 193, 229

Doyle, J. G., Byrne, P. B., & van den Oord, G. H. J. 1989, A&A, 224, 153

Doyle, J. G., & Mathioudakis, M. 1990, A&A, 227, 130

Doyle, J. G., van der Oord, G. H. J., & Kellett, B. J. 1992, A&A, 262, 533

Drake, S. A. 1980, Ph.D. Thesis

Drake, S. A., & Ulrich, R. K. 1980, ApJS, 42, 351

Drake, J. J., Ercolano, B., & Swartz, D. A. 2008, ApJ, 678, 385

Duncan, D. K., Vaughan, A. H., Wilson, O. C., et al. 1991, ApJS, 76, 383

Durney, B. R., De Young, D. S., & Roxburgh, I. W. 1993, Sol. Phys., 145, 207

Eason, E. L. E., Giampapa, M. S., Radick, R. R., Worden, S. P., & Hege, E. K. 1992, AJ, 104, 1161

Eberhard, G., & Schwarzschild, K. 1913, ApJ, 38, 292

Ehle, M., Pollock, A. M. T., Talavera, A., et al. 2004, User's Guide to the XMM-Newton Science Analysis System

Emslie, A. G., & Sturrock, P. A. 1982, Sol. Phys., 80, 99

Emslie, A. G., Kucharek, H., Dennis, B. R., et al. 2004, J. Geophys. Res., 109, 10104

Erdélyi, R., & Ballai, I. 2007, Astronomische Nachrichten, 328, 726

Evans, D. S. 1959, MNRAS, 119, 526

Fang, C., & Ding, M. D. 1995, A&AS, 110, 99

Favata, F., Micela, G., & Reale, F. 2000a, A&A, 354, 1021

Favata, F., Micela, G., Reale, F., Sciortino, S., & Schmitt, J. H. M. M. 2000b, A&A, 362, 628

Favata, F., Reale, F., Micela, G., Sciortino, S., Maggio, A., & Matsumoto, H. 2000c, A&A, 353, 987

Favata, F., Micela, G., & Reale, F. 2001, A&A, 375, 485

Favata, F., & Micela, G. 2003, Space Sci. Rev., 108, 577

Favata, F., Flaccomio, E., Reale, F., et al. 2005, ApJS, 160, 469

Feigelson, E. D., & Montmerle, T. 1999, ARA&A, 37, 363

Fletcher, L., & Hudson, H. 2001, Sol. Phys., 204, 69

Fletcher, L., & Hudson, H. S. 2002, Sol. Phys., 210, 307

Fletcher, L., Pollock, J. A., & Potts, H. E. 2004, Sol. Phys., 222, 279

Fletcher, L., Hannah, I. G., Hudson, H. S., & Metcalf, T. R. 2007, ApJ, 656, 1187

Foing, B. H., Char, S., Ayres, T., et al. 1994, A&A, 292, 543

Forbes, T. G., & Malherbe, J. M. 1986, ApJ, 302, L67

Franciosini, E., Pillitteri, I., Stelzer, B., et al. 2007, A&A, 468, 485

Fuhrmeister, B., Schmitt, J. H. M. M., & Hauschildt, P. H. 2005, A&A, 436, 677

Gan, W. Q., Rieger, E., & Fang, C. 1993, ApJ, 416, 886

Gan, W. Q., & Mauas, P. J. D. 1994, ApJ, 430, 891

García-Alvarez, D. 2000, Irish Astron. J., 27, 117

García-Alvarez, D., Jevremović, D., Doyle, J. G., & Butler, C. J. 2002, A&A, 383, 548

García-Alvarez, D. 2003, Ph.D. Thesis

García-Alvarez, D., Foing, B. H., Montes, D., et al. 2003, A&A, 397, 285

Gershberg, R. E. 1974, AZh, 51, 552

Gershberg, R. E. 1989, Mem. Soc. Astron. Italiana, 60, 263

Getman, K. V., Feigelson, E. D., Broos, P. S., Micela, G., & Garmire, G. P. 2008, ApJ, 688, 418

Giardino, G., Favata, F., Micela, G. & Reale, F. 2004, A&A, 413, 669

Giardino, G., Favata, F., Silva, B., et al. 2006, A&A, 453, 241

Giardino, G., Favata, F., Pillitteri, I., et al. 2007, A&A, 475, 891

Gold, T., & Hoyle, F. 1960, MNRAS, 120, 89

Gray, D. F., & Johanson, H. L. 1991, PASP, 103, 439

Grosso, N., Montmerle, T., Feigelson, E. D., André, P., Casanova, S., & Gregorio-Hetem, J. 1997, Nature, 387, 56

Güdel, M., Benz, A. O., Bastian, T. S., Furst, E., Simnett, G. M., & Davis, R. J. 1989, A&A, 220, L5

Güdel, M. 1992, A&A, 264, L31

Güdel, M. 1997, ApJ, 480, L121

Güdel, M. 2004, A&A Rev., 12, 71

Güdel, M., & Benz, A. O. 1993, ApJ, 405, L63

Güdel, M., Linsky, J. L., Brown, A., & Nagase, F. 1999, ApJ, 511, 405

Güdel, M., Audard, M., Briggs, K., et al. 2001, A&A, 365, L336

Güdel, M., Audard, M., Kashyap, V. L., Drake, J. J., & Guinan, E. F. 2003, ApJ, 582, 423

Güdel, M., Audard, M., Reale, F., Skinner, S. L., & Linsky, J. L. 2004, A&A, 416, 713

Gunn, A. G., Doyle, J. G., Mathioudakis, M., & Avgoloupis, S. 1994a, A&A, 285, 157

Gunn, A. G., Doyle, J. G., Mathioudakis, M., Houdebine, E. R., & Avgoloupis, S. 1994b, A&A, 285, 489

Haisch, B. M. 1983, in IAU Colloq. 71, Activity in Red-Dwarf Stars, ed. P. B. Byrne & M. Rodono, 102, 255

Haisch, B. M., Linsky, J. L., Bornmann, P. L., et al. 1983, ApJ, 267, 280

Haisch, B., Strong, K. T., & Rodono, M. 1991, ARA&A, 29, 275

Hall, J. C. 1996, PASP, 108, 313

Hannah, I. G., Christe, S., Krucker, S., Hurford, G. J., Hudson, H. S., & Lin, R. P. 2008, ApJ, 677, 704

Hawley, S. L., & Pettersen, B. R. 1991, ApJ, 378, 725

Hawley, S. L., & Fisher, G. H. 1992a, ApJS, 78, 565

Hawley, S. L., & Fisher, G. H. 1992b, ApJS, 81, 885

Hawley, S. L., Fisher, G. H., Simon, T., et al. 1995, ApJ, 453, 464

Hawley, S. L., Allred, J. C., Johns-Krull, C. M., et al. 2003, ApJ, 597, 535

Heinzel, P., Karlicky, M., Kotrc, P., & Svestka, Z. 1994, Sol. Phys., 152, 393

Hénoux, C., & Nakagawa, Y. 1977, A&A, 57, 105

Henry, T. J., Kirkpatrick, J. D., & Simons, D. A. 1994, AJ, 108, 1437

Hirayama, T. 1974, Sol. Phys., 34, 323

Hodgson, R. 1859, MNRAS, 20, 15

Houdebine, E. R., Foing, B. H., & Rodonò, M. 1990, A&A, 238, 249

Houdebine, E. R. 1992, Irish Astron. J., 20, 213

Houdebine, E. R., Foing, B. H., Doyle, J. G., & Rodono, M. 1993, A&A, 274, 245

Houdebine, E. R., Foing, B. H., Doyle, J. G., & Rodono, M. 1993, A&A, 278, 109

Houdebine, E. R. 2003, A&A, 397, 1019

Hudson, H. S. 1972, Sol. Phys., 24, 414

Hudson, H. S. 1991, Sol. Phys., 133, 357

Hudson, H. S., Acton, L. W., Hirayama, T., & Uchida, Y. 1992, PASJ, 44, L77

Hudson, H. S., Wolfson, C. J., & Metcalf, T. R. 2006, Sol. Phys., 234, 79

Hurford, G. J., Krucker, S., Lin, R. P., Schwartz, R. A., Share, G. H., & Smith, D. M. 2006, ApJ, 644, L93

Isobe, T., Feigelson, E. D., Akritas, M. G., & Babu, G. J. 1990, ApJ, 364, 104

Jakimiec, J., Sylwester, B., Sylwester, J., Serio, S., Peres, G., & Reale, F. 1992, A&A, 253, 269

Jevremović, D., Butler, C. J., Drake, S. A., O'Donoghue, D., & van Wyk, F. 1998, A&A, 338, 1057

Joy, A. H., & Humason, M. L. 1949, PASP, 61, 133

Kallenrode, M.-B. 2004, in Space physics: an introduction to plasmas and particles in the heliosphere and magnetospheres, ed. M.-B. Kallenrode, 182 – 183

Kane, S. R., Hurley, K., McTiernan, J. M., Sommer, M., Boer, M., & Niel, M. 1995, ApJ, 446, L47

Kane, S. R., McTiernan, J. M., & Hurley, K. 2005, A&A, 433, 1133

Kashyap, V. L., Drake, J. J., Güdel, M., & Audard, M. 2002, ApJ, 580, 1118

Kastner, J. H., Crigger, L., Rich, M., & Weintraub, D. A. 2003, ApJ, 585, 878

Katsova, M. M. 1990, Soviet Ast., 34, 614

Katsova, M. M., Livshits, M. A., & Schmitt, J. H. M. M. 2002, in ASP Conf. Ser. 277, Stellar Coronae in the Chandra and XMM-NEWTON Era, ed. F. Favata & J. J. Drake, 515

Klimchuk, J. A. 2006, Sol. Phys., 234, 41

Konstantinova-Antova, R. K., & Antov, A. P. 1995, LNP, 454, 87

Kopp, R. A., & Pneuman, G. W. 1976, Sol. Phys., 50, 85

Kopp, R. A., & Poletto, G. 1984, Sol. Phys., 93, 351

Kraus, J. D. 1966, in Radio Astronomy, ed. J. D. Kraus, 333 – 337

Krucker, S., & Benz, A. O. 1998, ApJ, 501, L213

Kunkel, W. E. 1970, ApJ, 161, 503

Lang, K. R., & Willson, R. F. 1986, ApJ, 305, 363

Lang, K. R. 2009, in The Sun From Space, ed. K. R. Lang, 253 – 336

Lin, R. P., & Hudson, H. S. 1971, Sol. Phys., 17, 412

Lin, R. P., & Hudson, H. S. 1976, Sol. Phys., 50, 153

Lin, R. P., Schwartz, R. A., Kane, S. R., Pelling, R. M., & Hurley, K. C. 1984, ApJ, 283, 421

Linsky, J. L. 2000, American Institute of Physics Conference Series, 522, 389

López-Santiago, J. 2005, Ph.D. Thesis

López-Santiago, J., Montes, D., Fernández-Figueroa, M. J., & Ramsey, L. W. 2003, A&A, 411, 489

López-Santiago, J., Montes, D., Gálvez-Ortiz, M. C., Crespo-Chacón, I., et al. 2010, A&A, 514, A97

Lu, E. T., & Petrosian, V. 1990, ApJ, 354, 735

Machado, M. E., Emslie, A. G., & Brown, J. C. 1978, Sol. Phys., 58, 363

Machado, M. E., Avrett, E. H., Falciani, R., et al. 1986, in The lower atmosphere of solar flares, ed. D. F. Neidig, 483

Machado, M. E., Emslie, A. G., & Avrett, E. H. 1989, Sol. Phys., 124, 303

Maggio, A., Pallavicini, R., Reale, F., & Tagliaferri, G. 2000, A&A, 356, 627

Maggio, A., Drake, J. J., Kashyap, V., et al. 2004, ApJ, 613, 548

Marino, A., Micela, G., & Peres, G. 2000, A&A, 353, 177

Martens, P. C. H., & Kuin, N. P. M. 1989, Sol. Phys., 122, 263

Martínez-Arnáiz, R., Maldonado, J., Montes, D., Eiroa, C., & Montesinos, B. 2010, A&A, 520, A79

Martínez-Arnáiz, R., López-Santiago, J., Crespo-Chacón, I., & Montes, D. 2011a, MNRAS, 414, 2629

Martínez-Arnáiz, R., López-Santiago, J., Crespo-Chacón, I., & Montes, D. 2011b, MNRAS, 417, 3100

Masuda, S. 1994, Ph.D. Thesis

Masuda, S., Kosugi, T., Hara, H., Tsuneta, S., & Ogawara, Y. 1994, Nature, 371, 495

Masuda, S., Kosugi, T., Hara, H., Sakao, T., Shibata, K., & Tsuneta, S. 1995, PASJ, 47, 677

Matthews, S. A., Brown, J. C., & van Driel-Gesztelyi, L. 1998, A&A, 340, 277

Mauas, P. J. D., Machado, M. E., & Avrett, E. H. 1990, ApJ, 360, 715

Mauas, P. J. D., & Falchi, A. 1996, A&A, 310, 245

Metcalf, T. R., Canfield, R. C., Avrett, E. H., & Metcalf, F. T. 1990a, ApJ, 350, 463

Metcalf, T. R., Canfield, R. C., & Saba, J. L. R. 1990b, ApJ, 365, 391

Metcalf, T. R., Alexander, D., Hudson, H. S., & Longcope, D. W. 2003, ApJ, 595, 483

Miklenic, C. H., Veronig, A. M., & Vršnak, B. 2009, A&A, 499, 893

Mirzoyan, L. V. 1984, Vistas Astron., 27, 77

Mitra-Kraev, U., Harra, L. K., Güdel, M., et al. 2005, A&A, 431, 679

Moffett, T. J. 1974, ApJS, 29, 1

Moffett, T. J., & Bopp, B. W. 1976, ApJS, 31, 61

Montes, D., Fernandez-Figueroa, M. J., de Castro, E., & Cornide, M. 1995, A&A, 294, 165

Montes, D., Fernández-Figueroa, M. J., Cornide, M., & de Castro, E. 1996, in ASP Conf. Ser. 109, Cool Stars, Stellar Systems, and the Sun, ed. R. Pallavicini & A. K. Dupree, 657

Montes, D., Saar, S. H., Collier Cameron, A., & Unruh, Y. C. 1999, MNRAS, 305, 45

Montes, D., & Ramsey, L. W. 1999, in ASP Conf. Ser. 158, Solar and Stellar Activity: Similarities and Differences, ed. C. J. Butler & J. G. Doyle, 226

Montes, D., Fernández-Figueroa, M. J., De Castro, E., Cornide, M., Latorre, A., & Sanz-Forcada, J. 2000, A&AS, 146, 103

Montes, D., Crespo-Chacón, I., Fernández-Figueroa, M. J., López-Santiago, J., García-Alvarez, D., & Foing, B. H. 2004, in IAU Symp. 219, Stars as Suns: Activity, Evolution and Planets, ed. A. K. Dupree & A. O. Benz, CD-910

Montes, D., Crespo-Chacón, I., Gálvez, M. C., et al. 2004, LNEA, 1, 119

Morishita H. 1987, in Selected Solar Hα photographs, Norikura Solar Observatory Publication.

Morrison, R., & McCammon, D. 1983, ApJ, 270, 119

Mullan, D. J. 2010, ApJ, 721, 1034

Murdin, P. 2001, in Encyclopedia of Astronomy and Astrophysics, ed. P. Murdin, 4 Volume Set

Neidig, D. F. 1989, Sol. Phys., 121, 261

Neidig, D. F., & Kane, S. R. 1993, Sol. Phys., 143, 201

Neupert, W. M. 1968, ApJ, 153, L59

Nordon, R., & Behar, E. 2007, A&A, 464, 309

Nousek, J. A., & Shue, D. R. 1989, ApJ, 342, 1207

Oranje, B. J. 1986, A&A, 154, 185

Oranje, B. J., Zwaan, C., & Middelkoop, F. 1982, A&A, 110, 30

Osten, R. A., & Brown, A. 1999, ApJ, 515, 746

Osten, R. A., Brown, A., Wood, B. E., & Brady, P. 2002, ApJS, 138, 99

Osten, R. S., Drake, S., Tueller, J., et al. 2007, ApJ, 654, 1052

Pace, G., & Pasquini, L. 2004, A&A, 426, 1021

Pallavicini, R. 1990, in IAU Symp. 142, Basic Plasma Processes on the Sun, ed. E. R. Priest & V. Krishan, 77

Pallavicini, R., Serio, S., & Vaiana, G. S. 1977, ApJ, 216, 108

Pallavicini, R., Golub, L., Rosner, R., Vaiana, G. S., Ayres, T., & Linsky, J. L. 1981, ApJ, 248, 279

Pallavicini, R., Golub, L., Rosner, R., & Vaiana, G. 1982, SAO Special Report, 392, 77

Pallavicini, R. 1988, Mem. Soc. Astron. Italiana, 59, 71

Pallavicini, R., Monsignori-Fossi, B. C., Landini, M., & Schmitt, J. H. M. M. 1988, A&A, 191, 109

Pallavicini, R., Tagliaferri, G., & Stella, L. 1990, A&A, 228, 403

Pan, H. C., & Jordan, C. 1995, MNRAS, 272, 11

Pan, H. C., Jordan, C., Makishima, K., et al. 1997, MNRAS, 285, 735

Parker, E. N. 1963, ApJS, 8, 177

Parker, E. N. 1975, ApJ, 198, 205

Parker, E. N. 1983, ApJ, 264, 642

Parker, E. N. 1988, ApJ, 330, 474

Parnell, C. E., & Jupp, P. E. 2000, ApJ, 529, 554

Patsourakos, S., & Klimchuk, J. A. 2009, ApJ, 696, 760

Payne-Scott, R., Yabsley, D. E., & Bolton, J. G. 1947, Nature, 160, 256

Perryman, M. A. C., Lindegren, L., Kovalevsky, J, et al. 1997, A&A, 323, L49

Petschek, H. E. 1964, NASA Special Publication, 50, 425

Pettersen, B. R. 1976, Institute of Theoretical Astrophysics Blindern Oslo Reports, 46, 1

Pettersen, B. R., & Coleman, L. A. 1981, ApJ, 251, 571

Pettersen, B. R., Coleman, L. A., & Evans, D. S. 1984, ApJS, 54, 375

Pettersen, B. R. 1989, Sol. Phys., 121, 299

Pettersen, B. R., & Hawley, S. L. 1989, A&A, 217, 187

Pettersen, B. R., Panov, K. P., Ivanova, M. S., et al. 1990, in IAU Symp. 137, Flare Stars in Star Clusters, Associations and the Solar Vicinity, ed. L. V. Mirzoian, B. R. Pettersen, & M. K. Tsvetkov, 15

Pettersen, B. R. 1991, Mem. Soc. Astron. Italiana, 62, 217

Phillips, K. J. H., Bromage, G. E., Dufton, P. L., Keenan, F. P., & Kingston, A. E. 1988, MNRAS, 235, 573

Pillitteri, I., Micela, G., Reale, F., & Sciortino, S. 2005, A&A, 430, 155

Poland, A. I., Milkey, R. W., & Thompson, W. T. 1988, Sol. Phys., 115, 277

Poletto, G., Pallavicini, R., & Kopp, R. A. 1988, A&A, 201, 93

Porter, J. G., Fontenla, J. M., & Simnett, G. M. 1995, ApJ, 438, 472

Priest, E. R. 1981, Book - Solar Flare Magnetohydrodynamics

Priest, E., & Forbes, T. 2000, Book - Magnetic Reconnection

Ramaty, R., & Mandzhavidze, N. 2000, in IAU Symp. 195, Highly Energetic Physical Processes and Mechanisms for Emission from Astrophysical Plasmas, ed. P. C. H. Martens, S. Tsuruta, & M. A. Weber, 123

Reale, F. 2002, in ASP Conf. Ser. 277, Stellar Coronae in the Chandra and XMM-NEWTON Era, ed. F. Favata & J. J. Drake, 103

Reale, F. 2003, AdSpR, 32, 1057

Reale, F. 2007, A&A, 471, 271

Reale, F., Serio, S., & Peres, G. 1993, A&A, 272, 486

Reale, F., Betta, R., Peres, G., Serio, S., & McTiernan, J. 1997, A&A, 325, 782

Reale, F., & Micela, G. 1998, A&A, 334, 1028

Reale, F., Peres, G., & Orlando, S. 2001, ApJ, 557, 906

Reale, F., Güdel, M., Peres, G., & Audard, M. 2004, A&A, 416, 733

Reeves, K. K., & Warren, H. P. 2002, ApJ, 578, 590

Rengarajan, T. N. 1984, ApJ, 283, L63

Robinson, R. D. 1989, in IAU Colloq. 104, Solar and Stellar Flares – Poster Papers, ed. B. M. Haisch & M. Rodonò, 83

Robrade, J., & Schmitt, J. H. M. M. 2005, A&A, 435, 1073

Rodonò, M., Houdebine, E. R., Catalano S., et al. 1989, in IAU Colloq. 104, Solar and Stellar Flares – Poster Papers, ed. B. M. Haisch & M. Rodonò, 53

Rosner, R., Tucker, W. H., & Vaiana, G. S. 1978, ApJ, 220, 643

Rucinski, S. M., & Krautter, J. 1983, A&A, 121, 217

Rust, D. M., & Hegwer, F. 1975, Sol. Phys., 40, 141

Rutten, R. G. M., & Schrijver, C. J. 1987, A&A, 177, 155

Rutten, R. G. M., Schrijver, C. J., Zwaan, C., Duncan, D. K., & Mewe, R. 1989, A&A, 219, 239

Ryutova, M., & Tarbell, T. 2003, Phys. Rev. Lett., 90, 191101

Saar, S. H., & Linsky, J. L. 1985, ApJ, 299, L47

Saar, S. H., & Schrijver, C. J. 1987, LNP, 291, 38

Saint-Hilaire, P., & Benz, A. O. 2005, A&A, 435, 743

Sakamoto, Y., Tsuneta, S., & Vekstein, G. 2008, ApJ, 689, 1421

Sanz-Forcada, J., & Micela, G. 2002, A&A, 394, 653

Serio, S., Reale, F., Jakimiec, J., Sylwester, B., & Sylwester, J. 1991, A&A, 241, 197

Schmitt, J. H. M. M., Collura, A., Sciortino, S., Vaiana, G. S., Harnden, F. R., Jr., & Rosner, R. 1990, ApJ, 365, 704

Schmitt, J. H. M. M., Fleming, T. A., & Giampapa, M. S. 1995, ApJ, 450, 392

Schmitt, J. H. M. M. 1997, A&A, 318, 215

Scholz, A., Coffey, J., Brandeker, A., & Jayawardhana, R. 2007, ApJ, 662, 1254

Schrijver, C. J. 1983, A&A, 127, 289

Schrijver, C. J., & Rutten, R. G. M. 1987, A&A, 177, 143

Schrijver, C. J., & Zwaan, C. 2000, in Solar and stellar magnetic activity, ed. C. J. Schrijver & C. Zwaan, 296-299

Sciortino, S. 2008, Mem. Soc. Astron. Italiana, 79, 192

Serio, S., Reale, F., Jakimiec, J., Sylwester, B., & Sylwester, J. 1991, A&A, 241, 197

Siess, L., Dufour, E., & Forestini, M. 2000, A&A, 358, 593

Slee, O. B., Budding, E., Carter, B. D., Mengel, M. W., Waite, I., & Donati, J.-F. 2004, PASA, 21, 72

Smith, D. M., Share, G. H., Murphy, R. J., Schwartz, R. A., Shih, A. Y., & Lin, R. P. 2003, ApJ, 595, L81

Smith, K., Güdel, M., & Audard, M. 2005, A&A, 436, 241

Smith, R. K., Brickhouse, N. S., Liedahl, D. A., & Raymond, J. C. 2001a, ApJ, 556, L91

Smith, R. K., Brickhouse, N. S., Liedahl, D. A., & Raymond, J. C. 2001b, in ASP Conf. Ser. 247, Spectroscopic Challenges of Photoionized Plasmas, ed. G. Ferland & D. W. Savin, 161

Spiesman, W. J., & Hawley, S. L. 1986, AJ, 92, 664

Stassun, K. G., Hebb, L., Covey, K., et al. 2011, 16th Cambridge Workshop on Cool Stars, Stellar Systems, and the Sun, 448, 505

Stauffer, J. R., Hartmann, L. W., & Barrado y Navascues, D. 1995, ApJ, 454, 910

Stelzer, B., Burwitz, V., Audard, M., et al. 2002, A&A, 392, 585

Stelzer, B., & Schmitt, J. H. M. M. 2004, A&A, 418, 687

Stelzer, B., Flaccomio, E., Briggs, K., et al. 2007, A&A, 468, 463

Strassmeier, K. G., Hall, D. S., Fekel, F. C., & Scheck, M. 1993, A&AS, 100, 173

Strüder, L., Briel, U., Dennerl, K., et al. 2001, A&A, 365, L18

Sturrock, P. A. 1966, Nature, 211, 695

Sturrock, P. A. 1968, in IAU Symp. 35, Structure and Development of Solar Active Regions, ed. K. O. Kiepenheuer, 471

Sundland, S. R., Pettersen, B. R., Hawley, S. L., Kjeldseth-Moe, O., & Andersen, B. N. 1988, in Activity in Cool Star Envelopes, Astrophysics and Space Science Library, 143, 61

Susino, R., Lanzafame, A. C., Lanza, A. F., & Spadaro, D. 2010, ApJ, 709, 499

Švestka, Z. 2003, in Dynamic Sun, ed. B. N. Dwivedi, 237

Sweet, P. A. 1958, in IAU Symp. 6, Electromagnetic Phenomena in Cosmical Physics, ed. B. Lehnert, 123

Sylwester, B., Sylwester, J., Serio, S., Reale, F., Bentley, R. D., & Fludra, A. 1993, A&A, 267, 586

Syrovatskii, S. I. 1978, Ap&SS, 56, 3

Tandberg-Hanssen, E., & Emslie, A. G. 1988, in The Physics of Solar Flares, ed. E. Tandberg-Hanssen & A. G. Emslie, Cambridge University Press

Testa, P., Reale, F., García-Alvarez, D., & Huenemoerder, D. P. 2007, ApJ, 663, 1232

Testa, P., Drake, J. J., Ercolano, B., et al. 2008, ApJ, 675, L97

Toner, C., & Gray, D. F. 1988, ApJ, 334, 1008

Torczon, V. 1991, SIAM J. Optimization, 1, 123

Torczon, V. 1992, Tech. Report 92-9, Dep. of Mathematical Sciences, Rice University, Houston

Tovmassian, H. M., Zalinian, V. P., Silant'ev, N. A., Cardona, O., & Chavez, M. 2003, A&A, 399, 647

Tsikoudi, V. 1982, ApJ, 262, 263

Tsujimoto, M., Feigelson, E. D., Grosso, N., et al. 2005, ApJS, 160, 503

Tsuneta, S., Hara, H., Shimizu, T., Acton, L. W., Strong, K. T., Hudson, H. S., & Ogawara, Y. 1992a, PASJ, 44, L63

Turner, M. J. L., Abbey, A., Arnaud, M., et al. 2001, A&A, 365, L27

Vaiana, G. S., Cassinelli, J. P., Fabbiano, G., et al. 1981, ApJ, 245, 163

van den Besselaar, E. J. M., Raassen, A. J. J., Mewe, R., van der Meer, R. L. J., Güdel, M., & Audard, M. 2003, A&A, 411, 587

van den Oord, G. H. J., Mewe, R., & Brinkman, A. C. 1988, A&A, 205, 181

van den Oord, G. H. J., Doyle, J. G., Rodono, M., et al. 1996, A&A, 310, 908

van den Oord, G. H. J., & Mewe, R. 1989, A&A, 213, 245

Vaughan, A. H., Preston, G. W., & Wilson, O. C. 1978, PASP, 90, 267

Verschuur, G. L., & Kellermann, K. I. 1988, in Galactic and Extragalactic Radio Astronomy, 6 – 11

Vilhu, O. 1984, A&A, 133, 117

Vilhu, O., & Walter, F. M. 1987, ApJ, 321, 958

Walter, F. M. 1982, ApJ, 253, 745

Walsh, R. W., & Ireland, J. 2003, A&A Rev., 12, 1

Wang, H., Qiu, J., Jing, J., & Zhang, H. 2003, ApJ, 593, 564

West, A. A., & Hawley, S. L. 2008, PASP, 120, 1161

White, N. E., Culhane, J. L., Parmar, A. N., et al. 1986, ApJ, 301, 262

Wolk, S. J., Harnden, F. R., Jr., Flaccomio, E., et al. 2005, ApJS, 160, 423

Wu, S. T., de Jager, C., Dennis, B. R. et al. 1986, in NASA Conf. Publ. 2439, Energetic Phenomena on the Sun, ed. M. Kundu & B. Woodgate, Chapter 5

Yoshimori, M. 1990, ApJS, 73, 227

Zwaan, C. 1981, in NATO ASIC Proc. 68, Solar Phenomena in Stars and Stellar Systems, ed. R. M. Bonnet & A. K. Dupree, 463

Zwaan, C. 1983, in Solar and Stellar Magnetic Fields: Origins and Coronal Effects, ed. J. O. Stenflo, 102, 85

Appendix A

Ongoing and future work # 1: spectroscopic monitoring of an additional sample of UV Ceti-type stars

A.1 Introduction

This appendix supplements the work described in Chapter 3, where we analysed high temporal resolution spectroscopic observations of the star AD Leo. On that star, we did not detect strong flares. However, we found very interesting short and weak variations in the chromospheric lines that were not accompanied by significant continuum changes in the optical wavelength range, which we interpreted as non white-light flares. We observed these events to be produced with a temporal frequency much higher than detected before for the stellar case. In fact, only a few such events had been previously observed on stars other than the Sun (see the paragraph just before § 3.3.1), although the typical solar flare has no detectable signature in white-light. With the aim of testing whether this kind of variations (non white-light flares happening very frequently) is or not common among UV Ceti-type stars, we monitored a sample of red dwarfs with spectral types K7 to M4. Details about these observations, including the targets, are given in § A.2. First results from this work are shown in § A.3. Preliminary results and some ideas for future work using these observations are summarized in § A.4.

A.2 Observations

All the stars in this appendix, except V1054 Oph, were observed in 21-25 March 2003.

The observations of V1054 Oph were performed during the same observing run than those analysed in Chapter 3. Information about the observing run for V1054 Oph is therefore specified in the first paragraph of § 3.2, while details about its data reduction are given in the last paragraph of the same section.

In the observing run that took place during 21-25 March 2003, spectroscopic observations were carried out with the 2.5 m Isaac Newton Telescope (INT) at the "El Roque

Table A.1: Additional UV Ceti-type stars that were monitored with high temporal resolution. Their names are listed together with their corresponding spectral type (SpT), a remark about their multiplicity (S for single stars, SB1 for singled lined spectroscopic binaries, SB2 for double lined spectroscopic binaries and T for triple star systems), the number of spectra taken of each star (N), and the minimum and maximum exposure times ($t_{\rm exp}$) and signal-to-noise ratios (SNR).

Star	SpT[a]	Remark	N	$t_{\rm exp}$ (s) min-max	SNR min-max
DK Leo	K7	S	91	60-300	19-56
CR Dra	M1	SB2	54	60-300	28-64
DT Vir	M1.5	S	89	60-180	14-61
VV Lyn	M2.5	SB1	24	120-600	20-43
V1054 Oph	M2.5	T	233	15-240	34-112
CE Boo	M3	S	36	90-240	23-41
DP Dra	M3	SB1 (?)	51	90-360	13-37
AD Leo	M3	S	32	60-240	22-73
BL Lyn	M3.5	S	24	120-600	10-24
YZ CMi	M4	S	18	360-600	15-50

[a]From the *CNS3R catalogue* at http://www.ari.uni-heidelberg.de/datenbanken/aricns/index.htm.

de los Muchachos" Observatory (La Palma, Spain)[1]. The Intermediate Dispersion Spectrograph (IDS) was used with the R1200B dispersion grating and the 2148x4200 EEV10a CCD detector. Data reduction was done using the same procedure as that described at the end of § 3.2. The observed wavelength range includes the Balmer series from Hβ to H_{11}, the He I λ4026 Å and the Ca II H & K lines. The reciprocal dispersion is 0.48 Å/pixel and the spectral resolution, determined as the full width at half maximum (FWHM) of the arc comparison[2] lines, is $\approx$ 1.2 Å. For this observing run, we selected some UV Ceti-type flare stars from the Pettersen's (1991) catalogue. The sample of stars was constructed taking the following items into account:

- Regarding the position of the star in the Celestial Sphere, the target must be observable in the moment and from the site in which it was going to be observed.
- Concerning the spectral type of the star, note that (for the purpose shown in § A.1) we were interested on UV Ceti-type flare stars with different spectral types.
- With respect to the visual apparent magnitude of the star, in order to perform a reliable detection of flares of the same type as those studied in Chapter 3, stars as bright as possible were needed for carrying out a high temporal resolution – from tens of seconds to a few minutes – spectroscopic monitoring.

Table A.1 shows the resulting sample of stars together with some relevant information. In order to achieve the highest possible temporal resolution for each target, we took series

[1]No observations were done in the 23 March 2003 night due to bad weather.

[2]The wavelength calibration was done by using spectra of Cu–Ar lamps

of spectra with exposure times as short as 60 s for the brightest stars[3] and up to 600 s for the faintest ones, with the spectra within a given series being separated only by the CCD readout time (less than 60 s for observations of V1054 Oph and ≈ 23 s for the remainder).

A.3 Results

Note that the aim of this appendix in not to give an exhaustive analysis of the flares detected during observations described in § A.2, but to show that the type of variability detected by us in AD Leo (see Chapter 3) is typical of UV Ceti-type stars. Therefore, in the following subsections we will discuss very briefly our results in terms of the observed increase in the equivalent width (EW) of the Hβ line.

A.3.1 Temporal evolution of the EW

For each star, in Fig. A.1 we have plotted the temporal evolution of the EW measured for the Hβ line. The strongest flares in our observations are marked with the symbol ↙ while the symbol ↓ is used to indicate other minor changes that may be due to weaker magnetic reconnection processes. The notes on individual results about the changes, their duration ($\triangle_{Time}$) and increase of EW(Hβ) relative to the level of EW(Hβ) before or after the variation ($\triangle_{EW(\mathrm{H}\beta)}$) are given bellow.

- ⋆ **DK Leo** showed a modulation along the different nights and frequent minor changes within each night. The first part of the observations in night 1 appears to be due to the beginning of a flare. Weak ($\triangle_{EW(\mathrm{H}\beta)} \approx$ - 0.3 Å) and short ($\triangle_{Time} \approx$ 10 min) increases occurred in night 2. Observations in night 5 could correspond to the gradual decay phase of a flare with minor changes lying over it.
- ⋆ **CR Dra** showed the same quiescent value during all the nights in our observations. Several minor changes took place during night 5 within a flare of greater intensity ($\triangle_{Time} >$ 60 min, $\triangle_{EW(\mathrm{H}\beta)} \approx$ - 0.5 Å).
- ⋆ **DT Vir** did not show significant variations until night 5, where the gradual decay of a long-lasting flare ($\triangle_{Time} >$ 200 min, $\triangle_{EW(\mathrm{H}\beta)} <$ - 1.5 Å) may be occurring.
- ⋆ **VV Lyn** did not show any significant change during the hour in which it was monitored.
- ⋆ **V1054 Oph**[4] is the star observed with the best time-coverage in this appendix. Four flares lasting 10 min < $\triangle_{Time}$ < 100 min with $\triangle_{EW(\mathrm{H}\beta)} \approx$ - 2 Å were detected. Some minor changes were also observed. The better-time coverage and larger total-time of observations for this star allowed us to estimate the flare frequency. We detect a mean of one flare per hour in the chromosphere of this star[5].

[3] Note that the better time-weather conditions in the observing run in which V1054 Oph was observed allowed us to observe this star with an exposure time as short as 15 s.

[4] Additional results from the observations described in this appendix for V1054 Oph are reported in the paper by Crespo-Chacón et al. (2004)

[5] Note that this flare-frequency is similar to that measured in Chapter 3 for AD Leo (see § 3.3.1)

- ⋆ **CE Boo** showed two contiguous flares during night 1 (the only night in which it was continuously monitored) with almost equal intensity and duration ($\triangle_{Time} \approx 30$ min, $\triangle_{EW(\mathrm{H}\beta)} \approx$ - 0.6 Å), starting the second one before the end of the first one.

- ⋆ **DP Dra** showed a flare decay in night 1, with frequent minor changes laying over it. Minor changes ($\triangle_{Time} \approx 10$ min, $\triangle_{EW(\mathrm{H}\beta)} \approx$ - 0.3 Å) are also observed in night 4. A large flare ($\triangle_{Time} \approx 60$ min, $\triangle_{EW(\mathrm{H}\beta)} \approx$ - 4 Å) appears in night 5.

- ⋆ **AD Leo** was observed again to investigate if the kind of variations studied in Chapter 3 occurred occasionally in this stars' chromosphere. The new observations of AD Leo confirm our belief that, independently on the date in which it is monitored, the latter kind of variations can be detected in its chromosphere. The flares detected during the new observations lasted $\triangle_{Time} \approx 20$ min, showing $\triangle_{EW(\mathrm{H}\beta)} \approx$ - 0.7 Å.

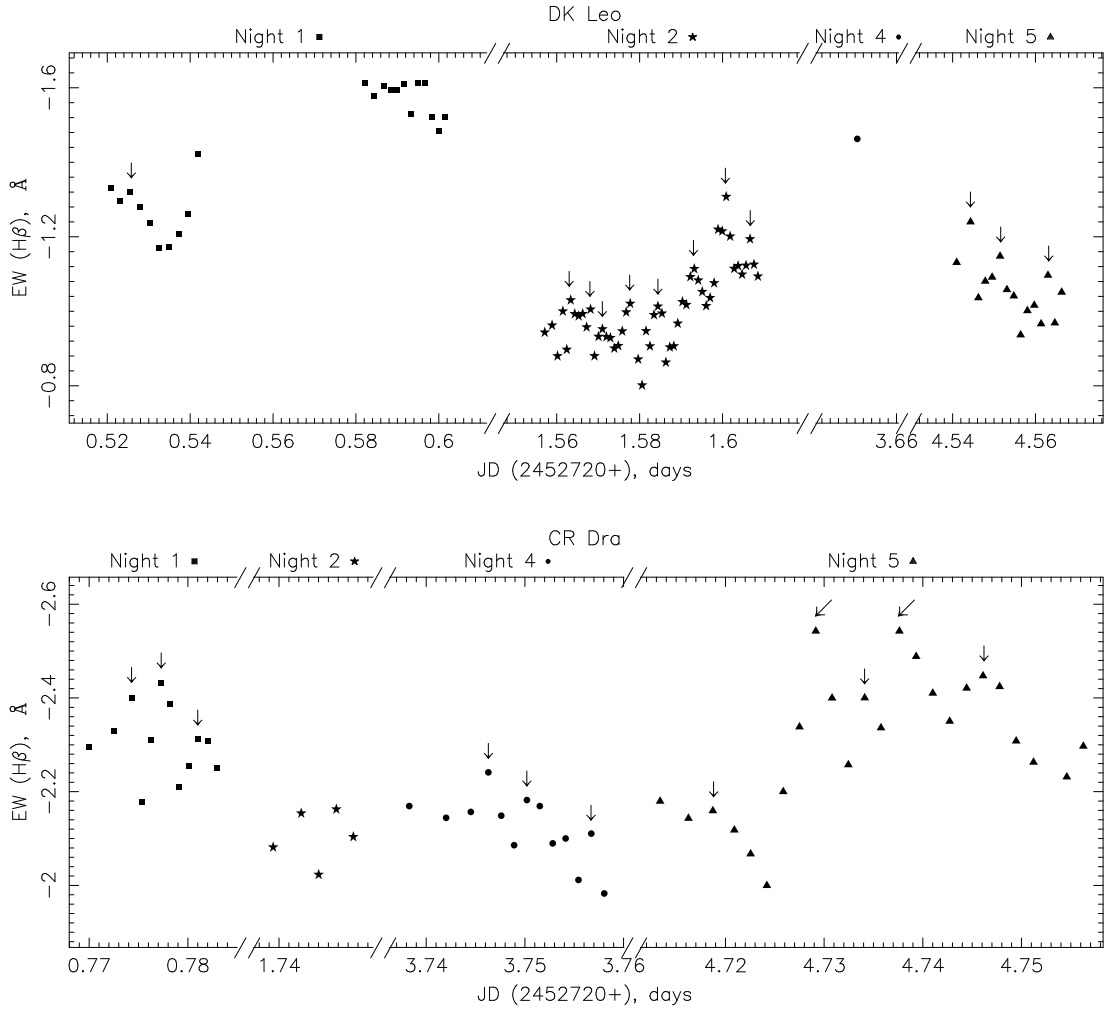

Figure A.1: Temporal evolution of the *EW* of the Hβ line for each star of the additional sample.

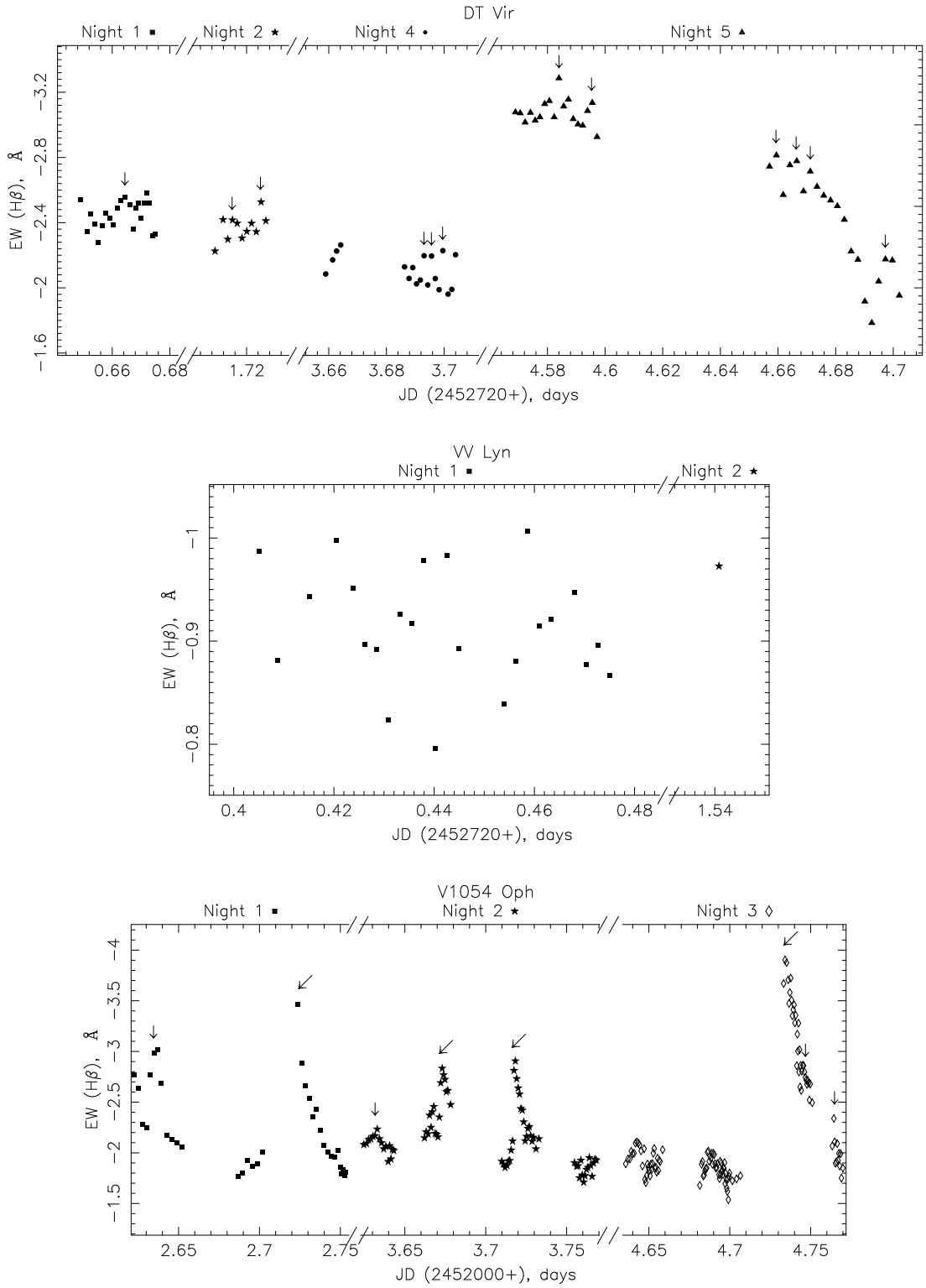

Figure A.1: Continuation.

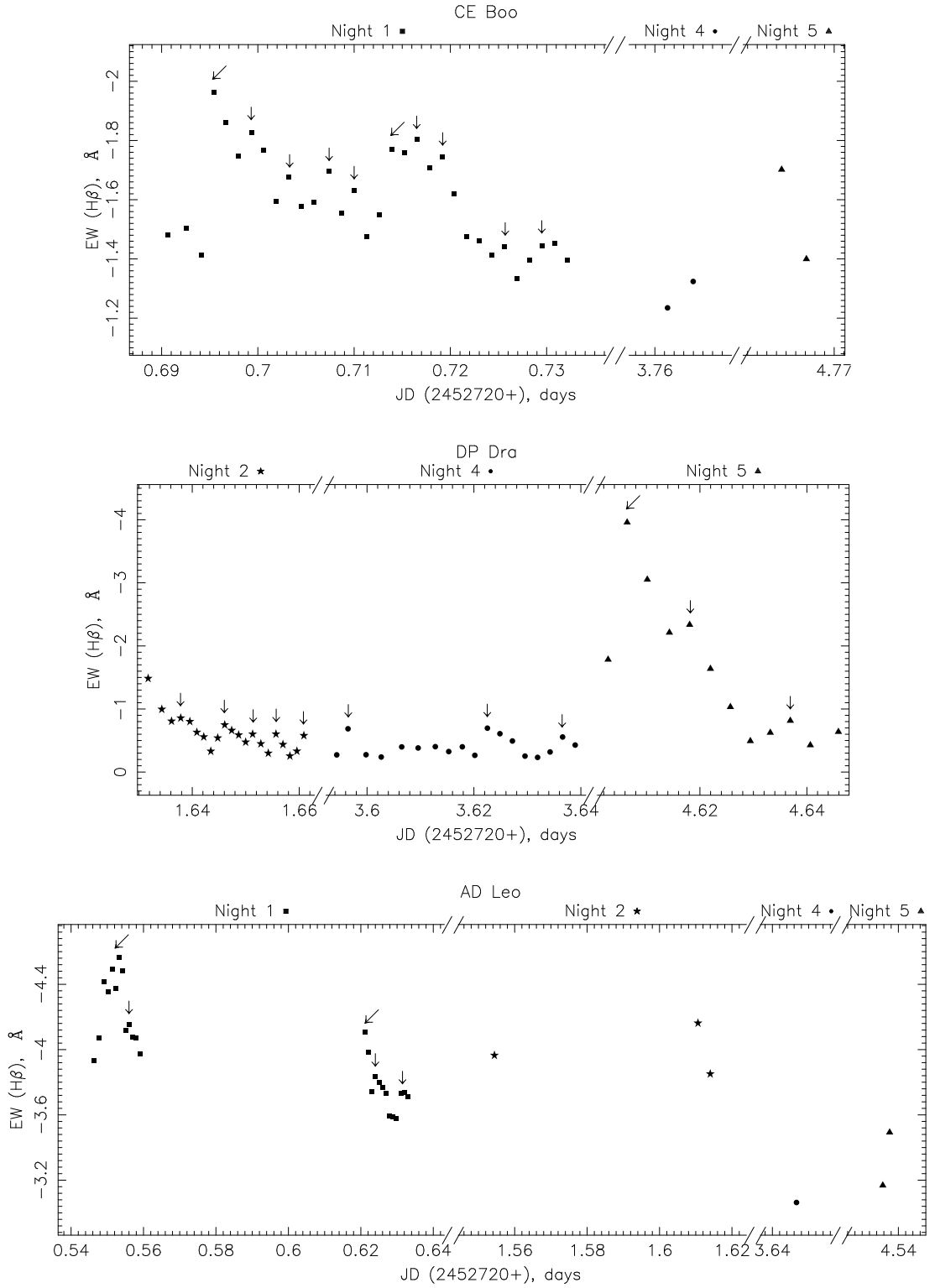

Figure A.1: Continuation.

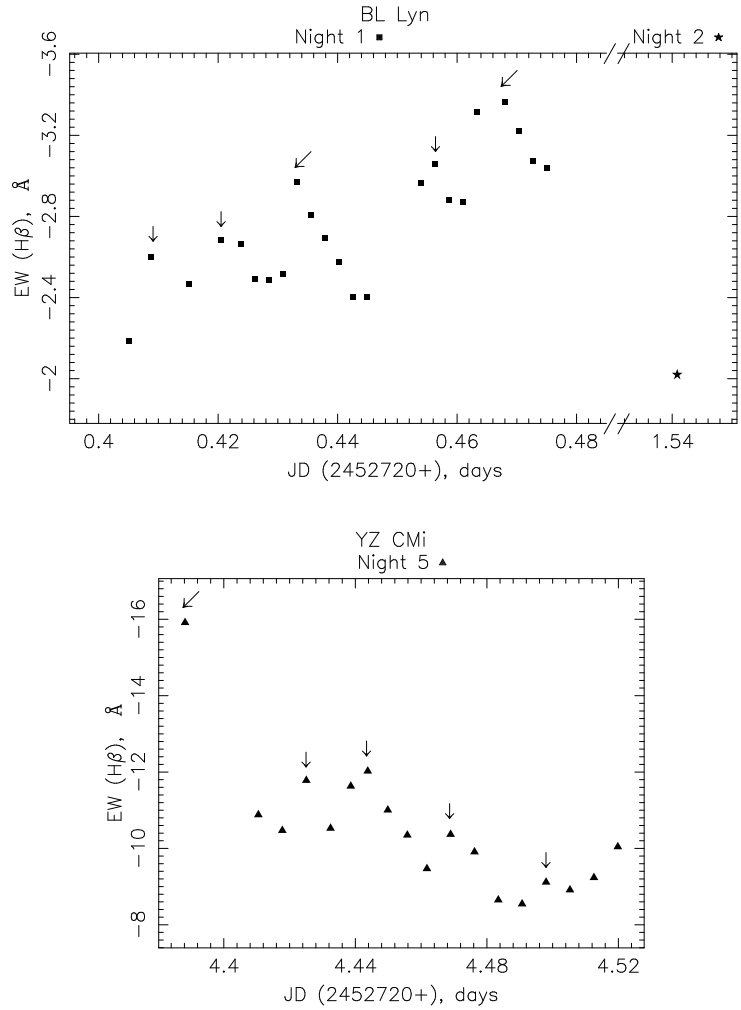

Figure A.1: Continuation.

- ⋆ **BL Lyn** showed a gradual increase in night 1 (the only night in which it was continuously monitored), during which minor changes and possibly two flares of equal duration and intensity ($\triangle_{Time} \approx 20$ min, $\triangle_{EW(\mathrm{H}\beta)} \approx$ - 0.7 Å) were observed.

- ⋆ **YZ CMi** was monitored only during night 5. A flare decay of a long-lasting and strong flare ($\triangle_{Time} > 180$ min, $\triangle_{EW(\mathrm{H}\beta)} <$ - 8 Å) was detected from the beginning to the end of the observation.

A.3.2 Spectral features

The quiescent spectrum of the observed UV Ceti-type stars has been plotted in Fig. A.2. The presence of molecular bands is evident in the coolest stars of our sample. In general, the cooler the star, the higher the *EW* of the chromospheric emission lines, even though for stars with the same spectral type it also depends on the level of activity (which varies

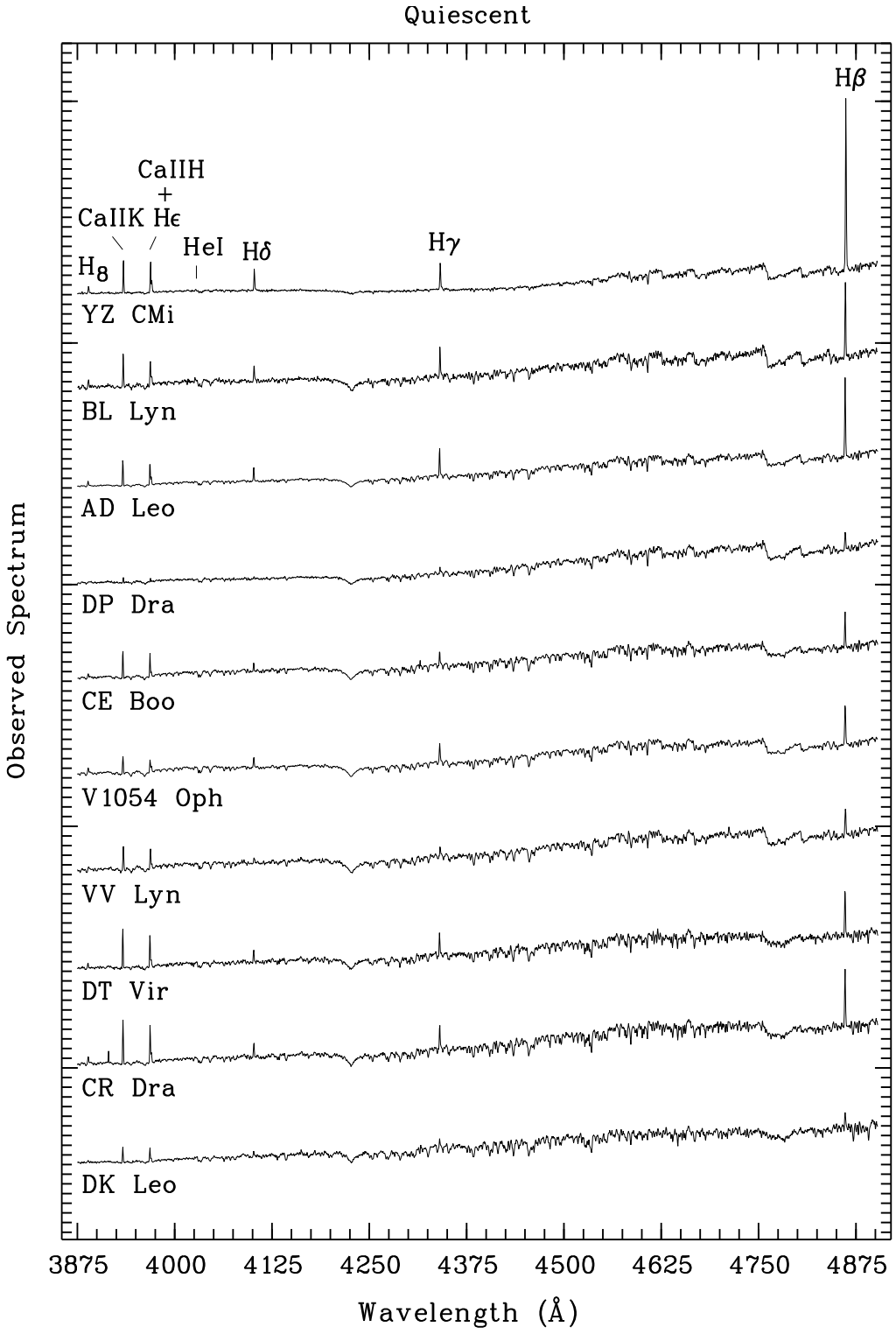

Figure A.2: Quiescent spectrum of the observed stars. The spectra are ordered by spectral type (the star with the latest spectral type is in the top).

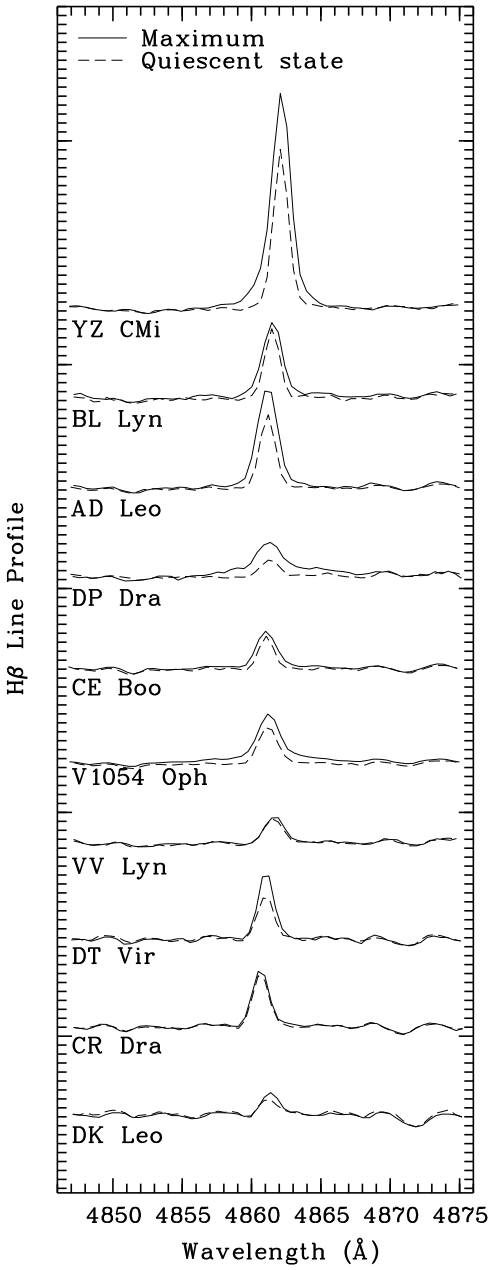

Figure A.3: Profile of the Hβ line in the quiescent state (dotted line) and in the spectrum corresponding to the maximum observed $\triangle_{EW(\mathrm{H}\beta}$ (solid line).

depending on the rotation velocity of the star).

For each star, Fig. A.3 shows the profile of the Hβ line in the quiescent state (dotted line) and in the spectrum corresponding to the maximum observed $\triangle_{EW(\mathrm{H}\beta)}$ (solid line). The enhancement and broadening of the wings of the Hβ line are noticeable only for V1054 Oph, CE Boo, DP Dra, AD Leo, BL Lyn and YZ CMi, that are the stars showing larger $\triangle_{EW(\mathrm{H}\beta)}$. The width and enhancement of the wings depend on the phase of the flare. They decrease during the gradual decay. This may be the reason why the enhancement

and broadening of the wings of Hβ are negligible for DT Vir, for which only the late decay of a flare was observed. On the other hand, all the stars with flares show an increase in the core of the Hβ line.

For all the stars, we overlapped the normalized observed spectra to find possible changes in the continuum during all the flares and minor changes detected by us. Significant changes were detected neither in the depth of the absorption lines nor in the shape of the continuum. Thus, within the analysed wavelength range, the flares appearing in Fig. A.1 only affect the emission in the chromospheric lines. They can therefore be classified as non white-light flares.

A.4 Preliminary conclusions and future work

A total of 10 UV Ceti-type stars with spectral type K7 to M4 were monitored with high temporal resolution. Since the available observing time (4 nights) was shared by all these stars[6], the time-coverage for each one of them was not as good as desirable. Nevertheless, non white-light flares lasting from ten to hundreds of minutes were detected in all of them except VV Lyn. For the star having the observations with the best time-coverage (V1054 Oph), we estimated a frequency of one flare of this type per hour. Thus, from observations in this appendix we conclude that the kind of flare-variability that was detected by us in the chromosphere of AD Leo (see Chapter 3) appears to be typical of UV Ceti-type stars.

The observations described in § A.2 will allow us to analyse the behaviour of different chromospheric emission lines (Balmer series, Ca II H & K lines and He I λ4026 Å) during the detected events. Physical parameters of the flaring plasma will be obtained by using an improved version of the procedure for Balmer Decrement line modeling (BDFP) that was described in § 3.4. Not only the maximum phase will be modeled with the BDFP, but also the time-evolution of the physical parameters will be derived for some of the detected flares. The obtained results will be included in the plots given in Figs. 3.10 and 3.11 to investigate those relationships with a larger sample of points (those figures only included results for the 9 flares modeled with the BDFP in Chapter 3).

[6]Excepting V1054 Oph, which was monitored in a different observing run (see § A.2).

Appendix B

Ongoing and future work # 2: peculiarities in the chromospheric activity indicators of flare stars

B.1 Introduction

The clear correlation between the strength of the atmospheric magnetic field and the outer-atmospheric emission in the solar atmosphere formed the underlying reason behind the search for similar trends in stars other than the Sun. Since the discovery of emission in the core of both the Ca II H & K lines in stellar spectra (Eberhard & Schwarzschild 1913), chromospheric magnetic activity has been extensively studied through this two features (Vaughan et al. 1978; Duncan et al. 1991). In addition to the Ca II H & K emission, there is a variety of outer-atmospheric emissions that serve as measures of magnetic activity. These activity diagnostics show similar, and interrelated, behaviour, as demonstrated in the early studies by Zwaan (1981) and Oranje et al. (1982).

The radiative emissions that measure the magnetic activity of cool stars can be expressed with different units (luminosity, flux density, or flux density relative to the bolometric flux density). However, Schrijver (1983) and Rutten & Schrijver (1987) demonstrated that the stellar level of activity is best expressed in terms of the radiative surface flux density: the luminosity introduces an extra dependence on stellar radius, whereas the flux density normalized by the bolometric flux density introduces a dependence on color.

When the (sometimes substantial) contribution from the (acoustically driven) basal atmosphere is subtracted from the observed emission, power-law relationships are found between the so-called *excess flux densities*[1] (see Eq. B.1, where $\Delta F_{\rm i}$ and $\Delta F_{\rm j}$ are the excess fluxes in two different lines, and $a_{\rm ij}$ and $b_{\rm ij}$ are two constant factors to be determined).

$$\Delta F_{\rm j} = a_{\rm ij} \Delta F_{\rm i}^{b_{\rm ij}} \tag{B.1}$$

Studies by different authors (e.g., Oranje 1986; Rutten et al. 1989) concluded that these power-law relationships extend over 2 – 5 orders of magnitude (depending on the

[1] The excess flux density in a given line $\Delta F_{\rm i}$ is the integrated line flux measured in the spectrum which results from subtracting the (acoustically driven) basal atmosphere.

activity diagnostic used) and do not generally depend significantly on either the luminosity class (for classes II-V)[2] or the spectral type (provided that the very cool stars beyond mid-M type are excluded). Not only single stars but also most active binaries obey the flux-flux relationships. The flux-flux relationships hold for all cool stars, with the following few exceptions: the W UMa contact systems deviate from the flux-flux relationships where the low-chromospheric Mg II h+k flux is involved, but not in other diagnostics; the very rapidly rotating, apparently single FK Com stars appear to deviate somewhat from some of the main flux-flux relationships (Bopp & Stencel 1981) as do the very young T Tauri stars with accretion disks (Schrijver & Zwaan 2000); M-dwarfs show clear departures from the main flux-flux relationships in some chromospheric lines (Pallavicini et al. 1982; Zwaan 1983; Oranje 1986; Schrijver & Rutten 1987; Rutten et al. 1989).

The sample of M-dwarfs in all these studies has been systematically biased towards the category of emission-line stars (see e.g., Oranje 1986; Schrijver & Rutten 1987; Rutten et al. 1989). Thus, they did not conclude whether the departures from the main flux-flux relationships observed for M-dwarfs are restricted to late-type dwarfs with clear emission-line characteristics, or whether these departures are common for a larger group of active late K- and M-type dwarfs. Moreover, for certain lines such as Hα, they only measured the emission above the continuum, neglecting any filling in of the Hα absorption line. In this appendix we show that departures from the main flux-flux relationships are only found for UV Ceti-type stars (i.e. K7e or Me flare dwarfs).

For this research, we used high resolution optical *echelle* spectra. Note that a noteworthy advantage of this spectra is that they cover a large fraction of the optical spectrum simultaneously. Therefore, they allow a simultaneous observation of a great deal of the activity diagnostics present in the optical range, avoiding the spread in the flux-flux relationships caused by temporal variability of activity levels. This fact implies a substantial improvement with respect to previous studies, where flux-flux relationships were obtained by using non-simultaneous observations of the activity diagnostics. In addition, for the lines observed in emission, we include its filling in component of the absorption feature, instead of measuring only its emission above the continuum. Details about data selection and analysis are given in § B.2. Results are shown in § B.3. Discussion about these results is given in § B.4. Some ideas for future work on this subject are summarized in § B.5.

B.2 Data selection and analysis

In a recent publication, López-Santiago et al. (2010) (hereafter LS10) made accessible to the scientific community a compilation of spectroscopic data from a survey of 144 chromospherically active young stars (spectral types F, G, K, M) in the solar neighbourhood[3]. Using the spectral subtraction technique (see § B.2.1), LS10 measured excess flux densities in the spectra obtained with high resolution echelle spectrographs (resolving power, $\Delta\lambda/\lambda$, ranging from 30000 to 60000). These spectra include all the optical chromospheric

[2]The supergiants (luminosity class I) do obey the relationships between chromospheric and transition-region fluxes, even though they do not emit a measurable soft X-ray flux.

[3]Most of these data were obtained and used by López-Santiago during his Ph.D. Thesis (López-Santiago 2005).

Table B.1: UV Ceti-type stars analysed in this work. Their names are listed together with their corresponding spectral type (SpT), photometric period ($P_{\rm phot}$, when available), remark about their multiplicity (S for single stars, SB1 for single lined spectroscopic binaries, SB2 for double lined spectroscopic binaries and T for triple star systems), total number of observations that are available in LS10 (N), and number(s) of the observing run(s) in which they were observed (ID, see Table. B.2).

Star	SpT	$P_{\rm phot}$ (days)	Remark	N	ID
FP Cnc	K7	–	S	2	10
HD 160934	K7	1.84	SB1	7	4, 10, 11
DK Leo	K7–M0	7.98	S	2	10
GJ 9809	M0	–	S	1	8
GJ 856B	M1	–	S	1	8
CR Dra	M1–M1.5	–	SB2	5	11
AD Leo	M3.5	2.7	S	6	3, 10
V647 Her	M4	1.34	S	2	11
EV Lac	M4	4.38	S	11	4, 7, 8

activity diagnostics from the Ca II H & K lines to the Ca II IR triplet, which are formed at different atmospheric heights and, therefore, temperatures. The LS10's sample contains 10 UV Ceti-type stars. Their names are given in Table B.1, together with some relevant information. Table B.2 lists the details about the spectral configuration of the LS10's observing runs in which these stars were observed. Note that the spectral resolution, determined as the full width at half maximum – FWHM – of the arc comparison lines, ranges between 0.08 and 0.35 Å.

This appendix is focused in the UV Ceti-type stars shown on Table B.1, although their excess flux densities in different activity diagnostics will be compared with those given for the remaining stars in LS10.

B.2.1 Determination of the excess flux densities

The (acoustically driven) basal atmosphere is common to active and non-active stars. Thus, non-active stars can be used as reference for subtracting both the photospheric and the (acoustically driven) basal contribution from the total emission of active stars. This subtraction is performed by applying the spectral subtraction technique (see below). In the resulting spectra, the equivalent width of the chromospheric activity diagnostics of interest ($\Delta EW_{\rm l}$, where the operator Δ implies that any basal contribution is to be subtracted) is measured. Since LS10's spectra are not flux-calibrated, excess flux densities are obtained from $\Delta EW_{\rm l}$ by using the calibration derived by Hall (1996) for converting equivalent widths into absolute surface fluxes.

Table B.2: Observing log: Number of the observing run (ID), date in which the corresponding observing run was performed, instrumental configuration (telescope, instrument and CCD chip), and spectral parameters of each observing run (spectral range, dispersion, and $FWHM$ of the arc comparison lines).†

ID	Date	Telescope	Instrument	CCD chip	Spectral range (Å)	Dispersion (Å/pixel)	$FWHM$ (Å)
3	18–22 01/2000	INT[a]	MUSICOS[b]	1024×1024 24μm TEK5	4430–10225	0.07–0.15	0.16–0.30
4	05–11 08/2000	INT[a]	MUSICOS[b]	1024×1024 24μm TEK5	4430–10225	0.07–0.15	0.16–0.30
7	21–24 09/2001	2.2 m[c]	FOCES[d]	2048×2048 24μm Site#1d	3510–10700	0.04–0.13	0.08–0.35
8	10–11 10/2001	TNG[e]	SARG[f]	2(2048×4096) 13.5μm EEV 4280	4960–10110	0.02–0.04	0.08–0.17
10	22–25 04/2002	2.2 m[c]	FOCES[d]	2048×2048 24μm Site#1d	3510–10700	0.04–0.13	0.08–0.35
11	01–06 07/2002	2.2 m[c]	FOCES[d]	2048×2048 24μm Site#1d	3510–10700	0.04–0.13	0.08–0.35

[a] 2.5 m Isaac Newton Telescope at the Observatorio del Roque de los Muchachos (La Palma, Spain).
[b] ESA-<AD>MUSICOS spectrograph developed as part of the MUlti-SIte COntinuous Spectroscopy project.
[c] 2.2 m Telescope at the German Spanish Astronomical Observatory CAHA (Almería, Spain).
[d] Fibre Optics Cassegrain Echelle Spectrograph.
[e] 3.5 m Telescopio Nazionale Galileo at the Observatorio del Roque de los Muchachos (La Palma, Spain).
[f] Spettrografo ad Alta Risoluzione Galileo.

†Information in this table is an extract from LS10.

Spectral subtraction technique

The spectral subtraction technique (see e.g. Montes et al. 1995, 2000, 2004, for some applications) was developed to subtract the underlying photospheric contribution from a stellar spectrum. In this way, the spectral emission originated at the chromosphere can be studied in detail. The photospheric background is artificially computed by constructing a synthesized spectrum with the program STARMOD, developed at the Penn State University (Barden 1985). When the synthesized spectrum is made up of real spectra of non-active stars with spectral types and luminosity classes matching those of each one of the components of the stellar system, in addition to the photospheric background, the basal chromosphere is also subtracted (see Martínez-Arnáiz et al. 2010). Since power-law relationships between the flux in different activity diagnostics only hold when the basal atmospheric contribution is subtracted, for our study we used real spectra of non-active stars to build each one of the synthesized spectra. Thus, each one of the synthesized spectra for LS10 consists of the sum of the rotationally broadened, radial-velocity shifted, and weighted spectra of all the inactive stars that are chosen to match the spectral types and luminosity classes of the components of each one of the active systems under consideration (also in LS10). In LS10, the inactive stars used as reference stars for synthesizing the spectra to be subtracted were observed during the same observing run as their respective active stars.

Converting equivalent widths to surface fluxes

Assuming that the continuum flux under a spectral line is constant throughout the spectral range covered by the line ($F_{c,l}$), the definition of the equivalent width implies that the flux in the line (F_l) can be obtained from its equivalent width (EW_l) by simply using Eq. B.2:

$$F_l = EW_l \cdot F_{c,l}, \tag{B.2}$$

where the continuum flux depends on the spectral line. Eq. B.2 can be used with continuum fluxes estimated for the surface of a star. In the latter case, Eq. B.2 provides stellar surface fluxes in the lines of interest. Hereafter in this chapter, fluxes in both the continuum and lines are always assumed to be surface fluxes.

Hall (1996) reported empirical relationships between the surface continuum flux and different colour indexes for the spectral regions containing the activity diagnostics Ca II H & K lines, Hα and the Ca II infrared triplet (IRT: λ8498Å, λ8542Å and λ8662Å). Excess flux densities (ΔF_l) given in LS10 for these activity diagnostics were calculated by using their corresponding ΔEW_l (measured in the subtracted spectra) and continuum value obtained with the Hall's (1996) calibration as input in Eq. B.2.

We note that the Hall's (1996) relationships are linear for the spectral type range covered by the stars in LS10 with the exception of the calibration for the Hα spectral region, for which Hall (1996) found small deviations from the linear trend for the stars with $B-V \geq 1.4$. This implies that the calibration by Hall (1996) for the Hα spectral region may not be valid for stars cooler than M2/M3. Thus, for the M2 and cooler stars in LS10, we have checked that the Hall's (1996) calibration provides reliable values also in the Hα region. With this aim, we compared the surface continuum flux in the Hα region obtained with the

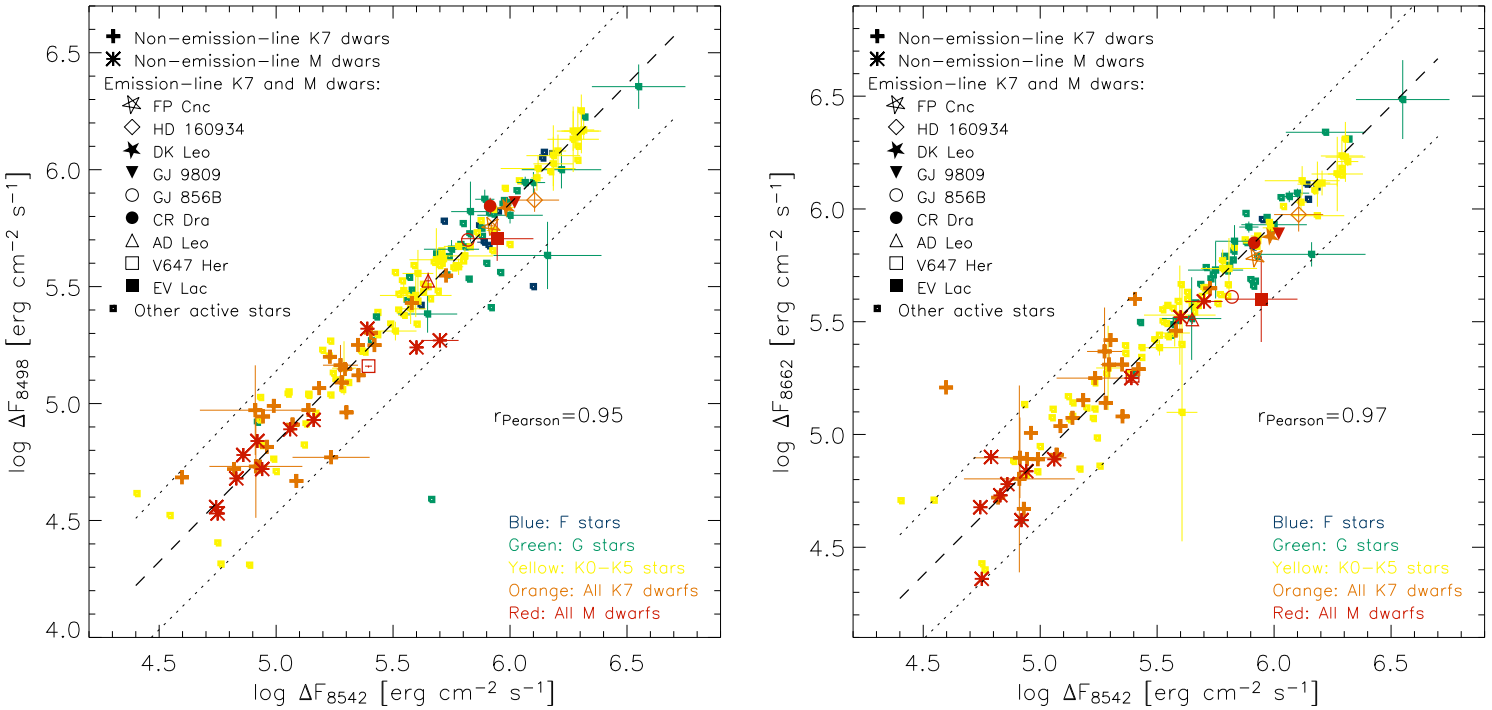

Figure B.1: Logarithmic flux-flux diagrams between different Ca II activity indicators (in particular, the Ca II IRT [λ8498Å, λ8542Å and λ8662Å] and the Ca II H & K lines). Note that the (acoustically driven) basal contribution is subtracted. Different colours correspond to different spectral types (see the lower legend in the right side of each plot). Each UV Ceti-type star is marked with a special symbol (see the upper legend in the left side of each plot). The symbol denoting non-emission-line K7 dwarfs is also different from the one with which non-emission-line M dwarfs are plotted, and both of them are also different from the symbol used for the remaining active stars in LS10. The dashed line in each plot shows the linear fit calculated by using the corresponding results for all the stars in the plot, excluding those calculated for the emission-line K7 and M dwarfs. Dotted lines are the upper and lower boundaries of the region with a 95 % confidence level of containing an observed point.

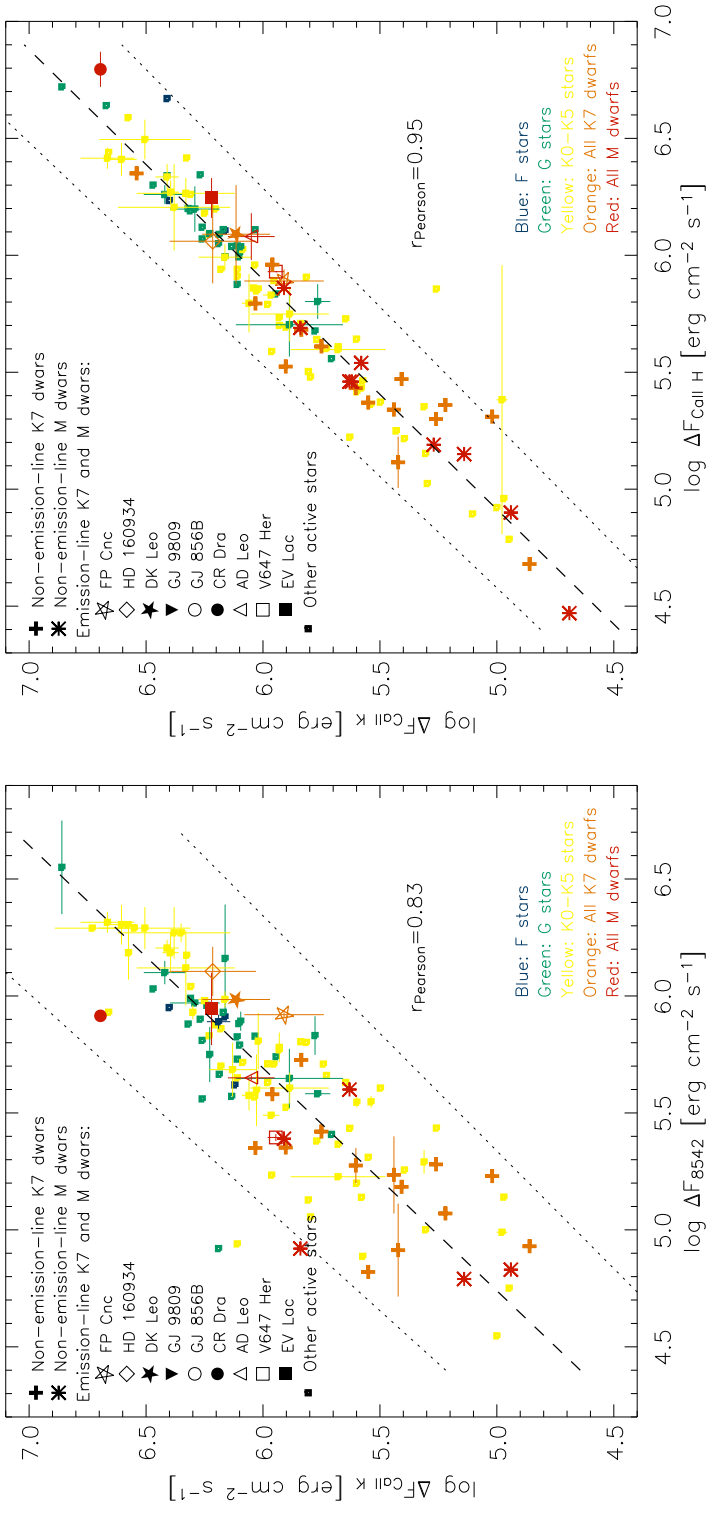

Figure B.1: Continuation.

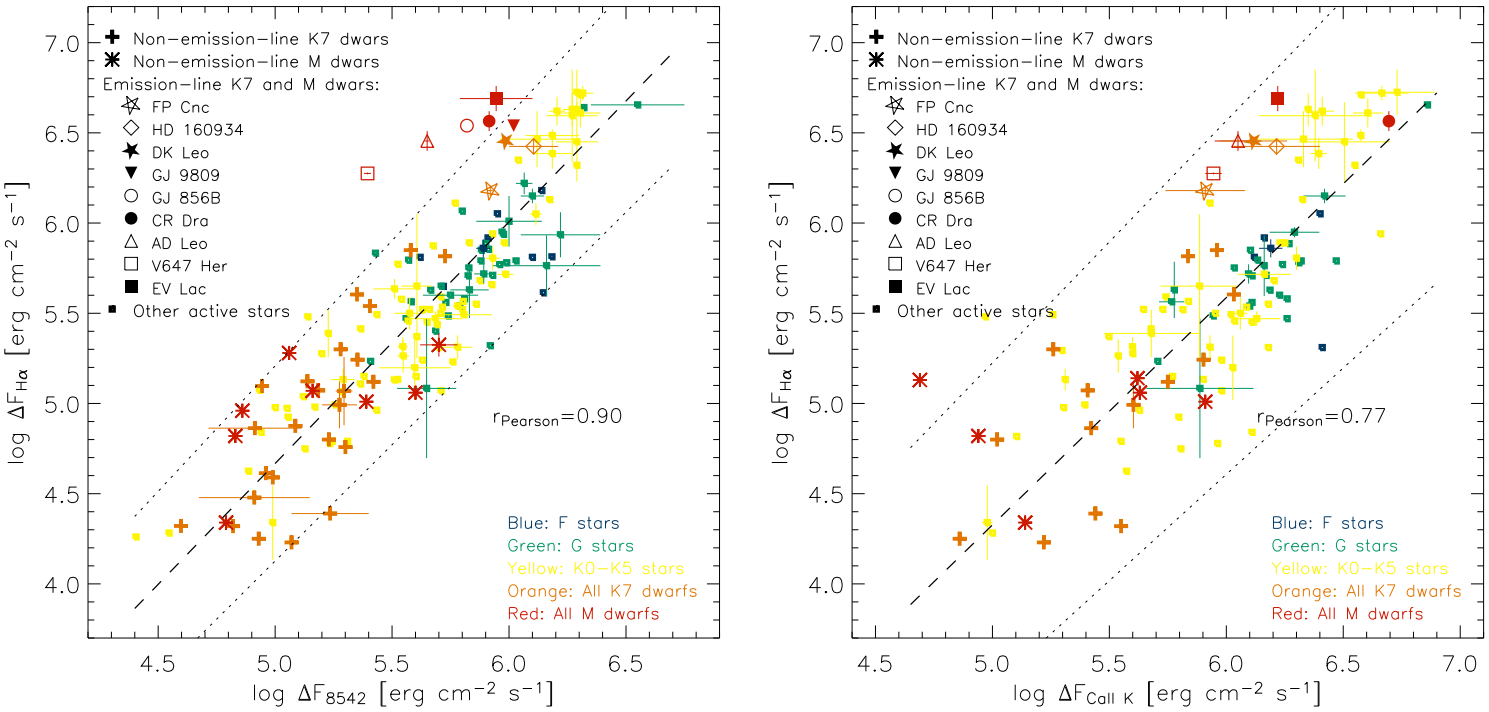

Figure B.2: Logarithmic flux-flux diagrams between the Hα line and the Ca II λ8542Å (left panel) and the Ca II K (right panel) lines. Note that the (acoustically driven) basal contribution is subtracted. The colours, symbols, dashed and dotted lines have the same meaning as those used in Fig. B.1.

Hall's (1996) calibration with those determined with the method given by West & Hawley (2008). For spectral types from M0 to L0, West & Hawley (2008) gives values for ratio of the Hα continuum region luminosity to the bolometric luminosity ($L_{\rm bol}$) as a function of both spectral type and color. This ratio is dubbed χ (see Eq. B.3), and when multiplied by the surface bolometric flux yields the surface continuum flux in the Hα continuum region.

$$\chi = L_{\rm c,H\alpha}/L_{\rm bol} = F_{\rm c,H\alpha}/F_{\rm bol} \tag{B.3}$$

The deviation between the flux in the Hα continuum region calculated by using the Hall's (1996) calibration, and the one obtained with the method by West & Hawley (2008) results to be always less than the corresponding uncertainty in the value from the latter method, being the maximum deviation ≈ 0.2 dex. Thus, the Hall's (1996) calibration for the continuum flux in the Hα region can be used for all the M stars in LS10 with the same level of confidence than the calibration by West & Hawley (2008).

B.3 Results

If Eq. B.1 holds, a linear relationship between the logarithm of two different excess flux densities is expected, that is:

$$\log \Delta F_{\rm j} = \log {\rm a_{ij}} + {\rm b_{ij}} \log \Delta F_{\rm i}, \tag{B.4}$$

where '$\rm b_{ij}$' and '$\log \rm a_{ij}$' are the slope and the intercept in the '$\log \Delta F_{\rm j}$' - axis.

In Figs. B.1 and B.2 we show the logarithmic diagrams between pairs of excess flux density in different activity diagnostics (namely, the Ca II H & K lines, the Ca II IRT [λ8498Å, λ8542Å, and λ8662Å] and the Hα line) for the stars in LS10[4]. We obtained the linear Pearson correlation coefficient ($\rm r_{Pearson}$) using only data for the stars with spectral types from F to K5 (i.e., excluding both emission- and non-emission-line K7 and M stars). The value of $\rm r_{Pearson}$ obtained for each pair of excess flux densities is shown in its corresponding plot. We obtained values of $\rm r_{Pearson}$ between 0.77 and 0.97, depending on the pair. Thus, a linear relationship with a positive slope is compatible with the points in each one of the pairs '$\log \Delta F_{\rm j}$' – '$\log \Delta F_{\rm i}$' analysed in Figs. B.1 and B.2. That is, Eqs. B.1 and B.4 hold.

The best linear relationship for stars with spectral types F to K5 in each panel of Figs. B.1 and B.2 is plotted as a dashed line. These relationships were determined using the method explained by Isobe et al. (1990)[5], and are given in Eqs. B.5 to B.10. For each one of these relationships, and taking the estimated error in both its slope and its intercept with the vertical axis into account, we calculated the upper and lower boundaries (dotted lines in Figs. B.1 and B.2) of the region with a 95 % confidence level of containing an observed point.

[4]For those stars observed more than once, we plot the median value from all their observations and err-type bars representing their maximum observed deviation from the median value in each direction

[5]When two variables (X and Y) are interrelated by a linear relationship, the best estimate for the underlying functional relation between them is the bisector of the two ordinary least squares regressions Y vs. X and X vs. Y (Isobe et al. 1990).

$$\log \Delta F_{\mathrm{CaII\ 8498}} = (-0.27 \pm 0.16) + (1.02 \pm 0.03) \log \Delta F_{\mathrm{CaII\ 8542}} \tag{B.5}$$

$$\log \Delta F_{\mathrm{CaII\ 8662}} = (-0.31 \pm 0.16) + (1.04 \pm 0.03) \log \Delta F_{\mathrm{CaII\ 8542}} \tag{B.6}$$

$$\log \Delta F_{\mathrm{CaII\ K}} = (0.0 \pm 0.3) + (1.05 \pm 0.06) \log \Delta F_{\mathrm{CaII\ 8542}}, \tag{B.7}$$

$$\log \Delta F_{\mathrm{CaII\ K}} = (0.00 \pm 0.19) + (1.02 \pm 0.03) \log \Delta F_{\mathrm{CaII\ H}}, \tag{B.8}$$

$$\log \Delta F_{\mathrm{H}\alpha} = (-2.0 \pm 0.3) + (1.34 \pm 0.05) \log \Delta F_{\mathrm{CaII\ 8542}}, \tag{B.9}$$

$$\log \Delta F_{\mathrm{H}\alpha} = (-2.0 \pm 0.5) + (1.26 \pm 0.08) \log \Delta F_{\mathrm{CaII\ K}}, \tag{B.10}$$

The slopes in the relationships between the pairs '$\log \Delta F_{\mathrm{j}}$' – '$\log \Delta F_{\mathrm{i}}$' (Eqs. B.5 to B.10) follow this trend: the larger the difference in atmospheric height at which the compared lines form, the larger the value of the slope. In results from previous studies by other authors, the same trend is found not only for chromospheric activity diagnostics (Montes et al. 1996), but also for transition region (Oranje 1986) and coronal activity indicators (Saar & Schrijver 1987).

A simple visual inspection of Fig. B.1 shows that all the K7 and M dwarfs (both emission-line and non-emission-line K7 and M dwarfs) follow the same trend as that defined by the rest of the active stars in the logarithmic diagrams between pairs of excess flux density when only Ca II lines are involved, since their corresponding marks lay within the region between the dotted boundaries in all the panels shown in this figure. However, even though non-emission-line K7 and M dwarfs, and even emission-line K7 dwarfs, follow the trend inferred from the hotter active stars in the logarithmic diagram $\Delta F_{\mathrm{H}\alpha}$ – ΔF_{8542}, the emission-line M dwarfs are clearly out of this trend (see left panel in Fig. B.2). We expect the emission-line M dwarfs having the same behaviour in the logarithmic diagrams between $\Delta F_{\mathrm{H}\alpha}$ and the excess flux density in the rest of the Ca II lines analysed by us. This is because, as seen above, the emission-line M dwarfs follow the same linear trend as that followed by the rest of active stars in each one of the logarithmic diagrams between ΔF_{8542} and the other Ca II lines analysed by us. The expected behaviour is in fact observed in the logarithmic diagrams $\Delta F_{\mathrm{H}\alpha} - \Delta F_{8498}$ and $\Delta F_{\mathrm{H}\alpha} - \Delta F_{8662}$, but when $\Delta F_{\mathrm{H}\alpha}$ is compared with $\Delta F_{\mathrm{CaIIK}}$ or $\Delta F_{\mathrm{CaIIH}}$, we find that the emission-line M dwarfs may follow the same trend as the rest of the active stars. Nevertheless, we note that the uncertainty in the measurements of the Ca II H & K lines is so high that the difference expected for emission-line M dwarfs could be masked by large spread in the measured values of excess flux densities in these two lines.

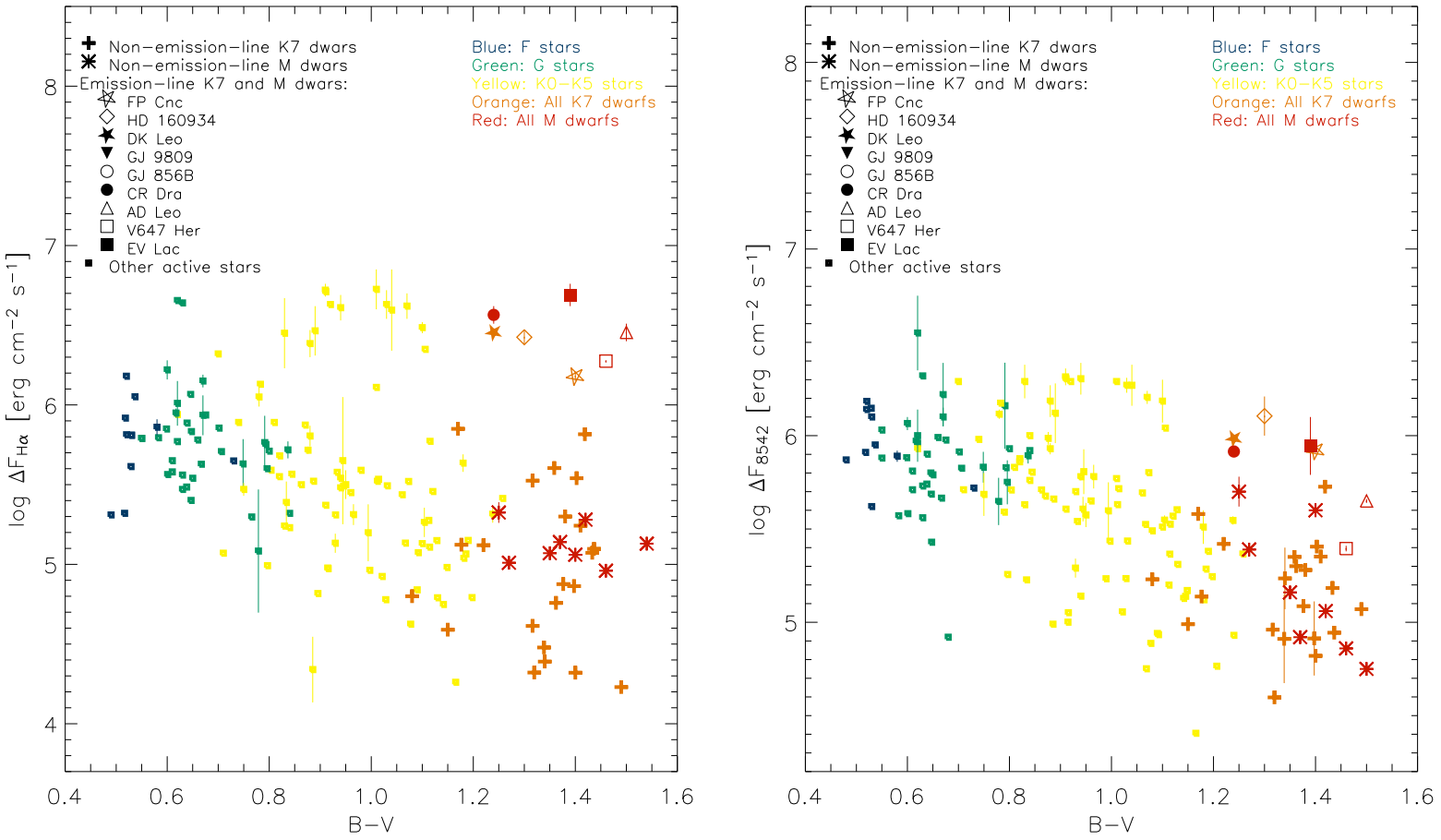

Figure B.3: *Left panel)* Excess flux density in the Hα line vs. colour index $B - V$. *Right panel)* Excess flux density in the Ca II λ8542Å line vs. colour index $B - V$. In both panels, colours and symbols have the same meaning as those used in Fig. B.1.

B.4 Discussion and preliminary conclusions

For the first time, we have shown that not all the M-type stars, but only M dwarfs with emission features deviate systematically from the trend established by hotter active stars in some chromospheric flux-flux diagrams. Schrijver & Rutten (1987) and Rutten et al. (1989) suggested the possible existence of a deficiency in the chromospheric emission of the Ca II H & K lines from M-type dwarfs. However, we note that the M stars showing departures from the main trend (emission-line M dwarfs) are just those M stars with stronger excess flux density in the Ca II H & K lines. Besides, the emission-line M dwarfs in LS10 are well-known flare stars. Thus, and bearing in mind that during flare events the growth of the Balmer lines is observed to be larger than that observed in the Ca II lines (see e.g. Chapter 3 Hawley et al. 2003; Crespo-Chacón et al. 2004), we wonder if flare-induced variations could be compatible with an Hα excess being the cause of the departure of emission-line M dwarfs from the trend followed by the rest of the active stars in the flux-flux diagrams of interest. In particular, in the following lines we investigate if flare events as those of Chapter 3 could induced these departures.

In Chapter 3 we reported results from a high temporal resolution spectroscopic monitoring of the star AD Leo (which is included in Figs. B.1 to B.2). Studying the temporal evolution of the Balmer series and Ca II H & K lines, we detected frequent (> 0.71 flares/hour) short and weak non white-light flares. Some of these events lasted as short as 14 min. Additional observations in Appendix A suggest that this kind of frequent short flares is common to occur on UV Ceti-type flare stars. The typical exposure times for the spectra in LS10 is ~ 25 min. Thus, one or at most two of this kind of flare events probably occurred on the UV Ceti-type flare stars during their observation. In Chapter 3, a typical value of 10^{30} erg was derived for the energy released in the Hα line by a flare event of the above type. This implies that this kind of flares would contribute with a mean Hα surface flux of the order of 10^5 erg cm^{-2} s^{-1}. Thus, one (or even two) of these events taking place on the emission-line M dwarfs during observations by LS10 would only introduce a little increase in their measured $\Delta F_{\mathrm{H}\alpha}$ if their quiescent emission were in the general trend followed by the rest of the active stars, but it would not account for the amplitude of their observed deviations (see e.g. the left panel in Fig. B.2). Moreover, the emission-line M dwarfs seems match a linear trend (but always different than the trend followed by the rest of the active stars) in the logarithmic diagrams plotting $\Delta F_{\mathrm{H}\alpha}$ vs. ΔF_{8542} or another line from the Ca II IRT[6]. Note that a trend like this could not be the result of some flare events of this type occurring randomly in the atmosphere of the emission-line M dwarfs during the time they were observed by LS10.

B.5 Future work

In Martínez-Arnáiz et al. (2011a,b) we have confirmed, using a larger sample of stars (including those in LS10, the 173 active stars in Martínez-Arnáiz et al. (2010), and additional observations of 21 late K and M stars), the clear departure of emission-line M

[6]The low number of emission-line M dwarfs in the LS10 sample prevents us from giving conclusive results in this respect.

dwarfs from the classical flux-flux relationships. As seen in this Appendix, these stars define an upper branch in some flux-flux diagrams. In this work we have shown that the stars in the secondary branch have saturated chromospheric and X-ray emission. From the study of several age spectroscopic indicators, we have also shown that the stars on the upper branch are younger than those stars situated on the lower branch. This result suggests that the stars move from one branch to the other during their evolution.

When plotting $\Delta F_{\mathrm{H}\alpha}$ and ΔF_{8542} vs. the index colour B - V for all the stars in LS10 (see Fig. B.3), a clear gap in excess flux densities is observed between emission-line M dwarfs and non emission-line M dwarfs. Moreover, no matter the spectral type, two different branches are observed in each one of these plots. It is our believe that this gap is the result of a rapid decay of the magnetic flux at a crucial stage of the stellar life that emission-line M dwarfs have not reached yet.

Böhm-Vitense (2007) found that solar-type stars can be divided into two groups, depending on the ratio between their activity cycle and their rotation period. The author interpreted this result as the consequence of a different dynamo at work in the stars, which produces a change in deep mixing. Additionally, our result about the flux-flux relationships suggests that a change occurs in a star during its evolution.

To confirm this hypothesis, it is needed to complete the sample with observations of weak-line T Tauri stars (very young stars without an accretion disk) and determine ages for each star in our sample. It would be also desirable to find stars in between the two branches. In addition, flux-flux relationships may be used to investigate the structure of the outer layers of the stars, their density and temperature stratification.